Imaging Corneal Stiffness with Optical Coherence Elastography

Mitchell A. Kirby

A dissertation

Submitted in partial fulfillment of the

requirements for the degree of

Doctor of Philosophy

University of Washington

2021

Reading Committee:

Matthew O'Donnell, Co-chair

Ruikang K. Wang, Co-chair

Tueng T. Shen

Program Authorized to Offer Degree:

Department of Bioengineering

University of Washington

Abstract

Imaging Corneal Stiffness with Optical Coherence Elastography

Mitchell A. Kirby

Chair of the Supervisory Committee:

Matthew O'Donnell

Ruikang K. Wang

Department of Bioengineering

Optical coherence elastography (OCE) can provide clinically valuable information based on local measurements of corneal stiffness. Corneal stiffness measurements may enable an individualized biomechanical model of the eye, monitor progression of ectatic changes in the cornea, and guide customized treatment plans. In this thesis, the physical structures which contribute to corneal biomechanical properties were described and a method presented to quantify elastic moduli responsible for corneal deformation using propagating elastic waves within the cornea. A fully non-contact system was developed to launch elastic waves using acoustic micro-tapping (AμT) and track their propagation with phase-sensitive optical coherence tomography (OCT). A nearly incompressible transversely isotropic (NITI) model of corneal biomechanics was developed for accurate reconstruction of elastic moduli. The biomechanical reconstruction method was

demonstrated in ex vivo porcine cornea and validated with conventional mechanical tests. This work provides a solid foundation that can be built upon to develop a non-contact, non-invasive clinical tool based on OCE to simultaneously map geometric (curvature and thickness) and elastic (Young's modulus and additional shear modulus) properties of the cornea. Future applications of this work include the potential for pre-operative diagnostics and direct evaluation of post-operative outcomes in refractive correction surgeries.

Acknowledgments

There have been significant contributions to this work from all members of both the BAIL and uWAMIT groups at UW BIOE. Contributions from John J. Pitre, Jr., David Li, Tueng Shen, Ruikang Wang, Matthew O'Donnell, Ivan Pelivanov, Shaozhen Song, Nhan Le, and Ryan T. Wallace are particularly recognized.

This work was supported, in part, by NIH grants R01-EY026532, R01-EY024158, R01-EB016034, R01-CA170734, and R01-HL093140, Life Sciences Discovery Fund 3292512, the Coulter Translational Research Partnership Program, an unrestricted grant from the Research to Prevent Blindness, Inc., New York, New York, and the Department of Bioengineering at the University of Washington.

This work was also supported by NSF graduate fellowship (No. DGE-1256082). This material was based upon the work supported by the National Science Foundation Graduate Research Fellowship Program under Grant No. DGE-1256082.

Kit Hendrickson is acknowledged for preparing a number of figure illustrations.

Dr. Yak-Nam Wang and the Center for Industrial and Medical Ultrasound at the University of Washington is acknowledged for their assistance in acquiring tissue samples.

Finally, none of this would have been possible without the support of friends and family.

Table of Contents

List of Figures

List of Tables

Chapter 1: Introduction

Nearly every human will experience some degree of worsening visual performance with age. As such, understanding and improving vision remains a high priority in Ophthalmology.

The modern era of imaging in Ophthalmology began with Hermann von Helmholtz's ophthalmoscope in 1851.[1] With the ophthalmoscope, a provider could visualize the retina, optic disc, and vitreous as a part of a routine eye examination. With the invention of the slit lamp in 1911, an illuminated magnified view of both the anterior and posterior segment of the eye provided additional information for clinical decision-making. Throughout the 20th century, the slit lamp was used to address and treat numerous conditions affecting the retina and lens, leading to the development of many modern interventions, including ophthalmic microsurgeries (Cataracts) and refractive surgeries (LASIK).[2] Ophthalmology was again revolutionized in the early 1990's with the development of optical coherence tomography (OCT), providing clinicians with micron-level resolution images of both ocular structures[3] and vascular function.[4,5] Sufficient diagnostic advantages have been demonstrated using computer-aided OCT and is now the gold-standard to monitor physiologic function in the posterior segment of the human eye.[6]

While significant progress has been made toward diagnosing and treating ailments of the posterior segment using OCT, treatment and monitoring of the anterior segment (comprising of the cornea and sclera) remains less developed. To-date, most diagnostic metrics of the anterior segment focus exclusively on shape and thickness measured using tomography or topography. Considering the cornea and sclera provide both protection from external irritants and account for 70% of the eye's refractive power, it is clear that they play a crucial role in visual performance. If corneal shape is not optimal, images formed on the retina will be aberrated.

Treating corneal shape as the primary determinant of visual performance, numerous procedures have been developed to correct for mis-shaped cornea. There are over 1 million refractive surgeries performed each year in the USA, yet there are no clinical tools that can predict corneal shape from interventions such as LASIK, PRK, or collagen-cross linking (CXL). Even though refractive surgeries have shown overall success in halting disease and improving vision, suboptimal visual outcomes and post-refractive corneal decompensation remain unpredictable for an individual patient. To optimize outcomes, a personalized biomechanical model based on quantitative maps of corneal mechanical moduli is needed to quantify both local biomechanical properties and predict final corneal shape.

There are numerous clinical tools available to assess corneal shape, yet there are currently none that directly map corneal elasticity. While technologies based on tonometry (e.g. Ocular Response Analyzer (ORA), Dynamic Scheimpflug Analyzer (DSA)) have shown some success in correlating biomechanical estimates with disease progression,[7,8] these methods rely on a number of novel metrics that indirectly assess elastic moduli responsible for corneal deformation.[9–13] Additionally, tonometry-based techniques often require a non-trivial IOP correction in finite element simulations[9,14] and assume a simple isotropic mechanical model, leading to high variability depending on experimental conditions. Thus, there are no clinically available tools to determine fundamental material parameters required for robust biomechanical models of corneal deformation.

There have been a number of methods proposed recently to measure tissue biomechanics using traditional imaging methods such as Computed Tomography (CT), Magnetic Resonance Imaging

(MRI), and Ultrasound Imaging (US). However, limitations in resolution and practicality (i.e. contact gel in US) prevent the methods from widespread use in anterior segment imaging.

Recently, optical coherence elastography (OCE) has been used to measure corneal stiffness at various length scales while simultaneously mapping shape in a single non-invasive measurement.[15] Advances in both the sensitivity and imaging speed of phase-sensitive optical coherence tomography (OCT) have led to non-contact imaging systems that track propagating elastic waves launched by low-amplitude excitation. Assuming an appropriate corneal mechanical model, dynamic OCE can measure in near real-time both the shape and biomechanical changes resulting from keratoconus and CXL surgery, with the potential for moduli mapping at high spatial resolution.[16–18]

The goal of this thesis is to outline biomechanical parameters of the human cornea that contribute to visual performance and can be used to aid in diagnosis and treatment of corneal disease. A theoretical basis of elastic wave propagation in the cornea was developed to provide a path to measure mechanical properties and demonstrated in ex vivo porcine tissue. Technical considerations are presented toward developing an imaging system with sufficient resolution, sensitivity, and speed for clinical use. Finally, preliminary results from in vivo OCE on an animal model as well as on human research tissue in a refractive stabilization procedure (namely, corneal cross linking, CXL) are included.

1.1 Specific Aims

The aim of this research was to address limitations preventing clinical adoption of optical coherence elastography (OCE). First, complex models of wave propagation in cornea-like

structures were developed and technical challenges discussed which enable quantification of localized elastic moduli using wave-field measurements. Next, a stable optical coherence tomography (OCT) system combined with a non-contact air-coupled ultrasound transducer was described to excite and track elastic waves in the cornea. Finally, the technique was demonstrated using ex vivo and in vivo animal models, as well as on ex vivo human tissue.

I. Develop accurate biomechanical models of elastic wave propagation within the cornea

To convert mechanical wave-fields into elasticity maps, proper mechanical models are required. In most OCE studies to date, the cornea was treated as either an isotropic bulk or semi-infinite material. As such, mechanical waves propagating in the cornea were treated as Rayleigh waves and the group velocity was inaccurately used to estimate the elastic modulus.[15,16,19–26] In this work, analytical solutions to wave propagation in media bounded above by air and below by water (similar to aqueous humor) were presented which demonstrate that group velocity approximations lead to an incorrect description of corneal elasticity. Additionally, the cornea is mechanically anisotropic.[27] Because it is a complicated material that cannot be characterized with a single elastic modulus, complex models are required to provide quantitative measurements from propagating elastic wave fields. A model of a nearly incompressible transversely isotropic (NITI) medium was presented based on tissue microstructure which enabled accurate quantification of elastic anisotropy (i.e. in-plane, E, and out-of-plane, G, shear moduli) using wave-based OCE.

II. Design and fabricate a non-contact OCT-system capable of high-resolution imaging based on elastic waves

Improved light sources and scanning methods in optical coherence tomography (OCT) have led to rapid growth in high-resolution, quantitative elastography based on imaged displacements and strains within soft tissue to infer local mechanical properties. In this work, a stable, phase-sensitive spectral-domain OCT system was built to analyze wave-fields generated via non-contact acoustic excitation. The non-contact acoustic micro-tapping OCE (AμT-OCE) system demonstrated nanometer-scale sensitivity to motion in the cornea. The system allowed for cross-sectional imaging of corneal shape and accurate reconstruction of propagating shear wave-fields in under 2 seconds. The ability to quantitatively contrast elasticity was demonstrated using controlled tissue-mimicking phantoms and validated via destructive mechanical testing. This work also demonstrated that the ultimate resolution in elasticity maps is defined by the wavelength of a propagating elastic wave signal, which in turn is defined by the focal zone of the excitation.[18]

III. Develop, optimize, and demonstrate an elastic modulus recovery routine in the cornea using AμT-OCE

The OCT system developed in Objective II demonstrated state-of-the-art signal to noise ratio (SNR) and was used to quantify elastic moduli in the cornea based on the biomechanical models of wave propagation developed in Objective I. Experimental wave-fields were captured and compared with analytical models for reconstructing elastic moduli of both tissue-mimicking phantoms and ex-vivo cornea samples. Quantitative measurements of corneal biomechanics were validated using the current gold standard of destructive mechanical testing.

1.2 Thesis Outline

Chapter 1. Introduction

Chapter 2. Cornea structure and anterior segment imaging

This chapter describes briefly collagen micro- and macro- structure as they relate to corneal function. Current clinical diagnostic systems and their limitations are presented and discussed, as well as a brief overview of corneal biomechanical properties and their role in clinical decision-making.

Chapter 3. Elastic waves in the cornea

This chapter presents a theoretical description of the biomechanical properties that determine corneal shape. A nearly incompressible transversely isotropic (NITI) material model was developed to describe elastic wave behavior in cornea-like material. Broad-band propagating elastic waves in NITI materials with a thickness on the order of the wavelength travel according to two independent shear moduli and provide a method to quantitatively measure corneal elastic moduli.

Chapter 4. Elastic wave imaging using Optical Coherence Tomography

The design and construction of a phase-sensitive OCT system capable of imaging elastic waves in tissue is presented and demonstrated in Chapter 4. A totally non-contact acoustic transducer was used to generate elastic waves and integrated with an OCT system with flexible timing control. The ability to measure elastic moduli was demonstrated and validated using tissue-mimicking phantoms. A framework describing system resolution and contrast was presented alongside a Finite-Element-Based simulation package.

Chapter 5. Quantifying elastic moduli in the cornea with AμT-OCE

A model-based fitting routine is presented to accurately quantify elastic moduli in corneal samples accounting for curvature, thickness, and mechanical anisotropy. AμT-OCE was demonstrated in ex vivo porcine cornea to accurately quantify biomechanical properties. Whole globe samples were retained, and corneas were scanned while inflated to various intraocular pressures. All results were validated using destructive mechanical testing.

Chapter 6. Future studies and limitations

In the body of this work, a fully non-contact system was developed to launch mechanical waves in the cornea using acoustic micro-tapping and track their propagation with ultra-fast OCT. The ability to simultaneously map geometric (curvature and thickness) and elastic (Young's modulus and additional shear modulus) properties was demonstrated and validated using ex vivo porcine cornea. However, there remain a number of steps required to provide a non-contact, non-invasive OCE system well suited for clinical use. The final chapter provides discussion on design requirements required for clinical translation. Preliminary results are presented using ex vivo human tissue to demonstrate the potential to monitor treatment and in vivo imaging using a Rabbit animal model.

Chapter 2. Cornea structure and anterior segment imaging

2.1 Corneal microstructure

The human cornea provides structure and function to the visual system, serving as a transparent protective barrier which accounts for two-thirds of the eye's refractive power.[28] The cornea structure, consisting of collagen fibrils embedded in a hydrated proteoglycan matrix, forms a clear refractive lens and is the primary determinant of visual performance.[29]

The unique structure and organization of collagen within the cornea is essential for preserving shape and maintaining transparency. Most of the collagen is Type I, containing fibrils within the stroma that run the entire plane of the cornea, presumably fusing with fibrils in the limbus or sclera.[30] The diameter of each collagen molecule (measured via x-ray diffraction) is on the order of 30- 250 nm[31,32] and arranged into fibrils which contain approximately 250 collagen molecules per cross-section. While the precise fibril spacing can be difficult to measure, intra-fibrillar spacing is approximately 60 nm from center to center.[33] The fibrils are more tightly packed in the anterior portion compared to the posterior, but are generally arranged within the stroma in 200 - 300 stacked sheets (1-2 μm thick) referred to as lamellae.[34] A majority of the fibrils have preferential orientation (measured via X-ray scattering) in the inferior-superior and nasal-temporal directions, becoming more circumferential near the limbus[35,36] with significant fiber branching and anastomosis, particularly in the anterior portion.[34] The lamellae lie within a protein rich, hydrated proteoglycan mesh that can swell with water to meet certain metabolic demands. It is largely assumed that the proteoglycan mesh determines the relative spacing of the fibrils[37,38] and ultimately determines the light scattering behavior of the cornea.[39]

Recently, Second Harmonic Generation (SHG) imaging has evolved into a very useful tool to reconstruct 3D structure of collagen fibers over tens of mm ranges.[40–43] In SHG, pulsed, focused, infrared femtosecond laser light is used in non-centrosymmetric materials (such as collagen fibers along the fiber axis) to excite and detect photons ½ the incident wavelength (double the frequency) to reconstruct high resolution, depth resolved images. SHG can resolve collagen organization at the macroscopic level, creating detailed images of bundles, fibrils, and lamellae. Through advances in computation, laser scanning, and digital mosaicking, detailed high-resolution 3D images of the cornea can be obtained.[34,40,42,44]

In **Fig. 2-1** (adapted from Ref[42]), 3D reconstruction of lamellar organization in human corneal collagen shows complex branching patterns, with distinct differences in the anterior and posterior portions of the cornea. The anterior part of the stroma exhibits a high-degree of inter-lamellar connectivity while the posterior lamellae contains little to no branching. Imaging results suggest that the complex micro-network of collagen bundles contribute to macro-scale deformation and strength.

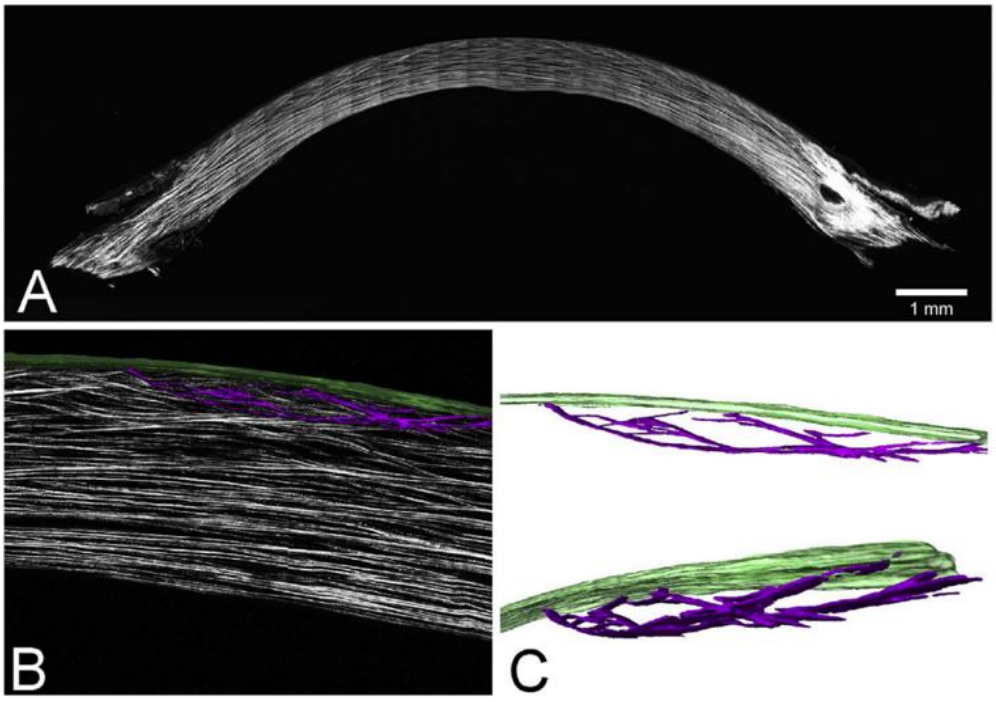

Figure 2-1. Corneal microstructure. SHG backscatter was used to contrast collagen in a human corneal cross-section (high-resolution macroscopy (HRMac), adapted from Ref[42]). a) 80 images stitched together to provide a wide field of view. The lamellar organization of the cornea can be appreciated in this image, where the sheets generally run along the width of the cornea. Note that in b) and c), the lamellae exhibit additional branching and complexity along the anterior surface.

Imaging methods to visualize corneal structure are essential in diagnosis and treatment of ocular diseases. However, clinically available systems remain largely dominated by tomography and topography techniques that do not provide collagen-level detail. Instead, diagnosis and management of corneal disease is often driven by corneal shape and thickness.

In topography, the anterior shape of the cornea is measured to detect refractive aberrations. If corneal shape is compromised, the reflecting pattern provides a qualitative measure of astigmatism. While this technique has been able to detect abnormal anterior elevation in

progressing keratoconus, it can only analyze the anterior surface and often mis-diagnoses ectasia on the posterior surface of the cornea.[45]

Tomographic techniques can be used to generate a three-dimensional image of the entire cornea. This is often achieved by rotating Scheimpflug cameras or OCT systems designed to image the anterior-segment.[45] There are clinically approved devices based on both techniques, and both have been used to map the anterior and posterior surface to detect abnormal corneal thinning. However, tomography does not provide information on the structural stability of the collagen that ultimately determine corneal performance.

2.2 Corneal biomechanics

In pathologies affecting the cornea, microstructural changes in collagen fibers and the proteoglycan-rich fluid that make up the stroma alter the macro-scale biomechanical response of the cornea.[46–48] Fibrous collagen is known to exhibit a unique tensile strength along the direction of the fibers. Because the tensile strength is much weaker perpendicular to the fibers, fiber orientation contributes significantly to the overall strength of the tissue. Clearly, the corneal constituents' mechanical properties regulate shape in order to focus light through the lens and onto the retina (**Figure 2-2**).[49,50] While biomechanical alterations in collagen micro-structure often correspond with a change in shape or thickness, structural changes likely follow mechanistic changes in collagen structure. As such, mechanical properties may provide more direct information on disease progression, providing higher diagnostic value and opening up the possibility of personalized models of corneal shape.[29,49–51]

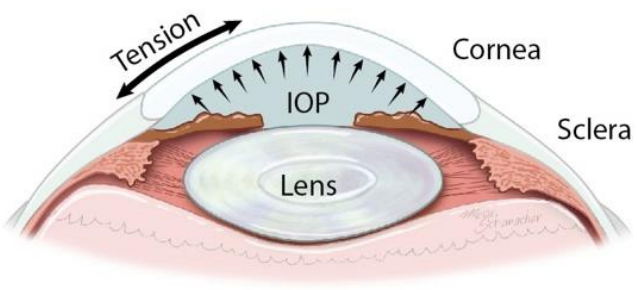

Figure 2-2. Static forces in healthy human cornea. Tissue constituents in the healthy cornea determine shape and focus light onto the lens.

Although corneal micro- and macro-structure contributions to corneal transparency have been relatively well characterized, the mechanisms that physically control corneal shape and focusing remain largely speculative. For example, a loss in lamellar inter-connectivity would presumably result in a higher degree of lamellar slippage while degradation in fiber strength along its axis would result in reduced tensile strength and a corresponding change in shape. For example, keratoconus (a progressive disease of the cornea that results in thinning and bulging) is associated with reduced interlamellar branching in the anterior portion and a measurable reduction in tensile modulus.[43] Reduced biomechanical stability due to lamellar slippage and collagen degradation has been suggested as a potential mechanism behind disease progression.[45,50,52,53]

Although the mechanisms behind corneal shape are well accepted to be biomechanical in nature, mechanical test results remain difficult to interpret depending on the experimental conditions. For example, the reported values of elastic moduli in human and animal eye tissue often vary for in vivo and in vitro conditions and according to both length scales and loading specifics determined by the method of evaluation. The reported differences between healthy and diseased tissue are large enough to potentially be clinically relevant (**Table 2-1**, adapted from [15]) and have even been used to drive clinical intervention. For example, keratoconic cornea are measurably less stiff than healthy ones,[49] an observation which led to clinical intervention increasing stiffness (e.g. cornea cross-linking).[54] In refractive-correcting procedures such as LASIK and photorefractive

keratectomy (PRK), an incision presumably releases stromal tension, inducing structural and shape changes that adjust focusing.[50]

Tissue Type	Measurement condition	Disease State	Young's Modulus
Cornea (Human)	Tensile Testing,[55] Orssengo-Pye algorithm,[56] Inflation Testing[57]	Normal Collagen cross-linking Middle Age (50-64) Old Age (65-05)	.29 -1.3 MPa 5.9 MPa 25 – 400 kPa 200 – 580 kPa
Cornea (Porcine)	OCE (air-puff)[21,58,59]	Collagen cross-linking	43.9- 110 kPa
Anterior Lens Capsule (Human)	Atomic Force Microscopy[60] Tensile Testing[61]	Normal Cataract Young Age Old Age	485 kPa 416 kPa 27.4 MPa 3.3 MPa
Lens nucleus (Human)	Micro-Bubble based Acoustic Radiation Force[62] Spin Test[63,64]	Middle Age (40-50 years old) Old Age (63-70 years old)	.19- 5.2 kPa 3-10.6 kPa
Retinal Tissue (Bovine) Retinal Tissue (Porcine)	Mathematical Model[65] OCE (Acoustic radiation force)[66]	Healthy Healthy	26 kPa 6.2 kPa
Sclera	Tensile testing[67] Biaxial Tensile Testing[68]	Healthy	2.6 MPa 14 MPa

Table 2-1. Reported values of Young's moduli for ophthalmic tissue in various physiologic states, at physiologically relevant pressures.

Reliable measurements of ocular mechanical properties have historically only been possible on ex vivo samples and have not yet impacted the clinic directly.[69] Even within ex vivo testing, there are large discrepancies between reported values of elasticity for fresh healthy cornea, depending on the loading method, reconstruction method, and assumed model (Table 2-2).

Tissue Type	Loading Condition	Loading Rate	Reconstruction Method	Assumed Model	Young's Modulus (E)	Shear Modulus (μ)
Porcine	15mmHg - 140mmHg Inflation/Displacement	Dynamic	FEM	Hyperelastic nonlinear Ogden material	300kPa[47]	-
Porcine	15mmHg - 30mmHg Inflation/Air-puff	Dynamic	FEM	Generalized Maxwell viscoelastic	2.6 MPa[70]	-
Porcine	15mmHg Inflation/Air-puff	Dynamic	FEM	Hyperelastic Mooney Rivlin	.99-1.59 MPa[71]	-

Porcine	Tensile	Quasi-static	Stress-strain	-	1.15-1.93 MPa[71]	-
Porcine	0mmHg - 40mmHg Inflation/Air-puff	Dynamic	Pressure-Deformation	Thin shell	.1-.3 MPa[72]	-
Porcine	Tensile	Quasi-static	Stress-strain	-	3.193±1.589 MPa[72]	-
Porcine	.75mmHg - 170mmHg Inflation	Dynamic	Pressure-Deformation	Thin shell	.15-.3 MPa[73]	-
Porcine	Tensile	Quasi-static	Stress-strain	-	.3-1.1 MPa[74]	-
Porcine	20mmHg Inflation/Air-Puff OCE	Dynamic	Modified Rayleigh-Lamb Equation	Isotropic Homogenous Viscoelastic	60 kPa[21]	-
Porcine	15mmHg - 30mmHg Inflation/Air-Puff OCE	Dynamic	Modified Rayleigh-Lamb Equation	Isotropic Homogenous Viscoelastic	41.8-157 kPa[58]	-
Porcine	Compression	Dynamic	Transient compression stress relaxation	Transverse Isotropic Biphasic	5.61±2.27 kPa (compression)[75] 1.33± .51 MPa (tension)[75]	-
Porcine	Compression	Quasi-static	Compressive strain	Transverse Isotropic Biphasic	.65-6.32 MPa[76]	-
Porcine	Oscillatory shear	Dynamic (.01-2 Hz)	Shear strain	-	-	2.5-9 kPa[77]
Porcine	0mmHg - 30mmHg Inflation	Quasi-static	Pressure-Deformation	Linear elastic	2.29±1.63MPa[78]	-
Porcine	15mmHg - 35mmHg Inflation/Air-puff	Dynamic	FEM	Linear isotropic viscoelastic	25.5 MPa (anterior)[79] .85 MPa (posterior)[79]	-
Porcine	15mmHg Inflation/Air-Puff OCE	Dynamic	Group Velocity	Homogenous linear isotropic	5.9±.6 kPa[59]	-
Porcine	Tensile	Quasi-static	Stress-strain	-	.8-2.2 MPa[55]	-
Porcine	Tensile	Quasi-static	Stress-strain	-	3.70± .24 MPa[80]	-
Human	Oscillatory shear	Dynamic (.01-2 Hz)	Shear strain	-	-	3-15 kPa[77]
Human	Tensile	Quasi-static	Stress-strain	-	.34-4.1 MPa[81]	-
Human	Acoustic Vibration	Dynamic (50-600Hz)	FEM	Linear isotropic viscoelastic	24.8 kPa (anterior) 19.8 kPa (posterior)[82]	-
Human	15mmHg - 35mmHg Inflation/Air-puff	Dynamic	FEM	Linear isotropic viscoelastic	.71MPa[79]	-
Human	Oscillatory shear	Dynamic (.03 Hz)	Shear strain	-	-	38.7±8.6 kPa[83]
Human	1D Shear	Quasi-static	Shear strain	-	-	10-90 kPa (Nasal-Temporal)[84] 10-150 kPa (Superior-Inferior)[84]

Human	Tensile	Quasi-static	Stress-strain	-	.8-2.6 MPa[55]	-
Human	Tensile	Quasi-static	Stress-strain	-	3.81± .40 MPa[80]	-
Human	Tensile	Quasi-static	Stress-strain	-	19.1±3.5 MPa[85]	-
Human	.75mmHg- 160mmHg Inflation	Dynamic	Pressure-Deformation	Thin shell	.25-3 MPa[57]	-
Human	.75mmHg- 170mmHg Inflation	Dynamic	Pressure-Deformation	Thin shell	.2-.6 MPa[73]	-
Bovine	1mmHg - 10mmHg Inflation/Piezo-shaker motion MRE	Dynamic (300 Hz)	FEM	Linear isotropic	40-185 kPa[86]	-
New Zealand White Rabbit	15mmHg Inflation/Air-puff	Dynamic	FEM	Nonlinear Hyperelastic Mooney Rivlin plus a Prony-series viscoelastic	5 MPa[87]	-
Rabbit	15mmHg Inflation/Air-Puff OCE	Dynamic	FEM	Homogenous linear isotropic	500-800 kPa[88]	-

Table 2-2. Reported values of elastic moduli in cornea. Summary of biomechanical test methods and Young's and shear moduli in healthy ex vivo cornea in a number of mammalian species. Reported moduli vary by up to four orders of magnitude depending on the loading technique and test configuration. Included are moduli for the low-strain region where they generally are near their lowest value. Best effort was taken to report values for fresh tissue samples.

In practice, corneal microstructure is too complex to model directly, so assumptions are made to simplify mechanical descriptions. The most common model assumes a nearly incompressible, isotropic, and linear elastic solid. For this case, a single elastic parameter, the Young's modulus E (or equivalently the shear modulus $\mu = E/3$), defines stiffness[15] and has been correlated with a number of pathologies and used to design interventions.[27]

Traditional measurements of the Young's modulus require ex vivo tissue samples loaded under tension or inflation, with reported E values for human cornea (in the low-strain region) of 800 kPa to 4.7 MPa[55,71,72,80,85] and 100 kPa to 3 MPa for inflation loading.[72,73,89] However, over an order of magnitude difference has been reported in tissue under shear loading.[77,83] Clearly there is a need

to validate and standardize in vivo methods capable of robust and reliable measurement of modulus that are in careful agreement with ex vivo studies under various methods of loading.

Recently, technologies based on tonometry (e.g. Ocular Response Analyzer (ORA - Reichert Technologies), Dynamic Scheimpflug Analyzer (DSA - Corvis ST – Oculus Opitkgerate GmbH)) have been developed to estimate in vivo corneal mechanical properties as part of an intraocular pressure (IOP) measurement. Early results suggest that tonometry may be a screening tool for disease progression in common conditions linked to changes in elasticity, such as glaucoma and myopia.[7,8] Although these measurement systems have sparked interest in monitoring corneal biomechanics, they have significant limitations.[8] In particular, they depend on experimental conditions and provide measurements of the tissue response to a dynamic mechanical stimulus over a large region of the cornea and sclera, rather than detailed analysis of fundamental material parameters required for robust biomechanical models of cornea deformation. Additionally, they do not account for the highly non-linear stress-strain relation between corneal tissue and pre-load (IOP), nor do they account for variations in corneal thickness. Thus, to date, there are no non-invasive tools that can provide the information needed to develop a personalized biomechanical model of the cornea suitable for screening, surgical planning, and treatment monitoring.

2.3 Elasticity imaging

Advancements in non-invasive imaging speed and sensitivity have led to the development of elastography, a promising technique that can measure elastic moduli in tissue at various length scales. Elasticity imaging requires a physical stress to deform (displace) tissue and the resulting displacements are measured to compute strains, detect vibrations, or track the propagation of a mechanical wave.[15] The stress–strain response of tissue, local vibration behavior, or mechanical wave content, can each be mapped spatially to solve for elastic moduli.

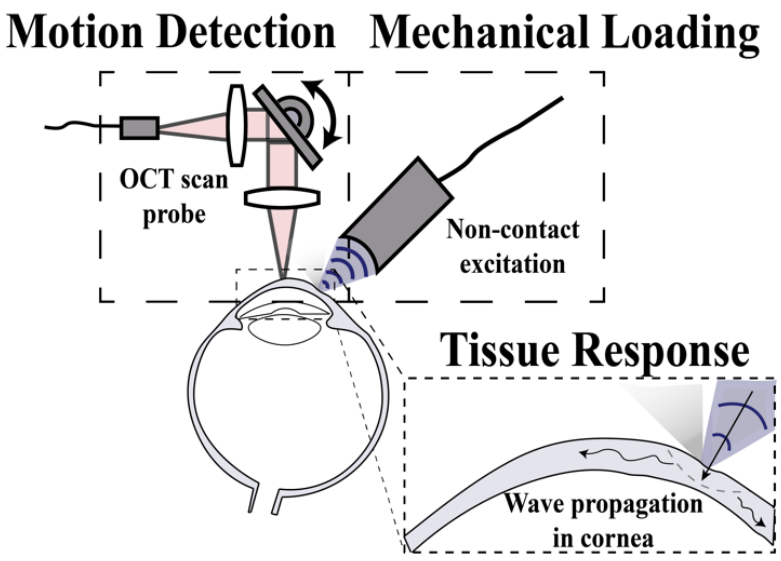

Figure 2-3. Schematic demonstrating a typical dynamic OCE system, based on AμT-OCE.

Elastography systems can be described in terms of the steps required to probe tissue elasticity: (1) mechanical loading, (2) motion detection, and (3) tissue response (**Figure 2-3**).

Typical approaches to mechanically load tissue can be characterized as static, or quasi-static compression,[90–94] vibration,[95–97] and transient excitation (wave propagation).[15,16,98–101] The specific method used to estimate tissue elasticity from localized motion must be considered at great length when choosing an excitation method. To this point, multiple methods have been used to mechanically load ocular tissue, including a curved plate,[102] wire-tip,[99,103] air-puff,[104–107] optical excitation,[108] acoustic radiation force (ARF),[109–111] and air-coupled ARF [or acoustic micro-

tapping (AμT)].[16,112,113] For visual reference, a summary of the primary characteristics of common excitation and detection methods are presented in **Figure 2-4**.

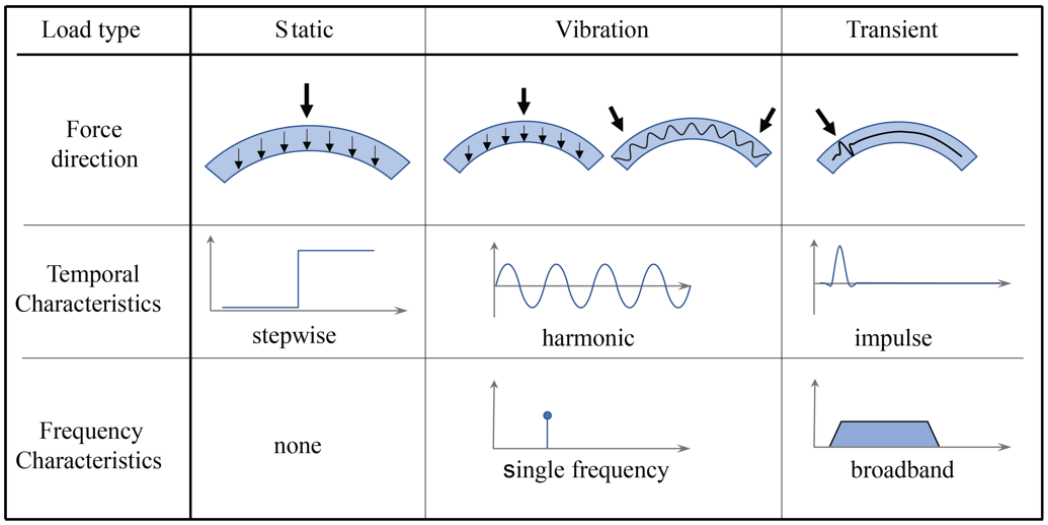

Figure 2-4. Common elastography loading types and the corresponding response

Early techniques to measure tissue response to load were developed using ultrasound and MRI. In these elastography techniques, relatively large tissue motion was related to local mechanical properties.[114–120] As MRI has inherently low spatial resolution with long imaging times, it is often not appropriate for clinical applications in the eye. An ultrasonic technique based on supersonic shear wave imaging (SSI) was introduced for corneal stiffness estimation, where SSI was performed on both ex vivo and in vivo porcine cornea, producing two- (2-D) and three-dimensional (3-D) maps of cornea stiffness.[121,122] However, SSI also has relatively low spatial resolution that remains largely limited by the host imaging modality of ultrasonography.[123] Additionally, it requires direct contact for acoustic coupling with the cornea, a feature that inherently causes patient discomfort and remains a practical challenge for translational ophthalmic research.

Optical coherence tomography is well-suited for imaging microscale displacements related to mechanical properties within the relatively transparent layers of the cornea and lens. OCT utilizes light scattering differences due to minute changes in the refractive index of different tissue and cell types to create a structural image of tissue. OCT has already been utilized for pachymetry and topography in some clinical settings.[124] In addition to micron-level spatial resolution, OCT can detect micro- and nanoscale tissue displacements over micro-second time frames.[125] Such sensitivity to motion has led to high resolution mapping of vasculature[126] and has made the transition from a benchtop system to clinical device, revolutionizing the way the retina is studied.[6] Because of the resolution and sensitivity characteristics, as well as clinical translatability, specific configurations of OCT are promising to measure mechanical moduli (referred to as optical coherence elastography (OCE)).

There has been progress in recent years to develop OCE for in vivo testing of corneal biomechanics. Currently, most OCE methods utilize static loading techniques, where an external load deforms soft tissue and the resulting strain is observed or measured with OCT to derive an elasticity map based on speckle tracking or signal phase.[92,94,127,128] Static approaches, however, are often limited by operator-dependence (variability in the applied deformation) and non-quantitative modulus estimates due to sensitivity to boundary conditions (such as uneven stress distribution).

In dynamic OCE, the inversion from a force-response to elastic moduli requires a temporally short axial displacement at a tissue surface to launch a mechanical wave within the sample. The resulting wave behavior (i.e., speed, dispersion, attenuation, etc.) depends on the mechanical properties and can be used to probe local elasticity. Dynamic OCE has been demonstrated widely in controlled environments using acoustic radiation force (ARF),[109–111] air-puff,[104–107] photothermal techniques,[108] and AμT[16,112,113] to induce a dynamic load. Phase-sensitive optical coherence tomography (PhS-OCT) has been used to detect surface and bulk acoustic waves propagating in phantoms, skin, and cornea, leading to quantitative maps of underlying tissue elasticity.

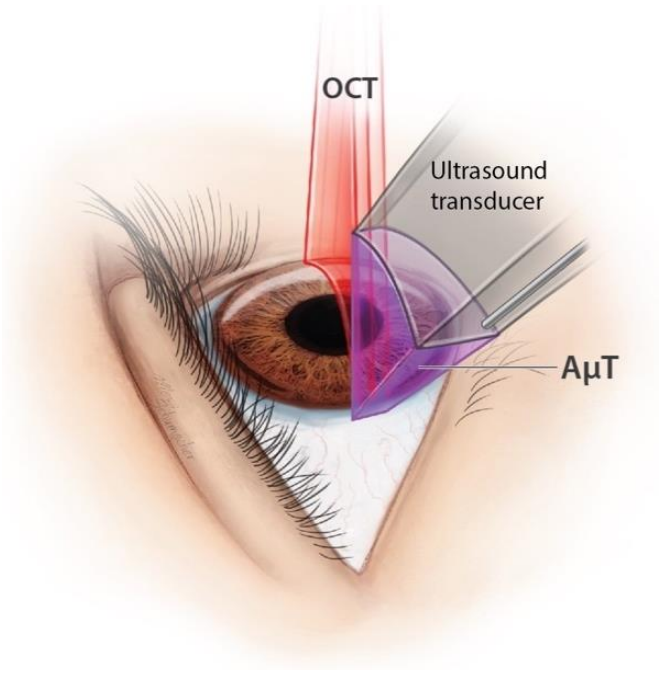

Figure 2-5. Schematic of AμT-OCE

Although systems based on transient excitation (i.e. an air-puff OCE system[129] and a contact-based loading method utilizing anesthetic drops[130]) have demonstrated some utility in a clinical setting, a truly noncontact system developed to both induce and measure small displacements within the eye will likely have the fastest path to clinical adoption. Thus, air-coupled ARF (AμT) paired with high-speed OCT[113] appears to be the most translatable in probing ocular biomechanics (**Figure 2-5**). Still, there remain numerous practical and theoretical issues regarding wave excitation and behavior that must be addressed to deduce a meaningful, quantitative measure of tissue stiffness.

While the internal stress distribution is not needed to reconstruct the modulus in dynamic OCE,[15] the relationship between wave behavior and elasticity is often complicated by conditions such as sample geometry, boundary conditions, excitation parameters, mechanical anisotropy, and viscosity, to name a few. To this point, rigorous modeling and finite-element-based (FEM) simulations have been developed to explore wave behaviors in the cornea.[131]

Using a combined FEM and experimental modeling approach, a number of limitations preventing dynamic OCE from providing spatial maps of elastic material parameters have recently been systematically addressed[15,18,27,132,133] and largely described within this work. For example, due to the cornea's finite thickness (bounded by air on one side and liquid on the other) complicated guided wave behavior was analyzed to prevent inaccurate interpretation of elastic moduli based on shear wave group velocity.[18,132,134,135] Additionally, corneal anisotropy between tensile and shear loading regimes was explored to develop a transversely isotropic (TI) model of the cornea which decoupled shear from tensile behavior, resolving a number of apparent paradox's in reported biomechanical properties,[27] an important step toward generalizing dynamic OCE for clinical translation.

Multiple steps in the design process were considered in this work to develop a clinically-driven OCE system capable of reliable and accurate measurements of elastic properties, thickness, and topography.

In the proceeding chapters, a theoretical analysis of tissue deformation and shear wave propagation in the cornea is presented. An exploration of elastic wave propagation in the cornea provided a reconstruction method to measure quantitative values of corneal stiffness. An air-coupled acoustic piezoelectric transducer combined with a highly sensitive phase-stable SD-OCT system is

described and used to generate and track elastic waves in corneal samples. The reconstruction method was used to measure both Young's modulus (E) and out-of-plane shear modulus (G) in the cornea that agreed with destructive ex vivo tests.

Robust and accurate measurements suggest that OCE may be used to illuminate biomechanical mechanisms behind corneal disease. Considering the connection between corneal microstructure and biomechanical stability, a system capable of high-resolution elastic modulus reconstruction may help launch large clinical studies in the future.

Chapter 3. Elastic waves in the cornea

Mechanical forces in the cornea largely determine the focusing power in both healthy and pathological tissue (**Figure 3-1a,b**). Thus, there is a need to develop a non-contact method to measure corneal biomechanical properties in vivo.

In 2016, an OCE technique capable of launching and tracking mechanical waves in near-real time (**Figure 3-1c**) was introduced at the University of Washington.[16] The technique used acoustic micro-tapping (AμT)[16,112] and fast, phase-sensitive, OCT (AμT-OCE)[17] to measure spatial variations in group velocity to demonstrate a volumetric rendering of shear wave speed in porcine cornea exposed to different intraocular pressures. While early application of AμT-OCE demonstrated that elastic waves could be generated and detected in corneal tissue non-invasively, numerous limitations remain that currently prevent clinical adoption.

Typically, wave-based OCE methods use the shear wave group velocity or dispersion to estimate tissue shear modulus, μ. However, group velocity approaches led to reported modulus values in the range of 1.8 – 52.3 kPa,[58,136] in close agreement with values obtained from torsional testing of ex vivo cornea (2.5 – 47.3 kPa),[77,83,84] but multiple magnitudes different from values obtained in strip extension or inflation testing. Estimates of tissue shear modulus can differ by multiple orders of magnitude based on the loading technique and corresponding constitutive equations (**Figure 3-1d**). Such discrepancies are not uncommon in biomechanical characterization of corneal stiffness and significantly limit clinical utility.

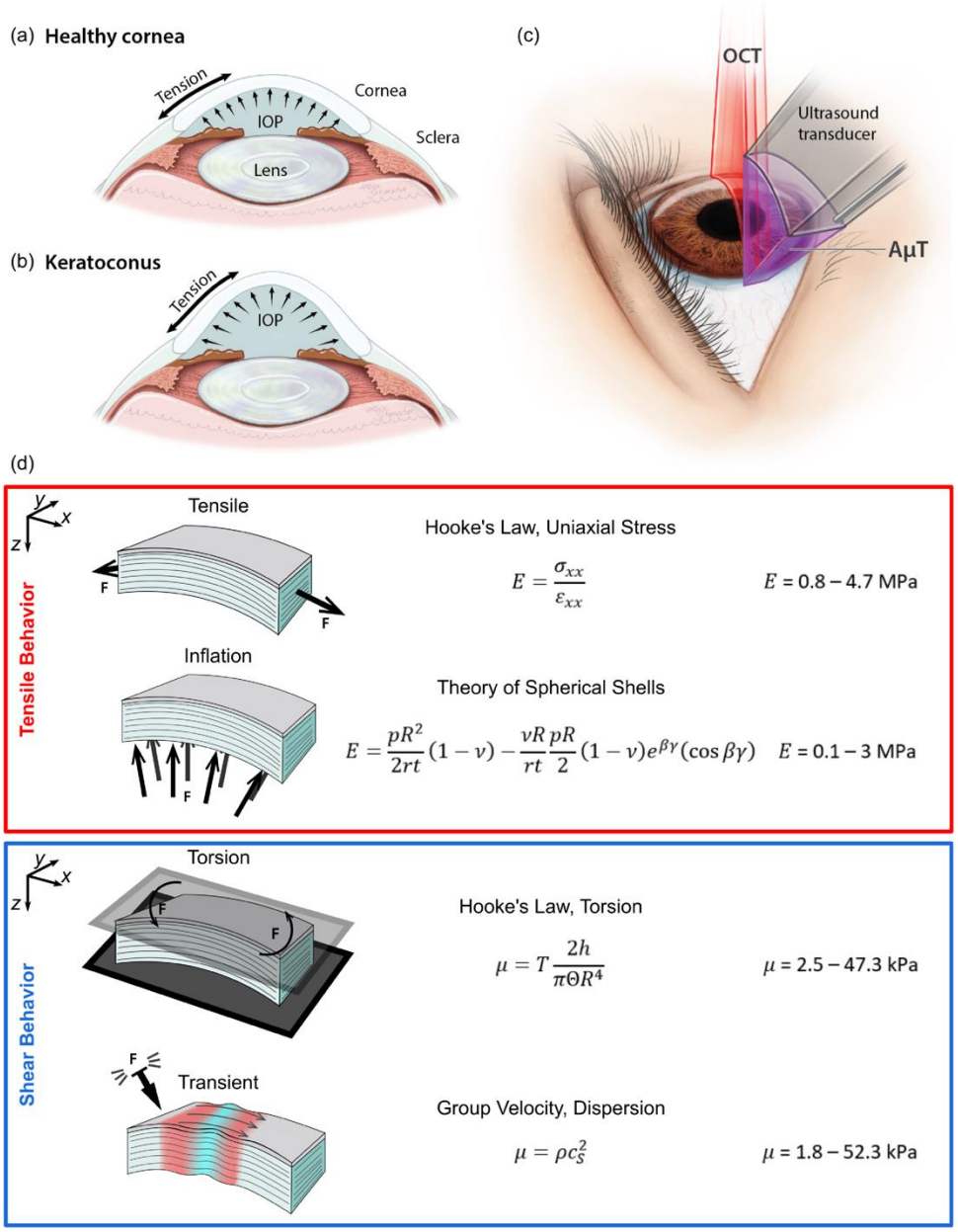

Figure 3-1. **Relationship between forces in the cornea and mechanical testing methods.** Mechanical forces in corneal tissue govern focusing power in (a) healthy and (b) pathological tissue (e.g. keratoconus). (c) Elastic shear waves generated in the cornea with a transient force (such as AμT) are typically tracked using optical coherence tomography to determine corneal mechanical properties without contact. (d) Summary of biomechanical test methods and corneal Young's and shear moduli from the literature. Reported moduli vary by up to four orders of magnitude depending on the loading technique and test configuration, suggesting that isotropic models cannot accurately describe corneal mechanics. In particular, tensile and inflation tests generally agree, as do shear and

transient tests. Values listed are for fresh samples (within two weeks), and best effort was taken to report moduli in the low-strain/preload region where they generally are near their lowest value.

In this chapter, corneal micro- and macro-structure are considered to build a mechanical model upon which induced deformations can be used to quantitatively measure corneal stiffness. The chapter starts with the simplest case of propagating elastic waves in an infinite isotropic media and then builds to complicated conditions more closely resembling the flat-plate structure of the cornea. To reconcile the discrepancy between reported corneal stiffness under shear versus tensile loading, a nearly incompressible transversely isotropic (NITI) model was developed which described how two shear moduli, μ, and G, largely govern the tensile and out-of-plane shear behavior independent of each other. A mathematical corollary is presented to connect elastic wave propagation in a bounded NITI material (such as the cornea) with the elastic moduli physically measured via destructive testing. The conclusion of this section is that careful analysis of propagating wave-packets in the cornea provide an avenue to reliably quantify anisotropic elastic moduli non-invasively.

3.1 Hooke's law

The stress σ and strain ε relationship in a linear elastic solid may be described using Hooke's law, written as

$$\sigma_{ij} = c_{ijkl}\varepsilon_{kl}, \tag{3.1}$$

where summation is implied over repeated indices. In its most general form describing an anisotropic solid, the fourth-rank stiffness tensor c_{ijkl} contains 21 independent elastic constants. For convenience, Equation 3.1 is often written in Voigt notation

$$\begin{bmatrix}\sigma_{xx}\\ \sigma_{yy}\\ \sigma_{zz}\\ \tau_{yz}\\ \tau_{xz}\\ \tau_{xy}\end{bmatrix} = \begin{bmatrix}C_{11} & C_{12} & C_{13} & C_{14} & C_{15} & C_{16}\\ * & C_{22} & C_{23} & C_{24} & C_{25} & C_{26}\\ * & * & C_{33} & C_{34} & C_{35} & C_{36}\\ * & * & * & C_{44} & C_{45} & C_{46}\\ * & * & * & * & C_{55} & C_{56}\\ * & * & * & * & * & C_{66}\end{bmatrix}\begin{bmatrix}\varepsilon_{xx}\\ \varepsilon_{yy}\\ \varepsilon_{zz}\\ \gamma_{yz}\\ \gamma_{xz}\\ \gamma_{xy}\end{bmatrix}, \quad (3.2)$$

where τ_{ij} denotes shear stresses, $\gamma_{ij} = 2\varepsilon_{ij}$ denotes shear strains, and stars denote symmetric entries (i.e. $C_{21} = C_{12}$).

Eq. 3.2 can be summarized as $\sigma = \boldsymbol{C}\varepsilon$, where $\boldsymbol{C}$ is the elastic modulus matrix. Note that $\boldsymbol{C}$ reduces to five constants in a transversely isotropic solid, three constants in a nearly incompressible transversely isotropic (NITI) solid assuming tensile isotropy,[27] and two constants in an isotropic solid.[15] The subscripts x, y, and z refer to standard Cartesian axes, shown for a material with similar shape to the cornea in **Figure 3-2.**

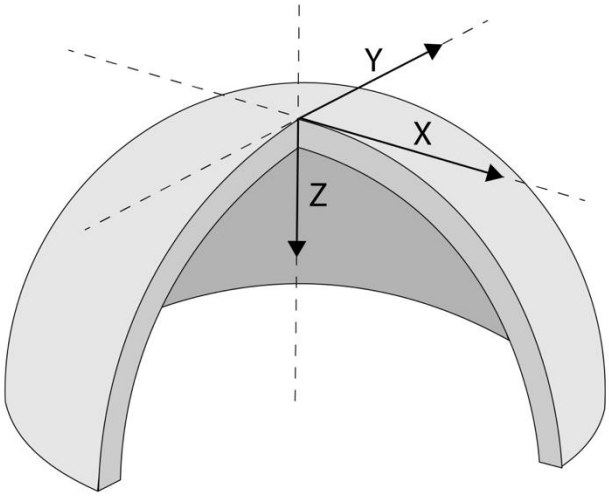

Figure 3-2. Corneal geometry and local coordinate axes used in analyzing stress strain relationships to mathematically describe tensile, torsional, and wave propagation tests.

3.2 Nearly incompressible isotropic solids

Most soft tissues, including the cornea, can be considered incompressible. To define a material as incompressible, first consider the case of an isotropic elastic medium. The stiffness matrix reduces to two constants: the Lamé parameters λ and μ. For a mechanically isotropic material, the stress-strain relation may be defined as

$$\begin{bmatrix}\sigma_{xx}\\ \sigma_{yy}\\ \sigma_{zz}\\ \tau_{yz}\\ \tau_{xz}\\ \tau_{xy}\end{bmatrix} = \begin{bmatrix}\lambda+2\mu & \lambda & \lambda & & & \\ \lambda & \lambda+2\mu & \lambda & & & \\ \lambda & \lambda & \lambda+2\mu & & & \\ & & & \mu & & \\ & & & & \mu & \\ & & & & & \mu\end{bmatrix}\begin{bmatrix}\varepsilon_{xx}\\ \varepsilon_{yy}\\ \varepsilon_{zz}\\ \gamma_{yz}\\ \gamma_{xz}\\ \gamma_{xy}\end{bmatrix}. \tag{3.3}$$

Assuming linear elasticity (i.e. small deformation) the incompressibility condition is defined as the case where the dilatation, θ, in the medium is zero:

$$\theta = \varepsilon_{xx} + \varepsilon_{yy} + \varepsilon_{zz} = 0 \tag{3.4}$$

Consequently, the trace of the strain matrix is zero ($\mathrm{Tr}(\varepsilon) = 0$). To solve for the strain matrix, Hooke's law must be inverted ($\varepsilon = \boldsymbol{C}^{-1}\sigma$), where $\boldsymbol{C}^{-1}$ is the inverse of the elastic modulus matrix, often referred to as the compliance matrix, and defined as:

$$\boldsymbol{C}_{\boldsymbol{I}}^{-1} = \frac{1}{\Delta}\begin{bmatrix}2(\lambda+\mu) & -\lambda & -\lambda & & & \\ -\lambda & 2(\lambda+\mu) & -\lambda & & & \\ -\lambda & -\lambda & 2(\lambda+\mu) & & & \\ & & & 1/\mu & & \\ & & & & 1/\mu & \\ & & & & & 1/\mu\end{bmatrix}, \tag{3.5}$$

where Δ is the determinant of $\boldsymbol{C}$ divided by the common factor 2μ and given by

$$\Delta = 2\mu(3\lambda + 2\mu). \tag{3.6}$$

As shown previously,[137] considering the Young's modulus (E) can be expressed in terms of the Lamé constants as

$$E = \frac{\mu(3\lambda + 2\mu)}{(\lambda + \mu)}, \tag{3.7}$$

and the Poisson's ratio (v) can be defined in terms of the Lamé constants as

$$v = \frac{\lambda}{2(\lambda + \mu)}, \tag{3.8}$$

the longitudinal terms of the compliance matrix ($\boldsymbol{C_l^{-1}}$) can be reduced to a more familiar notation:

$$\boldsymbol{C_l^{-1}} = \frac{1}{E}\begin{pmatrix} 1 & -v & -v \\ -v & 1 & -v \\ -v & -v & 1 \end{pmatrix}. \tag{3.9}$$

Here it can be appreciated that for any isotropic compressible medium, all longitudinal elastic properties can be fully characterized by two sets of complementary parameters, $[\lambda, \mu]$ or $[E, v]$.[138]

The incompressibility condition (Eq. 3.4) can be defined in terms of $[E, v]$ as

$$\theta = \frac{3(1 - 2v)}{E} P = 0 \tag{3.10}$$

where the mean internal pressure, P, is defined as

$$P = \frac{1}{3}(\sigma_{xx} + \sigma_{yy} + \sigma_{zz}). \tag{3.11}$$

It can be seen from Eq. 3.10 that for any load, v=1/2 to ensure that $\theta = 0$.

Rewriting the stress tensor for an isotropic media (Eq. 3.3) in terms of the dilatation provides

$$\sigma_{ij} = (\lambda\theta)\delta_{ij} + 2\mu\varepsilon_{ij}, \tag{3.12}$$

where δ_{ij} is the Kronecker delta function. The internal pressure may then be written as

$$P = \lambda\theta + \frac{2}{3}\mu\theta. \tag{3.13}$$

As $\theta \to 0$, the pressure remains finite only if $\lambda \to \infty$. Therefore, the internal pressure for a nearly-incompressible material may be defined by

$$P = \lim_{\substack{\lambda\to\infty \\ \theta\to 0}} \lambda\theta\,. \tag{3.14}$$

And the stress-strain relation can be rewritten as

$$\sigma_{ij} = P\delta_{ij} + 2\mu\varepsilon_{ij}. \tag{3.15}$$

Here, P is the internal hydrostatic pressure representing the stable product of a very large modulus (λ) with a vanishing trace of the strain matrix. It can vary both in space and time as determined by the loading function and the boundary conditions.

For an incompressible isotropic medium, only one material parameter is required to describe the deformation behavior for any loading condition. To demonstrate, consider the stress-strain relation for the case of a unidirectional (1-D) load along the *z*-direction, similar to that of tensile loading.

$$\sigma_{ij} = \begin{bmatrix} 0 & & 0 \\ & 0 & \\ 0 & & \sigma_{zz} \end{bmatrix} \tag{3.16}$$

For a nearly incompressible isotropic medium, the stress-strain relations simplify to

$$\begin{aligned} \sigma_{zz} &= P + 2\mu\varepsilon_{zz} \\ 0 &= P + 2\mu\varepsilon_{xx} \\ 0 &= P + 2\mu\varepsilon_{yy} \end{aligned} \tag{3.17}$$

Noting that θ approaches zero (i.e., $\varepsilon_{zz} = -(\varepsilon_{xx} + \varepsilon_{yy})$) for an incompressible material, the pressure term can be eliminated. Consequently, the stress-strain relation can be described as

$$\sigma_{zz} = 3\mu\varepsilon_{zz}. \tag{3.18}$$

Eq. 3.18 defines the linear relationship between applied 1-D stress and the axial strain along the same direction, where the proportionality constant is the elastic modulus. Thus, for nearly incompressible isotropic soft tissue,

$$\sigma = 3\mu\varepsilon = E\varepsilon \tag{3.19}$$

where E is the Young modulus (i.e., elasticity). Because an isotropic material will deform the same way regardless of the direction that a stress is applied, Eq. 3.19 indicates that any statically deformed, isotropic soft tissue can be completely characterized by the spatial distribution of a single material parameter, either shear (μ) or, proportionally, Young's (E) modulus.

Note that in practice, soft tissues are not completely incompressible, but their shear modulus, μ, is typically several orders of magnitude smaller than λ. Thus, to avoid possible confusion, we often use the terminology "nearly" incompressible media to describe soft tissue.

3.3 Elastic waves in a bulk isotropic media

Consider a semi-infinite, homogeneous, nearly incompressible elastic material. This fundamental case can be used to describe the basic principles of wave excitation and propagation when the thickness of tissue is much larger than the wavelength of propagating mechanical waves. In other words, bulk wave modes can be considered independent of boundary conditions. Though this is rarely the case in ocular tissue, this simple case serves as a starting point to discuss shear wave propagation.

Applying Newton's 2nd law to the constitutive relations for an isotropic material yields the equation of motion:

$$\rho \frac{\partial^2 \vec{U}}{\partial t^2} = \mu \Delta \vec{U} + (\lambda + 2\mu) grad\ div \vec{U} \tag{3.20}$$

where ρ is the mass density, λ and μ are the Lame constants (defined above), t is time, and $\vec{U}$ is the displacement vector of the propagating wave, which can be represented as

$$\vec{U} = \overrightarrow{U_l} + \overrightarrow{U_s}. \tag{3.21}$$

The longitudinal displacement ($\overrightarrow{U_l} = grad\phi$) and shear displacement ($\overrightarrow{U_s} = rot\psi$) are defined in terms of a scalar potential ϕ and vector potential ψ. Using these definitions, longitudinal (i.e., compressional) and shear waves satisfy independent equations of motion:

$$\begin{aligned} \rho \frac{\partial^2 \overrightarrow{U_l}}{\partial t^2} - (\lambda + 2\mu) \Delta \overrightarrow{U_l} = 0 \\ \rho \frac{\partial^2 \overrightarrow{U_s}}{\partial t^2} - \mu \Delta \overrightarrow{U_s} = 0 \end{aligned} \tag{3.22}$$

The term $(\lambda + 2\mu)$ is defined as the p-wave (bulk) modulus, B, of the material and is related to the wave speed for longitudinal (compressional) waves:

$$C_l = \sqrt{B/\rho} \tag{3.23}$$

Similarly, shear waves propagate at wave speed determined solely by the shear elastic modulus.

$$C_s = \sqrt{\mu/\rho} \tag{3.24}$$

For nearly incompressible materials, the p-wave modulus is orders of magnitude greater than the shear modulus. Thus, compressional waves travel at speeds much faster than shear waves and can be ignored over the time scales considered in OCE (i.e., compressional waves propagate far into the medium by the time measurable shear waves begin to propagate). Note that the bulk shear wave speed can be simply related to the shear (Young's) modulus and, therefore, can be used to quantitatively estimate tissue elasticity.

The classic approach to quantify elastic modulus uses tensile testing to induce a known stress while measuring strain. In the case of an isotropic material, it can be shown that the stress-strain relation provides an avenue for tensile, shear, and wave-based methods to determine equivalent moduli based on two Lamé constants. The value determined for μ is equivalent to that probed using both classic mechanical tests and shear wave propagation speeds.

Unfortunately, in most ocular tissues, pure bulk shear waves cannot be identified over the range of frequencies used in OCE since boundary conditions can significantly affect wave speeds. Thus, boundary conditions must be considered.

3.4 Rayleigh waves in isotropic media

Mechanical excitation at a free (i.e., air-material) boundary can produce mechanical disturbances which propagate along the medium surface (**Figure 3-3**) in addition to bulk waves which travel at longitudinal and shear speeds within the medium.

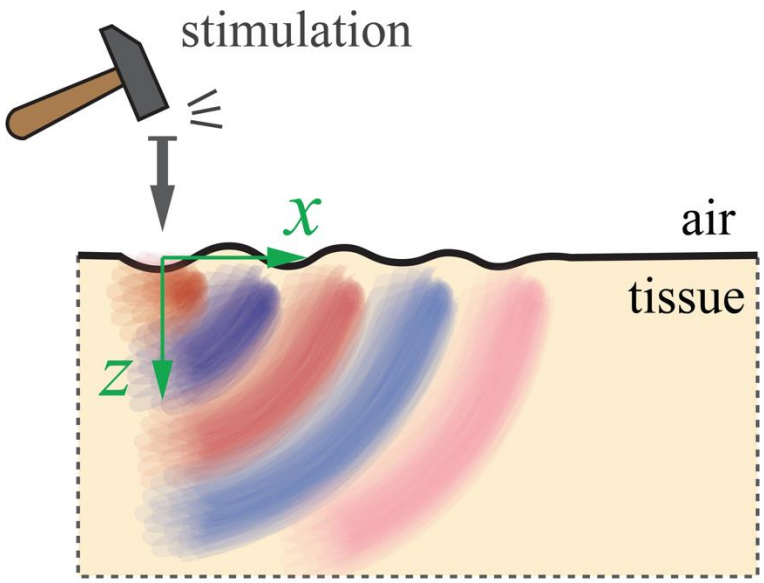

Figure 3-3. Rayleigh mechanical waves propagate along the air/tissue interface.

A mechanical disturbance along the medium surface is called a Rayleigh wave and must satisfy the boundary condition that longitudinal and shear stress components at the surface (based on the displacement component perpendicular to the surface) must be zero. For the 2-dimensional case (*xz*-plane), that is,

$$\begin{aligned} {\sigma_{xz}}^{tissue}\big|_{z=0} &= 0 \\ {\sigma_{zz}}^{tissue}\big|_{z=0} &= 0 \end{aligned} \tag{3.25}$$

at the tissue surface. Given this boundary condition and the equations of motion, the Rayleigh wave number obeys the polynomial equation:

$$\eta^6 - 8\eta^4 + 8(3 - 2\xi^2)\eta^2 - 16(1 - \xi^2) = 0\,, \tag{3.26}$$

where $\eta = C_R/C_s$ and $\xi = C_s/C_l$. Considering that ξ<<1 for nearly incompressible materials, this equation reduces to

$$\eta^6 - 8\eta^4 + 24\eta^2 - 16 = 0, \tag{3.27}$$

with primary root

$$\eta = \frac{C_R}{C_s} \cong 0.955. \tag{3.28}$$

Equation 3.28 corresponds to the Rayleigh wave (C_R is the Rayleigh wave speed), which, like the pure shear wave, depends only on the shear modulus, μ, in an isotropic media.[139] Thus, tracking the propagation of either shear or Rayleigh waves to locally estimate wave speed can be used to infer the shear modulus, μ and, therefore, tissue elasticity ($E = 3\mu$).

3.5 Scholte Waves in isotropic media

Shear and Rayleigh waves are sufficient to describe propagation in the region of a free boundary. However, only the anterior surface of the cornea has a true free mechanical boundary (air-tissue). Other ocular tissues (including the posterior surface of the cornea) can be better described with a liquid-tissue boundary. Additionally, the application of a coupling medium (such as in loading with acoustic transducers) can introduce liquid loading on the anterior surface of the cornea. From

a mechanical viewpoint, the water-tissue boundary can be considered as a semi-infinite nearly incompressible elastic medium loaded with liquid from one direction (**Figure 3-4**).

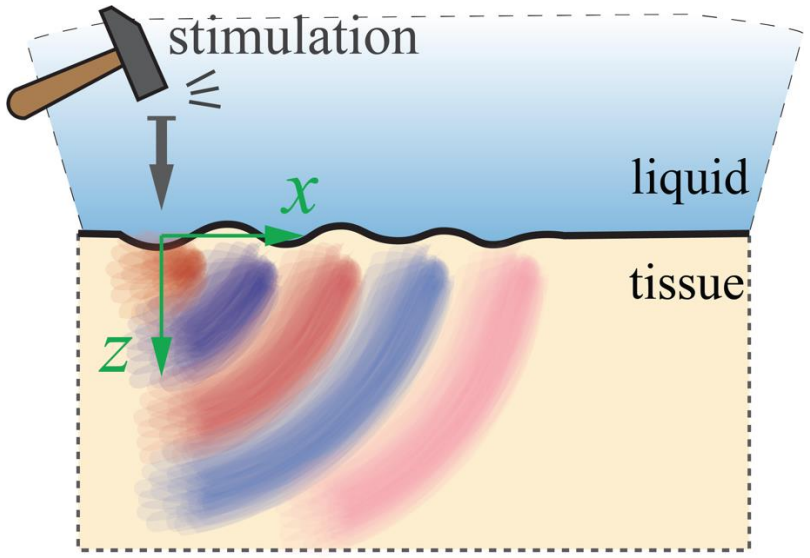

Figure 3-4. Scholte mechanical waves propagate along the liquid/tissue interface.

Shear waves do not propagate in the liquid, but the load changes the boundary conditions for a propagating interface wave. In this case, the normal stress component is equal to the pressure in the liquid, and the normal displacement components in the tissue must be equal at the interfaces. In this case the tangential component of stress is again taken as zero since fluids do not resist shear deformation:

$$\begin{aligned} {\sigma_{xz}}^{tissue}\big|_{z=0} &= 0 \\ {\sigma_{zz}}^{liq}\big|_{z=0} &= {\sigma_{zz}}^{tissue}\big|_{z=0} \\ {U_z}^{liq}\big|_{z=0} &= {U_z}^{tissue}\big|_{z=0} \end{aligned} \tag{3.29}$$

where the relationship $\mu = 0$ is taken into account for the liquid.[139]

A liquid-solid interface wave is often called a Scholte wave, obeying the polynomial equation for $\zeta = C_{Sch}/C_s$:

$$\zeta^6(1+\beta)^2 - 8\zeta^4(1+\beta) + 24\zeta^2 + 8\zeta^2\beta - 16 = 0 \tag{3.30}$$

where C_{Sch} is the speed of the Scholte wave, and (using the cornea with an acoustic gel as an example) $\beta = \rho_{gel}/\rho_{cornea}$. Noting that the densities of soft tissue (gel and cornea in this case) are approximately the same, i.e. $\beta \cong 1$, the numerical solution of the above equation gives the root:

$$\zeta = \frac{C_{Sch}}{C_s} \cong 0.846 \tag{3.31}$$

In other words, liquid loading slows the Rayleigh wave, converting it to a Scholte wave.[139] Again, the speed of this mode can also be characterized with a single elastic modulus. Note also that the liquid load allows a leaky wave solution. However, high attenuation of leaky waves make them very inefficient for tracking.

Rayleigh and Scholte waves have elliptical polarizations because both the U_x and U_z components of the waves are generally non-zero and π/2 phase shifted.[135] However, the vertical, U_z, component of the displacement is typically utilized as it is more easily detected by phase-sensitive OCT in an OCE system with vertically aligned OCT probes.

3.6 Guided waves in isotropic media

When a wave propagates in a medium with dimensions on the order of the mechanical wavelength, the medium becomes a waveguide. Cornea thickness is typically on the order of a single mm, that

(for most dynamic OCE systems) is on the same scale as the wavelength of an induced shear or surface wave. Thus, both the upper free boundary (air-cornea) and lower liquid-loaded boundary (cornea-aqueous humor) must be considered to accurately describe the propagation of guided waves in the cornea resulting from mechanical excitation at the air-cornea surface (**Figure 3-5**).

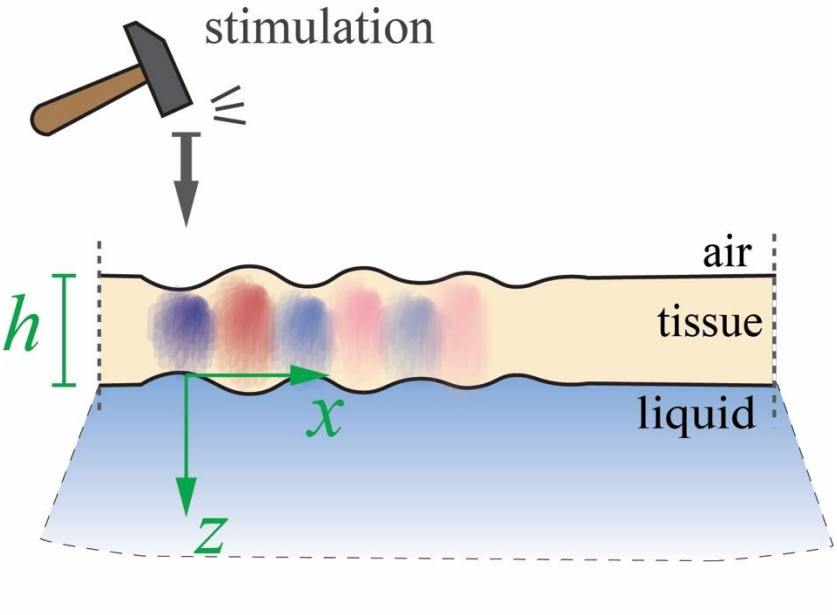

Figure 3-5. Guided mechanical waves propagate in a thin tissue layer bounded from one side by air and the other by liquid.

The equations describing guided waves in a flat- bounded layer are complicated. A simple equation like those presented above for surface waves is not possible and only a numerical solution can reliably determine the modulus.

For an isotropic elastic material, the scalar potential ϕ and vector potential ψ cannot be omitted. A general form for a vertically polarized plane wave propagating in a plate in the x direction can be represented as:

$$\phi_1 = [A_1 \exp(-q_1 z) + A_2 \exp(q_1 z)] \exp(i(kx - \omega t)$$
$$\psi_1 = [B_1 \exp(-s_1 z) + B_2 \exp(s_1 z)] \exp(i(kx - \omega t) \quad (3.32)$$

where $q_1 = \sqrt{k^2 - {k_l}^2}$, $s_1 = \sqrt{k^2 - {k_s}^2}$ and $k_l = \frac{\omega}{C_l}$ $k_s = \frac{\omega}{C_s}$, are wave numbers for longitudinal and shear waves in soft tissue, respectively. Note that when the guided wave exists in plates of thickness smaller than the wavelength, the dominating wave modes are called Lamb waves.

In this case, boundary conditions can be written in the form

$$\begin{aligned} &{\sigma_{xz}}^{tissue}\big|_{z=-h} = 0 \\ &{\sigma_{zz}}^{tissue}\big|_{z=-h} = 0 \\ &{\sigma_{zz}}^{liq}\big|_{z=0} = {\sigma_{zz}}^{tissue}\big|_{z=0} \\ &{\sigma_{xz}}^{tissue}\big|_{z=0} = 0 \\ &{U_z}^{liq}\big|_{z=0} = {U_z}^{tissue}\big|_{z=0} \end{aligned} \quad (3.33)$$

where *h* defines the plate thickness. Calculating the stress and displacement components from the scalar and vector potentials (Equation 3.32) and substituting them into boundary conditions (Eq. 3.34), a 5x5 matrix characteristic equation is obtained:

$$\begin{vmatrix} 0 & -2ik^2 & 2ik^2 & -(k^2+s^2) & -(k^2+s^2) \\ \rho_l\omega^2 & -\rho_T\omega^2 + 2\mu k^2 & -\rho_T\omega^2 + 2\mu k^2 & -2i\mu ks & 2i\mu ks \\ 0 & (-\rho_T\omega^2 + 2\mu k^2)\exp(kh) & (-\rho_T\omega^2 + 2\mu k^2)\exp(-kh) & -2i\mu ks \cdot \exp(sh) & 2i\mu ks \cdot \exp(-sh) \\ 0 & -2ik^2 \cdot \exp(kh) & 2ik^2 \cdot \exp(-kh) & -(k^2+s^2)\exp(sh) & -(k^2+s^2)\exp(-sh) \\ 1 & -1 & 1 & i & i \end{vmatrix} = 0 \quad (3.34)$$

where ρ_l and ρ_T are densities of the liquid and tissue, correspondingly.

Eq. 3.34 can only be solved numerically, resulting in the dispersion curves shown in **Figure 3-6**. These results can be compared to the blue curves showing the symmetric boundary condition case, i.e. tissue immersed in air, obtained using the same equation with $\rho_l = 0$. As is evident from the plot, several modes can exist simultaneously. Most exhibit significant dispersion over a broad frequency band. Comparing the results for a water-loaded plate and free boundary conditions, it can be seen that the fluid has a significant influence on wave propagation. In **Figure 3-6**, A_N and S_N indexes denote quasi- anti-symmetric and symmetric Lamb modes. Note, however, that this notation is valid only for the symmetrical boundary case. If only a single side of the plate is water-loaded, neither pure symmetric nor pure anti-symmetric modes exist. This fact is evident for the A_0 mode, which, for the case of tissue with free boundaries, has its high frequency limit equal to the surface wave speed C_S. For single-sided water loading, the limit is the Scholte wave described in the section above. Note that an approximate solution represented in matrix form for a cylindrical geometry,[9,10] and for the case of symmetrical boundary conditions of a water-immersed plate,[140] has also been found and described in detail.

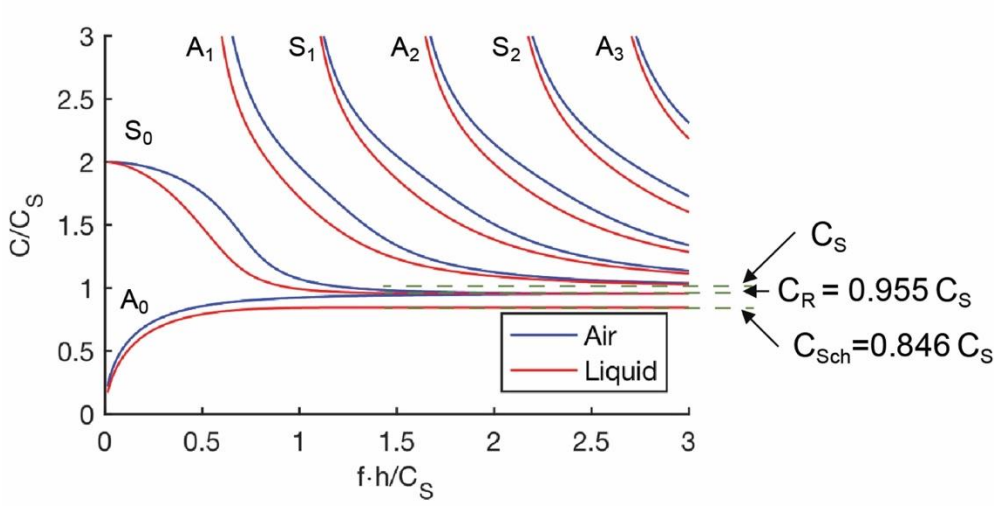

Figure 3-6. Phase velocity dispersion for guided waves in a thin tissue layer loaded from one side by a liquid and the other side by air.

There are a few important conclusions that arise from the finite thickness and liquid boundary condition. First, even when the material is purely elastic (no viscosity), guided modes are very dispersive. Simple measurement of the group velocity of propagating guided waves cannot be used to directly reconstruct the elastic modulus E. Measurements of corneal elastic moduli based on the group velocity yield values related to elastic properties but may lead to serious quantitative error as the result depends on the frequency range of group velocity calculation. To decode this complex wave behavior, dispersion analysis is required over a wide bandwidth. Consequently, a wideband mechanical wave source must be used to quantitatively estimate the elastic properties of the cornea from dynamic OCE measurements.

Second, wideband analysis of experimental data can be used to estimate high-frequency asymptotes of propagating guided waves, where the first asymmetric mode A_0 asymptotes to a Scholte wave with speed $C_{Sch} = 0.846C_s$, indicating a liquid load.[15] Note that for the case of air, this limit corresponds to that for a Rayleigh wave. The first symmetric mode, S_0, has the high-frequency asymptote of a Rayleigh wave, $C_R = 0.955C_s$, because it primarily propagates along the air-tissue interface. Other modes all asymptote to bulk shear waves propagating with speed C_S in the bulk material with properties equivalent to that of the tissue. Thus, if the asymptotic behavior of propagating guided waves can be estimated accurately over a region of the bounded material, then the elastic modulus can be accurately computed in that region independent of the specific geometry, assuming that viscous effects are not significant.

3.7 Vertical Inclusions and mode conversions

Detecting spatial heterogeneities in a mechanical structure can help monitor and treat disease progression. Thus, wave interactions with heterogeneous boundaries must be considered to provide quantitative moduli mapping of mechanically inhomogeneous tissue.

Starting with an infinite, homogeneous, nearly incompressible elastic material, consider a plane longitudinal (*l*-) or bulk shear (*s*-) wave propagating across the boundary (at plane $x = 0$) between two isotropic elastic media characterized with Lamé constants $\lambda_{1,2}$ and $\mu_{1,2}$, correspondingly (**Figure 3-7**). The propagation velocities of longitudinal ($C_l^{(1,2)}$) and shear ($C_s^{(1,2)}$) waves from both sides of the interface are:[141]

$$C_l^{(1,2)} = \sqrt{\left(\lambda^{(1,2)} + 2\mu^{(1,2)}\right)/\rho^{(1,2)}}$$
$$C_s^{(1,2)} = \sqrt{\mu^{(1,2)}/\rho^{(1,2)}} \tag{3.35}$$

Now consider plane waves propagating along the *x*-axis (normal to the *z*-axis), located within a bulk material. At the plane interface ($x = 0$), propagating waves are both reflected and transmitted according to the reflection and transmission coefficients primarily determined by the ratio $\left(\frac{C_{l,s}^{(2)}}{C_{l,s}^{(1)}}\right)$,[142] and the propagation speed is discontinuous at the boundary.

Only plane waves propagating in the $\pm x$ direction are allowed under these conditions and no other wave modes are generated at the interface. The amplitude of counter propagating wave packets is simply given by the transmission and reflection coefficients. These waves will not change their temporal shape; however, superposition of the counter-propagating plane waves in the $x < 0$ region

close to the interface will affect the apparent shape of the incident wave packet. Preservation of temporal wave shape is exploited in traditional time-of-flight reconstruction to locally estimate propagation speed and, thereby, infer the elastic modulus.[143] In the spatial domain, the original waveform can stretch or compress as a function of local propagation speed. This scaling has been exploited to locally estimate propagation speed based on the wavenumber, thereby inferring elastic modulus.[144–146]

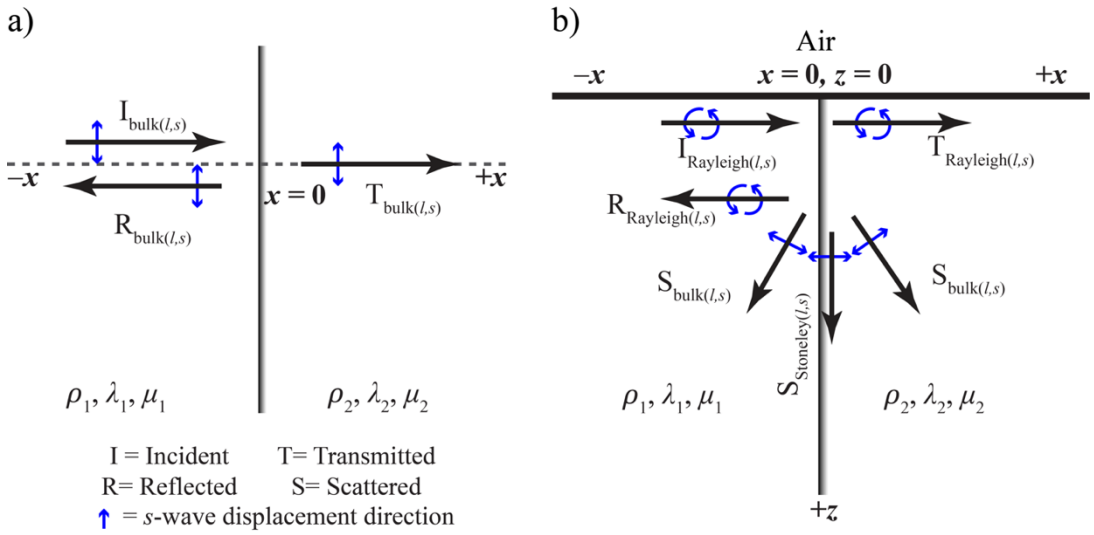

Figure 3-7. Elastic waves impinging on a vertical boundary (a) Bulk media void of surface boundary conditions. Incident and reflected plane bulk waves consist of both longitudinal (*l*-) and shear (*s*-) wave packets propagating normal to the interface. (b) Boundary conditions alter propagating Rayleigh wave shape. Tractional forces on the vertical boundary scatter energy in the form of bulk and Stoneley wave components in addition to the reflected and transmitted Rayleigh wave energy.

Consider Rayleigh waves propagating along the *x*- axis far from the excitation source where they can be easily isolated from bulk waves. For a nearly incompressible material such as soft tissue, the Rayleigh wave speed is simply related to the shear-wave speed,[142] hence, the shear elastic

modulus can be easily computed from the Rayleigh-wave speed.[15] Assuming negligible viscosity, the temporal shape and amplitude of the propagating surface wave does not change when viewed a sufficient distance from the excitation zone. This means simple time-of-flight measurements can accurately track propagation speed and directly convert the measurement to modulus. If this wave impinges on a vertical boundary (similar to the bulk case presented in **Figure 3-7a**), its energy is not fully distributed between reflected and transmitted Rayleigh waves; new modes are possible,[147] which greatly complicate the mechanical wave packet in this region.

Typical dynamic OCE systems are confined to imaging depths of about 1-2 mm due to light penetration limits in OCT. Consequently, mechanical waves tracked in OCE are launched and propagate in highly bounded media, typically with a free surface (air) defining one of the boundaries. Many mode types are possible in tissue with such boundary conditions, namely, Rayleigh, Love, Stoneley, Scholte or other types of guided waves.[15,142] Here, the simplest case of boundary effects typically encountered in dynamic OCE is considered (**Figure 3-7b**), where a temporally short axial load applied to the free surface ($z = 0$) between air and the propagation medium (i.e. soft tissue) is used to generate a bulk *l*- and *s*- wave that travels into the medium, as well as a Rayleigh wave that travels along the free surface.

To understand the effects of mode conversion in the neighborhood of the interface, the mechanical boundary conditions on strain (σ) must first be specified at ($x = 0, z > 0$) and ($x,\ z = 0$) interfaces:

$$\begin{aligned} {\sigma_{xz}}^{(1,2)}\big|_{z=0} &= 0 \\ {\sigma_{zz}}^{(1,2)}\big|_{z=0} &= 0 \\ {\sigma_{xz}}^{(1)}\big|_{x=0,z>0} &= {\sigma_{xz}}^{(2)}\big|_{x=0,z>0} \\ {\sigma_{zz}}^{(1)}\big|_{x=0,z>0} &= {\sigma_{zz}}^{(2)}\big|_{x=0,z>0} \end{aligned} \quad . \tag{3.36}$$

The boundary conditions must be applied to solutions of the general mechanical equations of motion in the medium,

$$\rho \frac{\partial^2 \vec{U}}{\partial t^2} = \mu^{(1,2)} \Delta \vec{U} + \left(\lambda^{(1,2)} + 2\mu^{(1,2)}\right) grad\ div \vec{U}, \tag{3.37}$$

where $\vec{U}$ is the displacement vector of the propagating wave and the superscripts $(1,2)$ correspond to the geometry in **Figure 3-7**.

For the given boundary conditions, not only are transmitted and reflected Rayleigh waves produced, but additional modes (such as a Stoneley wave propagating along the z-axis and bulk shear waves traveling at an angle to the z-axis) are launched.[147] The specific energies converted from the pure incident Rayleigh wave to secondary modes (longitudinal, shear, Stoneley, etc.) can be difficult to quantify, and will vary greatly for different geometries and stiffnesses.[148] Because the values of each converted mode differ depending on factors such as the ratio μ_2/μ_1, it is difficult to generalize how each mode will specifically affect the reconstruction with depth for the wide range of conditions typical of OCE. Scattered body waves emerging in a particular direction create a finite region where, even for different mixed-mode amplitudes, the signal will be distorted. This region of undefined wave behavior, i.e. a mixture of multiple propagating modes, will corrupt Rayleigh wave tracking and, hence, its speed reconstruction. We also note that the Rayleigh wave shape itself changes when passing the interface by transferring energy to other modes, making it very difficult to separate the Rayleigh wave from other modes near the interface.

Finding an analytical solution for all modes near the $x = 0$ interface is not a trivial problem, especially for broadband Rayleigh-wave pulses. To explore how vertical inclusions and mode conversions are related to reconstruction accuracy (and ultimately play a role in OCE spatial

resolution), detailed simulations and experimental measurements on model systems are described in Chapter 4. The specific geometry was designed to highlight wave-behavior close to an interface between two lateral regions with different shear moduli. Specifically, Rayleigh waves with varying frequencies were used to determine how close single-mode surface waves could approach a vertical interface without corruption due to scattering and mode-conversion. Note that even for bounded material such as the cornea, wave packets with high enough frequencies (i.e. small wavelengths relative to the corneal thickness) behave similar to Rayleigh waves. The ability to uniquely identify elastic waves from both sides of a mechanical interface is essential to quantitatively measure elastic modulus in regions with different stiffness and must be analyzed carefully.

3.8 Nearly incompressible transversely isotropic solids

Most work to date considered the cornea as an isotropic material. However, there are significant differences between tensile and shear loading tests suggesting that the cornea cannot be considered isotropic.[149]

Specifically, the fibril arrangement (**Figure 2-1**) in the cornea is such that hundreds of vertically stacked collagen lamellae, each 0.3-2.5 μm thick[31,32] have a preferred collagen orientation. The elastic properties of collagen fibers have been shown to be very different than those of corneal connective tissue,[46–48] suggesting that the preferred orientation results in asymmetric elastic properties. While some in-plane anisotropy has been reported,[74,136,150,151] its magnitude at low intraocular pressure (IOP) suggests that macroscopic mechanical behavior can be treated as isotropic in-plane.[16,74,152] Recent second harmonic generation imaging studies suggest that lamellar orientations are relatively random in-plane[40,41,153] and, as such, it is reasonable to assume

that cornea's in-plane elastic properties are isotropic. Still, out-of-plane properties can be very different.

One interpretation of the corneal structure, based on a fiber-composite model,[154] is that collagen fiber mechanical properties govern in-plane behavior, while those of the connective tissue matrix govern out-of-plane behavior. The simplest model capturing corneal mechanical anisotropy is that of a transversely isotropic (TI) material, with in-plane (*xy*- plane) isotropy and a symmetry axis (*z*) perpendicular to the lamellar structure.

For a general TI solid, the stress-strain relation is defined by five independent constants[138]:

$$\begin{bmatrix}\sigma_{xx}\\ \sigma_{yy}\\ \sigma_{zz}\\ \tau_{yz}\\ \tau_{xz}\\ \tau_{xy}\end{bmatrix} = \begin{bmatrix}C_{11} & C_{12} & C_{13} & & & \\ C_{12} & C_{11} & C_{13} & & & \\ C_{13} & C_{13} & C_{33} & & & \\ & & & C_{44} & & \\ & & & & C_{44} & \\ & & & & & C_{66}\end{bmatrix}\begin{bmatrix}\varepsilon_{xx}\\ \varepsilon_{yy}\\ \varepsilon_{zz}\\ \gamma_{yz}\\ \gamma_{xz}\\ \gamma_{xy}\end{bmatrix}. \tag{3.38}$$

Where $C_{12} = C_{11} - 2C_{66}$. Note that $i = 1{,}2$ dimensions are isotropic (consistent with the *xy*-plane). Considering that two of the three principal planes can be considered isotropic (where, for example C_{11} is equivalent to $\lambda + 2\mu$), the elasticity matric can be written as

$$\boldsymbol{C} = \begin{bmatrix}\lambda+2\mu & \lambda & \lambda+Q_1 & & & \\ \lambda & \lambda+2\mu & \lambda+Q_1 & & & \\ \lambda+Q_1 & \lambda+Q_1 & \lambda+2\mu+Q_2 & & & \\ & & & G & & \\ & & & & G & \\ & & & & & \mu\end{bmatrix}. \tag{3.39}$$

where

$$Q_1 = C_{13} - \lambda \tag{3.40}$$

$$Q_2 = C_{33} - (\lambda + 2\mu). \tag{3.41}$$

The inclusion of the parameter G here indicates that shear deformation can be different if shear stress is applied along the symmetry axis (z) compared to the deformation from a shear stress applied across it. The inclusion of Q_1 and Q_2 indicate that differences between C_{33} and C_{11}, and between C_{12} and C_{13} may be nonzero.[137]

As before, the dilatation of a material can be defined in terms of the normal strain components where the strains are related to the normal stresses σ_{xx}, σ_{yy}, and σ_{zz} and the longitudinal part of the compliance tensor $\boldsymbol{C}_{\ell}^{-1}$:

$$\varepsilon_{\ell} = \boldsymbol{C}_{\ell}^{-1}\sigma_{\ell}, \tag{3.42}$$

where

$$C_{\boldsymbol{\ell}}^{-1} = \frac{1}{\Delta}\begin{bmatrix} C_{11}C_{33} - C_{13}^2 & C_{13}^2 - C_{12}C_{33} & C_{13}(C_{12} - C_{11}) \\ C_{13}^2 - C_{12}C_{33} & C_{11}C_{33} - C_{13}^2 & C_{13}(C_{12} - C_{11}) \\ C_{13}(C_{12} - C_{11}) & C_{13}(C_{12} - C_{11}) & C_{11}^2 - C_{12}^2 \end{bmatrix} \tag{3.43}$$

$$\Delta = \det C_{\ell} = (C_{11} - C_{12})[(C_{11} + C_{12})C_{33} - 2C_{13}^2] \tag{3.44}$$

Eq. 3.43 and 3.44 can be expressed using $\alpha = \boldsymbol{C}^{-1}$, where

$$\boldsymbol{C^{-1}} = \alpha = \frac{1}{\Delta}\begin{bmatrix} \alpha_{11} & -\alpha_{12} & -\alpha_{13} & & & \\ -\alpha_{12} & \alpha_{11} & -\alpha_{13} & & & \\ -\alpha_{13} & -\alpha_{13} & \alpha_{33} & & & \\ & & & \Delta \cdot \alpha_{44} & & \\ & & & & \Delta \cdot \alpha_{44} & \\ & & & & & \Delta \cdot \alpha_{66} \end{bmatrix}, \tag{3.45}$$

components of the compliance matrix α_{ij} are defined using μ, G, $Q_1$and Q_2 as

$$\begin{aligned}
&\Delta = 4\mu\left((\lambda + 2\mu + Q_2)(\lambda + \mu) - (\lambda + Q_1)^2\right), \\
&\alpha_{11} = (\lambda + 2\mu + Q_2)(\lambda + 2\mu) - (\lambda + Q_1)^2, \\
&\alpha_{12} = \lambda(\lambda + 2\mu + Q_2) - (\lambda + Q_1)^2, \\
&\alpha_{13} = 2\mu(\lambda + Q_1), \\
&\alpha_{33} = 4\mu(\lambda + \mu), \\
&\alpha_{44} = \frac{1}{G}, \\
&\alpha_{66} = \frac{1}{\mu}.
\end{aligned} \tag{3.46}$$

Similar to the isotropic case, the longitudinal terms of the compliance matrix ($\boldsymbol{C_l^{-1}}$) can be written in terms of the Young's moduli and Poisson's ratios[137]:

$$\boldsymbol{C_l^{-1}} = \begin{pmatrix} \frac{1}{E_1} & \frac{-\nu_{12}}{E_1} & \frac{-\nu_{13}}{E_3} \\ \frac{-\nu_{12}}{E_1} & \frac{1}{E_1} & \frac{-\nu_{13}}{E_3} \\ \frac{-\nu_{13}}{E_3} & \frac{-\nu_{13}}{E_3} & \frac{1}{E_3} \end{pmatrix} \tag{3.47}$$

Adopting the terminology of $E_1 = E_T$ and $E_3 = E_L$, as well as $\nu_{12} = \nu_{TT}$, $\nu_{13} = \nu_{TL}$ and $\nu_{31} = \nu_{LT}$, transverse and longitudinal Young's moduli (E_T and E_L, respectively) and three Poisson's ratios can be expressed via components α_{ij}:

$$
\begin{aligned}
E_T &= \frac{\Delta}{\alpha_{11}}\,, \\
E_L &= \frac{\Delta}{\alpha_{33}}\,, \\
\nu_{TT} &= \frac{\alpha_{12}}{\alpha_{11}}\,, \\
\nu_{TL} &= \frac{\alpha_{13}}{\alpha_{11}}\,, \\
\nu_{LT} &= \frac{\alpha_{13}}{\alpha_{33}}\,.
\end{aligned}
\tag{3.48}
$$

Again, the incompressibility condition for soft tissue constrains the strain such that $Tr(\boldsymbol{\varepsilon}) \equiv \theta = 0$. Assuming $\Delta \neq 0$, the incompressibility condition can be expressed as

$$
\theta = \frac{2\mu(2\mu + Q_2 - Q_1)}{\Delta}\left(\sigma_{xx} + \sigma_{yy}\right) + \frac{4\mu(\mu - Q_1)}{\Delta}\sigma_{xx} = 0 \tag{3.49}
$$

where

$$
\Delta = 4\mu[\lambda(3\mu + Q_2 - 2Q_1) + (2\mu^2 + \mu Q_2 - Q_1^2)]. \tag{3.50}
$$

For the incompressibility condition where $\lambda \to \infty$ while $\mu, Q_1,$ and Q_2 remain finite, the stresses, internal pressure P, and dilatation θ terms can be written as:

$$
\sigma_{xx} = P + 2\mu\varepsilon_{xx} + Q_1\varepsilon_{zz} \tag{3.51}
$$

$$
\sigma_{yy} = P + 2\mu\varepsilon_{yy} + Q_1\varepsilon_{zz} \tag{3.52}
$$

$$
\sigma_{zz} = P + 2\mu\varepsilon_{zz} + Q_1\left(\varepsilon_{xx} + \varepsilon_{yy}\right) + Q_2\varepsilon_{zz} \tag{3.53}
$$

where $P = \lim_{\substack{\lambda\to\infty \\ \theta\to 0}} (\lambda\theta)$. Note that the stress-strain relations for an incompressible TI medium show that the elastic behavior is fully characterized by four material constants and the scalar pressure P.

For the limit where $\lambda \to \infty$, the incompressibility condition can be expressed in terms of the Young's moduli and Poisson's ratio as

$$\theta = \left[\frac{(1-\nu_{TT})}{\mathrm{E}_T} - \frac{\nu_{LT}}{E_L}\right]\left(\sigma_{xx}+\sigma_{yy}\right) + \frac{(1-2\nu_{LT})\sigma_{zz}}{E_L} = 0. \tag{3.54}$$

For Eq. 3.54 to be satisfied for any load, the Young's moduli and Poisson's ratios for a nearly-incompressible TI material, i.e. NITI material, can be approximated as:

$$\begin{aligned} E_T &= 3\mu + \mu\left[\frac{\delta}{4\mu+\delta}\right], \\ E_L &= 3\mu + \delta\,, \\ \nu_{TT} &= \frac{1}{2}\left[1+\frac{\delta}{4\mu+\delta}\right] = 1 - \frac{1}{2}\frac{E_T}{E_L}, \\ \nu_{TL} &= \frac{1}{2}\left[1-\frac{\delta}{4\mu+\delta}\right] = \frac{1}{2}\frac{E_T}{E_L}, \\ \nu_{LT} &= \frac{1}{2}, \end{aligned} \tag{3.55}$$

where $\delta = Q_2 - 2Q_1$. Note that δ is important to characterize Young's moduli along, E_T, and across, E_L, fibers. Additionally, most biological soft materials require that $\nu > 0$. This condition is satisfied for ν_{TT} only when $\mathrm{E}_T \leq 2E_L$.

By definition, the δ term accounts for non-zero differences between C_{33} and C_{11}, and between C_{12} and C_{13}. Assuming that tensional deformation is different along the fiber direction compared to that across it, both E_L and E_T change with δ (**Figure 3-8**).

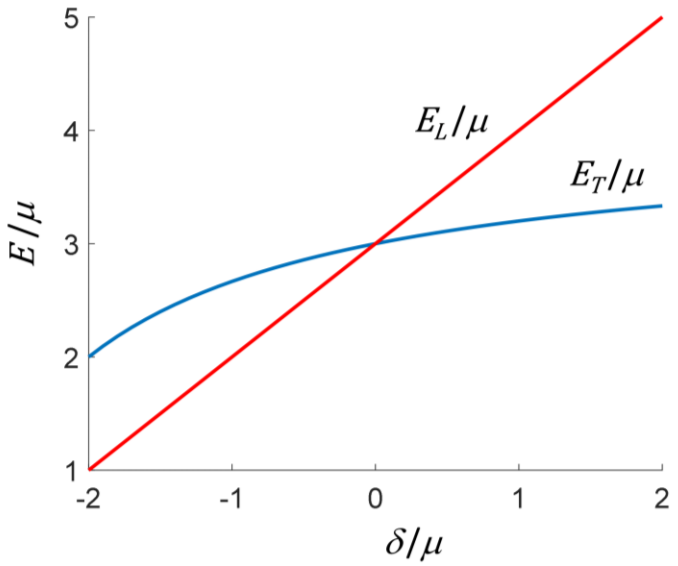

Figure 3-8. Young's moduli along and across NITI material symmetry axis z (perpendicular corneal surface) scaled to the shear modulus μ (E_L/μ and E_T/μ respectively) as a function of the ratio δ/μ.

The lower limit for the argument δ/μ is defined by the condition where ν_{TT} is positive. As such, $E_T \geq 2\mu$.

As $\delta \to \infty, E_T$ has an upper limit of 4μ. E_L is a linear function of δ.

The condition where $\delta/\mu < 0$ corresponds to a slow-axis NITI medium, where $C_{33} < C_{11}$. This situation occurs in the cornea due to random in-plane orientation of lamellae, where the symmetry axis corresponds to the direction perpendicular to the fibers. Thus, corneal tensile properties may be different when loaded in-plane compared to out-of-plane directions.

As shown in **Figure 3-8,** the difference between E_L and E_T may be defined by the parameter δ. However, the ratio E_L/E_T has a very narrow range for all δ allowed by the corneal symmetry:

$$1 < E_T/E_L < 2 \tag{3.56}$$

From Eq. 3.56, it's clear the range of E_T is highly restricted to:

$$2\mu < E_T < 3\mu \ . \tag{3.57}$$

The case of $E_T = 3\mu$, corresponding to $\delta = 0$, is equivalent to the assumption that corneal tensile properties are isotropic.[27] The case $E_T = 2\mu$, corresponding to $\delta = -2\mu$, is realized at the strongest possible corneal tensile anisotropy. While determination of the parameter δ can be difficult to measure directly, Eq. 3.55 suggests that measuring certain types of material deformation may be used to determine the relationship between in plane and out of plane tensile anisotropy.

In the case of tensile isotropy ($E_T = E_L$), $C_{13} = \lambda$ and $C_{33} = \lambda + 2\mu$. This is equivalent to $\delta = Q_1 = Q_2 = 0$, where the determinant in Eq. 3.43 becomes

$$\Delta = 12\mu^2\left(\lambda + \frac{2}{3}\mu\right), \tag{3.58}$$

which is nonzero, indicating that the stiffness matrix is invertible. Additionally, avoiding the singularity occurring at $Q_2 - 2Q_1 + 3\mu \neq 0$ is satisfied. For a NITI material assuming tensile isotropy, Eq. 3.39 therefore reduces to

$$\begin{bmatrix}\sigma_{xx}\\ \sigma_{yy}\\ \sigma_{zz}\\ \tau_{yz}\\ \tau_{xz}\\ \tau_{xy}\end{bmatrix} = \begin{bmatrix}\lambda+2\mu & \lambda & \lambda & & & \\ \lambda & \lambda+2\mu & \lambda & & & \\ \lambda & \lambda & \lambda+2\mu & & & \\ & & & G & & \\ & & & & G & \\ & & & & & \mu\end{bmatrix}\begin{bmatrix}\varepsilon_{xx}\\ \varepsilon_{yy}\\ \varepsilon_{zz}\\ \gamma_{yz}\\ \gamma_{xz}\\ \gamma_{xy}\end{bmatrix}. \tag{3.59}$$

This approximation corresponds to the case of a weakly anisotropic material, since the only anisotropy is due to the shear terms $C_{44} = G$. Consequently, only 2 parameters, μ and G, define corneal deformation and $E_T = E_L = E = 3\mu$.

Note that assuming $\delta = 0$ for the cornea may not be strictly accurate, but greatly simplifies the analysis of wave behavior for quantification of E and G using experimental data (detailed in Chapter 5). Using a simplified NITI material model rather than a simple isotropic model is an important step in quantifying anisotropic properties because it separates the effects of μ from G, which are much greater than any possible variations of E introduced by $\delta \neq 0$.

Finally, note that in the limit of an isotropic material, both the full TI and simplified NITI model correspond to the case where:

$$\begin{aligned} &Q_1 = Q_2 = 0, \\ &\mathrm{E}_T = \mathrm{E}_L = 3\mu, \\ &\nu_{TT} = \nu_{TL} = \nu_{LT} = 1/2. \end{aligned} \tag{3.60}$$

3.9 Elastic waves in a bulk NITI material

Transversely isotropic materials support three bulk waves (quasi-longitudinal, quasi-shear, and shear) whose wave speeds depend on the propagation angle. When the propagation direction lies in the *xy*-plane ($\vartheta = 90°$), three pure wave modes exist (one longitudinal and two orthogonal shear waves). Their wave speeds are

$$c_L = \sqrt{\frac{C_{11}}{\rho}}$$

$$c_{S1} = \sqrt{\frac{C_{44}}{\rho}}, \text{(polarized in } z\text{)}, \tag{3.61}$$

$$c_{S2} = \sqrt{\frac{C_{66}}{\rho}}, \text{(polarized in the } xy - \text{plane)}$$

where ρ is the material density.

For a general propagation angle, the polarization of propagating waves is not fully parallel or orthogonal to the propagation direction and, therefore, one quasi-longitudinal, one quasi-shear, and one shear wave should be considered. The following equations can be used to calculate their wave speeds[155]:

$$c_{qL} = \sqrt{\frac{C_{11}\sin^2\vartheta + C_{33}\cos^2\vartheta + C_{44} + \sqrt{M(\vartheta)}}{2\rho}}, \tag{3.62}$$

$$c_{qS} = \sqrt{\frac{C_{11}\sin^2\vartheta + C_{33}\cos^2\theta + C_{44} - \sqrt{M(\vartheta)}}{2\rho}}, \tag{3.63}$$

$$c_S = \sqrt{\frac{C_{66}\sin^2\vartheta + C_{44}\cos^2\vartheta}{\rho}}, \tag{3.64}$$

$$M(\theta) = [(C_{11} - C_{44})\vartheta + (C_{44} - C_{33})\vartheta]^2 + (C_{13} + C_{44})^2\sin^2 2\vartheta\,. \tag{3.65}$$

For the full NITI model, these equations can be written as

$$c_{qL} = \sqrt{\frac{(\lambda + 2\mu)\sin^2\vartheta + (\lambda + 2\mu + Q_2)\cos^2\vartheta + G + \sqrt{M(\vartheta)}}{2\rho}}, \tag{3.66}$$

$$c_{qS} = \sqrt{\frac{(\lambda + 2\mu)\sin^2\vartheta + (\lambda + 2\mu + Q_2)\cos^2\vartheta + G - \sqrt{M(\vartheta)}}{2\rho}}, \tag{3.67}$$

$$c_S = \sqrt{\frac{\mu\sin^2\vartheta + G\cos^2\vartheta}{2\rho}}, \tag{3.68}$$

$$M(\vartheta) = [(\lambda + 2\mu - G)\sin^2\vartheta + (G - \lambda - 2\mu - Q_2)\cos^2\vartheta]^2 + (\lambda + Q_1 + G)^2\sin^2 2\vartheta\,. \tag{3.69}$$

By evaluating these equations for a range of angles using approximate mechanical properties for cornea (ρ = 1000 kg/m^3, μ = 1 MPa, G = 20 kPa, and setting λ so that the average longitudinal wave speed is approximately 1540 m/s), and assuming tensile isotropy ($Q_1 = Q_2 = 0$, or $\delta = 0$), some intuition about bulk wave behavior in a NITI material can be gained. The quasi-longitudinal wave speed is nearly constant over all angles, with variations of ± 0.01%, while the quasi-shear waves' speeds show a large range of variability over angle (**Figure 3-9b**).

The mechanical behavior is symmetric with respect to rotations about the *z*-axis but varies with respect to the angle θ formed by the propagation direction and the *z*-axis (**Figure 3-9a**).

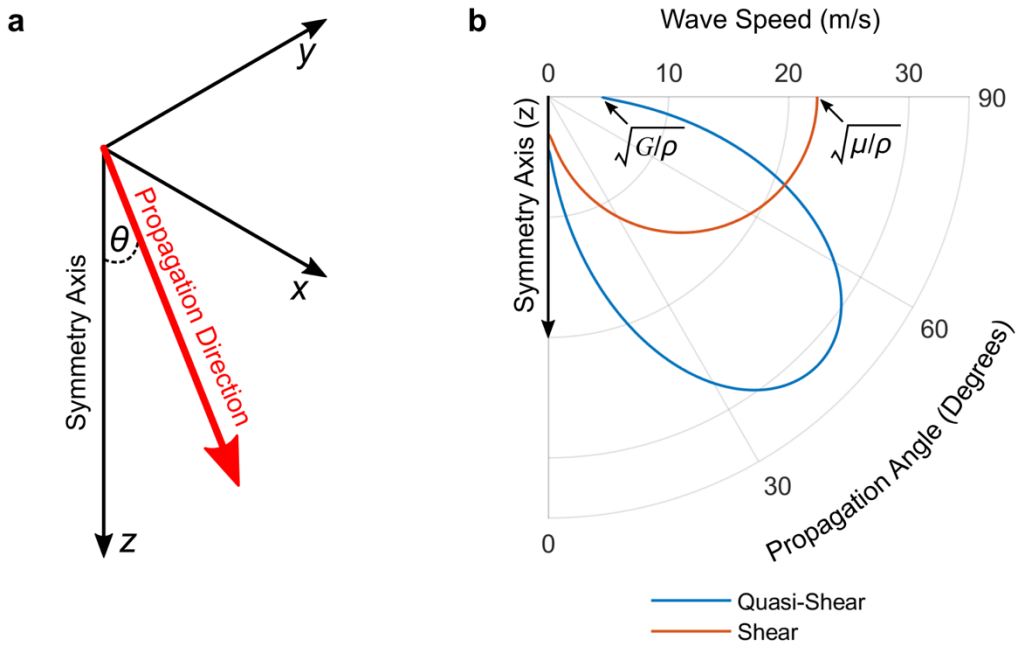

Figure 3-9. Angle-dependent shear wave speed in bulk NITI material (a) Coordinate system, symmetry axis, and propagation angle for a TI material. (b) Quasi-shear and shear wave speed as a function of propagation angle for a NITI material with properties representative of porcine cornea (ρ = 1000 kg/m^3, μ = 1 MPa, G = 20 kPa, λ = 2.37 GPa, $\delta = 0$).

3.10 Rayleigh waves a NITI media

When the xy-plane corresponds to a free surface, a Rayleigh wave propagates along the surface with speed c_R. The value of c_R can be found using the Stroh formalism.[156–159] Consider the solution of a Rayleigh wave propagating in the **m** = [1, 0, 0] direction, along the free surface defined by normal vector **n** = [0, 0, 1] (because of symmetry in the xy-plane, the propagation direction is arbitrary). The Stroh formalism defines the 3×3 matrices

$$Q_{ik} = c_{ijkl} m_j m_l - \rho c^2 \delta_{ik} \tag{3.70}$$

$$R_{ik} = c_{ijkl} m_j n_l \tag{3.71}$$

$$T_{ik} = c_{ijkl} n_j n_l \tag{3.72}$$

where c_{ijkl} is the fourth-order stiffness tensor, ρ is the density, and c is the wave speed. These matrices are combined to form the 6×6 Stroh eigenvalue problem,

$$\mathbf{N}\begin{bmatrix}\mathbf{a}\\ \mathbf{b}\end{bmatrix} = p\begin{bmatrix}\mathbf{a}\\ \mathbf{b}\end{bmatrix}, \tag{3.73}$$

where

$$\mathbf{N} = \begin{bmatrix} -\mathbf{T}^{-1}\mathbf{R}^T & \mathbf{T}^{-1} \\ \mathbf{R}\mathbf{T}^{-1}\mathbf{R}^T - \mathbf{Q} & -\mathbf{T}^{-1}\mathbf{R}^T \end{bmatrix}. \tag{3.74}$$

The eigenvectors contain the polarization vectors $\mathbf{a}$ and traction vectors $\mathbf{b}$ of harmonic waves that satisfy the free surface boundary condition. The displacements $\mathbf{u}$ and tractions $\mathbf{t}$ for these solutions are

$$\mathbf{u} = \mathbf{a} e^{ik(\mathbf{m}\cdot\mathbf{x} + p\mathbf{n}\cdot\mathbf{x} - vt)}, \tag{3.75}$$

$$\mathbf{t} = ik\mathbf{b} e^{ik(\mathbf{m}\cdot\mathbf{x} - vt)}. \tag{3.76}$$

The Rayleigh wave is formed by a linear combination of wave modes whose amplitude decay with depth. For this reason, only solutions where p has a positive imaginary part are considered. Below the limiting velocity of the material, the six eigenvalues occur in complex conjugate pairs $\begin{bmatrix}\mathbf{a}\\ \mathbf{b}\end{bmatrix}$, where only three modes form the Rayleigh wave. Furthermore, the free surface condition implies that the linear combination of the tractions must be zero,

$$\sum_{i=1}^{3} c_i \mathbf{t}_i = \mathbf{0}. \tag{3.78}$$

This is often rewritten in the following form:

$$ik\begin{bmatrix} | & | & | \\ \mathbf{b}_1 & \mathbf{b}_2 & \mathbf{b}_3 \\ | & | & | \end{bmatrix}\begin{bmatrix} c_1 \\ c_2 \\ c_3 \end{bmatrix} e^{ik(\mathbf{m}\cdot\mathbf{x}-vt)} = \mathbf{Bc} = \mathbf{0}, \tag{3.79}$$

which has a nontrivial solution if and only if the determinant of **B** is zero.

To solve for the Rayleigh wave speed, an iterative algorithm is required. At each iteration, a trial wave speed c is considered, and the Stroh eigenvalue problem is solved to obtain the relevant eigenvectors, as described above. The traction vectors are extracted and used to form the matrix **B** and calculate its determinant. This process is repeated until the absolute value of the determinant is minimized. The resulting wave speed corresponds to the Rayleigh wave speed c_R.

Following this procedure for the same representative NITI material used in the previous section (ρ = 1000 kg/m^3, μ = 1 MPa, G = 20 kPa, $\delta = 0$, and setting λ = 2.37 GPa so that the average longitudinal wave speed is approximately 1540 m/s), the Rayleigh wave speed in a cornea-like NITI solid is approximately $\sqrt{G/\rho}$.

The exact value varies slightly with the degree of anisotropy G/μ, from approximately $0.9553\sqrt{G/\rho}$ in the isotropic limit ($G = \mu$) to $\sqrt{G/\rho}$ in the highly anisotropic limit ($G \ll \mu$) (**Figure 3-10**).

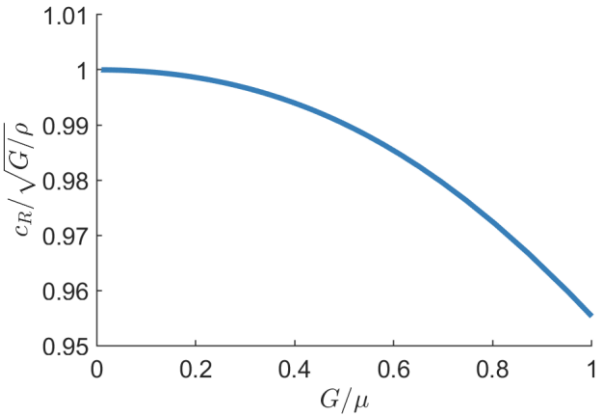

Figure 3-10. Rayleigh wave speed as a function of anisotropy. The Rayleigh wave speed is primarily governed by G in a NITI solid.

3.11 Guided waves in NITI media

As with the isotropic case, analytical solutions to elastic wave propagation in a bounded NITI material can be complex. To derive an analytic solution for guided waves in the cornea, first consider an infinite NITI layer of thickness h and density ρ bounded above by air and below by water (**Figure 3-11**). Assuming a general NITI material model, the stiffness tensor contains material constants λ, μ, G, and δ. Because the acoustic excitation employed in non-contact AμT-OCT generates a pseudo-line source, a plane strain state is assumed.

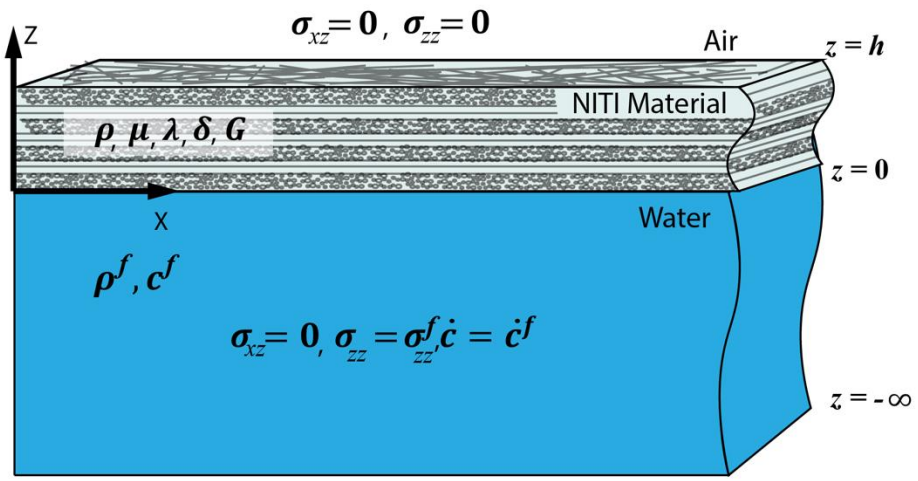

Figure 3-11. Geometry and boundary conditions displayed for a NITI plate bounded above by air and below by water.

To generalize, the following scales are introduced to nondimensionalize the terms:

Position: $\boldsymbol{x} \sim h$

Displacement: $\boldsymbol{u} \sim h$

Time: $t \sim h/\sqrt{\mu/\rho}$

Frequency: $f \sim \sqrt{\mu/\rho}/h$

Wavenumber: $k \sim h$

the dimensionless equations of motion yield the elastodynamic equations for a NITI material

$$u_{tt} = \beta^2 u_{xx} + \alpha^2 u_{zz} + \gamma^2 v_{xz} \tag{3.80}$$

$$v_{tt} = \alpha^2 v_{xx} + \xi^2 v_{zz} + \gamma^2 u_{xz} \tag{3.81}$$

$$\alpha^2 = \frac{C_{55}}{\mu} = \frac{G}{\mu} \tag{3.82}$$

$$\beta^2 = \frac{C_{11}}{\mu} = \frac{\lambda + 2\mu}{\mu} \tag{3.83}$$

$$\gamma^2 = \frac{(C_{13} + C_{55})}{\mu} = \frac{\lambda + Q_1 + G}{\mu} \tag{3.84}$$

$$\xi^2 = \frac{C_{33}}{\mu} = \frac{\lambda + 2\mu + Q_2}{\mu}$$

where, $\boldsymbol{u} = (u, v)$ is the dimensionless displacement field with x and z components, respectively; α, β, γ, and ξ are dimensionless parameters, and subscripts denote partial differentiation. In other words, the guided wave solution for a NITI material uses the elastic wave equations of the following dimensionless form:

$$u_{tt} = \left(\frac{\lambda + 2\mu}{\mu}\right) u_{xx} + \left(\frac{G}{\mu}\right) u_{zz} + \left(\frac{\lambda + Q_1 + G}{\mu}\right) v_{xz} \tag{3.85}$$

$$v_{tt} = \left(\frac{G}{\mu}\right) v_{xx} + \left(\frac{\lambda + 2\mu + Q_2}{\mu}\right) v_{zz} + \left(\frac{\lambda + Q_1 + G}{\mu}\right) u_{xz} \tag{3.86}$$

where *u* and *v* are the *x*- and *z*- components of the displacement, respectively, and subscripts denote partial differentiation.

Next, harmonic solutions are assumed for displacements of the form

$$u(x, z, t) = Ae^{i(kx + \ell z - \omega t)} \tag{3.87}$$

$$v(x, z, t) = Be^{i(kx + \ell z - \omega t)} \tag{3.88}$$

where k and ℓ are dimensionless angular wavenumbers, ω is the dimensionless angular frequency, and A and B are arbitrary constants.

Substituting these solutions into the governing equations yields the homogeneous linear system

$$\begin{bmatrix} q_\beta^2 + \frac{\alpha^2}{\beta^2}\ell^2 & k\ell\frac{\gamma^2}{\beta^2} \\ k\ell\frac{\gamma^2}{\alpha^2} & q_\alpha^2 + \frac{\xi^2}{\alpha^2}\ell^2 \end{bmatrix} \begin{bmatrix} A \\ B \end{bmatrix} = \begin{bmatrix} 0 \\ 0 \end{bmatrix} \tag{3.89}$$

where

$$q_\alpha^2 = k^2 - \frac{\omega^2}{\alpha^2} \tag{3.90}$$

$$q_\beta^2 = k^2 - \frac{\omega^2}{\beta^2}. \tag{3.91}$$

This has non-trivial solutions if and only if the determinant of the matrix is zero, resulting in a biquadratic equation for ℓ with four solutions

$$\ell^4 + \left[\frac{\alpha^2}{\xi^2}q_\alpha^2 + \frac{\beta^2}{\alpha^2}q_\beta^2 - \frac{\gamma^4 k^2}{\alpha^2\xi^2}\right]\ell^2 + \frac{\beta^2}{\xi^2}q_\alpha^2 q_\beta^2 = 0 \tag{3.92}$$

$$\ell = \pm\sqrt{\frac{1}{2}\left[\varphi \pm \sqrt{\varphi^2 - 4\frac{\beta^2}{\xi^2}q_\alpha^2 q_\beta^2}\right]} \tag{3.93}$$

$$\varphi = k^2\frac{\gamma^4}{\alpha^2\xi^2} - \frac{\alpha^2}{\xi^2}q_\alpha^2 - \frac{\beta^2}{\alpha^2}q_\beta^2 \tag{3.94}$$

Without loss of generality, we assume $B = 1$ and solve the corresponding coefficient A for each solution ℓ. This yields the following solutions, where the outer and inner ± signs match for each A and ℓ,

$$A = \pm\left[-\frac{\sqrt{2}\frac{\gamma^2 k}{\alpha^2}\sqrt{\varphi \pm \sqrt{\varphi^2 - 4q_\alpha^2 q_\beta^2}}}{\varphi + 2\frac{\beta^2}{\alpha^2}q_\beta^2 \pm \sqrt{\varphi^2 - 4q_\alpha^2 q_\beta^2}}\right] \tag{3.95}$$

The full solutions are therefore linear combinations of four partial waves,

$$u(x,z,t) = \sum_{j=1}^{4} C_j A_j e^{i\ell_j z} e^{i(kx-\omega t)} \tag{3.96}$$

$$v(x,z,t) = \sum_{j=1}^{4} C_j e^{i\ell_j z} e^{i(kx-\omega t)} \tag{3.97}$$

In the fluid domain, an acoustic material is assumed. The dimensionless acoustic wave equation in velocity potential form is

$$\dot{\boldsymbol{u}}^f = \nabla\Phi \tag{3.98}$$

$$p^f = -\frac{\rho^f}{\rho}\Phi_t \tag{3.99}$$

$$\Delta\Phi - \frac{1}{\delta^2}\Phi_{tt} = 0 \tag{3.100}$$

$$\delta^2 = \frac{\rho(c^f)^2}{\mu} \tag{3.101}$$

The general solution for the fluid domain takes the form

$$\Phi = C_5 e^{\xi z} e^{i(kx-\omega t)} \tag{3.102}$$

$$\xi = \sqrt{k^2 - \frac{\omega^2}{\delta^2}} \tag{3.103}$$

$$\mathrm{Re}(\xi) > 0 \tag{3.104}$$

The constants C_j were chosen so that the solutions satisfy the non-dimensionalized boundary conditions:

$$\begin{array}{ll} \sigma_{xz} = 0 & \text{at } z = 1 \\ \sigma_{zz} = 0 & \text{at } z = 1 \\ \sigma_{xz} = 0 & \text{at } z = 0 \\ \sigma_{zz} = \sigma_{zz}^f & \text{at } z = 0 \\ \dot{v} = \dot{v}^f & \text{at } z = 0 \end{array} \tag{3.105}$$

where the superscripts f denote quantities in the fluid domain $z < 0$. Substituting the general solutions into the boundary conditions yields a 5×5 homogeneous system for the coefficients, $\mathbf{Mc} = \mathbf{0}$. This system has nontrivial solutions if and only if the determinant of the matrix $\mathbf{M}$ (Eq. 3.106) is zero. For a given frequency ω, wavenumbers k can be found that satisfy the dispersion relation using numerical root-finding methods or by minimizing the absolute value of the determinant:

(3.106)

$$\mathbf{M} = \begin{bmatrix} (\ell_1 A_1 + k)e^{i\ell_1} & (\ell_2 A_2 + k)e^{i\ell_2} & (\ell_3 A_3 + k)e^{i\ell_3} & (\ell_4 A_4 + k)e^{i\ell_4} & 0 \\ [k(\gamma^2 - \alpha^2)A_1 + \beta^2 \ell_1]e^{i\ell_1} & [k(\gamma^2 - \alpha^2)A_2 + \beta^2 \ell_2]e^{i\ell_2} & [k(\gamma^2 - \alpha^2)A_3 + \beta^2 \ell_3]e^{i\ell_3} & [k(\gamma^2 - \alpha^2)A_4 + \beta^2 \ell_4]e^{i\ell_4} & 0 \\ \ell_1 A_1 + k & \ell_2 A_2 + k & \ell_3 A_3 + k & \ell_4 A_4 + k & 0 \\ k(\gamma^2 - \alpha^2)A_1 + \beta^2 \ell_1 & k(\gamma^2 - \alpha^2)A_2 + \beta^2 \ell_2 & k(\gamma^2 - \alpha^2)A_3 + \beta^2 \ell_3 & k(\gamma^2 - \alpha^2)A_4 + \beta^2 \ell_4 & \omega \rho^f / \rho \\ \omega & \omega & \omega & \omega & -i\xi \end{bmatrix}$$

The dispersion relation for a NITI layer bounded by air and water (derived from the partial wave solutions to the elastic wave equations satisfying corneal boundary conditions (**Figure 3-12a**)) was then explored for varying levels of anisotropy ($G = 20$ kPa, $h = 0.55$ mm, $\delta = 0$, varying μ). While the solution included an infinite number of quasi-antisymmetric (A) and quasi-symmetric (S_0) modes, only the first two (A_0 and S_0) travel at speeds which are typically captured in OCE. **Figure 3-12b** displays examples of A_0 and S_0 mode behavior for NITI materials with varying levels of anisotropy. As μ increased relative to G, the S_0 mode propagated with higher phase velocity at low frequencies (**Figure 3-12c**). In contrast, the high frequency asymptote of the A_0 mode was primarily governed by G, with μ controlling both the rate at which the A_0 mode approaches its asymptote and weakly affecting the asymptotic value (< 5%) (**Figure 3-12d**).

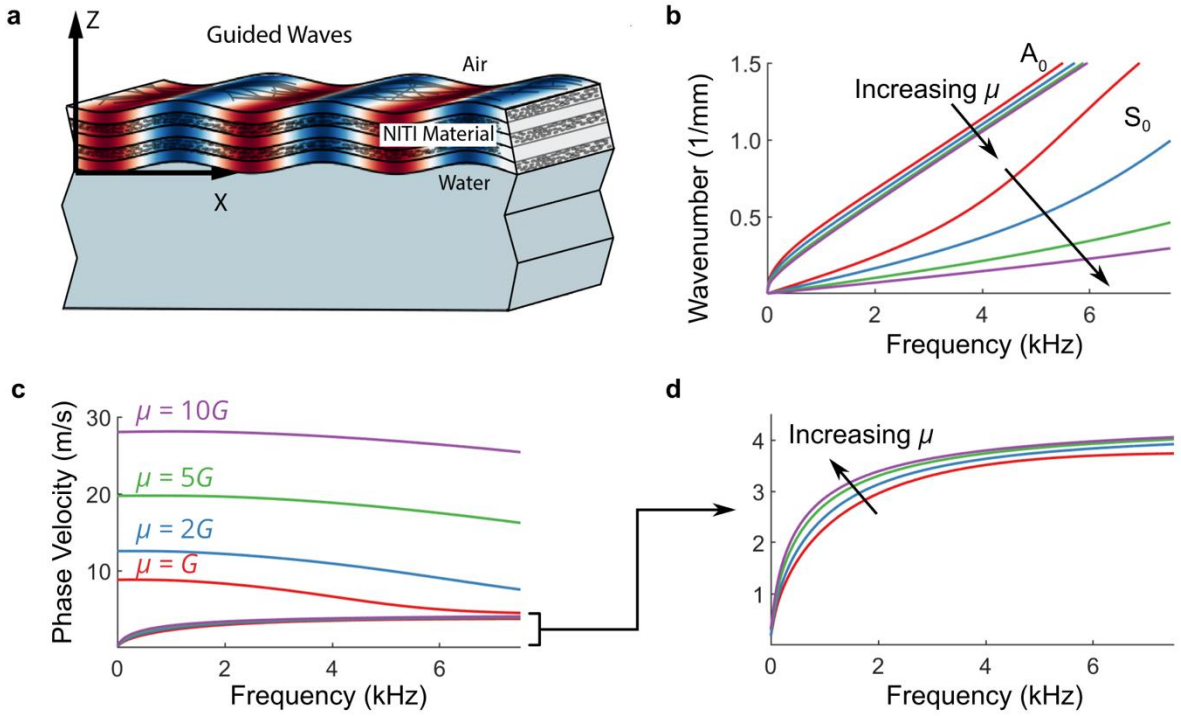

Figure 3-12. **Analytical solutions for guided wave behavior in a bounded NITI layer.** (a) Propagation of harmonic guided waves in cornea tissue, modeled as a NITI material layer bounded above by air and below by

water. Dispersion relations for propagating guided modes were derived from partial wave solutions to the elastic wave equations satisfying corneal boundary conditions. (b) The effect of increasing anisotropy on fundamental (zero order) A_0 and S_0 modes (G = 20 kPa, h = 0.55 mm, $\delta = 0$, varying μ) presented in wavenumber-frequency space. The behavior of the A_0 mode was primarily governed by G, and the S_0 mode by μ. (c) The same dispersion curves in phase velocity versus frequency representation. (d) Zoomed view of the A_0 mode in phase velocity versus frequency representation - the high-frequency asymptote of the A_0 mode governed primarily on G, with its low-frequency rate of change governed by μ.

The details of **Figure 3-12 b-d** provide an important conclusion. Due to the bounded NITI structure, the first quasi-antisymmetric (A_0) mode varies for unique combinations of G and μ. A closer view demonstrates that the high-frequency asymptote of the A_0 mode is primarily governed by G and the low-frequency rate of change governed primary by μ. While the Rayleigh wave speed in a NITI material is almost entirely defined by the modulus G, the cornea's finite thickness produces guided waves depending on both G and μ, allowing both parameters to be estimated in a single measurement provided that broad-band elastic waves are present.

Effects of incompressibility assumptions in guided NITI material

In general, a TI material contains five independent elastic constants (C_{11}, C_{12}, C_{13}, C_{33}, C_{44}) rather than the two (Lamé constants) of isotropic materials. As shown above, the incompressibility conditions in a NITI material reduce the number of independent elastic constants to four, μ, G, δ, and λ. Because $\lambda \gg \mu$, it does not affect the material deformation. Thus, to fully describe how a NITI material will deform under stress, μ, G, and δ are required. In the above presentation of guided mode structure, the material was assumed isotropic in its longitudinal terms, where $\delta = 0$. While this assumption is imperfect, it does not prevent accurate approximation of guided wave behavior in TI materials that are weakly anisotropic in their longitudinal terms.[160]

The relationship between Poisson's ratios and Young's moduli suggest that the shear anisotropy (μ/G) in the cornea is much greater than possible variations of E introduced by $\delta \neq 0$. Using representative values of G, μ, and λ for the cornea ($G = 20$ kPa, μ= 3 MPa, λ=2.37 GPa), **Figure 3-13** demonstrates that for the limiting case of $\delta = -2\mu$, there are negligible changes in the A_0 mode. Variations in C_{13} and C_{33} are second-order effects when utilizing guided shear waves to infer stiffness in nearly incompressible TI materials.

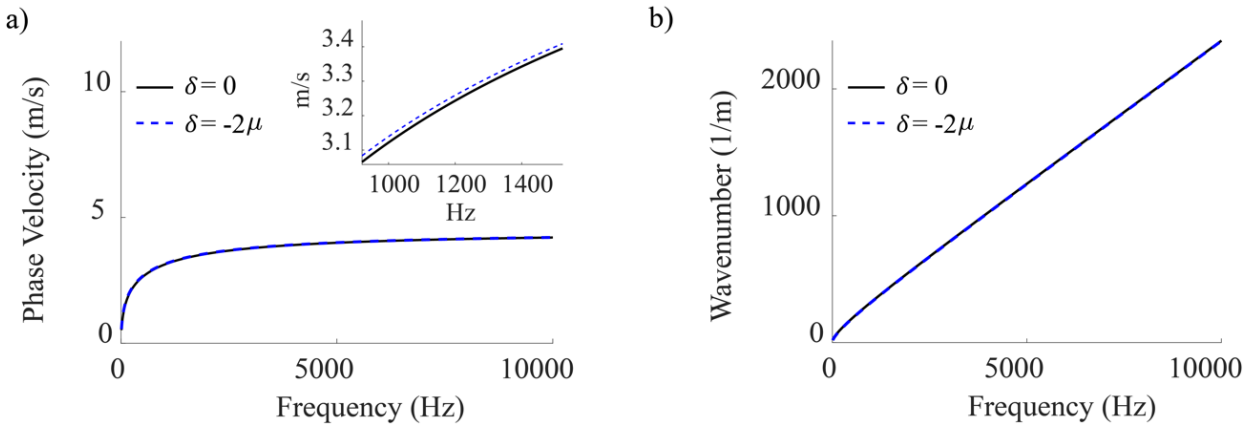

Figure 3-13. Effect of δ on A_0 mode phase velocity spectra. Shown in a) (*f-c* domain) with zoomed inset and b) wavenumber representation (*f-k* domain) for a TI material with tensile anisotropy defined by $\delta = 0$ and $\delta = -2\mu$. The guided A_0 mode in the cornea remains relatively insensitive to changes in δ, suggesting that the shear moduli μ and G dominate guided wave behavior. Note that $\delta = 0$ is consistent with previous work and was used in this work to generate the theoretical dispersion relation.

As a first approximation of the NITI model, variations in the C_{13} and C_{33} terms were assumed negligible as the A_0 mode remains functionally insensitive to δ. While the C_{13} and C_{33} assumption will play a role in the relationship between E and μ, corneal structure suggests that E=3μ is a reasonable assumption.

3.12 Destructive mechanical tests

An important take-away from the NITI model is that macro-level stiffness of the cornea may be defined by two shear moduli (G and μ), decoupling tensile/inflation responses from shear responses. In this section, equations are presented based on traditional destructive techniques to provide a basis for comparing elastic moduli in the NITI model with the wide body of existing literature. The relevant stress-strain relations for each test type depend primarily on one elastic parameter while remaining agnostic to the other. Furthermore, tensile and inflation measurements yield similar values, as with shear and transient methods.

Tensile testing of corneal strips.

In tensile tests, rectangular strips of ex vivo cornea are subjected to uniaxial tension. The corresponding strain is measured, and the Young's modulus quantified as $E = \sigma/\varepsilon$. In general, the orientation of the cornea strip lies in the *xy*-plane, and the direction of the applied stress aligns with the long axis of the strip. While anisotropy within the *xy*-plane has been reported by some studies, the degree of anisotropy at low IOP (low pre-stress)[16,74,150,161,162] suggests that cornea microstructure can be approximated with the NITI model as symmetric for any direction in the *xy*-plane. Thus, it is sufficient to consider only one orientation of the strip. Note that second order affects from the C_{13} and C_{33} assumptions are ignored in this derivation. As such, OCE-measured Young's modulus E is approximately equivalent to the tangential tensile modulus (E_T) measured in tensile extensometry, and which is of a primary interest in ophthalmology.

Consider uniaxial loading in the x direction. It is clear from this linear system that the shear strains are zero and consequentially any equations with G vanish, leaving

$$\begin{bmatrix} \sigma_{xx} \\ 0 \\ 0 \end{bmatrix} = \begin{bmatrix} \lambda + 2\mu & \lambda & \lambda \\ \lambda & \lambda + 2\mu & \lambda \\ \lambda & \lambda & \lambda + 2\mu \end{bmatrix} \begin{bmatrix} \varepsilon_{xx} \\ \varepsilon_{yy} \\ \varepsilon_{zz} \end{bmatrix}. \tag{3.107}$$

Solving the third row for ε_{zz},

$$\varepsilon_{zz} = -\frac{\lambda}{\lambda+2\mu}\left(\varepsilon_{xx} + \varepsilon_{yy}\right). \tag{3.108}$$

Substituting Eq. 3.108 into the second row of Eq. 3.107 and solving for ε_{yy} gives

$$\varepsilon_{yy} = -\frac{\lambda}{2(\lambda + \mu)}\varepsilon_{xx}. \tag{3.109}$$

Finally, substituting into the first row and defining the Young's modulus as $E = \sigma_{xx}/\varepsilon_{xx}$, the Young's modulus can be quantified via

$$E = \frac{\mu(3\lambda + 2\mu)}{\lambda + \mu}, \tag{3.110}$$

which in the incompressible limit $\lambda \to \infty$ gives $E = 3\mu$. From this, the moduli determined in a NITI material under tension will have an apparent Young's modulus that depends only on μ and not on G. Furthermore, an approximation can be found which relates μ to E.

Inflation tests of corneal buttons

In corneal inflation tests, a circular region of the cornea and sclera (called a trephinate) is often dissected from an ex vivo eye.[47,163] The cornea is clamped above a fluid-filled chamber and sealed around the scleral rim. The chamber is connected to a water column whose height is varied to simulate intraocular pressure (IOP). For a given pressure p, the test measures the rise of the corneal apex r. The corneal thickness h, radius of curvature R, and the contact angle at the clamped edge

γ are also estimated. Deformation of the cornea is then modeled using the theory of spherical shells.[164]

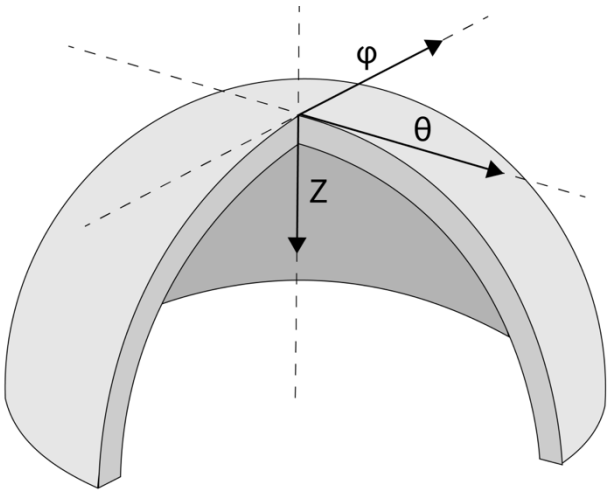

Figure 3-14. Corneal geometry and local coordinate axes used in analyzing stress strain relationships to mathematically describe inflation tests.

The corneal inflation test can be described by the coordinate system shown in **Figure 3-14.** The deformation of an infinitesimal shell element under pressure is governed by the normal stress resultants N_φ and N_θ, bending moments M_φ and M_θ, and shear stress resultant Q_φ. Here, φ represents the meridional coordinate (sometimes denoted by y in local element coordinates) and θ denotes the azimuthal coordinate (sometimes denoted as x in local element coordinates). The resultants and moments are defined:

$$N_\theta = \int_{-\frac{h}{2}}^{\frac{h}{2}} \sigma_\theta \left(1 - \frac{z}{R}\right) \mathrm{d}z\,, \tag{3.111}$$

$$N_\varphi = \int_{-\frac{h}{2}}^{\frac{h}{2}} \sigma_\varphi \left(1 - \frac{z}{R}\right) \mathrm{d}z\,, \tag{3.112}$$

$$M_\theta = \int_{-\frac{h}{2}}^{\frac{h}{2}} \sigma_\theta z \left(1 - \frac{z}{R}\right) \mathrm{d}z\,, \tag{3.113}$$

$$M_\varphi = \int_{-\frac{h}{2}}^{\frac{h}{2}} \sigma_\varphi z \left(1 - \frac{z}{R}\right) \mathrm{d}z\,, \tag{3.114}$$

$$Q_\varphi = \int_{-\frac{h}{2}}^{\frac{h}{2}} \tau_{\varphi z} \left(1 - \frac{z}{R}\right) \mathrm{d}z\,. \tag{3.115}$$

Balancing the forces and moments on the shell element and considering the relationship between strain and the deformed shape leads to a system of five equations describing the rise of the corneal apex following inflation.[47]

Hooke's law can be applied to assign a constitutive model to the shell using a local coordinate system of the shell element. The shell is assumed to be thin relative to its radius of curvature ($h \ll R$), thus a plane stress approximation can be applied. This yields the following stress-strain relation for the shell element:

$$\begin{bmatrix} \sigma_\theta \\ \sigma_\varphi \\ 0 \\ 0 \\ 0 \\ \tau_{\theta\varphi} \end{bmatrix} = \begin{bmatrix} \lambda + 2\mu & \lambda & \lambda & & & \\ \lambda & \lambda + 2\mu & \lambda & & & \\ \lambda & \lambda & \lambda + 2\mu & & & \\ & & & G & & \\ & & & & G & \\ & & & & & \mu \end{bmatrix} \begin{bmatrix} \varepsilon_\theta \\ \varepsilon_\varphi \\ \varepsilon_z \\ \gamma_{\varphi z} \\ \gamma_{\theta z} \\ \gamma_{\theta\varphi} \end{bmatrix}. \tag{3.116}$$

As with the tensile test, the shear strains vanish, and the solution will not depend on G.

Proceeding as in the tensile test, the third row can be solved for ε_z,

$$\varepsilon_z = -\frac{\lambda}{\lambda + 2\mu}\left(\varepsilon_\theta + \varepsilon_\varphi\right) \tag{3.117}$$

Substitute Eq. 3.117 into rows 1 and 2 to obtain a simplified system:

$$\sigma_\theta = \frac{4\mu(\lambda+\mu)}{\lambda+2\mu}\varepsilon_\theta + \frac{2\lambda\mu}{\lambda+2\mu}\varepsilon_\varphi, \tag{3.118}$$

$$\sigma_\varphi = \frac{2\lambda\mu}{\lambda+2\mu}\varepsilon_\theta + \frac{4\mu(\lambda+\mu)}{\lambda+2\mu}\varepsilon_\varphi. \tag{3.119}$$

For notational convenience, Eq. 3.118 and Eq. 3.119 can be converted from λ-μ (Lamé parameter) form to the Young's modulus and Poisson's ratio form using the following relationships:

$$\lambda = \frac{E\nu}{(1+\nu)(1-2\nu)}, \tag{3.120}$$

$$\mu = \frac{E}{2(1+\nu)}. \tag{3.121}$$

to obtain

$$\sigma_\theta = \frac{E}{1-\nu^2}\left(\varepsilon_\theta + \nu\varepsilon_\varphi\right), \tag{3.122}$$

$$\sigma_\varphi = \frac{E}{1-\nu^2}\left(\varepsilon_\varphi + \nu\varepsilon_\theta\right). \tag{3.123}$$

For an incompressible material, $\nu = 0.5$, the stresses depend only on the Young's modulus $E = 3\mu$, as these stresses are the only terms that appear in the stress resultants and bending moments. The apical rise measured in an inflation test depends on the resultants and moments, and so also depend only on μ. Thus, like the tensile test, an inflation test of a NITI material will measure μ and not G.

Shear torsional test of corneal buttons

In torsional tests of corneal trephinates (such as in parallel-plate rheometry) a cylindrical section of ex vivo cornea (with thickness h and radius R) is placed between parallel platens and a rotational deformation Θ is applied to the sample. The torque T at the top platen is often measured, and Hooke's law for shear is used to estimate the shear modulus of the sample. The torque can be given by the integral

$$T = \int_0^R \int_0^{2\pi} \tau_{\theta z} r \, \mathrm{d}\theta \mathrm{d}r \,. \tag{3.124}$$

The transformation from Cartesian coordinates to cylindrical coordinates gives the shear stress and strain

$$\tau_{\theta z} = -\sin\theta \, \tau_{xz} + \cos\theta \, \tau_{yz}, \tag{3.125}$$

$$\gamma_{\theta z} = -\sin\theta \, \gamma_{xz} + \cos\theta \, \gamma_{yz}. \tag{3.126}$$

For the stress-strain relation in a NITI material (Eq. 3.39), the in-plane shearing is described by

$$\tau_{xz} = G\gamma_{xz}, \tag{3.127}$$

$$\tau_{yz} = G\gamma_{yz}. \tag{3.128}$$

Substituting Eqs. 3.127 and 3.128 into 3.125,

$$\tau_{\theta z} = G\gamma_{\theta z}. \tag{3.129}$$

The shear strain and stress can be approximated as

$$\gamma_{\theta z} = \frac{r\Theta}{h} \tag{3.130}$$

$$\tau_{\theta z} = \frac{Gr\Theta}{h} \tag{3.131}$$

Evaluating the torque integral and solving for G provides

$$G = T\frac{2h}{\pi\Theta R^4}. \tag{3.132}$$

Clearly, a shear torsional test will provide an estimate of G only and is not influenced by μ.

3.13 Conclusions

To summarize, a nearly incompressible transversely isotropic (NITI) model of the cornea was presented to describe corneal biomechanics. The NITI model differs from the isotropic model in that shear and tensile behavior are decoupled, potentially resolving the apparent paradox in reported biomechanical properties based on different loading techniques. Mechanical tests that probe these behaviors independently will report greatly different Young's moduli in materials with high level of shear anisotropy such as the cornea. The shear behavior is governed by an independent modulus, which we refer to as G, and the tensile behavior is governed by the modulus μ, which can be approximately related to the Young's modulus $E = 3\mu$ assuming tensile isotropy. Limiting conditions on the deformation assumptions were presented as a potential avenue to more accurately relate μ to the Young's Modulus in the future.

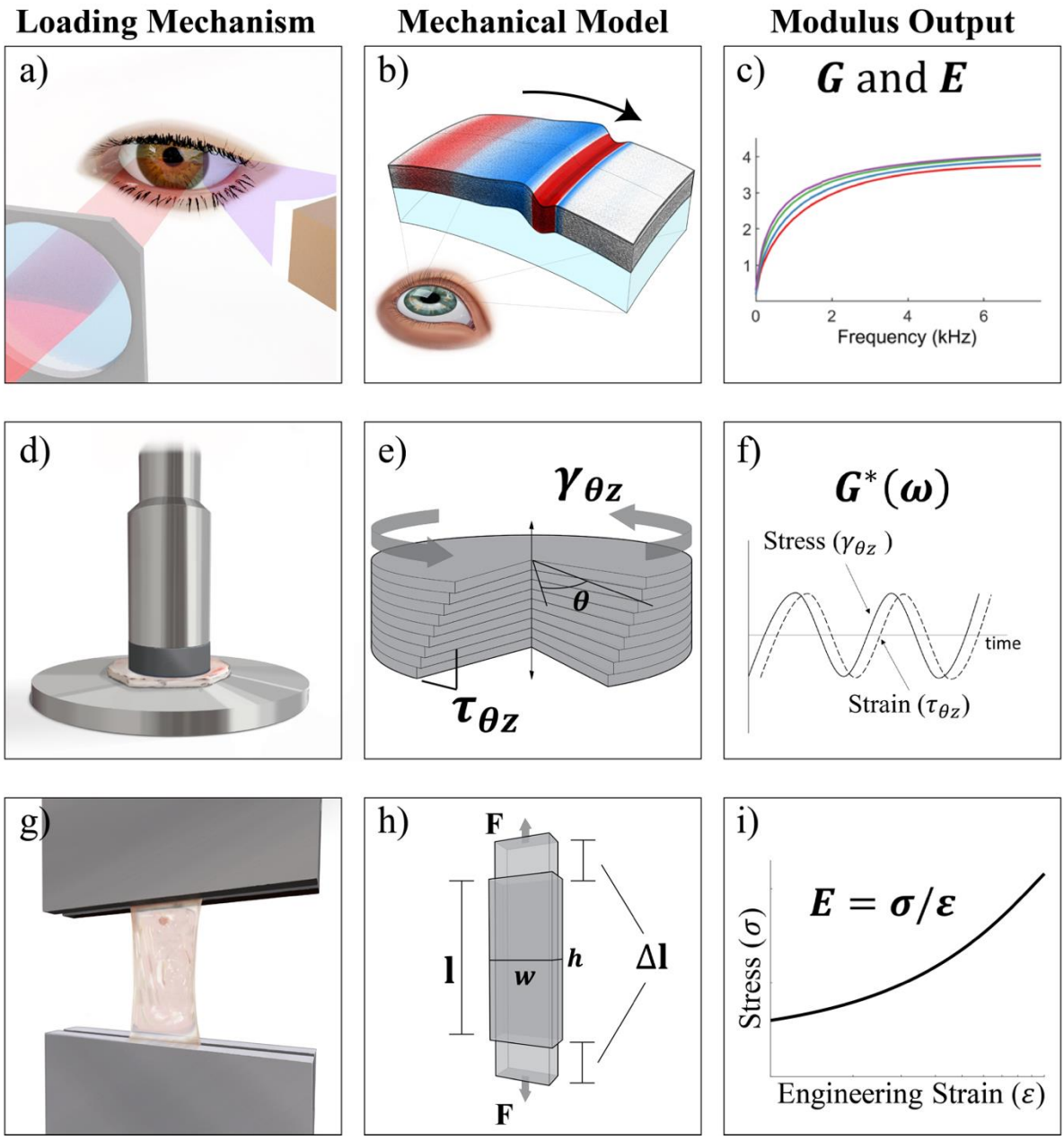

Figure 3-15. **Loading techniques used to measure anisotropic elastic moduli.** a) Representative display of AμT-OCE system to generate and image elastic waves in the cornea. The purple triangle focus represents non-contact acoustic loading through air and the red line-scan displays approximate scan range for OCT-based detection of wave-fields. b) Guided elastic waves propagating in a NITI material such as the cornea. c) A solution to the dispersion equation was iteratively solved in the Fourier spectrum to reconstruct both elastic moduli, *E* and *G*, that most closely resemble the measured waveform in the cornea. d) Representation of ex vivo parallel plate rheometry of the cornea. e) Material model demonstrating assumed geometries and shear stress-strain relationships. f) Calculation of the complex shear modulus *G** using measured shear stress and strain. g) Representation of corneal

strips loaded in extensometer. h) Material model demonstrating assumed geometries and loading in tensile testing. i) Calculation of the Young's modulus, E, in extension testing.

Finally, the derivations in this chapter provide an avenue for robust and accurate measurements of corneal elastic moduli using propagating elastic waves. The model intuitively links cornea microstructure to the observed mechanical response, where collagen lamellae contribute to the stiff behavior under tension and inflation (MPa range) and the layered structure allows internal slip, producing the softer response of shear and transient tests (kPa range). Constitutive equations were derived which describe corresponding material properties based on different loading techniques (**Figure 3-15**). The model presented suggests that clinical stiffness measurements made with OCE may be used to connect the field of non-destructive in vivo testing with the extensive body of ex vivo literature. Bridging this gap is an important step in clinically translating OCE and may help launch large clinical studies in the future.

Chapter 4. Elastic wave imaging using Optical Coherence Tomography

Optical coherence tomography (OCT), based on the principle of optical interference, is well suited to measure tissue displacements due to local vibrations and strains. In this chapter, an OCT system combined with an air-coupled acoustic transducer capable of launching and detecting mechanical waves is presented. The system described can detect near shot-noise limited vibrations in addition to imaging corneal microstructure using phase-sensitive OCT based on spectral domain OCT (SD-OCT). To ensure maximum performance relative to theoretical expectations, care was taken to select optical components that minimize incompatibility, spectral response, and misalignment. In this system, best effort was made to select suitable components for optimum phase stability. Detailed design parameters related to the light source, spectrometer design, system stability, acoustic excitation, system timing, and final performance are presented. The non-contact system described within this chapter was used to demonstrate how the OCT signal may be used to reconstruct high-resolution images of tissue elasticity based on the constitutive equations of the previous chapter.

4.1 SD-OCT system hardware

A phase-sensitive spectral domain optical coherence tomography system (**Figure 4-1**) was built to track propagating mechanical waves via local tissue displacements. To generate propagating elastic waves, a trigger signal was sent to a home-built air-coupled ultrasound transducer providing a temporally and spatially focused acoustic wave that transferred energy to the tissue, effectively generating a tens-of-nanometer to micron-scale displacement. The system utilized a Michelson-type fiber-optic interferometer combined with an optical spectrometer and line scan camera for

depth encoding and was optimized for noise reduction using polarization-maintaining (PM) fibers in all components (as opposed to conventional single mode (SM) fibers).

The light source was a broadband superluminescent diode (SLD) with a near-Gaussian spectral profile and maximum output power of 30 mW (SLD1018P, Thorlabs, NJ) coupled into a PM-fiber with radiation aligned along the slow axis. The central wavelength was 1310 nm, with a FWHM of 45 nm. Linearly polarized light was then coupled into a broadband PM circulator (PMCIR-1310_FC/APC, OZ-optics, Ottawa, Canada) and then into a 2x2 99/1 PM beam combiner (Fused-22-1310-7/125-99/1, OZ-optics, Ottawa, Canada). One percent (1%) of the power was directed toward the reference arm through a variable attenuator (VOA50PM, Thorlabs, NJ) and into a variable optical delay line (ODL-200, OZ-Optics, Ottawa, CA) terminated by an in-fiber reflector having near 100% reflection at the 1310 nm wavelength.

All optical components were mounted on an isolated stage equipped with rubber damping and placed on an active pneumatic isolation table (PTS602, Thorlabs, NJ). Together, the OCT system combined with non-contact acoustic excitation is referred to as acoustic-microtapping OCE (AμT-OCE).

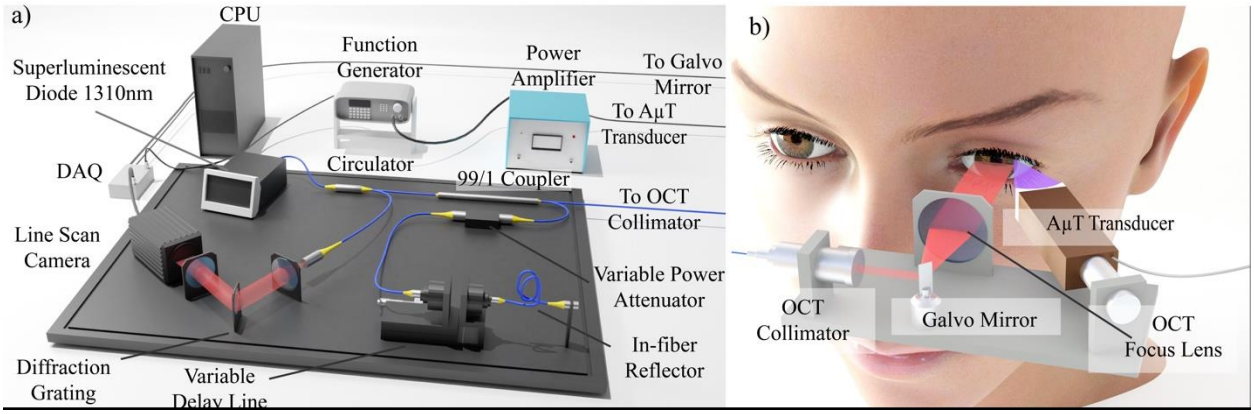

Figure 4-1. AμT-OCE system a) components and connections based on a phase-stable polarization maintaining SD-OCT configuration. b) Close-up of AμT-OCE imaging arm showing optical and acoustic focus alignment on a stylize human for display

In the following sections, design parameters, performance metrics, and system limitations are presented to provide additional information on the phase-stable OCE system.

4.2 Laser source

In OCT, the axial resolution (detailed below) is inversely proportional to the bandwidth of the light source. Additionally, image contrast and imaging depth are largely determined by wavelength dependent light-tissue interactions. Thus, both the optical spectrum of the light source and the optical properties of the desired tissue must be considered when choosing an appropriate light source.

In this system, a 1310 nm center wavelength light source was used based on trade-offs between near-infrared transmittance within the cornea, component availability, and the requirement to image the full thickness of the cornea. It is worth noting in **Figure 4-2a** that the cornea is very transparent over the visible and NIR range (380 nm-1100 nm).[165,166] Both scattering and water

absorption begin to dominate at wavelengths above 1400 nm.[166] Thus, light scattering around 1300 nm provides an avenue to contrast corneal structures using OCT.[167]

a) b)

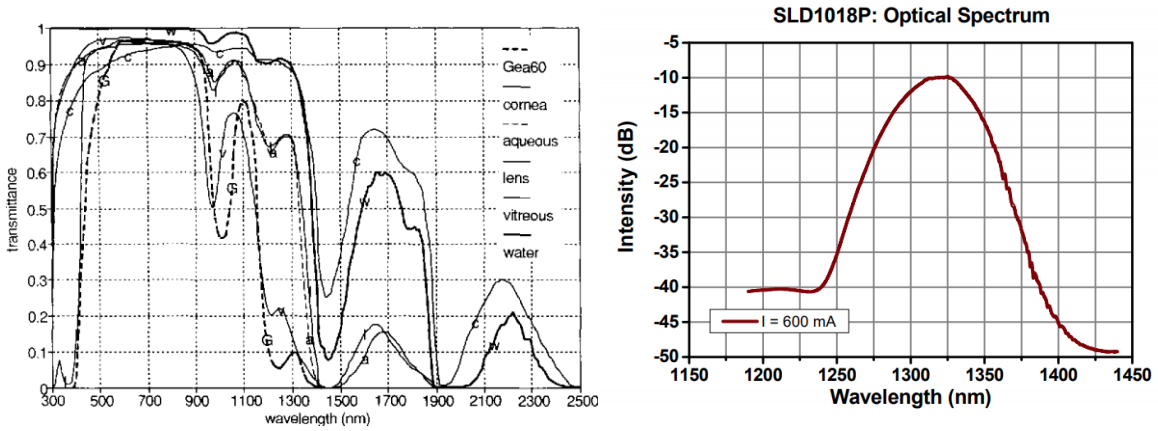

Figure 4-2. Spectral characteristics of cornea and light source. a) Transmittance spectra in the cornea (adopted from Berg and Spkreijse[166]). Thin dashed line refers to transmittance in aqueous solution, middle dashed line refers to lens, and lower dashed line to vitreous. The heavy dashed line refers to a combination of cornea, retina, aqueous solution, and water. The heavy continuous line corresponds with 1 mm of pure liquid. Note that transmittance here is combined absorption and scattering. b) Optical spectrum of SLD (SLD1018P, Thorlabs, NJ).

The light source used was a Superluminescent Diode (SLD) (SLD1018P, Thorlabs, NJ) with a center wavelength of 1310 nm and optical bandwidth (3 dB) of 45 nm (**Figure 4-2b**) with 30 mW maximum output power. The SLD was housed in a standard 14-bin butterfly package and controlled using a compact temperature controller (CLD1015, Thorlabs, NJ) providing temperature control to stabilize the power and optical spectrum.

The broadband infrared light emitted from the laser was connected to a FC/APC polarization maintaining fiber and directed to an optical circulator to re-direct reflected light to the spectrometer and prevent energy from re-entering the light source.

4.3 Reference arm

Following light emission and passage through the optical circulator, the light from the SLD was split into two paths with a specially designed 99:1 polarization maintaining fiber-based coupler. 99 percent of the emission power was delivered to the sample arm for tissue scattering, while 1 percent of the power went toward a static reference mirror, referred to as the reference arm.

The reference arm is a stable reflector used to determine the zero-delay, or matching path length between reference and sample arm, of the OCT system. To minimize environmental noise, a polarization-maintaining in-fiber reflector having near 100% reflection at the 1310 nm wavelength was utilized. To ensure polarization-stability, the fiber connected to the reflector was 1 m in length and mechanically fixed using a 3D-printed mount.

To maximize stability, simplify alignment, and match reference arm power with corneal back-scatter intensity, a variable attenuator (VOA50PM, Thorlabs, NJ) and variable optical delay line (ODL-200, OZ-Optics, Ottawa, CA) were utilized. The variable attenuator allowed up to 99% attenuation without optical spectrum clipping. The optical delay line allowed for 200 μm of travel to simplify alignment between reference and sample arm distances.

4.4 Sample arm

The sample arm of an OCT system is essentially the imaging probe that delivers light to the sample of interest. The energy delivered at the sample is part of the Michelson interferometer that is first split by the 99:1 polarization maintaining coupler. The 99% bean energy was passed through ~2 m of polarization maintaining fibers and connected to a collimator (F280APC-C, Thorlabs, USA)

which passed a collimated beam into free space. The size of the mirror was chosen to accommodate the theoretical $1/e^2$ beam diameter of 3.4 mm to avoid loss of energy.

The collimated beam was directed toward a single galvanometer scanning system with a mounted mirror (MicroMax Model 677XX, Cambridge Technology, Bedford, MA). The galvanometer allowed for precision motor control with a maximum travel of ± 15 degrees. The galvanometer was paired with a servo driver board to control voltages and determine the mirror position angle according to the input voltage signal. For example, at 0-voltage, the orientation of the mirror is 45 degrees relative to the incident beam. To limit OCT image aberration and system vibration, the acceleration and control of the galvanometer used a stable power source with a measured voltage jitter of ± 10 mV. The rotation angle was controlled by an analogue command signal from a computer to scan the sample arm beam in one direction.

The beam redirected from the galvo-controlled mirror impinged on a lens that focused the light toward the sample of interest. The incident power on the sample at focus was approximately 2.5 $\frac{\mathrm{mW}}{\mathrm{cm}^2}$, well within the safety limits for ophthalmic imaging of the cornea.[168] Note that safety limits for the cornea are more lenient than the retina, with guidelines suggesting safe application of near-infrared light as high as 30 $\frac{\mathrm{mW}}{\mathrm{cm}^2}$.[169]

The focal length, total size of the focusing lens, and total angle of deflection from the galvo-controller determined the x-scanning range. The system was optimized for corneal imaging where a 60 mm focal length lens with a 2-inch aperture allowed for a stable 10 mm scan range.

Because light scattering in the cornea is generally low, the focusing lens was intentionally placed 60 mm beyond the focal plane from the galvo-controlled mirror to increase reflection normal to

the incident beam to increase SNR. The oblique incident angle introduced distortion in the corneal shape of the final OCT cross-section that was corrected for as a part of an automated surface detection algorithm in the final signal processing.

4.5 OCT axial resolution

The axial resolution limit in SD-OCT is determined by the central wavelength and bandwidth of the laser source,[170] related to the coherence length of the emitted energy.

The coherence length can be written as:

$$l_c = \frac{4 \ln 2}{n\pi} * \frac{\lambda_0^2}{\Delta\lambda}, \tag{4.1}$$

where λ_0 is the central wavelength, and $\Delta\lambda$ is the FWHM, and n is the refractive index. The resolution in an OCT system is typically defined as $\frac{1}{2}$ the coherence length, or $\frac{l_c}{2}$, which is related to the spectral bandwidth of the light source by[4]

$$\frac{l_c}{2} = \frac{2\sqrt{\ln(2)}}{\Delta k} = \frac{2\ln(2)}{\pi} \frac{{\lambda_0}^2}{\Delta\lambda}, \tag{4.2}$$

where k here is the optical wavenumber. For wavelengths typically used in biological applications, the axial resolution is roughly in the micrometer scale. The theoretical axial resolution determined by the light source (in air, refractive index n = 1) was 16.8 μm. Note that axial resolution is decoupled from lateral resolution.

4.6 OCT lateral resolution

The lateral resolution in OCT is determined by the objective lens in the sample arm.[4] The resolution is defined by the spot size of the sample beam and written as

$$R_r = 2w_0 = \frac{4f\lambda_0}{\pi D} \approx 1.22\frac{\lambda_0}{2NA_{obj}}, \tag{4.3}$$

where $2w_0$ is the spot size diameter of the beam, and *f* the focal length of the sample arm objective lens. *D* is the beam diameter incident onto the lens and NA_{obj} is the numerical aperture of the objective lens.

There is a trade-off between the lateral resolution and depth of focus.[4] Typically, the depth of focus in OCT is often related to the optical Rayleigh length,

$$Z_R = \frac{\pi w_0^2}{\lambda_0}, \tag{4.4}$$

with the optimal imaging range typically defined as $2Z_R$. In this case, $2Z_R$ was around 1 mm, providing a theoretical lateral resolution between 14.7 µm - 29.43 µm over typical corneal thicknesses.

Note that the collimated beam impinged on the galvo-controlled mirror at an angle and often off-center of the focusing lens. As such, the incident beam experienced some aberration (elliptical shape and diffraction) reducing the actual lateral resolution by a small percentage.

4.7 Spectrometer design

Light back-scattered from the sample arm and reference mirror were combined in the fiber coupler and then delivered to the spectrometer. Spectral domain OCT requires that the recombined signal

is appropriately sampled in the Fourier Domain using a spectrometer based on the line-scan configuration, where broad-spectrum light is incident on a grating which separates the spectrum to detect each wavelength using a CCD camera as a function of the wavenumber, k.

The spectrometer was designed so that the spectral range of the line-scan camera accurately sampled the full spectrum of the light source such that the total spectral range, $\Delta\Lambda$, was not reduced relative to the full width half-maximum (FWHM) of the light source. Thus, the axial resolution was not limited by the detection electronics.

The spectral sampling is associated with the axial spacing domain following a Fourier Transform (FT). The relationship between the spectral range ($\Delta\Lambda$) and the pixel spacing (bins in the axial spatial domain, z) is:

$$\Delta\Lambda = \frac{1}{2}\frac{\lambda_0^2}{\frac{\Delta z}{2}}, \tag{4.5}$$

where Δz was the pixel spacing in the z-domain and λ_0 was the center wavelength of the spectrum.[171]

To ensure appropriate pixel spacing, the coherence function (determined by the source) must be distinguishable from neighboring pixels. Thus, pixel spacing was greater than ½ the axial resolution, or $\frac{l_c}{4}$. Substituting $\frac{l_c}{4}$ in Equation 4.5 for $\frac{\Delta z}{2}$ will maximize the imaging range while maintaining source limited resolution:

$$\Delta\Lambda = \frac{1}{2}\frac{\lambda_0^2}{\left(\frac{l_c}{4}\right)} = \frac{\pi}{2\ln 2}\,\Delta\lambda \tag{4.6}$$

The full spectral range of the CCD array detector was greater than 102 nm considering the spectral components of the SLD.

Since the camera had a finite number of elements, *N*, the spatial sampling density was set according to the spectral sampling resolution, $\frac{\Delta\Lambda}{N}$. If the full spectrum is illuminated by $\frac{\Delta\Lambda}{N}$, the resolution and imaging depth are maximized. For the CCD array used in this system (N=1024), this occurs at $\frac{\Delta\Lambda}{N} = .01\ \mathrm{nm/pixel}$. It is important to note that $\Delta\Lambda$ can be increased without losing resolution, at the expense of imaging depth. The spectral spacing between pixel elements was greater than $\frac{\Delta\Lambda}{N} = .01\ \mathrm{nm/pixel}$, thus the entire spectrum was resolved.

If the spectrometer has a specified bandwidth, and N pixels, the total axial imaging range, l_{max}, over which signals can be measured is given by:

$$l_{max} = \frac{\Delta z}{2}\frac{N}{2} = \frac{\ln(2)}{2\pi}\frac{\lambda_0^2}{\Delta\lambda}\,N \tag{4.7}$$

The division of $\frac{N}{2}$ is important due to the conjugate symmetry of the FT of a real spectrum where only half of the pixels will contain unique information. Considering that the $\Delta z = \frac{l_c}{4}$ (1/2 the axial resolution), the maximum imaging range achieved was 4.308 mm.

In SD-OCT, there is a measurable reduction in sensitivity as the distance from the zero-delay is increased. This reduction in sensitivity is determined by both the shape of each wavelength beam illuminating the CCD array, and the rectangular (RECT) function imposed from sampling with a finite-sized pixel in the CCD array. As an object moves away a set distance (Δl) from the zero-

delay line (defined as the matched path-length between the reference and sample arm), the measurable OCT oscillation is given as:

$$I(k) = s(k) * \cos(k\Delta l) \tag{4.8}$$

Where $s(k)$ is the spectral intensity distribution of the light source and Δl is the path length difference between the reference mirror and reflector. The fringe visibility, or the amplitude of the cosine oscillation, directly determines the signal strength in the *z*-domain after a FT.

The focusing lens of the spectrometer allowed the CCD to sample the cosine term in Equation 4.8 in the *k* domain using a finite number of pixels. A convolution of the pixel size with the Gaussian spectral resolution yields the following expression for sensitivity reduction, R_s, as a function of the imaging depth, z[172]:

$$R_s\,(z) = \frac{\sin^2\left(\frac{\pi z}{2l_{max}}\right)}{\left(\frac{\pi z}{2l_{max}}\right)^2} \exp\left(-\left(\frac{\pi^2 w^2}{8\ln 2}\right)\left(\frac{z}{l_{max}}\right)\right), \tag{4.9}$$

where l_{max} was the maximum scan depth, and *w* an experimental parameter based on the ratio between the actual spectral resolution and the theoretical spectral resolution. Here it can be appreciated that finite pixel spacing contributes to the signal fall-off.

The transfer of the lens system in the spectrometer from the object space (diffraction grating) to the image space (CCD array) caused additional aberration at the focal spot of the spectrometer. The goal of the optical design was to optimize the beam-shape on each CCD pixel based on the spectral range, $\Delta\Lambda$, CCD size, and diffraction angle. The diffraction angle was determined by the grating, which is defined by its resolving power, R_{diff} (dimensionless), and given by[173]

$$R_{diff} = \frac{\lambda_{max}}{\delta\lambda} = mN_g, \tag{4.10}$$

Where $\delta\lambda$ was the maximum achievable spectral resolution of the grating, *m* the diffraction order, N_g the total number of grooves illuminated on the grating surface, and λ_{max} the maximum wavelength of the system. In order to achieve the system limit of $\Delta\Lambda = \delta\lambda$, the total number of illuminated grooves was determined by $\frac{\lambda_{max}}{\Delta\Lambda}$. For the upper limit of the spectrum used in this system ($\lambda_{max} = 1332.5$ nm and $\Delta\Lambda = .01$ nm) at least 13,3801 grooves must be illuminated.

The groove density, G_d, of the diffraction grating was used to determine the minimum aperture size of the collimating lens to achieve the necessary spectral resolution according to:

$$C_d = \frac{\lambda_{max}}{\Delta\Lambda\, m}\frac{1}{G_d}. \tag{4.11}$$

Considering the components readily available (G_d=1200 grooves/mm), the smallest possible aperture to ensure more than 13,3801 grooves were illuminated required a collimating lens aperture of 13.07 mm. A fiber to free-space adapter with an aperture diameter of 1.3 mm (SM1FCA, Thorlabs, NJ) was paired with a 25.4 mm diameter achromatic lens with a focal length of 60 mm to generate a beam size approximately 25 mm, ensuring appropriate spectral sampling from the diffraction grating.

The diffraction grating required the incident and reflected light to pass through at a specific angle. The optimal angular dispersion of the grating is given by:

$$\sin\theta_i + \sin\theta_d = mG_d\lambda_0, \tag{4.12}$$

where θ_i was the incident angle, θ_d dispersion angle, m the diffraction order, and G_d the groove density. Assuming the Litterow condition (diffraction angle equal to the incident angle (θ_i=θ_d)), θ_d was determined to be 51°. Inspection of the first order maximum amplitude confirmed this value.

Once the collimated light passed through the diffraction grating, each grating element acted as a point source, emitting each wavelength of light at a different angle. Thus, each beam had a total 'cone' between lens and detector. The focal length of the imaging lens focused each beam to a width based on the spectral range ($\Delta\Lambda$), total size of the CCD array (d_{CCD}), diffraction angle (θ_d), and groove density, G_d:

$$f_l = \frac{\cos(\theta_d)}{G_d} * \frac{d_{CCD}}{\Delta\Lambda} \tag{4.13}$$

For the system described herein, the focusing lens can be no longer than $f_l = 148$ mm. Due to limited optics supply, and to avoid decreasing resolution (at the expense of the total imaging range), a 2" diameter, $f_l = 100$ mm lens was used.

It has been shown that the optimum spot size at the spectrometer is $\frac{1}{4}$ the size of a single CCD pixel.[170] The expected spot size (at the center wavelength, λ_0) at the spectrometer was calculated using:

$$w_0 = \frac{2f_l\lambda_0}{\pi C_d}, \tag{4.14}$$

where C_d = 25 mm. The expected spot size was well below the $\frac{1}{4}$ threshold ($\frac{w_0}{w_{pixel}} = .17$).

Finally, the optical spectrometer consisted of a collimator ($f_{lc} = 50$ mm), transmission grating (1200 lines/mm), achromatic focusing lens ($f_l = 100$ mm), and a high speed 1024-pixel line scan InGaAs CCD camera (1024-LDH2, Sensors Unlimited, New Jersey, USA). The camera was designed to work at 1300 nm with a total wavelength response between 800nm-1700nm. The Quantum Efficiency (QE) was approximately 85% at 1300 nm. The total width of the line-scan detector was 25.6 mm and each pixel optical aperture height was 500 μm.

4.8 Data acquisition

The SD-OCT system was controlled using a computer/processor interface. In short, the system was designed to acquire signals by synchronizing acoustic excitation, scan position, and camera acquisition. The data acquisition control interface was implemented in LabVIEW (National Instruments Corp., TX, USA) using a program largely designed and written by Dr. Shaozhen Song and modified for the components listed above. In this section, camera acquisition and data storage are discussed.

Most components of the system utilized the NI (National Instruments Corp., TX, USA) platform hosted on a high-performance PC with 2.8 GHz quad-core Intel Core i7 CPU. An analogue output card (NI PCI-6713) was used to send both the galvanometer scanner driving signal and camera trigger signal. The maximum update rate of the board was 1 MS (mega-sample)/sec. An image acquisition card (NI PCIe-1429) was used to initialize, configure, and transfer data from the line-scan camera using the CameraLink interface.

A flow chart of the data acquisition program is presented in **Figure 4-3**. The program first captured a background reference image by sampling the spectrum from the reference beam (or by loading

previously captured data). The reference beam spectrum was captured by sequentially prompting the user to shade the sampling arm before sending a trigger signal to the camera to capture an A-line acquisition representative of the background signal. After acquisition of the reference data, the analogue output system and NI-IMAQ system were initialized. In this sequence, the NI PCI-6713 card output a trigger signal and galvanometer driving signal to sync the scan position and image acquisition using NI PCIe-1429.

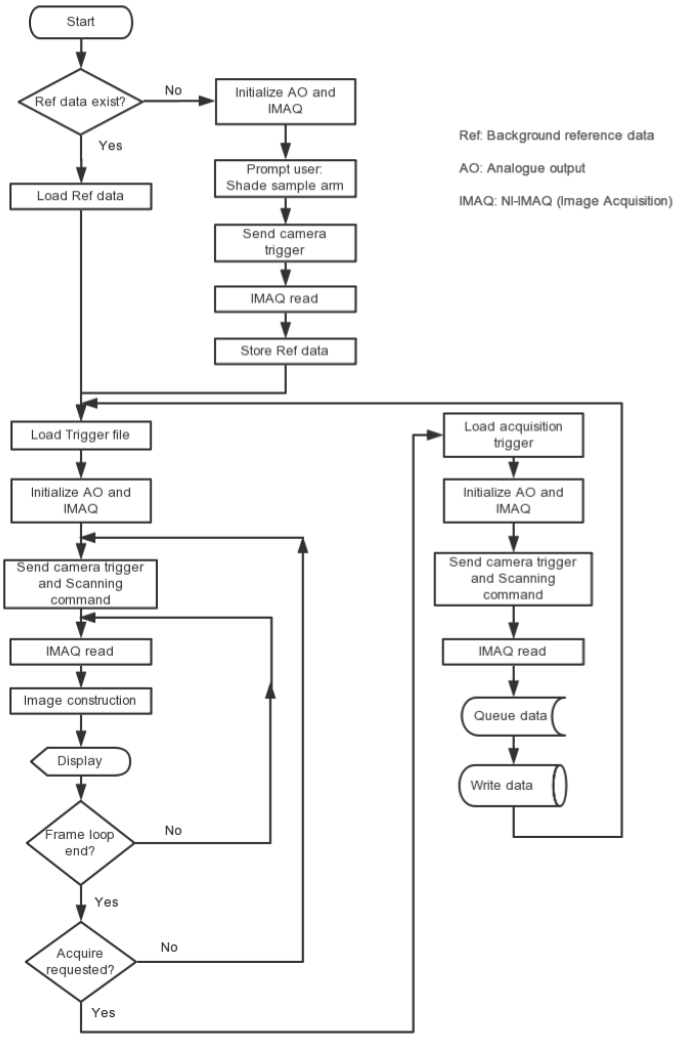

Figure 4-3. Flow chart of the data acquisition control interface as implemented in a LabVIEW (National Instruments Corp., TX, USA) graphical user interface (GUI). Figure adapted from Song, S.[174]

The OCT system was operated either in real-time mode for corneal imaging and alignment or acquisition mode for tracking elastic wave propagation and saving data for off-line analysis. The scanning protocols of these two modes were controlled separately. A pre-defined trigger file (detailed in Section 4.13) was loaded followed by AO (analogue output) and IMAQ (National Instruments IMage AcQuisition) initialization. The raw camera data was collected for storage or processed in LABVIEW for real-time display. Because shear wave tracking required fast data acquisition, the data transfer rate required the camera to transfer to the PC faster than the hard drive writing speed. To avoid data overflow, part of the RAM was preserved as a cache zone for raw-data storage until written to the hard drive. In real-time mode, the CPU reconstructed OCT images from raw data acquired from the line-scan camera at approximately 40 frames per second and displayed in real-time.

4.9 Dispersion compensation

The governing equation in Fourier domain OCT is based on

$$F_s(z) \propto FT\{A_s(k)\}, \tag{4.15}$$

where z was the depth, k the wavenumber, and $A_s(k)$ the total backscattered signal detected by the spectrometer. Note that while it is possible to detect $A_s(k)$ as a linear function of k,[175,176] spectrometers commonly employed in SD-OCT require a digital rescaling of wavelength (λ) into wavenumber (k), resulting in the loss of signal sensitivity at increasing depths.[177,178] Additionally, the polarization maintaining fibers and optical components along the sample beam and reference

beam are not identical and can introduce different dispersion patterns which reduce the axial resolution of the system.

A numerical dispersion compensation technique was used to correct the dispersion on the detected spectrum.[174] Briefly, the interference spectral signal sampled by the line-scan camera is subtracted by the reference signal (acquired using only the reference arm). A third-order function to transform dispersed *k*-space to evenly sampled *k*-space was constructed using an optimization routine that maximized the magnitude of the post-FFT OCT signal at a specific location. To determine the re-sampling parameters, a reflector (glass cover slip) was placed ~0.5 mm from the zero-delay line and the reflection amplitude used to determine an optimized *k*-space function. The spectrum of each acquisition was then re-sampled (interpolated) according to the discrete point set on the *k*-space function curve to recover an evenly-spaced k-space interferogram. The numerical re-sampling in *k*-space corrected for system dispersion and provided near-theoretical axial resolution with a significant improvement in the signal to noise ratio.

4.10 OCT signal reconstruction

The dispersion compensated spectral interference fringes may be expressed as[46]

$$i(k) = \frac{1}{2}\Phi S(k)\delta k\left\{R_R + \sum_n R_n + 2\sqrt{R_R}\sum_n \sqrt{R_n}\cos[2k(z_n + \delta z_n)]\right\}, \qquad (4.16)$$

where *S(k)* is the source power spectral density, *k* the wave number, δk the spectral resolution of the spectrometer, Φ the detector sensitivity, R_R the reference arm reflectivity, and R_n the reflectivity of the sample at depth z_n, where z_n was physically described as the integer multiple of the discrete sampling interval in the *z*-direction (determined by $m\pi/\delta k$, where *m* was the positive

or negative integer of the A-scan array). The δz_n term was from sub-resolution deviations in position of the local scatterer from the signal at the discrete location, z_n, and *i(k)* was the integration over the A-scan exposure time.

To generate depth-encoded reflection profiles, a discrete Fourier transformation of *i(k)* was performed to give the complex signal defined by

$$I(z_n) = \Gamma(z_n) \exp(jk_0 \delta z_n) \tag{4.17}$$

where $\Gamma(z_n)$ describes the unity-amplitude z-domain autocorrelation function, and k_0 the center wavenumber of the source. Note that this representation is simplified and the reader is referred elsewhere for a more detailed description.[4]

A single reconstruction of depth-encoded reflectivity is referred to as an A-scan and can be displayed in real-time using the LabVIEW program GUI or saved for processing. Note that the δz_n term can be used for sub-wavelength motion detection using phase-differences between sequential A-lines.

4.11 SD-OCT system performance

The system resolution and roll-off were experimentally measured using a glass cover-slip placed approximately 0.6 mm from the zero-delay line. 15,000 consecutive A-lines were acquired at a single location at a rate of 90 kHz (**Figure 4-4a**). The recorded spectrometer signal was averaged and then the absolute value of the FT was calculated (linear scale, **Figure 4-4b**). Treating the first cover-slip surface as a point-source reflector, the FWHM of the peak was used to estimate the

resolution of the system. Following numerical dispersion compensation, the effective axial resolution was experimentally measured as approximately 20 μm.

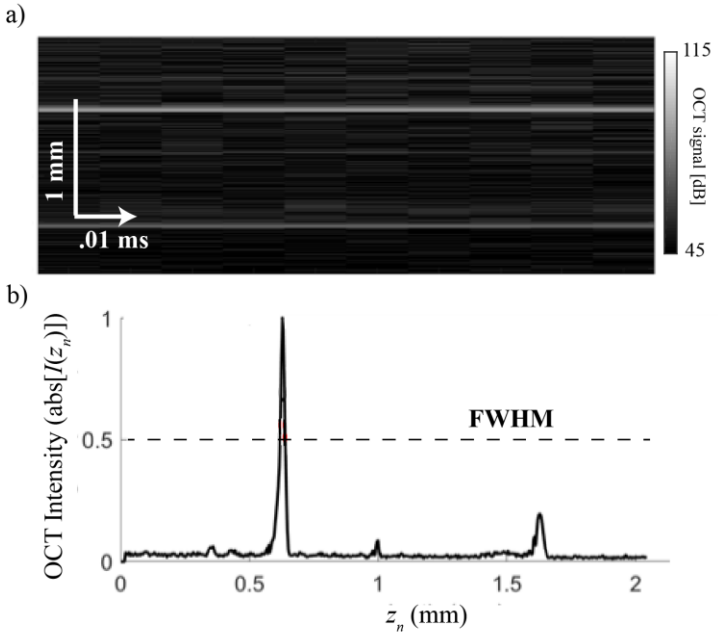

Figure 4-4. Repeated scan of glass-coverslip for measuring axial resolution. a) Log-compressed intensity ($I(z_n)$) in 10 consecutive A-scans (cropped from the 15,000 acquired scans for display) of a glass cover-slip acquired at 90 kHz. b) Linear-scale intensity normalized to the peak value to demonstrate 20 μm system resolution at full-width-half-maximum (FWHM).

Note that the polarization-maintaining fibers were specially made for 1310 nm with a functional bandwidth of 40 nm (as opposed to the 45nm light source). For a 40 nm bandwidth, the theoretical resolution was 19.5 μm, very close to what was experimentally measured.

The signal-fall off was then measured using a reflecting mirror placed at different depths (0 mm-1.5 mm) relative to the zero-delay line. The data was log compressed and the peak of the signal at each depth used to determine system roll-off.

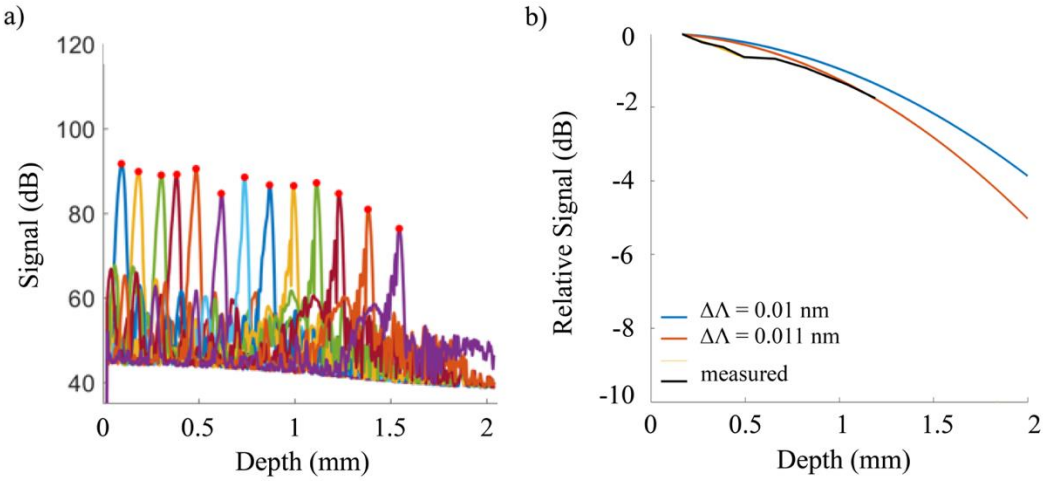

Figure 4-5. OCT roll-off measured with reflective mirror. a) Signal intensity at various locations. The surface signal (max intensity) is identified with a red dot. b) Theoretical and measured roll-off of signal in SD-OCT system.

The measured spectral resolution was approximately .011 nm/pixel (close to the theoretical value of $\Delta\Lambda = 0.01$ nm) as calculated according to the measured sensitivity fall off (Equation 4.9). The focus was placed at approximately 0.5 mm and the confocal function due to focusing was not taken into account. It is important to note that $\Delta\Lambda$ can be increased slightly without losing resolution, at the expense of imaging depth. As light is often attenuated due to signal fall-off and tissue optics, the maximum imaging range is not required. The spectrometer performance appeared well tuned over the imaging depths necessary for the cornea.

4.12 SD-OCT sensitivity to motion

The phase term of each complex signal, while random in nature, was exploited between successive scans to detect sub resolution motion within a sample.[179] For each scan location (x,z), the phase term may be defined as

$$\varphi_{opt}(x,z) = im[I(z_n)] = im[E(z_n)\exp(jk_0 2\delta z_n)]. \quad (4.18)$$

As sub-resolution deviations from the z-location (δz_n) define the relative position of $\varphi_{opt}(x,z)$, the phase will remain constant if scatterers located at (x,z) remain stationary. If the particle vector displacement deviates axially (along z), the phase term will shift according to

$$\Delta\varphi_{opt}(x,z,t) = 2n\bar{k}\,\Delta U_z(x,z,t) \quad (4.19)$$

where and $\bar{k}$ the average wave number. Equation 4.19 may be rearranged to readily solve for $\Delta U_z(x,z,t)$ by,

$$\Delta U_z(x,z,t) = \frac{\Delta\varphi_{opt}(x,z,t)\bar{\lambda}}{4\pi n} \quad (4.20)$$

where ΔU_z the displacement between scans.

In practice, the displacement term is defined as the change in scatterer position between scans and reported by the depth-resolved vibration speed,[92]

$$U_{zt} = \frac{\Delta\varphi_{opt}(x,z,t)\bar{\lambda}}{4\pi n f_s^{-1}} \quad (4.21)$$

where f_s is the scan rate. The vibration speed was spatially and temporally mapped, enabling fast detection of propagating elastic waves.

The minimum detectable change in phase, and thus the minimum detectable displacement amplitude, was approximated by system noise and inversely related to SNR (i.e., 1/ SNR).[180] This expression has been shown to hold in practice as a quick estimate of displacement sensitivity.

Using this method, the noise-floor of the OCT system was calculated by first acquiring multiple A-scans without the light source to acquire a measure of camera noise, measured at approximately 45 dB. Next, the sample arm was blocked, and the reference arm illuminated and tuned so that the signal from the reference arm was just over 45 dB. Finally, an angled neutral density (ND) filter was placed in front of a static reflector placed 0.5 mm below the zero delay (**Figure 4-6a**) and the peak reflection calculated to be approximately 104 dB (**Figure 4-6b**), corresponding to an SNR of ~ 60 dB. At this SNR, the shot-noise limited sensitivity to displacement was approximately 650 pm (in air).

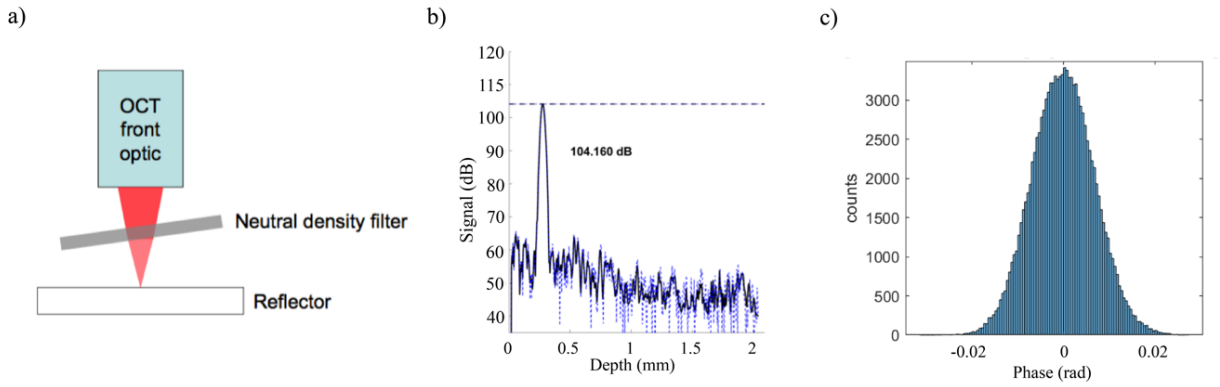

Figure 4-6. Measured OCT SNR and phase stability a) Schematic of reflector and ND filter (adapted from Jiang et al.[181]) b) Optimum system SNR was determined with the reflector at the focus of the imaging arm lens. The peak signal minus the noise floor was used to calculate a best-case SNR of ~ 60 dB. c) Experimentally measured phase variations over 1500 consecutive A-scans demonstrated a standard deviation of ~ 7 mrad, corresponding with a sensitivity to motion of ~ 500 pm in water.

Due to the nature of multiple scanning components and environmental noise, the phase stability was also directly measured following the protocol of Jiang et al.[181] 1500 consecutive A-scans were acquired at 90 kHz with the galvo-controlled mirror driver set at a static voltage. The difference in the phase term was determined over the duration of the static M-scan. The standard deviation of

the phase difference between successive scans was measured as ~ 7 mrad. (**Figure 4-6c**) Using Equation 4.21, the minimum detectible displacement was approximated as 700 pm in air, and 500 pm in water. An additional experiment was conducted with the scanning mirror near the maximum displacement angle (~12 degrees), which resulted in a stability to motion closer to 1 nm.

The upper range of measurable displacement is determined by the change in detected phase between each scan. If the scatterer travels far enough to induce an absolute value greater than a π phase shift, phase wrapping occurs. Discontinuities in the phase shift can be corrected using phase-unwrapping algorithms, where corrections of up to five wrapping discontinuities have been reported.[90] In practice, elastic waves excited via non-contact acoustic generation tend to fall within the nm range and do not produce significant phase wrapping.

Finally, the system demonstrated the ability to accurately measure displacements with amplitudes ranging from 0.5 nm- 250 nm using the phase-difference method (equation 4.2). However, due to jitter in the galvanometer mirror at the edge of the scanning range, the lower range was closer to 1 nm.

To conclude, the SD-OCT system described within can measure elastic waves in the cornea which propagate with amplitudes greater than 1nm.

4.13 Acoustic micro-tapping transducer

As outlined in Chapter 3, measurements of wideband acoustic wave propagation provide an avenue to obtain quantitative measurements of corneal biomechanics. As such, a temporally short, spatially sharp, force must be synchronized with the SD-OCT system to both excite and measure elastic waves.

Independent of the source mechanism, the bandwidth of generated mechanical waves depend on the temporal and spatial characteristics of the excitation push. However, an infinitesimally short pulse for mechanical wave excitation is actually not optimal. To get the maximum pushing force, pump intensity should be confined during the time of stress relaxation across the excitation beam. Thus, the duration of the excitation push should be

$$T_{push} <\approx \frac{d}{C_s}\,, \tag{4.23}$$

Where C_s is the bulk shear wave speed described in Chapter 3. Note that if the push intensity is not confined during the time of stress relaxation (push duration (*T*) exceeds stress-relaxation time), bandwidth is constrained by *T*.

The push amplitude must be large enough to deliver an axial displacement that can generate a laterally traveling mechanical wave without damaging tissue. The resulting wave amplitude is determined primarily by the excitation force but will be affected by local physiology as well. A stiffer tissue will have a smaller displacement magnitude for an equivalent excitation profile compared to a more easily deformable sample. The local tissue stiffness, in combination with OCT signal-to-noise ratio, will determine the necessary push strength (within safety limits) to launch a detectable wave within the sample.

If the excitation is an infinitesimally short push, the mechanical wave bandwidth (BW) is determined by relaxation of the stress across the excitation beam, which occurs according to:

$$BW \approx \frac{C_s}{d} \tag{4.22}$$

where d is the size of the push cross-section. Similarly, the characteristic wavelength of the generated mechanical wave is simply on the order of d.

The bandwidth/wavelength relationship of the mechanical wave determines the spatial resolution of reconstructed elastic modulus maps (detailed in Section 4.16). Thus, a well-designed dynamic OCE system should incorporate a highly-focused, non-contact method to launch detectible, multiple-kHz bandwidth, mechanical waves in the cornea.

A simple visualization of these relationships is presented in **Figure 4-7**.

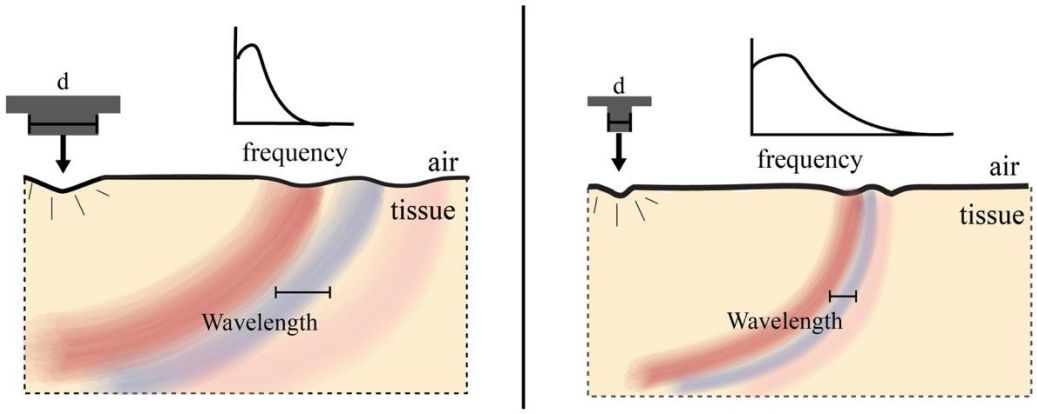

Figure 4-7. Wave characteristics from different push profiles on the same medium, assuming the excitation time always satisfies Equation 4.23.

For diagnostic mapping of elastic modulus, a highly localized non-contact acoustic radiation force (ARF) is desirable to launch detectable elastic waves within the cornea. In 2016, Ambrozinski et. al. described the first generation of ceramic-based piezoelectric transducers capable of launching mechanical waves in the cornea, referred to as Acoustic Micro-Tapping (AμT).[16,112] The reflection-based approach converted acoustic energy to mechanical energy (reflection-based ARF)

at an air/tissue interface to launch a wave-packet with nano- to micrometer displacement amplitudes and sub-mm to micron-scale wavelength.[16]

Such transducers are not readily available on the market and require in-house manufacturing. The transducer used in the OCE system here consisted of a matching layer (a 0.45 μm pore size nylon membrane filter, Cat. No. 7404–004, "GE Healthcare UK Limited", UK) bonded to the transducer surface with a silicone adhesive. The piezoceramic element was cut from a piezo-cylinder (cat.# 42–1041, APC International Ltd, USA) to create a 9 mm long section of 75 degrees. The outer and inner diameters of the transducer were 30 mm and 26 mm, respectively.

To define the spatial shape of the acoustic pressure in air, a raster scan of the acoustic field (**Figure 4-8a**) was taken near the focus of the air-coupled AμT transducer with a needle hydrophone (HNC-1000, Onda, Sunnyvale, CA, USA). Note that the location of the focusing lens in the OCT system required that the transducer was tilted by (45 ± 2)°. When exciting elastic waves in the cornea, the tilt allows the acoustic excitation to be nearly normal to the tissue with the focus approximately equal to 400 μm. To measure the actual focus width when the transducer is tilted relative to a flat surface (such as tissue-mimicking phantoms described in Section 4.15), the field was sampled along a 45° line passing through the focus of the transducer (dashed white line, **Figure 4-8a** and black line, **Figure 4-8b**). The acoustic intensity $I(x)$ along the tilted line was approximately Gaussian with a full-width-at-half max (FWHM) of ~ 600 μm (**Figure 4-8b**).

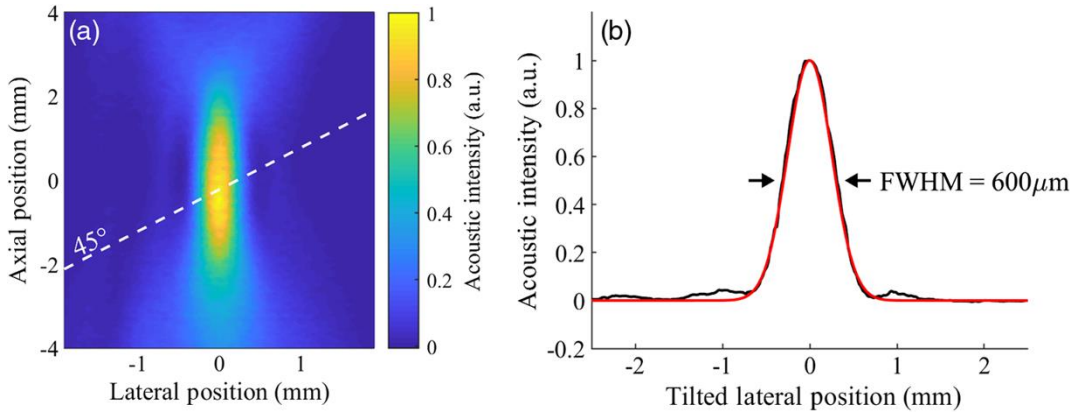

Figure 4-8. Spatial shape of the acoustic pressure in air (a)Acoustic field intensity measured near the focus of the AμT transducer and 45-degree tilted cutline (dashed, white). (b) Measured acoustic intensity along the 45-degree tilted cut line (black) and Gaussian approximation with 600 μm full-width-at-half-max (red). Note that the center-focus provided a 400 μm FWHM.

In reflection mode, the radiation pressure of the acoustic force (P, force per unit area) is

$$P = \frac{(1+R^2)I}{C_l} \tag{4.22}$$

where R is the reflection coefficient at the air/medium interface, I is the acoustic intensity ($\frac{\mathrm{W}}{\mathrm{cm}^2}$) and C_l the sound speed. For air-coupled ultrasound, the reflection coefficient at the air– tissue boundary is nearly one (R ≅ 1) so that the radiation force can be approximated as $P = \frac{2I}{C_l}$. Since the sound speed in air is low (about 340 m⁄s) and nearly all acoustic intensity is converted into radiation pressure, significant force can be produced at modest acoustic pressures. At an acoustic intensity of about 1 $\frac{\mathrm{W}}{\mathrm{cm}^2}$, the pressure amplitude in the transducer focus (i.e. the amount of force passed into the tissue) was approximately 7 kPa. Because the shear wave excitation is reflection-based, most of the acoustic energy (99.9%) is reflected from the sample surface, leading to acoustic exposures well below limits for ophthalmic applications.[182]

Early AμT-generated waves required a relatively long temporal duration of 250 μs to produce a measurable wave.[16] The AμT transducer was driven with a chirped signal ranging from .95 MHz to 1.05 MHz, and an input voltage of 250 V. The resulting wave-packets had upper-frequency cut-offs of approximately 2 kHz and propagated with ~10 - 40 nm displacements. However, (as shown in Chapter 3) the dispersion behavior used to accurately quantify unique combinations of μ and G in the cornea require broadband signals closer to 5 kHz.

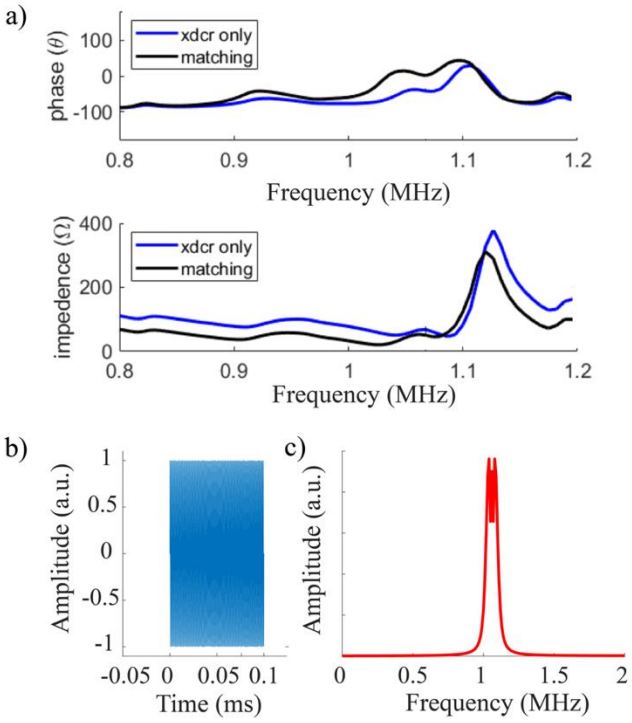

Figure 4-9 Impedance of AμT transducer and driving waveform. a) The phase (above) and impedance (below) of the transducer was measured with the matching circuit (black) and without (blue). The 0-phase crossing corresponds with a nearly all real impedance centered at 1.05 MHz with the addition of the matching circuit. b) The corresponding chirped waveform in time (left) and frequency (right) domains used to drive the AμT transducer.

To improve the efficiency of the transducer, a matching circuit was constructed so that a nearly all-real voltage was applied to the transducer. Based on impedance matching (**Figure 4-9a**), a

chirped (1 MHz- 1.1 MHz) waveform centered at 1.05 MHz (**Figure 4-9b, c**) was used to drive the acoustic transducer via a waveform generator (Agilent Technologies 33220A, Santa Clara, CA). The linear chirp minimized potential standing wave effects. The waveform generator received a trigger signal from the NI PCI 6713 analogue output card (detailed in Section 4.14) delivered via a DAC (digital analogue converter) module that then passed the 650 V (peak to peak in amplitude) signal through a 55-dB power amplifier (ENI A300) before passing through a home-made matching circuit and finally driving the AμT transducer.

Increased input voltages and shorter temporal push durations provide higher frequency content and better spatial resolution in wave-based elastography. Note that field localization is limited by diffraction, so a high US frequency is desired to deliver a spatially sharp push. Increasing the pump US frequency, however, is limited by strong US attenuation in air (proportional to frequency squared)[183,184] and would require additional tuning in transducer materials and matching circuit design. Due to the short distance between transducer and sample, ~1 MHz acoustic waves were shown to efficiently excite mechanical waves. Sufficient wave displacements were realized using push duration of 100 μs (as opposed to previous designs with 250 μs push duration). This allowed the bandwidth of measurable waves in the cornea to increase from 2-3 kHz to as high as 5 kHz. By efficiently generating detectable waves using a shorter duration push, the modified AμT transducer used in this work demonstrated state-of-the art performance in non-contact excitation of spatially sharp, broadband elastic waves.

4.14 M-B mode scan protocol

In mechanical wave imaging, scan requirements are more complex than typical OCT. Detecting mechanical wave motion requires fast scanning and accurate timing between elastic wave

generation, scanning mirror position, and camera synchronization.

For vibrational analysis, the scan speed is determined by the Nyquist sampling theorem, the size of the imaging region, and the frequency of vibrations used to probe the sample. For example, a wave traveling at 5 m/s will take 1 ms to cross an imaging range of 5 mm (note: corneal wave speeds tend to be between 1-15 m/s).[162] To have truly microscale OCE resolution of, say, 100 μm, the wave must be captured at no fewer than 50 locations. To capture a 5 m/s wave at 50 locations over a 5 mm region, a frame rate of at least 50 kHz is necessary. As wave speeds in corneal tissue higher than 5m/s are common, a clinically practical OCE system may even require frame rates in excess of 50 kHz. Historically, the limitation of scan speed has hindered OCE development. However, recent developments in system design have allowed OCE imaging to approach practical requirements.

Similar to ultrasound elastography based on ARF scanning,[185] M-B scan protocols may be used in OCE to achieve effective frame rates in the tens of kHz range. Conventional M-mode imaging repeats axial scans at a fixed location to achieve dynamic imaging with the highest temporal resolution allowed by the imaging device (A-scan rate). By repeating targeted dynamic events (loading scheme), the M-B scan protocol can provide effective high frame rates to track dynamic processes in the space-time domain. The M-B scan method demonstrated by Song et. al[20,99] (**Figure 4-10**) utilized multiple excitations to collect repetitive A-Scans (M-mode scans) at multiple spatial locations. Each M-scan sequence at different locations can be matched in time to generate B-frames for effective data collection fast enough to capture mechanical wave propagation at multiple locations within a sample. The technique has been demonstrated with an equivalent frame rate of up to 92 kHz.[186]

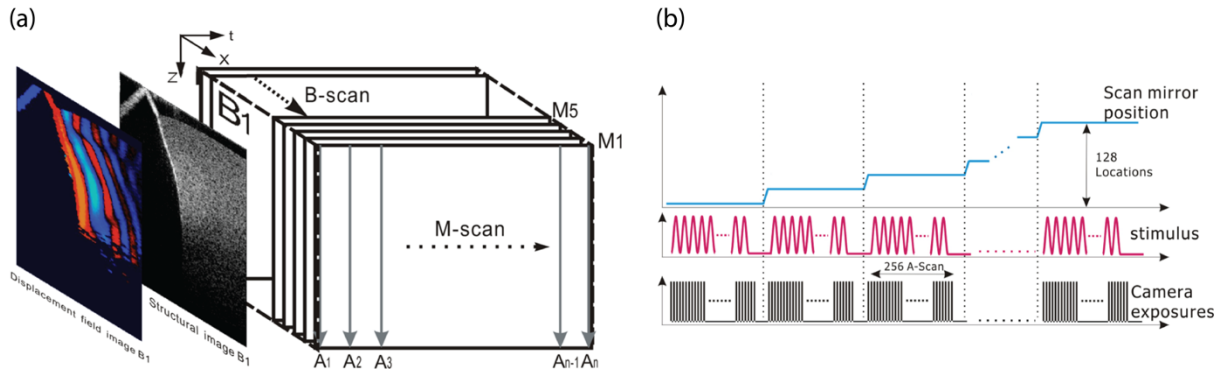

Figure 4-10. MB scan protocol a) demonstrating how a 3-dimensional (*x*, *z*, *t*) data set is generated. (Figure reproduced from Song et. al.)[20] b) Timing schematic of scanning protocol. (Figure reproduced from Song et. al.)[99] The schematic here shows a repeated stimulus, such as with generating waves at a single frequency. In the system described within, only a single stimulus was applied for each scan mirror position.

To control the generation and tracking of propagating shear waves, the OCT system operated in M-B mode. To control timing between camera, scanner, and acoustic excitation, "trigger files" were created prior to OCT imaging acquisition, pre-defining the scanning protocol and acquisition timing. Using the NI PCI 6713 analogue output card, 4 channel signals were output using a DAC (digital analogue converter) module and sent to the corresponding control ports using grounded and isolated BNC cables. The output was triggered using a TTL signal generated by the same AO card. The trigger file contained the scanning mirror driving pattern as well as the camera and acoustic trigger signal. A MATLAB (MathWorks, Natick, MA) code was used to generate trigger files and integrated in LabVIEW using a user-friendly GUI (graphic user interface).

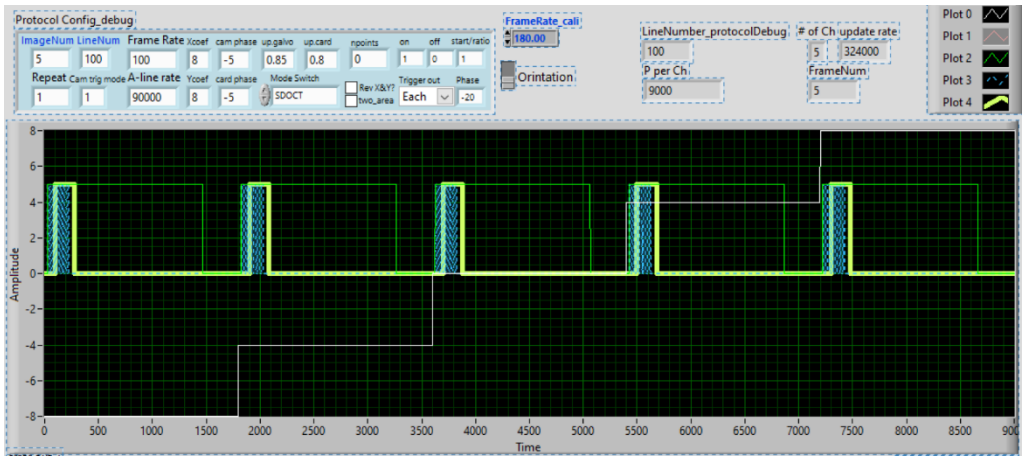

Figure 4-11. Example trigger file to control SD-OCT and AμT timing, generated in the LABVIEW GUI. In this example, the white plot corresponds to the AO for galvanometer position control, the rising edge of the yellow is used to trigger the AμT transducer, the blue corresponds with camera acquisitions and the green box with camera initialization. Note that a long camera duty cycle (~20%) is shown here to visualize each timing signal.

An example trigger file is shown in **Figure 4-11** to demonstrate 5 acoustic excitations corresponding with 5 different M-scan clusters of 100 consecutive A-scans (acquired at 90 kHz), taken at 5 different locations. The camera duty cycle in this example was ~20% to enable visualization of the individual channel signals. Note that the camera duty cycle was operated closer to 95% in experiments. Two channels of the trigger file are allocated for scanning mirror positioning control, where Channel 1 (not displayed in **Figure 4-11**) is a triangle wave, with typical rising time ratio of 85% and used to control the linear scan of the galvonometer to generate the cross-sectional scanning (corresponding with the OCT B- scan) used for real-time imaging display. Note that during the wave-acquisition sequence, Channel 1 is synced with the control signal (Channel 2, white, in **Figure 4-11**) that is sent to the wave-form generator to launch each acoustic pulse at each location. The acoustic trigger signal is a square function that sends a trigger to the waveform generator on the rising edge with a step time equal to one repeat M-scan period. On

channel 3, an IMAQ trigger is sent to the NI PCIe-1429 image acquisition card to trigger camera data acquisition (green box in **Figure 4-11**). Channel 4 is the gating trigger for camera exposure that samples each corresponding A-scan. The camera is operated in "internally timed, externally gated" mode, which allows the camera to repeat exposures according to its internal clock when the external trigger is TTL high. The maximum speed of the camera used in the OCE system described within was 91,991 lines per second for 1024 pixels (12-bit data collection). The exposure time was typically ~17 μs.

4.15 AμT-OCE in tissue-mimicking phantom

There are a number of differences in system design, scanning protocols, and imaging contrast which make OCE and OCT capabilities different. The following section demonstrates how the system described can be used to quantitatively measure elasticity based on the constitutive equations described in Chapter 3. OCE system performance was demonstrated using simplified tissue-mimicking phantoms to provide a framework that was then applied to biological tissue.

As there are no current 'gold-standard' techniques to perform non-contact quantification of elastic moduli, phantom measurements were compared with destructive mechanical testing techniques. The elastic moduli of both thick and thin (relative to the shear-wave wavelength) mechanically isotropic phantoms without inflation pressures were determined using AμT-OCE and compared with results of shear rheometry and tensile testing.

Mechanically isotropic light scattering phantoms were prepared using a combination of PVA and $Ti0_2$.[18] First a 4:1 ratio of dimethyl sulfoxide (DMSO, CAS: 67-68-5, EMD Millipore Corp.) was mixed into water using a stir plate. A concentrated stock solution of 0.3 wt. % titanium

nanoparticles suspended in water was prepared using a tip sonicator (Digital Sonifier 450, Branson, Danbury, CT, USA) for 3 minutes (30% duty cycle) at an amplitude of 30% to disperse nanoparticles in solution and tune the phantom's optical properties. The nanoparticle solution was added to the DMSO solution to achieve a nanoparticle concentration of 0.025 wt. %. Two (2) wt. % PVA (146-186 kDa, >99% hydrolyzed, CAS: 9002-89-5, Sigma-Aldrich) was then added to the solution. It was covered and stirred on a hot plate maintaining a temperature of 120 °C for approximately 1 hour to dissolve the PVA. Once fully dissolved, the solution was degassed using a vacuum chamber to remove any bubbles.

Molten PVA solution was then poured into circular molds with a diameter of 5 cm, with variable thickness up to heights of 4 cm, before storing at - 20 °C for up to 12 hours to solidify. Casted phantoms were allowed to harden at room temperature and then placed in a water bath to diffuse DMSO out of solution. The bath was changed regularly for a minimum of 48 hours to remove all DMSO and the phantoms were stored in deionized water to prevent dehydration.

Multiple (5) thick (~4 cm) PVA phantoms were then placed with the surface at the focus of both the OCT focusing lens and the AμT transducer (**Figure 4-12a**). Multiple (5) thin PVA phantoms were suspended on top of water to force asymmetric boundary conditions. The thickness in the thin phantoms ranged from 400 μm-1 mm, as measured with OCT (assuming refractive index n = 1.3) and verified with a digital micrometer.

Each OCE measurement consisted of an M-B scan, where near the beginning of a sequence of 512 repeated A-scans (M-scan), at each location, a 600 V peak-to-peak, 100 μs-long, linear chirp (bandwidth of 1 MHz to 1.1 MHz) was delivered to the acoustic transducer. The push was delivered ~0.5 ms after the start of the A-scan acquisition. The pulse/M-scan sequence was

captured at 256 spatial locations, 54.7 µm between adjacent locations, across the image plane sequentially to create a 3-D cube (z, x, t). A complete M-B scan consisted of 1024 depth × 256 lateral locations × 512 temporal frames (captured at 90,000 frames per second) with an effective imaging range of 1.5 mm × 10 mm (axial × lateral) (**Figure 4-12 b,c**). One full M-B scan took 1.33 s.

The resulting three-dimensional dataset was then used to reconstruct the propagating wave based on the OCT-measured local particle vibration velocity. The axial vibration velocity at a given location ($\Delta U_z(x,z,t)$) was obtained from the optical phase difference between two consecutive A-line scans at each location.

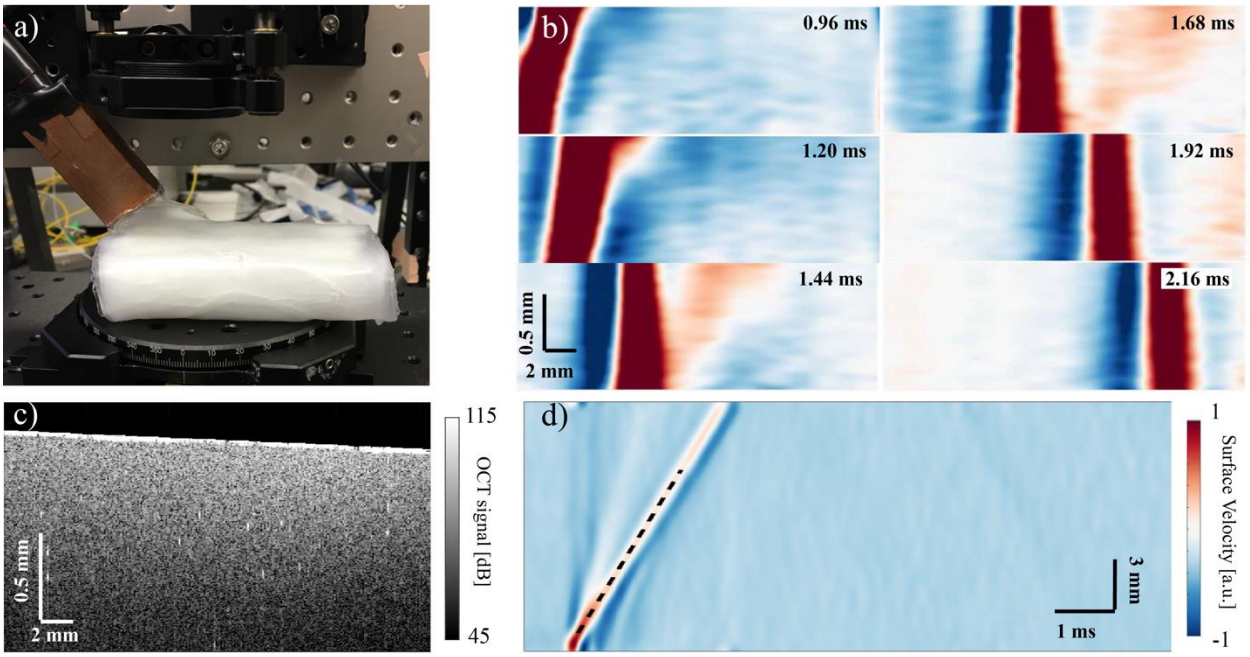

Figure 4-12. AµT-OCE in tissue mimicking phantom. a) Imaging arm with OCT and AµT focus co-aligned with the surface of PVA phantom. b) Snap-shots of axial motion (surface velocity) captured in the *xz*-plane at different time points relative to the start of camera acquisition. c) Log-compressed OCT B-scan of phantom structure. d) *xt* -

plot of axial motion along the surface of the phantom. The dotted line corresponds with the group velocity (C_R= 4.7 m/s) as calculated using the Radon Sum Transform.[187]

The elastic-wave induced vibrations were measured at the surface of the phantom using an automatic identification with an edge detection algorithm. Phase data in a 183μm window below the surface were extracted and averaged using spatial weighting with one half of a Gaussian window (HWHM = 90 μm, weight decreasing with depth) to generate the *xt* plot used to determine the Rayleigh wave group velocity (**Figure 4-12d**).

Elastic moduli were quantified using OCE measurements performed on both bulk and layered samples from the same phantom batch. In the layered sample, the Young's modulus (E) was quantified by fitting the guided modes in *f-k* domain to the A_0-mode of the isotropic thin-plate solution.[15,18,132] The modulus in the thick phantom was quantified by directly inverting the group velocity of the Rayleigh wave (C_R) to obtain the Young's modulus according to

$$E = 3\rho\left(\frac{C_R}{0.955}\right)^2, \tag{4.23}$$

where ρ is the density (assumed to be $\rho = 1000\,\frac{\mathrm{kg}}{\mathrm{m}^2}$). A Radon Sum method[187] was used in time-of-flight reconstruction of the surface wave group velocity in thick phantoms.

A total of 5 thin (~1 mm) and 5 thick (~4 cm) phantoms were used for system benchmarking. In each phantom, 5 repeated scans were performed, and moduli quantified using the appropriate model. The standard error of the modulus varied less than 1% from the mean across the 5 repeated scans in every phantom (both thick and thin), demonstrating reliable system repeatability. The difference between the mean elastic moduli measured in the thin and thick phantoms ($\frac{|E_{thin}-E_{thick}|}{E_{thin}}$)

was 3.5%, consistent with the previously reported difference of less than 3%.[18,132] Finally, the moduli from both sets of phantoms (10 total) were averaged to get the OCE-measured elastic modulus (**Figure 4-13a**).

Following OCE measurements, circular slabs were cut from all phantoms and tested with a parallel plate rheometer (Anton Paar MCR 301 Physica). The frequency-dependent out-of-plane shear behavior was measured over a range of 0.1-16 Hz using a 25 N compressive preload and a peak shear strain of 0.1%. This yielded estimates of the frequency-dependent storage and loss moduli, corresponding to the real and imaginary parts of the complex shear modulus (**Figure 4-13a**). In a lossless isotropic media, the shear storage modulus is proportional to the Young's modulus according to $E = 3\mu$.

The Young's modulus was directly measured in stress-strain testing using linear strips (~6 mm wide) cut from the same samples and pneumatically clamped (2752-005 BioPuls submersible pneumatic grips, 250N max load) at a width of ~15mm. A 50mN pre-load was applied. The samples were stretched at 2mm/min (Instron model 5543) over a range of 1-10% strain and repeated across 3 cycles. The Young's modulus was then computed from the instantaneous slope of the stress-strain curve over this strain range.

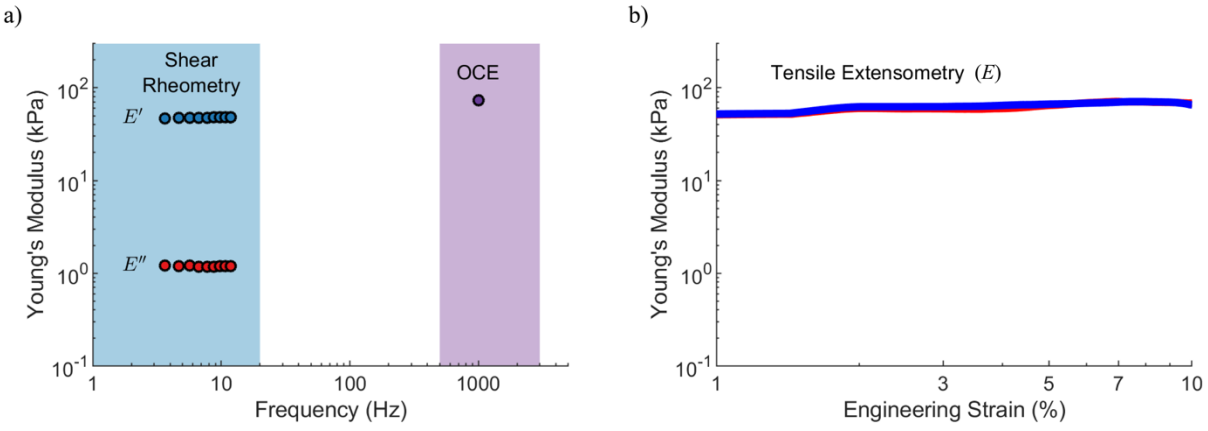

Figure 4-13. Quantitative elastic modulus in tissue mimicking phantom. Comparison between Young's modulus in a PVA phantom measured with a) parallel-plate rheometry and AμT-OCE. Note that error-bars corresponding to the standard deviation are smaller than the marker size. b) The mean tangential modulus for strips taken from the thin (red) and thick (blue) phantoms. The standard deviations (averaged across all strain values) for strips cut from the thick and thin phantoms were ± 6 kPa and ± 5 kPa, respectively.

The mean (and standard error,) in Young's modulus quantified in extensometry, AμT-OCE, and rheometry was 65 ± 2 kPa, 74± 2 kPa, and 48 ± 2 kPa, respectively. The lossless isotropic material model was supported by the frequency-dependent rheometry and strain-dependent tensile test results.

The storage (*E*') modulus from rheometry is close to, but slightly lower than, the Young's modulus from OCE based on the average of measurements for multiple tissue-mimicking (PVA cryogel) phantoms. For all measurements, the ratio between OCE and rheometry was in the range of 1.3-1.5 (30%-50% error). These results are consistent with Minton et.al[188], where a significant poro-/viscoelastic effect in PVA phantoms was shown to produce an apparent stiffness (1.57-1.71 times lower than the peak stiffness) under sustained compression in rheometry. Note that unlike phantom materials such as agarose with high viscosity[189], PVA's low viscosity should have little effect over the frequency range of our OCE measurements (0.5 kHz – 3 kHz). On average, the ratio between OCE and extensometry was 1.14 (14% error). Even with the poro-/viscoelastic effect of compression in PVA material, OCE-measured moduli was within 50% of the values determined by destructive testing in both methods.

PVA scanning and mechanical testing confirmed that when analyzed with the appropriate mechanical model, the AμT-OCE system described here can accurately determine equivalent elastic moduli compared to destructive testing techniques.

4.16 Spatial resolution in wave-based OCE

Elastography, like all medical imaging modalities, can be characterized in terms of spatial resolution (how small a feature can be seen), contrast resolution (how small a difference in the imaging parameter, shear modulus for the case of OCE, can be detected), and artifact level (how well are spatially resolved, high contrast features related to true tissue properties). As shown in this chapter, spatial resolution in dynamic OCE is determined more by the properties of propagating mechanical waves than the limitations of the typical OCT imaging system.

Definition of Spatial Resolution

Generally speaking, spatial resolution in an image is defined as the minimum distance between two objects at which they can be considered individuals.[190–194] The general definition of spatial resolution based on the Rayleigh criterion has historically been adopted in OCE and characterized in terms of the system point spread function (PSF) (i.e. the apparent size of a point source in an image). Using this approach, the propagating elastic wave used to infer modulus in dynamic OCE was typically assumed to behave as a step function at a material interface perpendicular to the propagation direction. Thus, the spatial resolution in dynamic OCE was usually defined by the lateral (perpendicular to light propagation direction) resolution of the optical measurement system. As dynamic OCE does not image isolated sources (propagating mechanical waves are tracked to determine local speed), the image depends on factors such as the size of the object being imaged and the characteristics of the mechanical load. Consequently, the image cannot be treated as the convolution of an input with a PSF, and the general definition of spatial resolution must be modified.

A more appropriate definition for spatial resolution in dynamic OCE is thus the minimum size of an inclusion, in a homogeneous background, for which propagation speed (and thereby, elasticity) can be differentiated from the background without sacrificing quantitative contrast. That is, an inclusion must be differentiable from the background with an elasticity value based on the true elastic modulus contrast between inclusion and background.

Ultimately the resolution in OCE is determined by the probing mechanism (elastic wave propagation), detection mechanism (OCT), and the mechanical model. The probing mechanism determines the appropriate model used to estimate mechanical properties, and is directly related to resolution defining unique limitations for different OCE methods.[22,98,195]

To accurately reconstruct the propagating wave speed near the boundary for the case of a vertical inclusion, two counter-propagating modes must be differentiated to locally estimate the propagation speed of the wave packet traveling in the transmission direction. For shear-wave imaging in dynamic elastography systems, a directional filter[196] is usually applied to wavefield data gathered by the imaging system to extract one of the wave packets. If an ideal directional filter can be designed that does not distort the wave packet, then the spatial resolution of the elasticity map can approach the resolution of the primary imaging system (i.e., OCT-scale resolution for dynamic OCE). However, practical directional filters applied to data with finite bandwidth and finite signal-to-noise ratio (SNR) cannot preserve the spatial resolution of the primary imaging system even for this highly simplified case of plane wave propagation in an infinite medium. While this degradation is only amplified for more practical conditions encountered in dynamic OCE, it is not difficult to design a directional filter that improves reconstruction accuracy without limiting resolution to the finite bandwidth of the filter. In other

words, directional filtering will inevitably limit spatial resolution in the ideal case of wave packets traveling only in the $\pm x$ direction but does not serve as the limiting factor in typical dynamic OCE.

Finding an analytical solution for all modes near a vertical interface is not a trivial problem, especially for broadband Rayleigh-wave pulses. Thus, to explore how vertical inclusions and mode conversions are related to OCE spatial resolution, both detailed simulations and experimental measurements were made on model systems described in detail in Chapter 3. The specific geometry was designed to highlight wave-behavior close to an interface between two lateral regions with different shear moduli. Specifically, Rayleigh waves with varying frequencies were used to determine how close single-mode surface waves could approach a vertical interface without corruption due to scattering and mode-conversion. Note that even for bounded material such as the cornea, wave packets with high enough frequencies (i.e. small wavelengths relative to the corneal thickness) behave similar to Rayleigh waves. The ability to uniquely identify elastic waves from both sides of a mechanical interface is essential to quantitatively measure elastic modulus in regions with different stiffness.

Numerical Simulation

A finite element (FEM) simulation was designed to provide an ideal, noise-free comparison between theoretical and experimental data. The elastic wave equation was solved using OnScale (OnScale 2018, onscale.com, Redwood City, CA, USA). The domain consisted of two linearly elastic regions separated by a vertical plane (**Figure 4-14**). Simulations were run with input bulk *s*-wave speeds (C_s) on either side of the vertical plane as $C_{s(1)}$ = 4.4 m/s (19.36 kPa) and $C_{s(2)}$ = 2.5 m/s (6.25 kPa), typical values for biological tissue. Density (ρ = 1000 kg/m^3) and *l*- wave speed

(C_l = 158.2 m/s) were uniform throughout the domain. These properties correspond roughly to a Poisson's ratio (v) of 0.4995.

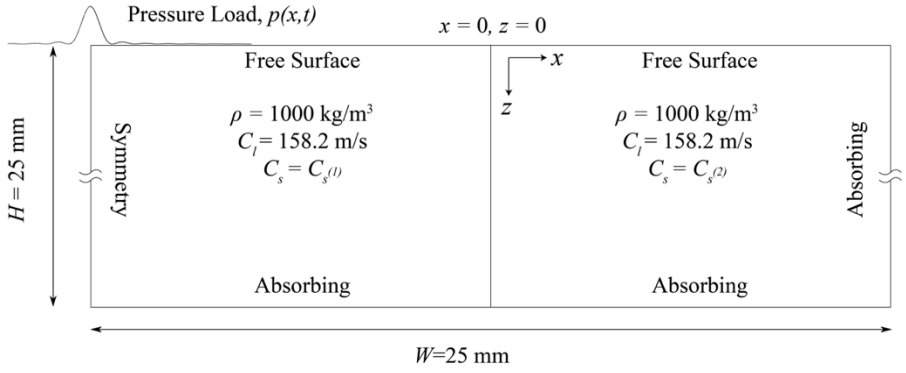

Figure 4-14. **Geometry and boundary conditions used in the two-part elastic wave propagation model.**

Extensive testing was performed with the OnScale solver for the propagation of mechanical waves in nearly incompressible linear elastic media to ensure that numerical solutions for Rayleigh wave excitation and propagation were not corrupted by numerical dissipation or dispersion and were accurate for the input Poisson's ratio (v = 0.4995). Because soft biological tissues typically exhibit a longitudinal wave speed (≈ 1540 m/s) orders of magnitude higher than the shear wave speed (1-10 m/s), a number of computational challenges including long simulation times, increased floating point error, and the formation of spurious solutions due to hourglassing[197] (i.e., artificial, zero-energy strains) are common.

In practice, it is not necessary to directly model the true longitudinal wave speed, as numerical solutions will tend to converge in the limit of $C_s \ll C_l$ when the longitudinal wave speed is sufficiently high. To verify this, we compared numerical solutions for different longitudinal wave speeds from 12.2 m/s to 353.6 m/s with the theoretical solution predicted by the elastodynamic Green's function convolved with the spatial and temporal push profiles.[198,199] In all cases, the shear

wave speed was set as 2.5 m/s. Far-field waveforms show close agreement to the theoretical solution, particularly when the longitudinal wave speed exceeds 158.2 m/s (Poisson's ratio > 0.4995) (**Figure 4-15**). The difference between numerical and exact solutions was quantified using the ℓ_2 error. Results indicate that it is not necessary to set the true value of C_l = 1540 m/s (typical for soft tissues) in the simulations. Any C_l corresponding to Poisson's ratio larger than 0.4995 will produce the same wave propagation over the time scales used in these simulations. Using this fact, simulation times can be dramatically reduced, spurious solutions due to hour glassing can be virtually eliminated, and floating-point error in the numerical solution can be minimized.

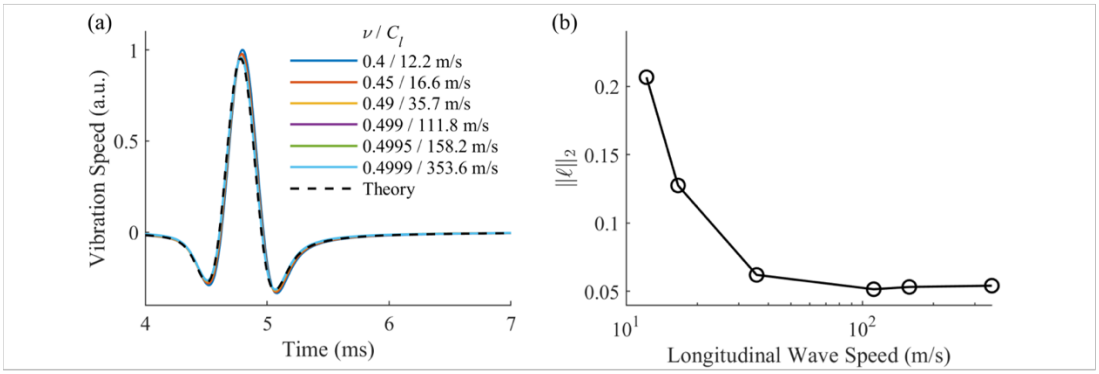

Figure 4-15. Determination of C_l in FEM simulation. (a) Rayleigh wave profiles with various input longitudinal wave speed (v/C_l) at a lateral distance of 10 mm from the excitation. (b) Signal shapes converge to the analytic solution (defined by the Green's function) for Poisson's ratios higher than 0.4995 (C_l = 158.2 m/s). Signal excitation parameters for pressure load were $d = 600$ μm and $T = 240$ μs. The shear wave speed was 2.5 m/s.

A spatially- and temporally-varying pressure was applied along the top boundary of the domain (z = 0) to simulate the acoustic push applied by the AμT transducer in our experiments. A Gaussian model was used to define the spatial push profile:

$$P(x) = \frac{(1+R^2)I(x)}{C_{air}} \approx \frac{2}{C_{air}} \cdot P_0 \cdot \exp\left[-4 \cdot \log 2 \cdot \left(\frac{x}{d}\right)^2\right], \tag{4.24}$$

where R and C_{air} are the reflection coefficient and *l*- wave speed of air, respectively ($R \approx 1$, C_{air} = 340 m/s), P_0 = 5 kPa is the amplitude of the applied pressure, and d = 600 μm is the push width, defined here as the FWHM of the acoustic intensity.

The temporal push profile was given by a super-Gaussian function

$$s(t) = \exp\left(-16 \cdot \log 2 \cdot \left(\frac{t - t_0}{T}\right)^4\right), \tag{4.25}$$

where T is the push duration, defined as the full-width-at-half-maximum of the envelope function $s(t)$. A time delay (t_0) was introduced to avoid impulsive loading at time t = 0. The push profile was centered, and full symmetry was assumed at the left boundary.

The spatial pulse width (PW) of the generated Rayleigh wave will obey the inverse relationship in Equation 4.23, expanding in space as a function of the temporal pulse duration. Limiting the bandwidth of the pulsed wave will increase the spatial pulse width of the generated mechanical wave, regardless of what pushing method is chosen. For this experiment, the spatial profile $I(x)$, was set to have an equivalent d =600 μm, and the push duration (T) was varied (250 μs, 300 μs, 450 μs, and 545 μs) to reduce spectral content in the simulated mechanical wave.

The bottom and right boundaries were set to be absorbing layers to minimize reflections. The domain was discretized with linear finite elements on a regular rectangular grid with a minimum of 40 elements per wavelength (equivalent to a grid spacing of 2.75 μm). Because under-integrated linear elements are prone to spurious solutions, we applied Belytchko-Bindeman strain hourglass suppression.[197] The equations were integrated in time using an explicit time-stepping method to generate the full vibration velocity vector (time derivative of the dynamic displacement vector) at

each space and time point. Only the vertical component of the vibration velocity was analyzed for direct comparison to experimental results. Note that additional information on the FEM simulation platform can be found in Ref.[131,132]

It's worth noting that the numerical solution for the case of a semi-infinite material includes wave energy which propagates ahead of the Rayleigh-mode. This disturbance is evidence that the Rayleigh wave equation has additional solutions besides the primary Rayleigh root. One possible solution is a super-shear evanescent wave coupled to a plane shear wave in the medium,[200,201] and has been observed experimentally in multiple studies[202–204] and described in detail by Pitre et. al.[133] For this analysis, the primary Rayleigh root solution is treated as the incident wave-mode and the incident wave energy leading the primary disturbance is ignored. We also note that this 'fast-mode' is generated due to mode-conversion at the vertical interface and serves as a further disruptor when tracking the Rayleigh wave speed in the near-field region close to a boundary.

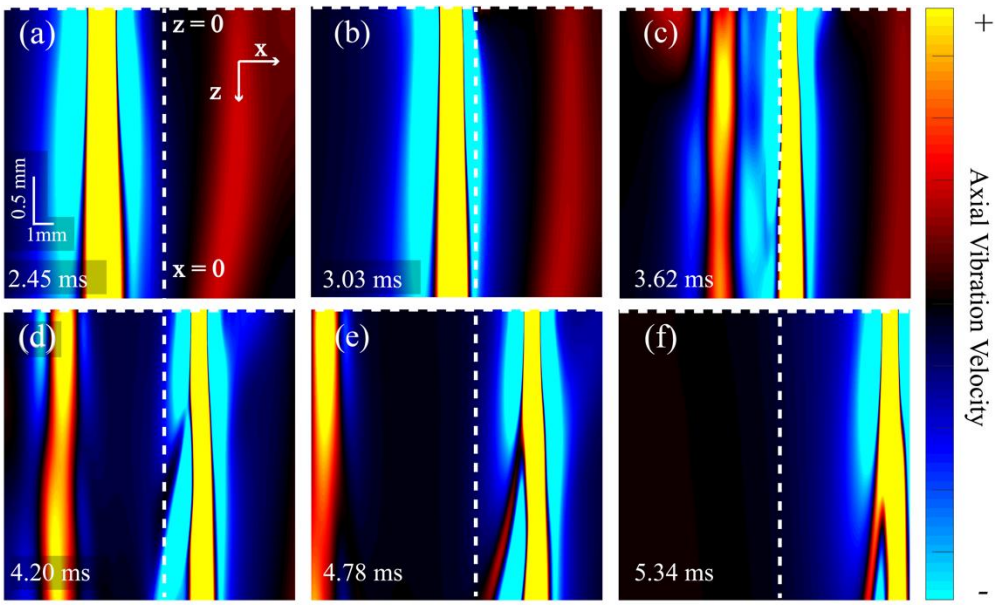

Figure 4-16. **Snap-shots of the simulated 2D vibration-speed field** at various time-steps for the model geometry shown in Figure 4-14. (a) The incident elastic wave energy in the $-x$ region is due solely to the Rayleigh mode. Fast wave energy due to a secondary Rayleigh wave solution (seen in the $+x$ region) separates from the incident Rayleigh wave and does not affect the incident pulse shape. (b-f) Upon interaction with the $x = 0$ boundary, mode conversion can be clearly seen in each panel. Vertical and horizontal dashed white lines denote the $x = 0$ and $z = 0$ boundary, respectively. The dynamic range is scaled to 30% of the maximum value and an uneven aspect ratio is used to highlight mode conversion in depth.

OCE imaging of two-part tissue mimicking phantom

Boundary effects were explored experimentally using an elastic tissue-mimicking material (polyvinyl alcohol (PVA)-based) with controllable mechanical properties (synthesized similar to that in Section 4.15) but with the inclusion of a vertical boundary with varied stiffness (**Figure 4-17**). Phantoms with dissimilar mechanical properties were prepared with varying concentrations of PVA (4% and 6%). The 4% PVA solution was allowed to cool down to 35 °C in a mold with a central barrier prior to casting the 6% PVA solution. The TiO_2 nanoparticle concentration was

slightly increased in the 4% PVA solution to visualize separate regions. The barrier was removed and the 6% PVA solution was cast into the pre-existing phantom, resulting in a 10 cm x 20 cm x 10 cm welded-surface, 2-part material.

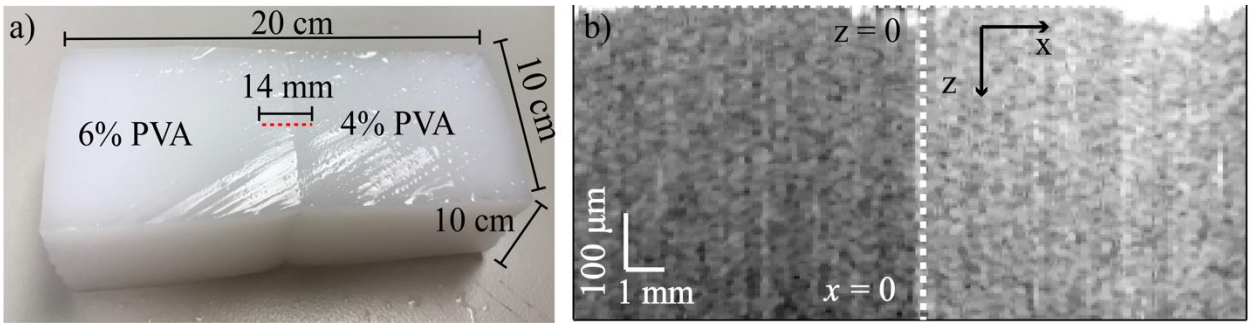

Figure 4-17. Tissue-mimicking phantom with vertical mechanical boundary. a) 2-part PVA phantom block with welded boundary. Red dotted line denotes OCT B-scan line. b) OCT structural image of 2-part welded phantom. Hard 6% PVA material on the left and the soft 4% PVA on the right. A non-uniform aspect ratio is used for visualization.

To generate a planar Rayleigh wave, the AµT transducer was directed at the phantom material to induce a localized displacement.[16,112] The ultrasound transducer was fixed at an angle (~ 45° to vertical) above the phantom to avoid blocking the probe beam from the OCT system, which resulted in ~0.6 mm push width, equal to that of the numerical simulation. The ultrasound excitation was focused on the sample surface 5 mm in the $-x$ direction from the initial OCT observation point to allow Rayleigh waves to fully separate from simultaneously generated bulk *l*- and *s*- waves. Four pulse durations (100 µs, 200 µs, 400 µs, and 600 µs) were used in the experiment.

For AµT (same as for laser excitation of ultrasound)[205], when a surface wave signal is excited by an infinitesimally short (in time) push, the spectral characteristics of the propagating signal are

defined by the spatial width of the push. When the push duration is not infinitesimally short in time, signal spectral characteristics are determined by the convolution of the spatial and temporal push functions. To make experimental propagating signal shapes and spectra match those of the simulations, the push duration can be adjusted. Thus, simulation parameters were tuned slightly so that experimental and simulated propagating signals had close spectral and temporal shapes.

Elastic waves were tracked in the phantom material using an A-line rate of 46.5 kHz and each M-B scan consisted of 512 M-scans at 256 locations (dx = 54.7 μm), forming one complete M-B scan (1024 depth × 256 lateral locations × 512 frames) with an effective imaging range of 1.5 mm × 14 mm (axial × lateral). The total acquisition time for one M-B scan was 3.66 s. The M-B scan dataset was used to track the propagating wave disturbance using the local vibration velocity.

Multiple raw vibration velocity field measurements were acquired and averaged to suppress Gaussian-distributed system phase noise. The number of repeats for each push duration (100, 200, 400, 600) μs were 20, 16, 12, and 8, respectively, so that the average signal-to-noise ratio (SNR_{OCE}) in each data set was approximately the same (50 dB). SNR_{OCE} was quantified using the noise floor (Amp_{noise}, defined as the maximum amplitude of the phase variation along signal-averaged M-mode sequences with no wave propagation (static)), relative to the maximum amplitude of the vibration speed from the incident Rayleigh wave, Amp_{signal}, in each signal-averaged data set, and quantified using $SNR_{OCE} = 20 \log_{10} \frac{Amp_{signal}}{Amp_{noise}}$.

Once signal-averaged displacement sets were acquired, both simulation and experimental data underwent identical pre-processing that included a directional filter to suppress wave reflection at the boundary by masking the second and fourth quadrants of the 2D Fast Fourier Transform (FFT) spectrum.[206] Wave amplitude was normalized at each lateral location and a temporal bandpass

filter applied to remove system noise and side-lobe excitation components using a Gaussian window centered at the peak frequency and bandlimited at the -20 dB cutoff.

The spatial pulse width of the Rayleigh wave in experimental and simulated data was defined fully in the hard (PW_1) and soft (PW_2) regions as the full-width-at-half-maximum of the signal envelope (**Figure 4-18**). The spectral content was defined by the center frequency (normalized first moment of the spectral amplitude bound by -20 dB)[207], F_c, and the maximum frequency (upper frequency at -6 dB), F_{max}, of the power spectrum following a Fast Fourier Transform of the wave disturbance far from any source or boundary (**Figure 4-18c**). As wave speed is constrained by the material properties of the medium, wavelengths are long for low-frequency excitation. Conversely, the spatial pulse width is shorter for broadband (high-frequency) excitation.

In a linear elastic material, the frequency of a harmonic wave must be conserved as it passes through the interface between two media. As a pulsed wave is simply the superposition of signals over a wide range of frequencies, the pulsed signal spectra will also be conserved, and the pulse width will scale in space as a function of the wave speed. The measured pulse width in the soft portion approximately (due to mode conversions at the interface) scaled linearly with the change in wave speed ($PW_2 = PW_1 \left(\frac{C_{s(2)}}{C_{s(1)}}\right) \cong \left(\frac{2.5\text{m}/s}{4.4\text{m}/s}\right) \cdot PW_1$) for all data sets.

To simplify the analysis of resolution at the interface, mean pulse width (PW_{mean}) as $PW_{mean} = \frac{1}{2}(PW_1 + PW_2)$ was introduced, defining a characteristic wavelength of the Rayleigh wave in the region close to the interface.

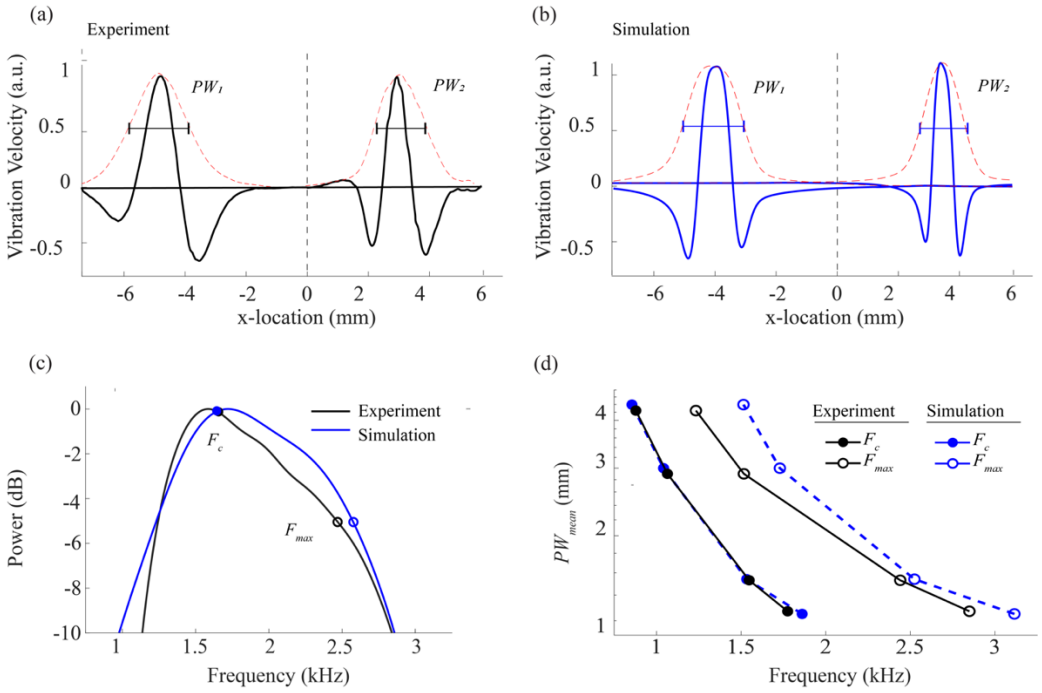

Figure 4-18. Spatial and temporal characteristics of experimental and simulated waves. a) Normalized vibration speed of example experimental Rayleigh wave fully in the hard and soft region (PW_{mean} = 1.53 mm). Full-width-at-half-maximum of the envelope (dotted red line) is used to quantify pulse width on both sides of the x = 0 boundary, noted with a vertical dotted line. (b) Normalized vibration speed of example simulated Rayleigh wave quantified fully in the hard and soft region (PW_{mean} = 1.54 mm), respectively. Both (a) and (b) are at time points t_1 = 2.43 ms and t_2 = 4.62 ms relative to the wave-front entering the field of view. (c) Spectral power of experimental and simulated Rayleigh wave just below the surface ~one pulse width from the x = 0 boundary in the $-x$ direction. The center frequency (F_c) and upper limit (F_{max}) are used to define the spectral characteristics of the pulsed wave. (d) Measured mean pulse width ($PW_{mean} = \frac{1}{2}(PW_1 + PW_2)$) and the corresponding spectral characteristics for all simulated and experimental data sets.

Spatial reconstruction of group velocity

Two-dimensional (2D) group velocity maps were then reconstructed from simulated and experimental data with different pulse widths. Typically, in time-of-flight reconstruction the maximum of the normalized cross-correlation (NCC) function is used to determine the time delay

(Δt) between a reference and delayed waveform spaced by Δx to estimate wave velocity. For experimental data sets corrupted by noise, jitter error will reduce the accuracy of the time lag associated with the maximum magnitude of the normalized cross-correlation (NCC).[208] By assuming sample homogeneity over spatial regions of interest, reconstruction kernels can be expanded over small spatial domains to generate more accurate speed estimates. However, expanding the reconstruction kernel size will reduce lateral resolution around any inhomegeneity.[52]

As bulk shear and Stoneley waves launched at an interface travel in different directions from the parent Rayleigh wave packet, mode mixing will be spatially dependent, producing an artifact close to the interface in the wave-speed reconstruction. This effect has been recognized as an 'edge-effect' in MRE,[209] and modulus quantification is often only considered accurate when viewed approximately ½ of a pulse width from any boundary or source.[210,211] Thus, image details with spatial variation less than about one-half of the elastic pulse width cannot be used to directly determine local elastic modulus assuming a single-propagating wave-mode.

System noise (relative to wave amplitude (SNR)) will further reduce reconstruction resolution and accuracy. In practice, phase-stability of the OCT system determines the minimum detectable displacement (vibration velocity) based on the time-delay between reference and delayed signals. For a homogenous material, noise will shift the maximum of the cross-correlation function away from the actual peak, referred to as jitter error. The predicted jitter magnitude is the minimum error achievable by any unbiased time delay estimation algorithm. As SNR decreases, jitter will increase. It has been shown that time-delay estimation error is worse for very short window sizes, and can be improved with higher SNR.[123,208]

Assuming single-mode propagation, detector spacing must be wide relative to the mechanical wavelength to minimize jitter using a single kernel window size. For an inclusion, the effective detector spacing to accurately reconstruct time delays will play a role in the final OCE resolution. The lateral resolution of OCT (determined by the numerical aperture of the objective lens in the imaging system, typically tens of micrometers) can provide spatial sampling much finer than typical acoustic wavelengths,[3] allowing an over-determined set of time-delay terms to greatly improve the accuracy of local wave-speed measurements,[212] a feature used here to improve reconstruction accuracy. While current systems can detect nm-scale displacements,[181,213,214] both OCE resolution and reconstruction accuracy may be improved by sub-nm-scale displacement sensitivity, allowing accurate time-delay reconstruction of low amplitude waves with very small detector spacing.

To optimize the tradeoff between resolution and accuracy, a multiple-kernel-weighted-averaging approach (MKWA) was used to improve reconstruction accuracy and minimize the loss in spatial resolution. The MKWA method reduced jitter error by calculating time-delays for all available kernel sizes (bound by $x \pm k_x/2$, where the detector spacing (Δx) in each case was denoted as the kernel size, k_x) centered at all locations. The local velocity for each kernel spacing was determined using the NCC function for waveforms assuming elastic wave propagation parallel to the surface. Quadratic interpolation of the lag term about the max was employed to refine the lag-time measurement.

The wave speed at all locations for an over-determined list of velocities was expressed as the sum of the product of wave speed measurements using different kernel sizes and their corresponding weights:

$$C_R(x,z) = \sum_{i=1}^{n_k} w_i \cdot C_{R^i}(x,z) \tag{4.26}$$

$$w_i = \frac{2(n_k - i + 1)}{n(n_k + 1)}, i \in [1, 2, \ldots n_k] \tag{4.27}$$

where $C_{R^i}(x,z)$ represents the wave speed at location (x, z) reconstructed using the i^{th} kernel. w_i denoted the weight for each kernel spacing, and n_k was the number of kernels used for wave speed reconstruction.

Due to jitter error in time-of-flight reconstruction, it is practical to increase detector spacing to improve the accuracy of the measured wave speed. However, increasing the kernel size will reduce spatial resolution. For direct comparison between MKWA and the single kernel method, an equivalent kernel size based on the weighting function (Eq. 4.27) was defined as follows:

$$k_{equivalent} = \frac{\sum_{i=1}^{n_k} w_i \cdot k_i}{\sum_{i=1}^{n_k} w_i}, \tag{4.28}$$

where w_i represented the weight for the i_{th} kernel, k_i the spacing of the ith kernel, and n_k the number of kernels used. 2D group velocity maps were calculated in experimental and simulated data sets using single and equivalent kernel sizes ranging from the minimum OCT scan interval to the maximum spatial pulse width of the elastic wave.

Reconstruction accuracy as a function of increasing weighted averages (increasing n_k in Equation 4.27 and 4.28) was compared to the single kernel time-of-flight reconstruction using the experimental data set corresponding to $PW_{mean} \cong 1.54$ mm (**Figure 4.18**). Assuming a quasi-semi-infinite homogeneous phantom (i.e. forward propagating Rayleigh Wave only), with wave speed

values generated using an unbiased estimator, variation in the local wave velocity, C_R, can be used to define reconstruction accuracy as:

$$SNR_{C_R} = 10 * \log_{10}\left(\frac{\overline{C_R}}{\sigma(C_R)}\right) \tag{4.29}$$

where $\overline{C_R}$ was the average group velocity in a defined region. $\overline{C_R}$ was determined using a 1-D edge profile generated using a depth-averaged set of MKWA wave speeds. The 2-D velocity field was centered at each z-location and the mean taken over a depth equal to one third of the minimum measured pulse width. $\sigma(C_R)$ represented the corresponding variance of the group velocity. For this analysis, SNR_{C_R} was calculated in the experimentally equivalent $C_{s^{(1)}}$ and $C_{s^{(2)}}$ regions for all regions in z, excluding velocity values within one pulse width of the $x = 0$ boundary. The measured SNR_{C_R} from equivalent kernel values are summarized in **Table 4.1**.

Increasing the kernel size to compute spatial gradients along the x- direction improved accuracy at the expense of OCE spatial resolution. The loss (%) in OCE resolution as a function of increasing kernel size for both single kernel and MKWA methods was quantified using the antisymmetric sigmoid fitting function described below (Eq. 4.30) for the equivalent noise-free simulated data set. The minimum kernel size, equal to the grid spacing (2.75 μm), is representative of super-resolution OCT.[215,216] The minimum kernel size will not reduce resolution and was used as a baseline for determining any relative reduction in resolution with increasing k_x.

The tradeoff between SNR_{C_R} gain and spatial resolution loss using MKWA versus single kernel processing is summarized in the table below:

Kernel Size (k) (relative to spatial pulse width in soft material)	**SNRc_R (dB)**		**% loss in spatial resolution**	
	Single k	MKWA (equivalent k)	Single k	MKWA (equivalent k)
10%	**19.7**	**27.8**	**0.3**	**0.1**
20%	20.6	29.5	1.3	1.1
30%	21.7	31.1	3.0	1.9
40%	22.6	32.3	3.9	3.1
50%	23.4	33.4	5.4	4.8
60%	24.5	34.3	7.8	6.2

Table 4-1. Measured SNR_{C_R} and spatial resolution loss between single kernel and MKWA methods.

For a kernel size $\frac{1}{10}^{\text{th}}$ the minimum pulse width, the MKWA method provides an 8.1 dB increase in reconstruction accuracy, and a negligible increase in the measured transition zone. Conversely, the single kernel method reduced spatial resolution at the equivalent kernel size and is more affected by noise-induced jitter error. Based on this analysis, all wave speed images constructed from experimental data used MKWA processing with an equivalent kernel size of $\frac{1}{10}^{\text{th}}$ the minimum pulse width. For consistency, noise-free simulation data sets were reconstructed using the MKWA method with the same equivalent kernel size.

The two-dimensional (2D) group velocity maps reconstructed from simulated and experimental data are shown in **Figure 4-19**. The simulation had a mean pulse width (PW_{mean}) of 1.54 mm and $PW_{mean} = 4.40$ mm. The experimental data had a $PW_{mean} = 1.53$ mm and $PW_{mean} = 4.24$ mm.

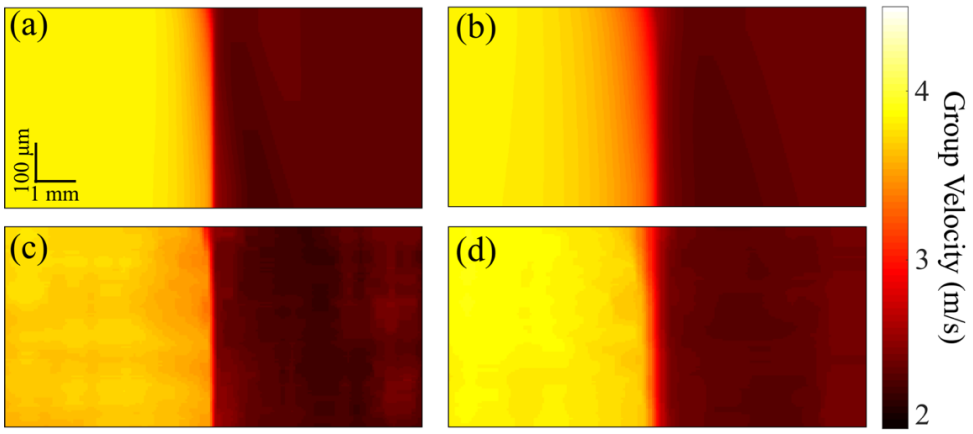

Figure 4-19. Two-dimensional (2D) group velocity maps from simulated and experimental data. Group velocity reconstruction from simulation data with (a) PW_{mean} = 1.54 mm and (b) PW_{mean} = 4.40 mm. Experimental group velocity reconstructed with (c) PW_{mean} = 1.53 mm and (d) PW_{mean} = 4.24 mm.

Experimental measurement of spatial resolution

Antisymmetric sigmoid fitting was applied to each depth-averaged edge profile to quantify the transition zone between the media. To minimize any influence due to a non-vertical interface, the boundary between the two parts of the phantom at each depth was aligned before performing depth averaging. A different fitting function was employed to define the transition region on either side of the $x = 0$ boundary, where each transition profile was combined with its centrosymmetric copy to form a single-part edge profile for sigmoid fitting. The sigmoid function on either side of the boundary was expressed as:

$$C_{R_{fit}} = \frac{a}{1 + e^{-bx}}. \tag{4.30}$$

Half of the -6 dB cut-off of the first order derivative of $C_{R_{fit}}$ with respect to x was used to quantify the transition size on both sides of the vertical boundary. The total transition zone was equal to the sum of the measured transition on either side of the boundary.

As demonstrated in **Figure 4-20**, mode-converted waves on the order of the pulse width affect the estimated wave speed close to the boundary, resulting in a finite transition size before stabilizing to the true Rayleigh wave-speed.

The mode-converted bulk shear and Stoneley waves traveling into the medium degrade reconstruction accuracy, manifesting as features in the group velocity map that are not reflective of the actual geometry (i.e. artifact). A directional filter can mitigate this effect in the negative x direction ($-x$) but is still insufficient to remove scattered wave-packets that travel at an angle normal to the $z = 0$ surface, particularly in the positive x direction ($+x$). Additionally, the temporal wave-shape change due to boundary traction forces will limit the NCC from accurately reconstructing a propagation speed directly on either side of the boundary. The structural OCT image confirmed that the vertical boundary in the phantom was normal to the surface ($< 1°$) to ensure that no unexpected wave modes were generated.

The depth-averaged group velocity measurements and the corresponding sigmoid-fit profiles are normalized and displayed in **Figure 4-20**. The transition size was defined as the full-width-at-half-maximum of the first derivative of the sigmoid fit, with respect to the lateral direction of the fitting function. Note that the small 'bump' appearing on the $+x$ side of the boundary right after the transition zone (**Figure 4-20a**) is an artifact resulting from averaging the 2D velocity reconstruction at a depth relative to the wavelength. Because the reconstructed group velocities at each depth were centered before averaging, and depth averaging was performed relative to the elastic pulse width, any artifact in the reconstruction affected each data set in the same way. Aligning the boundary prior to depth averaging also ensures that transition zone 'blurring' was not a result of depth averaging.

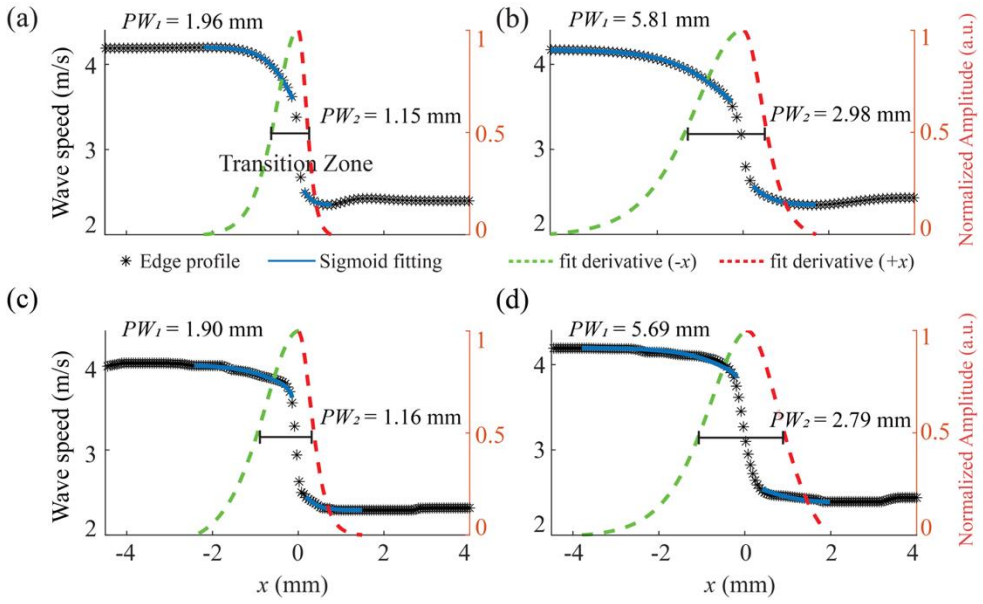

Figure 4-20. **Depth-averaged transition edge profiles with superimposed anti-symmetric sigmoid fittings.** (solid blue line) and first order fitting derivatives (dashed line, green for hard part, red for soft part). FEM simulation examples are shown for (a) PW_{mean} = 1.54 mm, and (b) PW_{mean} = 4.40 mm. Experimental examples for (c) PW_{mean} = 1.53 mm, and (d) PW_{mean} = 4.24 mm.

Results show that the total size of the transition zone region scaled linearly as a function of incident and transmitted spatial pulse widths (**Figure 4-21**). The spatial width of the pulsed wave changed as a function of the local velocity, thus quantification based on the first derivative of the asymmetric fitting function determined the transition size relative to the pulse width uniquely in the hard ($-x$) and soft ($+x$) portion of the model.

When a single Rayleigh wave-mode was incident on a vertical boundary, experimental and simulated results demonstrated a linear relationship between the pulse width and the size of the blurred region, where the transition out of, or into, the other material occurred in space at approximately $\frac{1}{4}$ the size of the spatial pulse width in each material. This result indicated that to accurately differentiate between two regions with different moduli, a finite region equal to at least

$\frac{1}{2}$ the mean pulse width, ($PW_{mean} = \frac{1}{2}(PW_1 + PW_2)$) must be considered. Thus, the ultimate resolution in dynamic OCE may be approximated by $\frac{1}{2}PW_{mean}$.

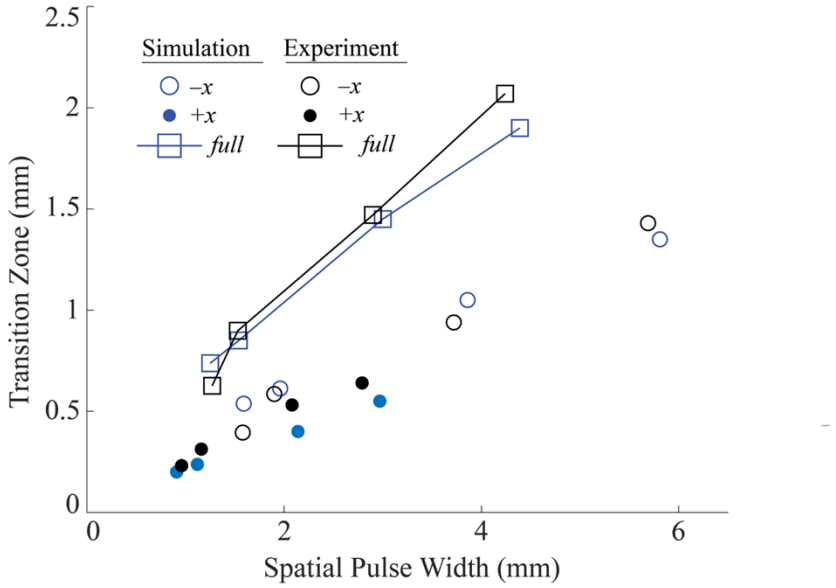

Figure 4-21. **Transition zone as a function of pulse width, *PW***, on either side of the $x = 0$ interface (labeled as $-x$ and $+x$ respectively for the left and right sides of the $x = 0$ interface). The full transition zone (labeled $'full'$) relative to the mean pulse width in both media ($PW_{mean} = \frac{PW_1 + PW_2}{2}$) is also shown for both experiment and simulation.

To examine the relationship between resolution and contrast for more complex internal boundaries, the wave-field generated by a Rayleigh wave passing through a three-part, horizontally layered material was simulated. The two outer layers were assigned shear wave speeds of C_s = 2.5 m/s, while the inner layer, representing a stiff inclusion, was assigned a shear wave speed of C_s = 5 m/s. The simulated push excitation was applied in the first outer layer, generating a Rayleigh wave with a spatial pulse width of 0.5 mm. This corresponded to a maximum potential spatial pulse width of 1 mm in the hard inclusion. For the wave speeds in this arrangement (2.5 m/s, 5 m/s), considering

that frequency is conserved, the mean pulse width was: $PW_{mean} = 0.75$ mm. The width of the middle layer was varied (1 mm, 0.5 mm, 0.25 mm, and 0.1 mm) to examine whether group velocity reconstruction could accurately resolve the inclusion.

The reconstruction presented the inclusion at nearly full contrast with minimal artifact (**Figure 4-22a, b**) when the inclusion width was greater than the mean pulse width. The contrast began to deviate proportionally when the inclusion size reduced relative to PW_{mean} (as seen for the case of 0.5 mm, 0.25 mm, and 0.1 mm inclusion width (**Figure 4-22c -h**). At an inclusion size equal to one tenth the PW_{mean}, (**Figure 4-22g, h**), the reconstruction detected the vertical inclusion, but with very poor contrast. We conclude that the minimum inclusion size that can be reconstructed with full contrast is approximately equal to the mean pulse width PW_{mean}. Note here that the minimum inclusion size is twice the transition zone between two media because the inclusion consists of two vertical interfaces, with a transition region of $\frac{1}{2}PW_{mean}$ at each. A corollary of the previous analysis is that full resolution at maximum contrast may be achieved for smaller inclusion sizes using shorter pulse width (i.e. higher bandwidth) waves.

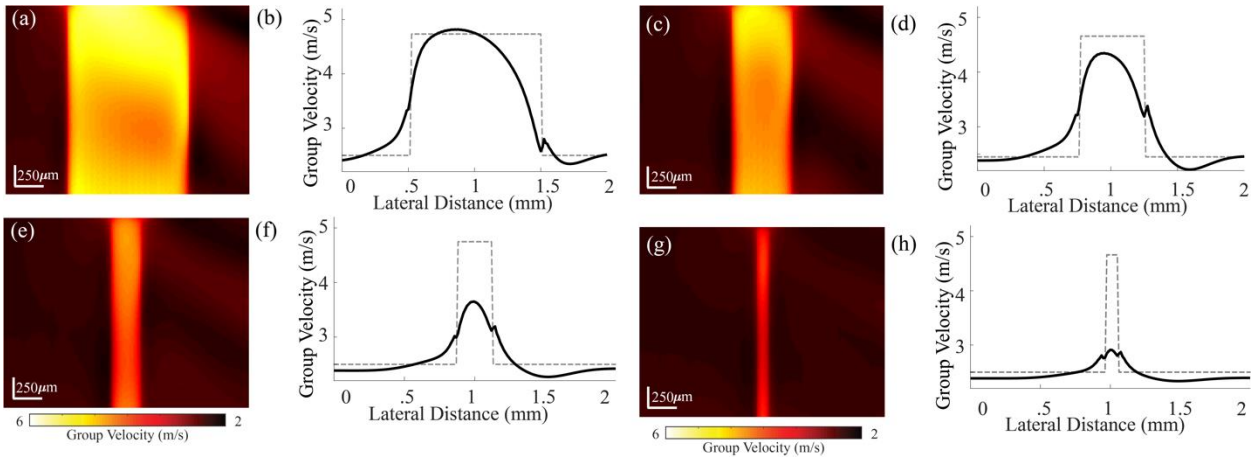

Figure 4-22. **Wave-speed maps in soft (2.5 m/s) media with a hard (5 m/s) inclusion**. The incident spatial pulse width was measured as 0.5 mm, and the maximum potential pulse width was 1 mm, resulting in $PW_{mean} =$

0.75 mm. The inclusion width was (a, b) 1 mm, (c, d) 0.5 mm, (e, f) 0.25 mm, and (g, h) 0.1 mm. The theoretical velocity value (dotted gray-line), and the depth averaged reconstruction curve (black-line) for the corresponding group velocity reconstruction is illustrated in (b, d, f, and h).

As more complex geometries are introduced, boundary conditions become even more disruptive to reconstruction accuracy. Due to the elliptical nature of particle motion in a Rayleigh wave, local stresses transfer energy along both lateral and axial directions. These multi-dimensional traction forces can generate complicated wave fields at all interfaces. Once a single-mode wave interacts with an inclusion boundary, wave components are guided along the boundary, mode-convert, diffract, and interfere with the original wave shape, reducing correlation and negatively affecting spatial resolution in complex boundary conditions.

To illustrate this point, a 5 m/s semi-circular inclusion (6 mm wide, 3 mm deep) was simulated at the center of a 2.5 m/s media (**Figure 4-23**) and probed using a Rayleigh wave with mean pulse width, PW_{mean}, of 0.75 mm and 4.5 mm, respectively. The boundaries of a semi-circular inclusion were better defined when reconstructed using PW_{mean}= 0.75 mm (**Figure 4-23b**) compared with PW_{mean} = 4.5 mm (**Figure 4-23c**). Note that boundary regions are corrupted in the reconstruction even for PW_{mean}= 0.75 mm due to mode conversions.

For longer pulse widths (lower frequency) waves, the reconstructed image identified the inclusion but could not accurately quantify modulus, highlighting the importance in defining both image contrast and resolution.

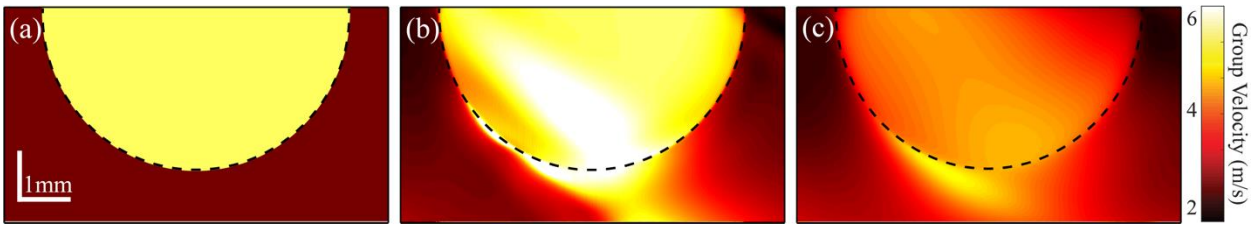

Figure 4-23. **A hard (5 m/s) semi-circle (3 mm radius) inclusion imbedded in a soft (2.5 m/s) media** was simulated. Prescribed model wave speeds are shown in (a). 2D group velocity reconstruction from incident wave with (b) PW_{mean} = 0.75 mm and (c) PW_{mean} = 4.5 mm.

Summary of lateral resolution in wave-based OCE

To summarize, the typical dynamic OCE procedure is to: 1) launch a broadband mechanical wave within a sample using a temporally short, spatially sharp excitation force (akin to shear wave elasticity imaging,[20,217] acoustic radiation force imaging,[218] and transient MR elastography[219]); 2) track the propagating elastic wave in real time (B-M mode)[16,220] or with M-B mode[20,99] OCT scanning; 3) use local displacement (vibration velocity) fields to estimate mechanical properties.[15,22,221] Under highly controlled conditions, the estimated wave velocity can define the shear modulus (stiffness) within a small region.[15,20,23,98,99,222] Even with typical limitations imposed by a practical measurement system (i.e., measurement noise will introduce additional imperfections), the numerical simulations and experimental studies in tissue-mimicking phantoms presented here demonstrate that OCE spatial resolution is fundamentally limited by the properties of propagating mechanical waves.

As complicated boundaries change wave shape and generate interfering wave-modes, a quantitative, artifact-free time-of-flight reconstruction cannot be done until the parent mode has separated from the complex displacement field. It follows that the local material properties will

play a role in the achievable resolution. Thus, resolution cannot be defined simply by the detection mechanism of OCT.

If a Rayleigh wave encounters an inclusion with a modulus different from that of the original propagation medium, the pulse width of the incident wave, and any generated wave-modes, will scale as a function of the relative differences in C_s, and the resolution will be defined by the local pulse width. As we have shown, the minimum resolvable feature (e.g. any interface with elastic modulus differential) in a system will be approximately equal to ½ the mean spatial pulse width at all locations within the imaging field. The minimum inclusion size reconstructed at full contrast is twice this limit and corresponds approximately to the mean pulse width at the inclusion interface.

Note that when the inclusion modulus is unknown, the resolution in OCE can be defined only approximately because the mean pulse width depends on both the inclusion and surrounding medium moduli. Defining the resolution by the probe pulse width is not accurate and can either underestimate or overestimate it depending on inclusion properties. Additionally, in many cases where bounded geometries are imaged, even relative wave speed differences (i.e., relative contrast) are influenced not only by shear elastic modulus, but also by geometric factors such as medium thickness (e.g., in the cornea).[88]

Another way to improve resolution is to utilize more complicated reconstruction methods to quantify material stiffness. To accurately recover spatial resolution to a fraction of the pulse width for an arbitrary imaging environment, full wave field reconstruction should be performed at a fine spatial scale similar to current coarse spatial scale methods in Magnetic Resonance Elastography (MRE).[209,223–226] The general case of wave field reconstruction often assumes local homogeneity, a valid assumption when probing regions spaced by approximately ½ the wavelength of a harmonic

elastic wave. Consequently, extrinsic variables can significantly influence the spatial resolution as defined in this study.

In conclusion, the spatial resolution in dynamic OCE when tracking mechanical wave propagation near an interface is ultimately limited by the characteristic wavelength of the mechanical wave, or by the pulse width for broadband signals. The ability to accurately reconstruct an inclusion with contrast nearing that of the physical modulus breaks down when the mean pulse width is greater than the size of the physical inclusion. In the AμT-OCE system described here, the best spatial resolution that can be realized is equal to the focal width of the acoustic transducer, or 400 μm.

4.17 AμT-OCE system summary

The design and configuration of an AμT-OCE system that can characterize and image quantitative elastic moduli in soft tissue was described herein. The performance of the system was characterized and defined using OCT structural resolution, sensitivity, motion detection, elastic reconstruction accuracy, and elastographic resolution. The performance and accuracy was validated using controlled tissue-mimicking phantoms against gold-standard destructive methods.

Because the AμT-OCE system demonstrated accurate quantification of elastic moduli without damaging soft material (using the appropriate mechanical model), it was concluded that the system was reliable to quantify moduli in the cornea.

Chapter 5. Quantifying elastic moduli in the cornea with AμT-OCE

To date, most reports of OCE in the cornea assumed a Rayleigh-wave model and utilized group velocity to reconstruct corneal elasticity.[15,16,19–26] However, the group velocity is often incorrectly interpreted as a direct measurement of the bulk shear wave speed (C_s) in the cornea. While a single-mode bulk wave is often the case for mechanical waves produced in magnetic resonance elastography (MRE) and in ultrasound-based shear wave elastography (SWE), it is not the case in highly heterogeneous materials or in media greatly influenced by mechanical boundary conditions such as the cornea. For the elastic pulse widths typically excited in the cornea, assuming that group velocity is directly related to modulus has resulted in reports of moduli which span multiple orders of magnitude.[27]

In this chapter, it is shown that both group velocity and an isotropic Rayleigh model are inappropriate for the cornea. Because the cornea is an incompressible material layer bounded by air at the top and water (aqueous humor) on the bottom, guided waves with strong geometric dispersion should be expected (see Chapter 3) and thus require complex elastic reconstruction techniques.

The cornea is also mechanically anisotropic. As such, wave behavior in the cornea cannot be accurately described using an isotropic model, even taking geometric dispersion into account.

In Chapter 5, ex vivo porcine cornea were imaged using the AμT-OCE system (described in Chapter 4) and an inversion routine is presented to quantify the anisotropic elastic moduli (described in Chapter 3) responsible for corneal deformation. AμT-OCE-measured moduli were

shown to closely agree with elastic moduli measured via destructive testing techniques (parallel-plate rheometry and tensile extensometry).

5.1 Group Velocity in bounded media

Numerical simulations and experimental studies in purely elastic (negligible viscosity) homogenous soft materials with thickness on the order of the cornea are presented to demonstrate quantitative errors in elastic modulus values when the finite thickness is not taken into account.

Numerical Simulation of Elastic Waves in Bounded Media

First, numerical simulations were performed with the finite element method (FEM) in OnScale described in Chapter 4. Using the numerical model, effects of intrinsic (shear modulus) and extrinsic (geometry and mechanical wave bandwidth) parameters on both group and phase velocity measurements were explored in a purely elastic isotropic material. The simulation provided a system with infinite signal to noise ratio (SNR).

In the simulation, Rayleigh wave excitation and propagation in both bulk and bounded linear-elastic material were investigated. The simulated material models can be seen in **Figure 5-1**. The shear wave speed in the material in both models was $C_s = 5$ m/s ($\mu = 25$ kPa).

A spatially and temporally compact force was applied to the medium with a Gaussian profile in space (characteristic width of $d = 250$ μm) and a super Gaussian temporal profile with a characteristic time constant $T = 100$ μs. In one set of simulations, $d = 0.25$ mm, i.e. twice narrower than the focus of the acoustic excitation, to explore high bandwidth (short pulse-width) behavior.

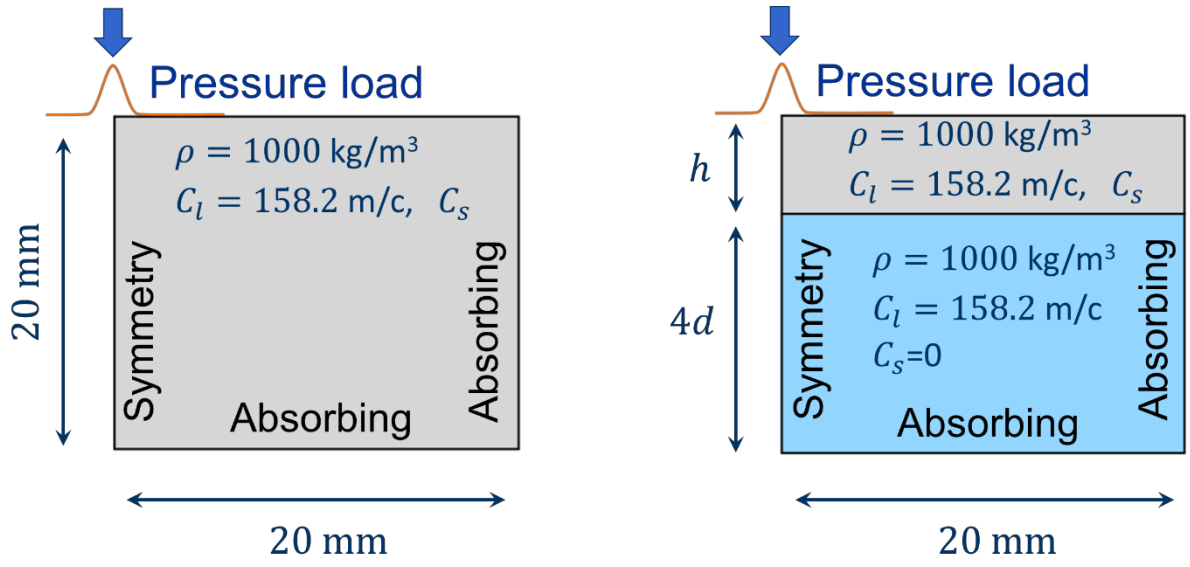

Figure 5-1. **Finite element model in OnScale.** (formally PZFlex): geometry and boundary conditions for a nearly incompressible semi-infinite medium (a) and a layer bounded on its bottom with water (b).

The bounded tissue model consisted of two, layered, linear elastic materials under plane strain (**Figure 5-1b**). The longitudinal wave speed in the lower medium was similar to that of water (closely approximating the anterior chamber of the eye) and the shear wave speed was set to $C_s = 0$ m/s. Note that this region can support longitudinal waves but not shear waves due to the matched density and longitudinal wave speed with the upper tissue region ($\rho = 1000$ kg/m^3, $C_l = 158.2$ m/s) and mismatched shear wave speeds. The thickness of the lower layer was set to four times the estimated wavelength in the top layer to minimize interactions between the "leaky" longitudinal wave and the lower boundary. The top layer thickness was $h = 1$ mm.

A space-time (*xt*) trace of the simulated vertical vibrations along the surface of each material is shown in **Figure 5-2**, where the left column corresponded to the Rayleigh wave (bulk material), and the column on the right to the guided wave (thin material). A horizontal slice of the *xt* plot

(shown with a dashed white line) denotes the temporal profile of the propagating signal 10 mm from the excitation point (**Figure 5-2e,f** respectively).

As seen in **Figure 5-2c,e**, the temporal profile of the Rayleigh wave had a simple shape which did not change with distance once it traveled multiple pulse-widths from the excitation zone. In this case the normalized cross-correlation coefficient (NCC) between two signal profiles measured at different spatial positions along the surface was equal to one, suggesting that cross-correlation based calculation of the group velocity provided an accurate propagation speed over all *x* positions. Because medium viscosity is omitted in the analysis, the calculated group velocity was equivalent to the phase velocity of the Rayleigh wave and reconstruction was accurate in the case of a thick (relative to the wavelength), non-viscous, material.

In the layer bounded by water on its bottom (as shown in **Figure 5-2**), the *xt* shape became very complex (see **Figure 5-2d**). The complex signals were due to highly dispersive guided modes that coexist and propagate along the medium surface. Note that analytical solutions to expected wave behavior in bounded media can be found in Chapter 3.

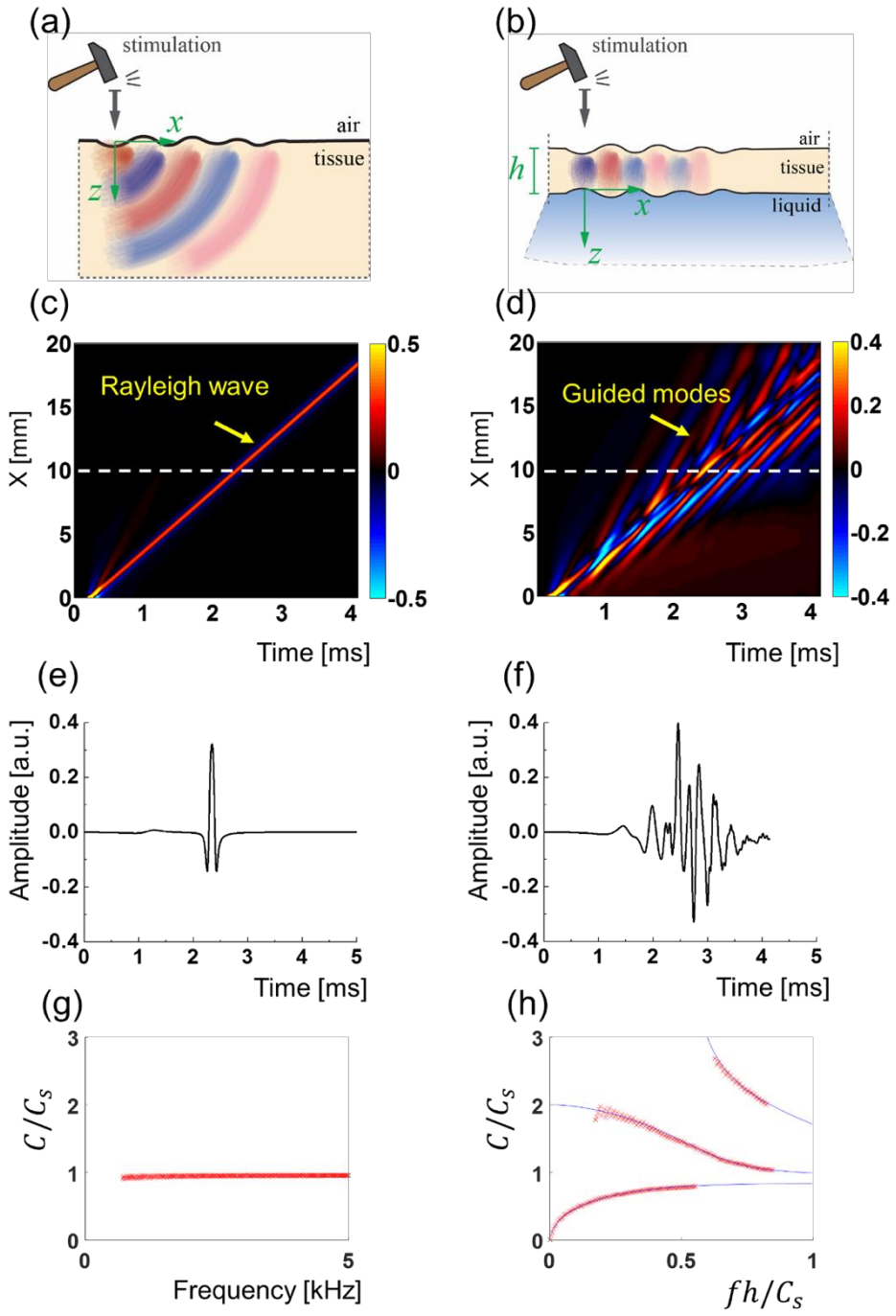

Figure 5-2. Mechanical waves along the surface of a nearly incompressible linear elastic medium simulated in OnScale. Spatial and temporal parameters of the push were $d = 250$ μm and $T = 100$ μs respectively. Layer thickness was $h = 1$ mm. The bulk shear wave speed was $C_s = 5$ m/s ($\mu = 25$ kPa). Results are shown for a semi-infinite material with air at the upper boundary in a,c,e,g) and a 1 mm thick tissue layer bounded with a liquid from

the bottom in b,d,f,h). (a) and (b) show schematic representations of wave excitation and propagation (previously published in Ref[15]); (c) and (d) show wave fields (*xt* plots) along the medium surface displayed over an arbitrary dynamic range scaled to the signal maximum; (e) and (f) show temporal profiles of Rayleigh and guided waves at a 10 mm distance from the excitation point (shown with a white dashed line in c and d) respectively; and (g) and (h) show phase velocity dispersion plots for Rayleigh and guided waves, respectively: numerical simulation (red crosses) superimposed on the analytical solution (solid lines). This figure was previously published in Ref[132].

A 2-D Fourier transform was applied the simulated signal wave fields (*xt* plots) in wavenumber and frequency (*fk*) coordinates to compute the phase velocity dispersion.[227,228] The simulation results were superimposed on the analytical solution (see Chapter 3) in **Figure 5-2g** and **h**.

As shown in **Figure 5-2**, the high frequency cutoff (or bandwidth) of the propagating waves determine how closely the measured signal corresponds with the analytical solution. This can be related to different excitation methods used in OCE which produce different characteristic frequencies of generated mechanical waves. For example, air-puff techniques generate broadband signals up to approximately 1 kHz bandwidth while the AμT transducer described in Chapter 4 can produce mechanical waves with frequency components closer to 5 kHz.

To generalize the geometric dispersion of guided waves for different shear wave speeds and medium thickness, the frequency was scaled to the medium thickness and shear wave speed according to:

$$f_d = \frac{fh}{C_s}. \tag{5.1}$$

The dimensionless f_d can be applied to a wide range of experimental conditions encountered in OCE. Note that the large majority of reported wave-based OCE experiments (to date) performed

on the cornea were over a small range of f_d. For example, a typical human cornea (thickness h = 0.5 mm, $C_s \cong 5$ m/s) probed over a 400 Hz bandwidth (typical for air puff[105,107]) would result in $f_d \cong 0.04$. Note that a 5 kHz bandwidth (such as demonstrated with AμT) would result in $f_d \cong 0.5$.

To explore the relationship between group velocity and signal bandwidth (i.e. apparent speed over a specific range on the dimensionless frequency scale), a low-pass (LP) Gaussian filter was applied to simulated data to artificially limit the signal bandwidth. The filter cutoff frequency was indicated by a vertical dashed arrow in the central column of **Figure 5-3**. The upper row of **Figure 5-3** presents the case where the signal spectrum was limited by $f_d \cong 1$. In this case the complicated wave field (*xt* plot) shown in the left panel produced three propagating guided modes (shown by red crosses in the phase velocity dispersion panel (central panel)), consistent with the analytical solutions presented in Chapter 3. The elasticity map in the right panel was produced using the group velocity at every position in the medium and normalizing it to the true (input) shear wave speed. In the bounded material, the elasticity map appeared heterogeneous, with dramatic deviations from the true shear wave speed. The reconstructed heterogeneities were not representative of the intrinsic material parameters and should be considered artifacts dominated by the medium thickness and signal bandwidth.

When the signal spectrum was limited by $f_d \cong 0.5$ (second row in **Figure 5-3**), both the *xt* plot and reconstructed elasticity map were visibly different due to the limited signal bandwidth. Further limiting the signal spectrum by $f_d \cong 0.25$ (third row in **Figure 5-3**) and $f_d \cong 0.1$ (bottom row in **Figure 5-5**) resulted in a single propagating guided mode which appeared to make the 2-D group

velocity distribution more homogeneous. Limiting f_d dramatically reduced the average group velocity relative to the true shear wave speed.

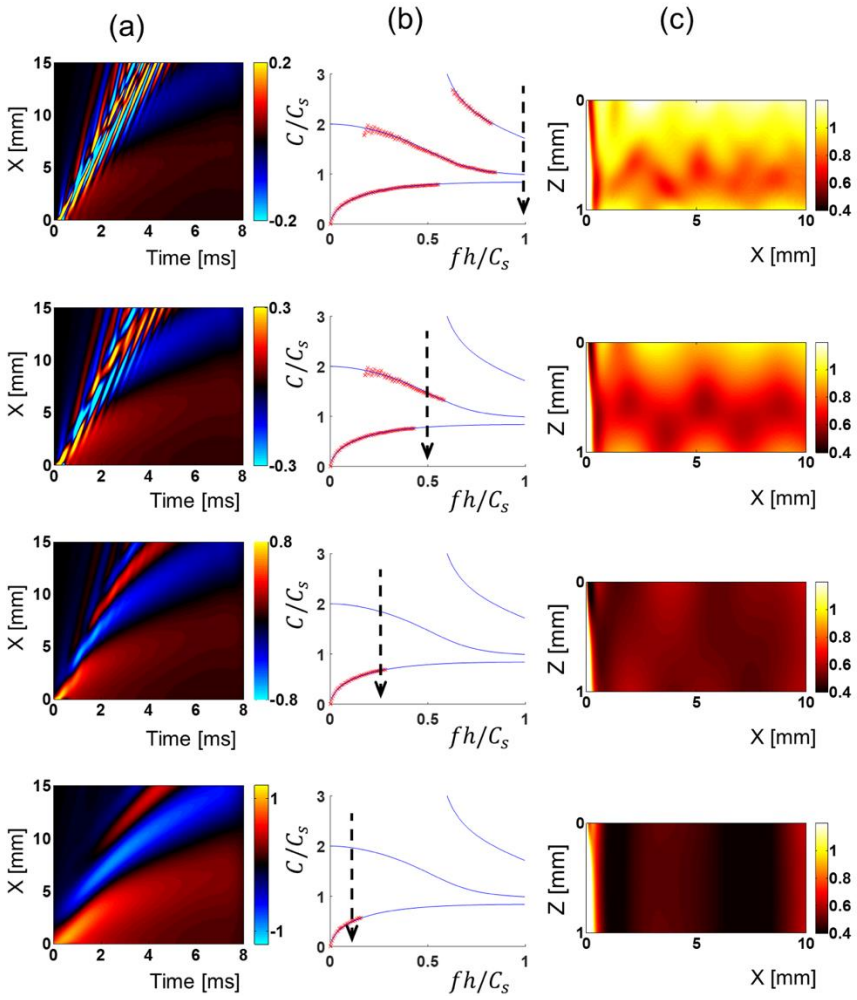

Figure 5-3. Mechanical wave propagation in a layer of nearly incompressible linear elastic medium bounded with water on the bottom simulated in OnScale. Column (a) showed XT plots calculated along the tissue surface and obtained for different signal bandwidths (BW), so that ($BW * \frac{h}{C_s} = 1, 0.5, 0.25, 0.1$) respectively, for the rows from top to bottom. Column (b) showed the phase velocity dispersion computed from the wave fields of column (a) – red crosses, superimposed on the analytical solution (solid lines), respectively. Column (c) showed two-dimensional (2-D) group velocity images normalized to the true shear wave speed. In this case the displayed value

was 1 for a group velocity estimate which equaled the true shear wave velocity at every point in the *xz* plane using NCC-shift method for the same $BW * \frac{h}{C_s}$ values, respectively. This figure was previously published in Ref[132].

AμT-OCE in Bounded Media

Next, thin-plate polyvinyl alcohol (PVA)-based phantoms were created using protocols described in Chapter 4. In this experiment, multiple thin-plate phantoms were cast in circular molds with a diameter of 5 cm. The thickness was controlled by adding only enough molten PVA solution to cover the bottom of the mold and then rotating the mold to evenly distribute the solution. Multiple thin slabs were created and then physically sized using OCT structural imaging. During imaging, each PVA phantom was suspended on top of water to force asymmetric boundary conditions, similar to the medium diagram used in numerical simulations (see **Figure 5-4**). To estimate the true shear wave speed of the phantoms, group velocity measurements were taken at the surface of a separate 15 mm thick phantom (synthesized from the same batch) and used to determine C_s based on the Rayleigh wave equation.

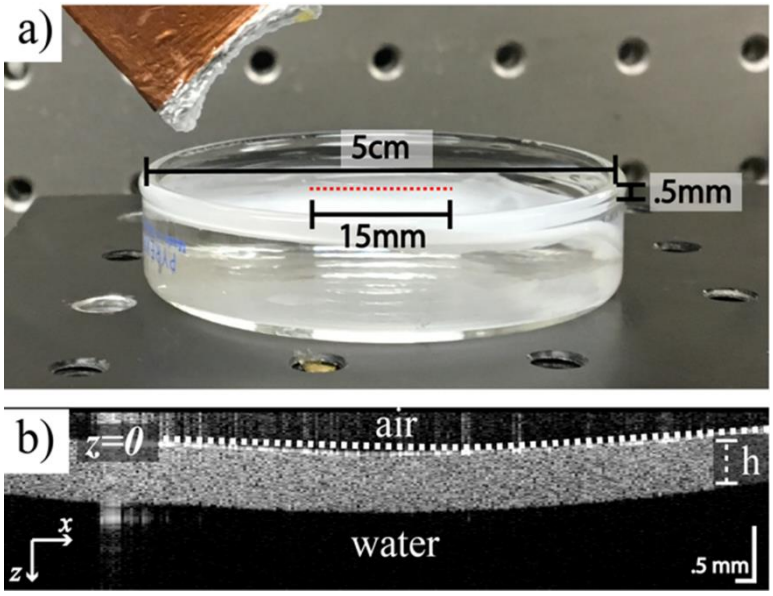

Figure 5-4. Thin tissue mimicking phantoms bounded by air and water. a) Experimental setup showing a 0.5 mm thick PVA phantom suspended on water boundary. The AμT transducer can be seen in the upper left. The red dotted line denotes OCT B-scan range. b) OCT structural image (B-scan) of thin-plate phantom. Note: uneven aspect ratio displayed to highlight phantom structure. This figure was previously published in Ref[132].

Elastic waves were tracked in the phantom at 46.5 kHz. Each M-scan consisted of 512 A-scans in the same location repeated at 256 locations (B-scans) horizontally across the imaging plane (dx = 58.6 μm), forming one complete M-B scan (1024 depth × 256 lateral locations × 512 frames) with an effective imaging range of 1.5 mm × 15 mm (axial × lateral). The total acquisition time for one M-B scan was 3.66 s. The acoustic push was applied for T = 100 μs (same as in the numerical simulation) and focused to the edge of the OCT imaging range.

The vertical displacement due to elastic wave propagation was measured using the optical phase difference between successive scans assuming a refractive index of n = 1.33. The vibration speed was recorded at different time points in the xz plane and a 2-D FFT was applied to compute phase velocity dispersion curves. Group velocity maps in the xz plane were obtained with the correlation method described in detail in Chapter 4 and Ref.[18] Finally, the average group velocity over the 2-D image was calculated.

Experimental results presented in **Figure 5-5** through **Figure 5-7** show behavior similar to that of the simulations. To facilitate comparison between simulation and experiment, experimental results were split into three figures corresponding to different ranges of dimensionless frequency (f_d) and displayed alongside numerical simulations in OnScale for the same medium parameters.

The maximum value of the dimensionless bandwidth that was reached experimentally was $BW * \frac{h}{C_s} \cong 0.5$. The shear wave speed was measured to be $C_s = 3.8$ m/s for the bulk 15 mm thick sample

using the group velocity method and then used to compute theoretical curves for phase velocity dispersion (solid blue lines in panels (b) and (e) in **Figure 5-5** through **Figure 5-7**). Note, that the layer thickness measured with OCT structural imaging was $h \cong 0.5$ mm (similar to the human cornea), compared to the 1 mm thickness (similar to porcine cornea) used in the simulation.

Wave fields (*xt* plots) of propagating mechanical waves near the sample surface from experimental data were represented in panels (a) in **Figure 5-5** through **Figure 5-7,** each with different signal bandwidths. To reduce the signal bandwidth, LP filtering was applied to experimental data in the same way as the simulated data. To compare with experimental data, *xt* plots were also obtained from numerical simulations for the same medium parameters (panels (d) in **Figure 5-5** through **Figure 5-7**). 2-D group velocity images computed with experimental data normalized by measured C_s (panels (c) in **Figure 5-5** through **Figure 5-7**) were compared with numerically simulated data (panels (f) in **Figure 5-5** through **Figure 5-7**). In both experiment and simulation, there were numerous artifacts in the *xz*-plane due to multiple dispersive modes in the bounded layer.

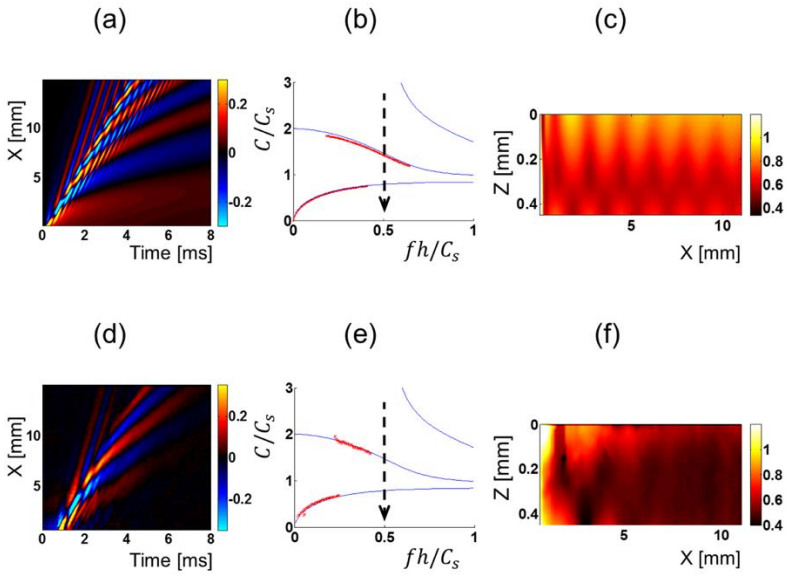

Figure 5-5. OCE- measured mechanical wave propagation in PVA bounded with water on the bottom compared to numerical simulations in OnScale with dimensionless signal bandwidth was approximately $\boldsymbol{BW * \frac{h}{C_s} = 0.5}$. *xt* plot (wave field) calculated along the surface of the simulated material a) and phantom d). Phase velocity dispersion computed from the wave field of (a, d) for b) simulation and e) experiment. The red crosses were experimental data superimposed on the analytical solution (solid lines). Two-dimensional (2-D) group velocity images normalized to the true shear wave speed (i.e., displayed value is 1 for a group velocity estimate equaling the true shear wave velocity) obtained for every point of the *xz*-plane from c) simulation and f) experiment. This figure was previously published in Ref[132].

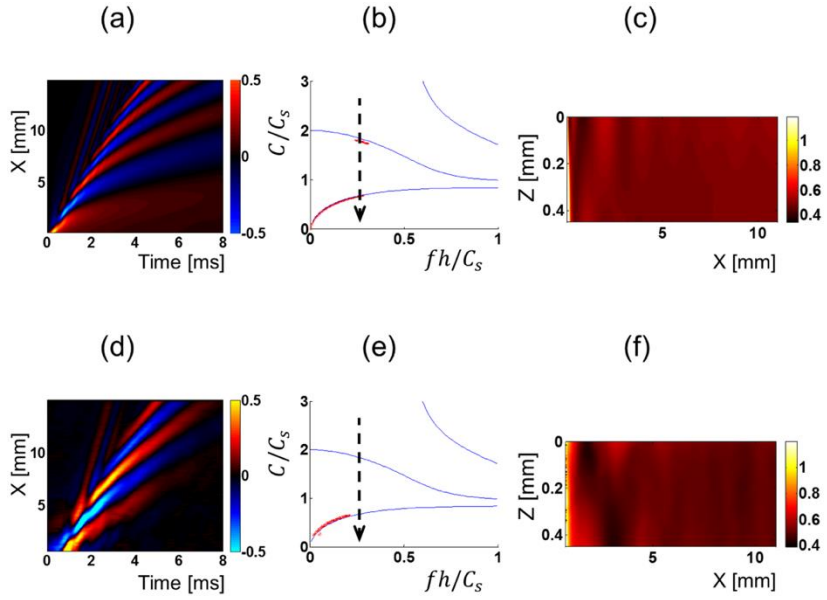

Figure 5-6. OCE- measured mechanical wave propagation in PVA bounded with water on the bottom compared to numerical simulations in OnScale with dimensionless signal bandwidth approximately $\boldsymbol{BW * \frac{h}{C_s} = 0.25}$. *xt* plot (wave field) calculated along the surface of the simulated material a) and phantom d). Phase velocity dispersion computed from the wave field of (a, d) for b) simulation and e) experiment. The red crosses were experimental data superimposed on the analytical solution (solid lines). Two-dimensional (2-D) group velocity images normalized to the true shear wave speed (i.e., displayed value is 1 for a group velocity estimate equaling the true shear wave velocity) obtained for every point of the *xz*-plane from c) simulation and f) experiment. This figure was previously published in Ref[132].

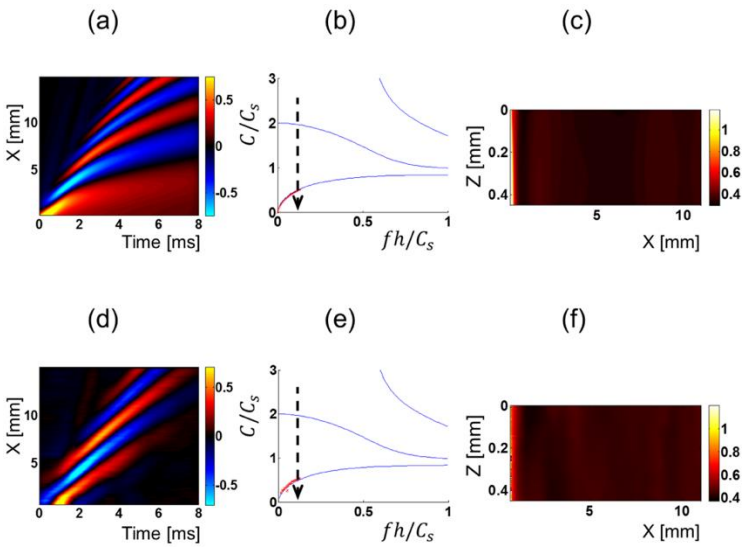

Figure 5-7. OCE- measured mechanical wave propagation in PVA bounded with water on the bottom compared to numerical simulations in OnScale with dimensionless signal bandwidth was approximately $\boldsymbol{BW * \frac{h}{C_s} = 0.1}$. *xt* plot (wave field) calculated along the surface of the simulated material a) and phantom d). Phase velocity dispersion computed from the wave field of (a, d) for b) simulation and e) experiment. The red crosses were experimental data superimposed on the analytical solution (solid lines). Two-dimensional (2-D) group velocity images normalized to the true shear wave speed (i.e., displayed value is 1 for a group velocity estimate equaling the true shear wave velocity) obtained for every point of the *xz*-plane from c) simulation and f) experiment. This figure was previously published in Ref[132].

The image artifacts depend on multiple parameters, such as signal bandwidth, layer thickness, shear wave speed and temporal profile of the excited mechanical wave. Imaged artifacts in the phantom were smoothed at distances larger than 5 mm for $BW * \frac{h}{C_s} = 0.5$ (**Figure 5-5f**) due to medium viscosity and geometric spreading of the elastic wave in the phantom, limiting the signal bandwidth.

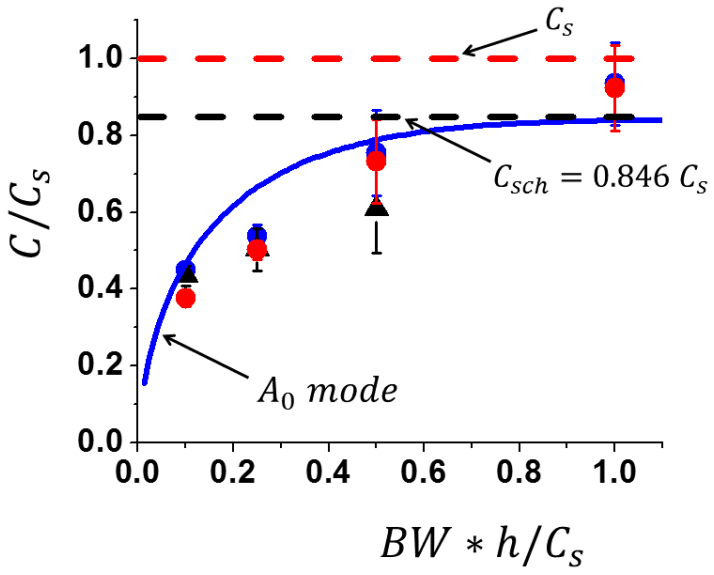

Figure 5-8. Mean group velocity in *xz*- plane as a function of signal bandwidth. Blue (obtained for a 1 mm thick simulated material) and red (obtained for a 0.5 mm thick simulated material). The circular dots correspond to numerically simulated 2-D group velocity distributions (column (c) in **Figure 5- 3** and panels (c) in **Figure 5-5** – **Figure 5-7**, respectively). Black triangles correspond to the mean group velocity in the *xz* plane for a 0.5 mm thick PVA sample. The solid blue line presents the dispersion curve for a guided mode of the lowest order (i.e. A0 mode). The dashed black line corresponds to the Scholte wave velocity asymptote for this mode (described in Chapter 3). Dashed red line corresponds to the true shear wave velocity. Error bars show variance of group velocity estimates in the *xz* plane. This figure was previously published in Ref[132].

Figure 5-8 shows group velocity estimates averaged over the 2-D distributions (over 10 mm x 1 mm area in case of a 1mm thick medium and over 10 mm x 0.45 mm for a 0.5 mm thick medium) shown in **Figure 5-5** through **Figure 5-7**. The near field area (~0.8 mm, or two pulse-widths from the AμT source) was excluded from group velocity averaging. As demonstrated, the average group velocity approached the true shear wave speed (shown by a red dashed line in **Figure 5-8**) as the bandwidth was increased. Notably, broader bandwidths also demonstrated higher group velocity variance, as evidenced by the artifacts seen in the elasticity maps. For f_d significantly lower than 1, the group velocity estimate generally followed the dispersion curve for

the guided mode of the lowest order, approaching zero in the limit of $f_d \to 0$. Note that the high frequency asymptote for the lowest order mode was a Scholte wave having a propagation speed of $C_{Sch} = 0.846C_S$. Both numerical simulations and experimental studies resulted in similar average group velocity estimates (both deviating from the accurate value) when the signal spectra was limited with the same f_d, even though the details of the measurements (e.g., medium thickness, excitation width, and shear wave speed) were different.

In conclusion, when using OCE to image layered tissue, multiple dispersive propagating modes should be expected. Group velocity estimates in bounded material were quantitatively incorrect due to multiple propagating guided modes and produced strong artificial fluctuations in the *xz*-plane while generally underestimating the true stiffness.

Clearly, alternative methods must be used to reconstruct the shear modulus (elasticity) from wave field data in the cornea. For example, high frequency asymptotes of guided waves approaching the Rayleigh and Scholte wave speeds (when $f_d \to \infty$) may provide an accurate measurement of tissue elasticity. For more complex geometries, wave field inversion algorithms similar to those used in MRE[226] must be considered.

In this section, the analytical solution to elastic waves which propagate in an isotropic thin-plate material was in close agreement with the measured phase dispersion. As such, a model-based dispersion calculation can quantify elasticity (i.e. Young's modulus, *E*) in experimental data of isotropic materials by fitting the guided modes in *fk* space to an isotropic thin-plate solution.[15,18,132] As shown by Pelivanov et. al, the difference in moduli quantified from thick and thin phantoms was less than 3%,[18,132] demonstrating accurate quantification of elastic moduli in an isotropic thin-plate material.

5.2 Effect of corneal curvature on elastic wave propagation

In the analytical solutions presented in Chapter 3, the cornea was modeled as a flat material. In reality, the cornea is not flat, but curved. The goal of this section was to address how much the curvature of the cornea will affect guided wave behavior.

It was suggested previously that the dispersion relation of guided waves in a curved plate varies from the flat plate according to the relationship between the wavelength, the radius of curvature, and the layer thickness. Dispersion relations for azimuthal modes in a cylindrical shell and meridian modes in a spherical shell were derived by Krauklis and Molotkov[229], who describe the dispersion behavior in two regimes:

$$(1)\ \frac{\lambda}{R} > \frac{h}{\lambda} \tag{5.2}$$

$$(2)\ \frac{\lambda}{R} < \frac{h}{\lambda}$$

Condition (1), where the radius is small compared to the wavelength and thickness relationship, states that dispersion is strongly influenced by the curvature of the shell, where dispersion is stronger for spherical modes than cylindrical modes. Condition (2) corresponds to mild curvature, and the dispersion is mainly governed by the terms obtained for a flat plate.

As detailed in Chapter 4, the expected elastic wavelength was determined by a combination of the product $C_s T$ and d. For a typical acoustic micro-tapping excitation, we had T = 100 μs and d = 500 μm. Consider one example where c_s = 4 m/s, this gives $c_s T/d$ = 0.8, and a wavelength λ on the order of 0.4 - 0.5 mm. Combining these estimates (and assuming R = 6.5 mm, h = 0.5 mm)

resulted in $\lambda/R \approx 0.08$ and $h/\lambda \approx 1$. This approximation suggested condition (2), where curvature can be neglected.

For additional validation, a finite element model was developed in OnScale to estimate the effect of curvature on the dispersion behavior. The model was similar to that described in Chapter 4 but featured a few distinct differences in both geometry and post-processing.

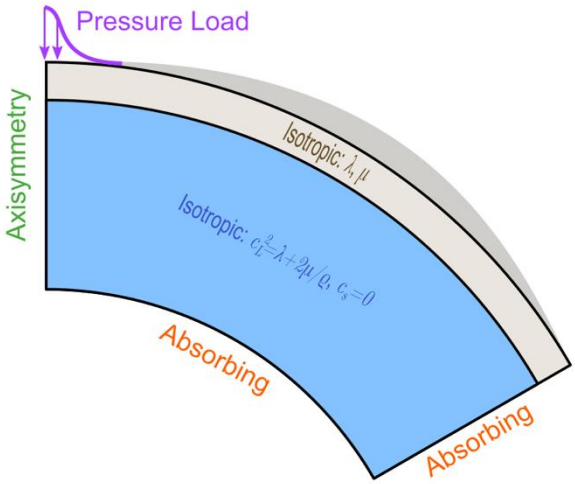

Figure 5-9. Curved geometry used to study guided waves in a spherically curved layer. The full model geometry can be considered a solid of revolution obtained by revolving the domain shown about the axisymmetric boundary. This figure was previously published in Ref[27].

The finite element model consisted of a rectangular domain of thickness h = 0.55 mm bent to an outer radius of curvature of 6.5 mm (**Figure 5-9**). In this example, an axisymmetric (as opposed to plane) strain state is assumed. The simulated layer was assumed to be isotropic with density ρ = 1000 kg/m^3, shear wave speed C_S = 4 m/s, and longitudinal wave speed $c_L = 35C_S$. The simulated tissue layer was atop a water layer, modeled as an elastic solid with shear wave speed C_S = 0 m/s. The water layer had a density and longitudinal wave speed matched to the tissue layer. Outer edges

of the domain were set as absorbing boundaries. The spatio-temporal push profile was defined as in Chapter 4 with a Gaussian profile in space and a super-Gaussian profile in time. The domain was discretized with linear finite elements on a regular conformal grid with at least 40 elements per elastic wavelength.

Solving the model produced a pseudo-point source solution equivalent to a numerical approximation of the Green's function. The wave field solution for a line source, such as the one used in our AμT experiments, was obtained by convolving the Green's function with the source distribution. We numerically evaluated this convolution integral along a linear path on the spherical surface using trapezoid integration. This yielded a wave field along the entire spherical surface.

In general, the wave field was more complex compared to the flat plate plane strain approximation. However, extracting the wave field from the mid-plane normal to the line source (as would be measured using OCE), we find that the flat plate and spherical models produced very similar wave fields (**Figure 5-10a,b**). Analyzing the 2D Fourier spectrum of the spherical model along this mid-plane demonstrated that the isotropic dispersion relation for a flat plate (described in Chapter 3 and detailed in Section 5.2) provided a close fit to the numerical solution (**Figure 5-10c**). This was expected, as the radius of curvature of the cornea is large relative to its thickness.[229,230] Thus, it appears reasonable to neglect corneal curvature in analyzing guided wave behavior in the cornea.

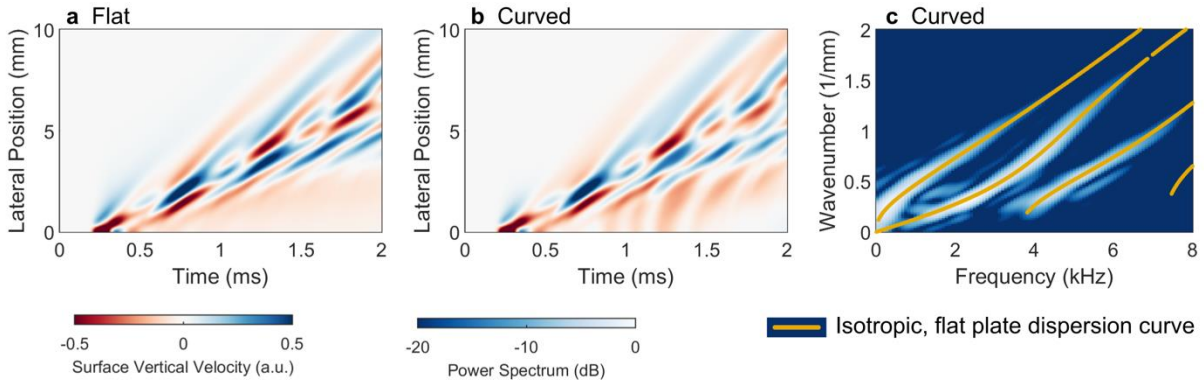

Figure 5-10. Simulated surface vertical velocity wave fields in a (a) flat plate and (b) spherically curved layer were very similar. (c) The 2D Fourier spectrum for the spherically curved layer closely matched the theoretical dispersion curves obtained for a flat plate (yellow markers). This figure was previously published in Ref[27].

5.3 Quantifying elastic moduli in porcine cornea using the NITI model

As shown in Section 5.1, the cornea's bounded geometry produced dispersive guided waves, which must be analyzed in frequency-wavenumber (*fk*) space (or equivalent phase velocity- frequency (*cf*) space) to quantify elasticity. In addition to having a thin-plate structure, the cornea is strongly anisotropic and, at the very least, an additional shear modulus must be introduced to accurately quantify corneal biomechanics (detailed in Chapter 3). Thus, a secular equation describing guided modes determined from partial wave solutions to the elastic wave equation assuming a flat NITI layer bounded by air and water (described in Chapter 3) can be used to quantify elastic moduli in the cornea.

In this section, a bounded nearly incompressible transversely isotropic (NITI) medium model was applied to experimental wavefields in corneal samples to quantitatively measure elastic moduli in porcine cornea. The results were compared with both literature values and directly with mechanical tests.

Numerical simulation of wave behavior in a bounded NITI layer

Although an analytical solution exists for guided waves in a NITI layer, it is not valid near the mechanical wave excitation source (near field) and does not describe how energy is distributed among guided modes in a NITI layer. To explore the expected signal in a NITI material, the finite element model described in Chapter 4 was expanded to explore a NITI layer with dimensions similar to the cornea. The NITI model simulation is described in full in Ref.[27]

In the simulated model, a thin elastic layer of thickness h = 0.55 mm and density ρ = 1000 kg/m^3 was bounded above by air (free surface condition) and below by a layer of water (**Figure 5-11**). The elastic layer was modeled as a NITI material with parameters λ, μ, and G, while the water layer is modeled as an isotropic solid with a density ρ^f = 1000 kg/m^3, shear wave speed $c_s = 0$, and longitudinal wave speed $c_L = \sqrt{(\lambda + 2\mu)/\rho}$.

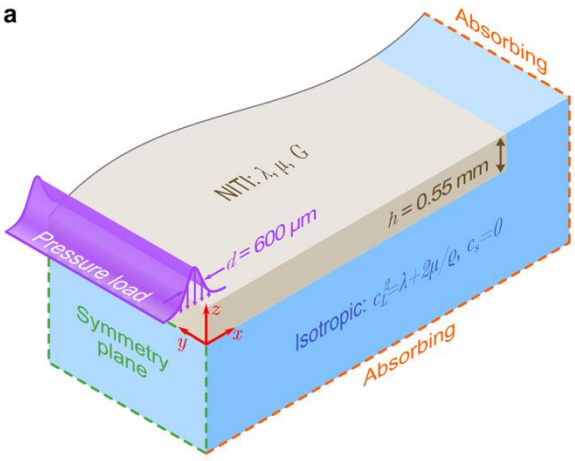

Figure 5-11. Finite element model geometry used to simulate guided wave propagation in a NITI model of the cornea.

The bottom and right boundaries of the domain served as absorbing conditions to minimize reflections as elastic waves traveled beyond the computational domain. To ensure stability at the boundary, the water layer extended along the right edge of the tissue domain and maintained the boundary condition. Symmetry was assumed with respect to the yz-plane.

A temporally- and spatially-varying pressure load $P(x,t)$ was applied to the top boundary with a full-width-at-half-max (FWHM) d = 600 μm. The temporal push profile in this simulation was modeled by a super-Gaussian function with FWHM T = 100 μs. A small offset t_0 is included to avoid impulsive loading at t = 0. The full form of the pressure load was given by

$$P(x,t) = P_0 \exp\left[-4(\ln 2)\left(\frac{x}{d}\right)^2\right] \exp\left[-16(\ln 2)\left(\frac{t-t_0}{T}\right)^4\right], \tag{5.3}$$

where the pressure amplitude P_0 was an arbitrary constant (5 kPa in this study). The incompressibility constraint was enforced by requiring that the ratio $\sqrt{(\lambda+2\mu)/\mu}$ = 35. In the isotropic limit $G = \mu$, this provided a Poisson's ratio of ν = 0.4996.

The NITI layer was simulated with G = 20 kPa, and incremental increases in μ were simulated (μ = 20 kPa, 40 kPa, 100 kPa, 1 MPa) to explore varying degrees of mechanical anisotropy. All simulations used an explicit time-stepping method to generate the full displacement and velocity fields at each space and time point, but only the vertical velocity component was used in the analysis. Velocity data were directional and band-pass filtered using the same processing as OCE experiments to facilitate comparison.

Figure 5-12 shows *xt* plots and corresponding 2D Fourier spectra for increasing μ. Temporal changes in the simulated surface velocity field over a range of lateral positions were recorded from

the simulated data and unit-less surface vibrations used to illustrate the spatio-temporal behavior of the surface wave field in the simulated OCE measurement (**Figure 5-12a** and **Figure 5-12b**). A two-dimensional Fourier transform was applied to analyze guided wave dispersion. In the isotropic limit ($\mu = G$), the *xt* plot (**Figure 5-12c**) showed multiple interacting guided waves, with A_0 and S_0 modes both visible in the spectrum (**Figure 5-12g**), similar to what was described in Section 5.2. As anisotropy increased ($\mu > G$), *xt* plots (**Figure 5-12d-f**) changed dramatically. Interference between A_0 and S_0 modes decreased at $\mu = 2G$ and was nearly absent at $\mu = 5G$. Furthermore, as μ increased, the shape of A_0 and S_0 modes shifted. Energy in the S_0 mode also decreased, disappearing almost entirely for $\mu \geq 5G$ (**Figure 5-12-j**).

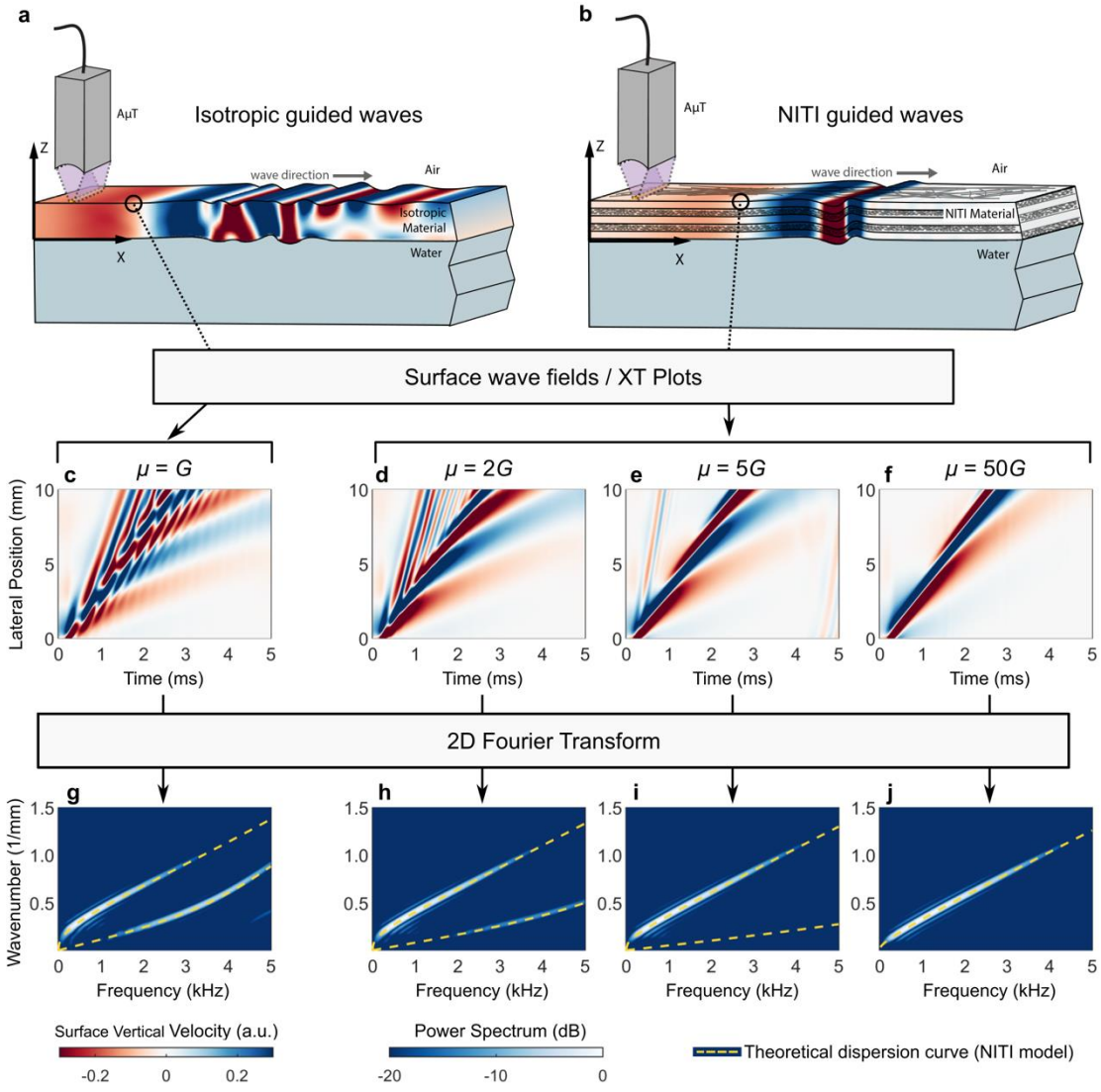

Figure 5-12. **Numerical solutions for guided wave propagation in a bounded NITI medium.** Guided mode wave fields simulated in OnScale for (a) isotropic and (b) NITI layers. Guided wave excitation was simulated with the AμT line source. Guided mode wave fields were extracted from the material surface to yield *xt* plots (c-f) and corresponding 2D Fourier spectra (g-j, presented on a log scale over a 20 dB display dynamic range) for various levels of anisotropy. A 0.55 mm thick NITI layer (G = 20 kPa; μ = 20 kPa, 40 kPa, 100 kPa, 1 MPa) was considered. This figure was published previously in Ref.[27]

The simulation results strongly suggest that if the NITI model can accurately describe wave-behavior in the cornea, then only one mode, A_0, should be visible in cornea experiments. This is

in contrast to an isotropic layer of the same thickness, where multiple high order modes were observed.

Elastic wave propagation in porcine cornea imaged with AμT-driven OCE

In this section, a numerical solution for guided wave propagation in a bounded NITI material with unique in-plane elastic moduli (Young's Modulus, E) and out-of-plane shear modulus (G) was found which best matched AμT-OCE waveforms in ex vivo porcine cornea samples. All studies were carried out in accordance with institutional guidelines and regulations for tissue studies. All experimental protocols followed standard operating procedures established by the University of Washington for the use of animal tissue acquired from an abattoir in research studies.

First, porcine eyes (n = 6) were carefully enucleated from healthy adult animals (3-5 months old, 36-75 kg) by a specialist immediately following euthanasia. All excess tissue was removed to expose the sclera and the remaining whole globe was rinsed with an ocular hydrating solution (balanced saline solution, BSS). Whole globes were placed in a mold containing a damp sterile cotton pad to stabilize samples and mimic in vivo boundary conditions. A 20-gauge needle connected to a bath filled with BSS was inserted through the temporal wall of the sclera to apply a controlled internal hydrostatic pressure (intraocular pressure, IOP). The IOP was controlled by raising and lowering the bath and was calibrated previously using porcine whole globes where an additional 20-gauge needle was inserted into the wall of the sclera and attached to a digital hydrostatic pressure sensor. Following calibration, only a single needle insertion was performed in all AμT-OCE experiments. The reservoir height was adjusted to maintain IOP between 5 and 35 mmHg. Each sample was held at the corresponding pressure for 5 minutes prior to scanning, over which a single drop of BSS was applied to prevent corneal dehydration.

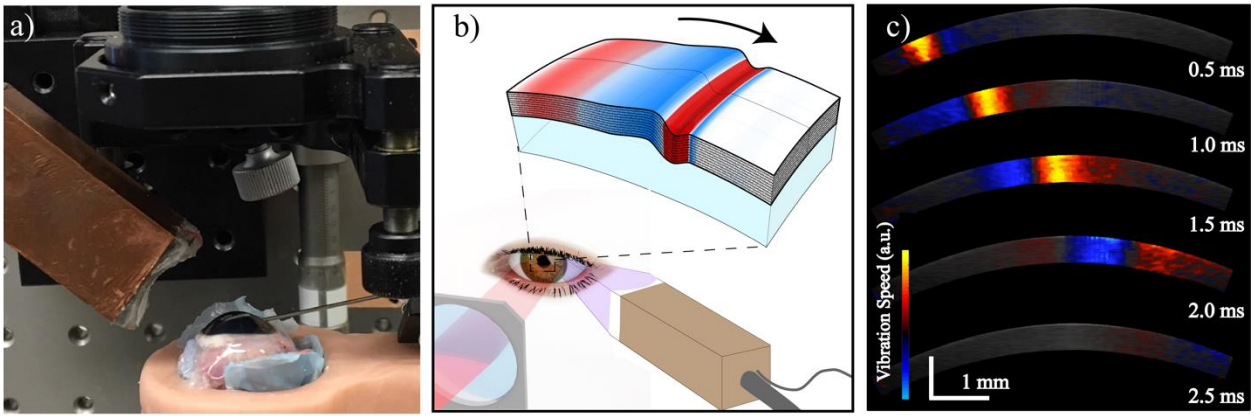

Figure 5-13. AμT-OCE to generate and track elastic waves in porcine cornea. a) AμT-OCE imaging system with cornea inflated to 10mmHg. b) Representative image of elastic wave-pulse propagating within the cornea. c) Snapshots of elastic wave propagation at different time-points detected using phase-sensitive OCT. The cornea was inflated to an IOP of 5mmHg and was approximately 0.7 mm thick.

The AμT-OCE experimental set-up is shown in **Figure 5-13a**. The OCT system operated at a 46.5 kHz effective frame rate and was used to track guided waves in an isotropic polyvinyl alcohol (PVA) cryogel as well as in porcine cornea, providing experimental measurements to compare with theoretical predictions. AμT-OCE was performed on the surface of a thin isotropic PVA phantom as well as freshly excised porcine cornea with IOP incrementally increasing from 5-35 mmHg, generating mechanical waves with bandwidths up to 4 kHz. A stylized schematic of elastic wave propagation in the cornea is shown in **Figure 5-13b**. All data collected had 512 A-scans repeated in the same location (M-scan) at 256 different horizontal locations (B-scan) across the imaging plane (dx = 54.7 μm), forming a complete M-B scan (1024 depth × 256 lateral locations × 512 temporal frames) with an effective imaging range of 1.5 mm × 10 mm (axial × lateral). One full M-B scan took 3.66 s.

The three-dimensional dataset used to reconstruct the propagating wave based on the OCT-measured local particle vibration velocity assumed a refractive index in the cornea and phantom of n = 1.38. Snapshots of displacements associated with elastic wave propagation superimposed on the structural image of the cornea are shown in **Figure 5-13c**. Note that in this experiment, a different light source was employed (broadband super-luminescent diode with a 1310 nm center wavelength and 86 nm spectral BW (Denselight Ltd., Singapore) with similar power but reduced stability. The system was able to reliably detect displacements greater than ≈ 5 nm. Each sample was scanned at room temperature and imaging took no longer than 1 hour per sample. The mean thickness of the cornea samples was measured using OCT to be 0.71 ± 0.11 mm.

The surface signal (*xt* plot) in both an isotropic phantom and cornea was measured by automatic detection of the sample surface using an edge detection algorithm. Phase data in a 183 μm window below the surface were then extracted and averaged, weighted using one half of a Gaussian window (HWHM = 90 μm, weight decreasing with depth).

Quantitative moduli estimates in bounded materials such as the cornea require a method to determine the dispersion relation most closely matching observed guided wave modes. In the OCE experiment, the OCT signal phase difference was used to reconstruct the vertical component of the velocity field. Displacements along the surface of the cornea was extracted to create an *xt* representation of the wave-field (**Figure 5-14a**) before a two-dimensional Fourier Transform was applied to produce a frequency-wavenumber (*fk*) representation (**Figure 5-14b**). This spectrum was then compared to a theoretical dispersion relation to obtain modulus estimates.

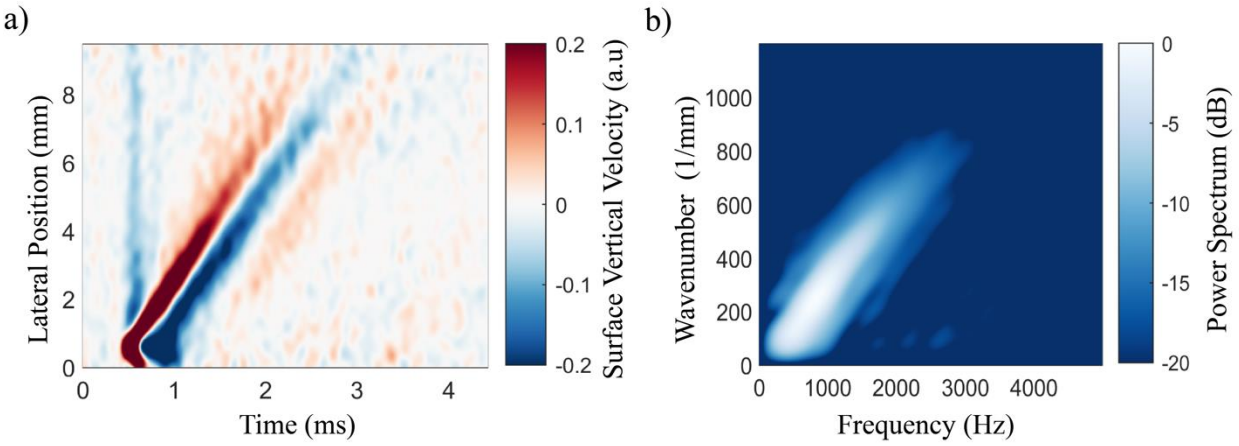

Figure 5-14. AμT-OCE generated and measure displacements along the surface of the cornea inflated to 10 mmHg. a) *xt* representation of the surface wavefield detected in **Figure 5-13**. c) *fk* representation of the waveform following a two-dimensional Fourier Transform.

Mode-tracing routine

A common approach to compare theoretical dispersion with experimental data is to algorithmically identify local peaks of the *fk* spectrum. This would ideally trace the central portions of each mode to produce "measured" dispersion curves which can be compared against theoretical solutions. The measured peaks would be converted to the frequency-phase velocity (*fc*) domain using the relationship between the phase velocity c (m/s), frequency f (Hz), and wavenumber k (m^{-1}) : $c = f/k$.

In **Figure 5-15**, *fk* maps were reproduced from experimental data captured in both a PVA phantom bounded on water and inflated porcine cornea to illustrate that this process is often prone to error. A peak-finding algorithm was applied to the *fk* spectra in **Figure 5-15a** and **Figure 5-15d**, which yielded the narrow dispersion curves shown in **Figure 5-15b** and **Figure 5-15e**. The *fk* values were then converted to phase velocities (**Figure 5-15c** and **Figure 5-15f**). The peak-finding algorithm

required tuning various parameters such as the minimum peak heights, minimum peak distances, and minimum peak prominence. Even with well-chosen parameters, spurious points were detected that were not related to the actual mode (for example, **Figure 5-15e** and **Figure 5-15f**).

Compared to the full *fk* spectra, the peak-finding representation ignored the fact that a number of spurious points contained much less energy than the points covered by the best-fit dispersion curves. The errant points must either be manually cleaned from the data prior to fitting dispersion curves or weighted carefully to ensure that they do not introduce fit errors (note that the 'actual' fits shown in **Figure 5-15** are based on the modified *fk* domain method presented next and do not use spectral peaks).

Another technical challenge with spectral peak finding is that more than one peak may be returned for each frequency. This follows physically from the dispersion relation, where multiple modes can exist at any given frequency. However, spurious peaks make it difficult to algorithmically sort modes from noise.

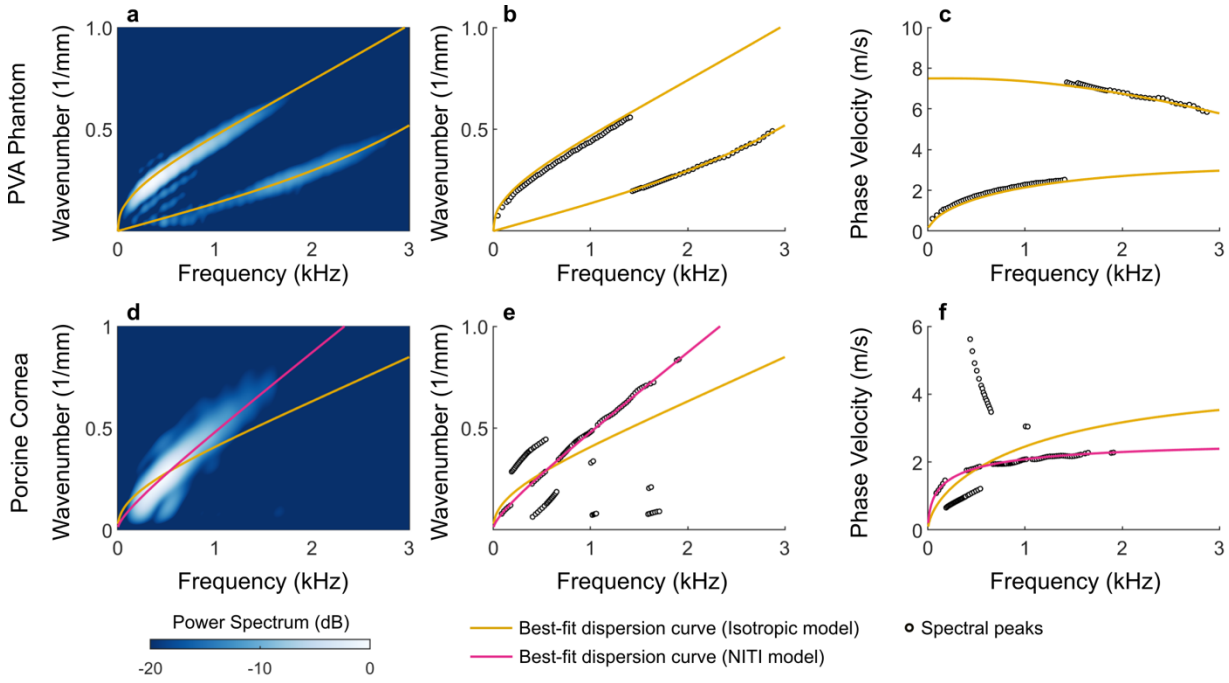

Figure 5-15. Dynamic OCE dispersion analysis based on the peak finding method is shown for PVA phantom (a-c) and porcine cornea (d-f). (a,d) The *fk* spectra are computed from the surface *xt* fields displayed over a 20 dB dynamic range. (b,e) Local peaks of the *fk* spectra were identified algorithmically (white circles). (c,f) peaks identified in the *fk* space were then converted to the frequency-phase velocity representation and compared with theoretical solutions to the dispersion relation (yellow and pink lines). This figure was previously published in Ref[27].

To avoid issues associated with peak tracing, a fitting routine was developed based on the full *fk* spectra. Note that theoretically, the optimal way to determine μ is from the phase velocity spectrum of the S_0 mode, which is largely defined by μ (see Chapter 3). Unfortunately, numerical simulations and OCE measurements show that excitation at the air/cornea interface transfers little energy to the S_0 mode, making it nearly impossible to detect. The absence of an S_0 mode is strong evidence of anisotropy, but also means that the A_0 mode alone must be used to evaluate both G and μ. Because the S_0 mode was not observed in corneal measurements, only the A_0 mode was used in the mode-tracing routine.

The comparison between theoretical dispersion and experimental waveforms was performed in the frequency-wavenumber domain using a simplex optimization method (*fminsearch*, MATLAB, MathWorks, Natick, MA). Fitting the theoretical dispersion relation was performed by maximizing the following objective function:

$$\Phi(\mu, G) = \frac{1}{N_f} \sum_f \sum_k w(f, k; \mu, G) |\hat{v}(f, k)|^2 - \beta \left| \frac{\mu}{\lambda} \right| \tag{5.4}$$

where $\hat{v}$ was the normalized 2D Fourier spectrum of the measured surface velocity data. The function $w(f, k; \mu, G)$ was related to the A_0 mode solution for a NITI ($G < \mu$) or isotropic ($G = \mu$) material. The first term described the energy covered by the dispersion curve, normalized by the number of FFT bins included in the fit (N_f). The second acted as a regularization term that ensured that the ratio μ/λ remained small, thus satisfying the nearly-incompressible assumption.

In Eq. 5.4, β was set to 1, based on an L-curve analysis.[47] The value of λ was updated at each iteration according to $\lambda = \rho c_L^2 - 2\mu$. At a given frequency f and given the current parameter set (μ, G), the dispersion relation solver returned the wavenumber associated with the A_0 mode, k_0. Let Δk be the sampling interval in the wavenumber. The weight function w was then defined as

$$w(f, k; \mu, G) = \begin{cases} e^{-\frac{1}{2}\left(\frac{k - k_0(f, \mu, G)}{1.2\Delta k}\right)^2}, & |k - k_0(f, \mu, G)| \leq 3\Delta k \\ 0, & \text{otherwise} \end{cases} \tag{5.5}$$

where the weights were assigned at each frequency with a peak value at the wavenumber of the theoretical dispersion curve with weights which decayed (with a Gaussian distribution) as the distance from the theoretical curve increased.

Note that this optimization was not posed as a least-squares error problem. Rather, the optimization sought to maximize the spectral energy contained in a small weighted window around the A_0 mode. The dispersion relation estimated the location of the A_0 mode (e.g. the wavenumber of the mode for a given frequency) but cannot predict the spectral energy in a frequency-wavenumber bin (which depends on the method used to excite guided waves). Essentially, the method found the dispersion curve that overlaps with the maximum amount of spectral power. A number of physical parameters were considered fixed, including the corneal density (ρ = 1000 kg/m^3), corneal longitudinal wave speed (C_l = 1540 m/s), and mean corneal thickness (measured from B-mode OCT images). The cornea was assumed bounded from below by water with a density of 1000 kg/m^3 and longitudinal wave speed of 1480 m/s.

To assess how well the NITI solution fit the experimental data, a goodness-of-fit metric was introduced based on an "unconstrained, global optimum" for the objective function, $\Phi_{\max}$. At each frequency f, the following optimization problem was found:

$$k_{\max} = \underset{\tilde{k}}{\operatorname{argmax}} \sum_{k} \tilde{w}\left(f, k; \tilde{k}, \mu, G\right) |\hat{v}(f,k)|^2 \tag{5.6}$$

$$\tilde{w}\left(f, k; \tilde{k}, \mu, G\right) = \begin{cases} e^{-\frac{1}{2}\left(\frac{k-\tilde{k}}{1.2\Delta k}\right)^2}, & \left|k-\tilde{k}\right| \leq 3\Delta k \\ 0, & \text{otherwise} \end{cases} \tag{5.7}$$

$$\Phi_{\max}(\mu, G) = \frac{1}{N_f} \sum_f \sum_k \tilde{w}(f, k; k_{\max}, \mu, G) |\hat{v}(f, k)|^2 \tag{5.8}$$

This was equivalent to finding the Gaussian-weighted window containing the most spectral energy at each frequency independently and summing those contributions to the total mode energy. Since $k_{\max}$ may vary at each frequency independently from the dispersion relation, $k_{\max}$ may not follow the mode shape exactly and may not even be smooth. However, this means that $\Phi_{\max}$ represents an upper bound on the value of Φ calculated during fitting. We therefore compared the following goodness-of-fit measures:

$$g_{\text{iso}} = \frac{\Phi_{\text{iso}}}{\Phi_{\max}} \tag{5.9}$$

$$g_{\text{NITI}} = \frac{\Phi_{\text{NITI}}}{\Phi_{\max}} \tag{5.10}$$

Where Φ_{iso} was determined for the isotropic case by constraining $\Phi(\mu, G)$ so that $\mu = G$ and applying Eq. 5.5. Φ_{NITI} allowed for a solution which covered the maximum energy with unique combinations of μ and G. Thus, g_{NITI} and g_{iso} indicated what portion of the maximum possible mode energy was captured by a given A_0 dispersion curve for NITI and isotropic models, respectively, with values near 1 indicating that the theoretical dispersion curve captures almost all of the mode's energy.

Quantitative measurement of elastic moduli in the cornea

Figure 5-16 compared OCE-measured surface velocity fields obtained for an isotropic PVA phantom and porcine cornea inflated at an IOP of 5 mmHg. Guided waves were apparent in the

isotropic phantom (**Figure 5-16b**). The 2D spectrum of the XT wave field from the PVA phantom on water clearly demonstrated two guided modes. Fitting an isotropic dispersion relation to the PVA-data yielded a shear modulus estimate, μ_{PVA} = 14.4 kPa (**Figure 5-16c**, yellow curves). Porcine cornea display very different behavior, with the wave energy concentrated in a single dispersive mode (**Figure 5-16e**). Two-dimensional spectra highlighted differences between PVA and cornea wave fields (**Figure 5-16c,f**). Clearly, only the A_0 mode was present in porcine cornea (**Figure 5-16f**), as predicted by numerical simulations above.

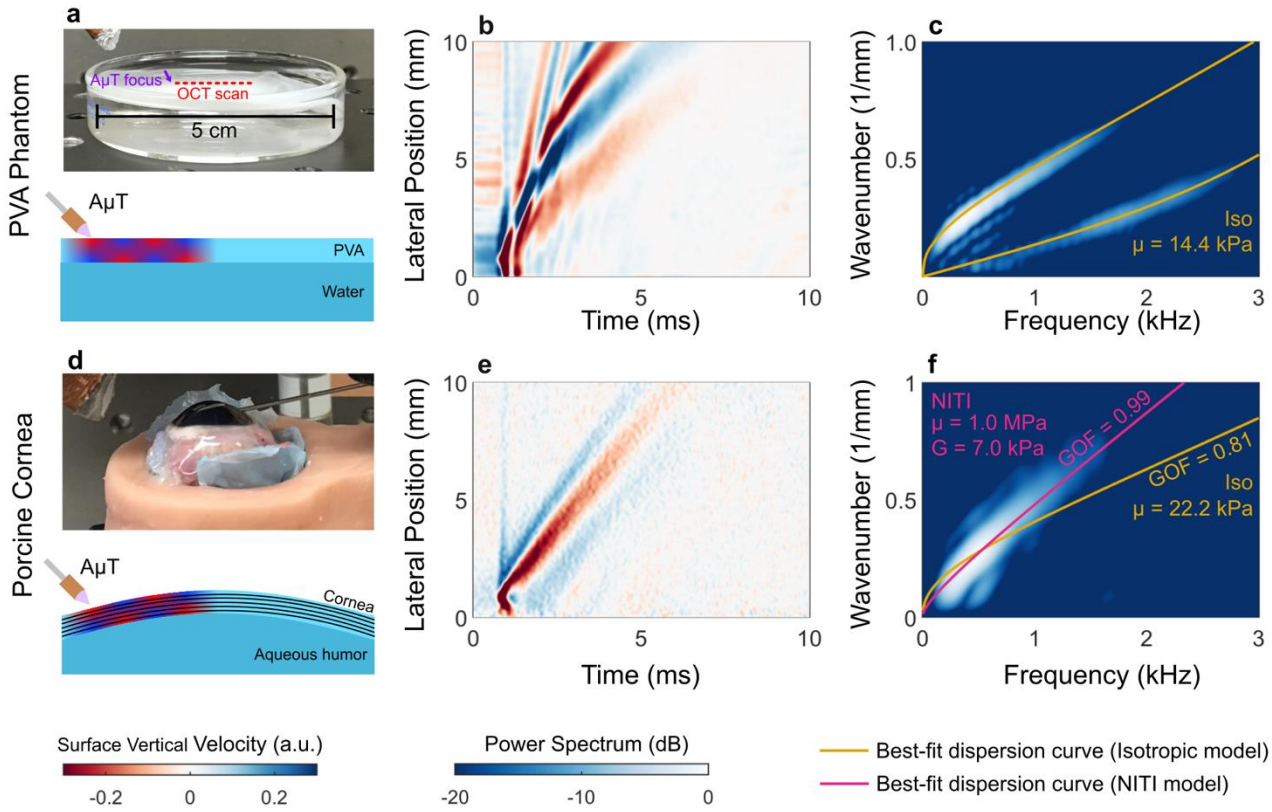

Figure 5-16. **AμT-OCE estimation of elastic moduli in an isotropic phantom and ex vivo porcine cornea.** a) OCE experiment in an isotropic thin PVA phantom bounded above by air and below by water. b) The guided wave field excited by AμT were extracted at the phantom surface (*xt* plot) and a 2D Fourier transform is applied to obtain the frequency-wavenumber spectrum (c, presented on a log scale over a 20 dB display dynamic range). Dispersion

curves for an isotropic material were then fit to the spectrum (c, yellow line). The behavior was markedly different from porcine cornea d) in both the *xt* plot e) and wavenumber-frequency spectrum. This figure was previously published in Ref[27].

In porcine cornea, only the A_0 mode was fit to both isotropic and NITI dispersion relations. Isotropic fits produced an estimate of the isotropic shear modulus whereas NITI fits produced estimates of both G and μ. Using the simplex optimization method described above, dispersion curves were found that closely matched the mode structure in 2D spectra. The isotropic model provided a poor fit (**Figure 5-16f**, yellow curve). In contrast, the NITI model closely followed the A_0 mode (**Figure 5-16f**, pink curve). This trend was consistent for IOP ranging from 5-20 mmHg (**Figure 5-17**).

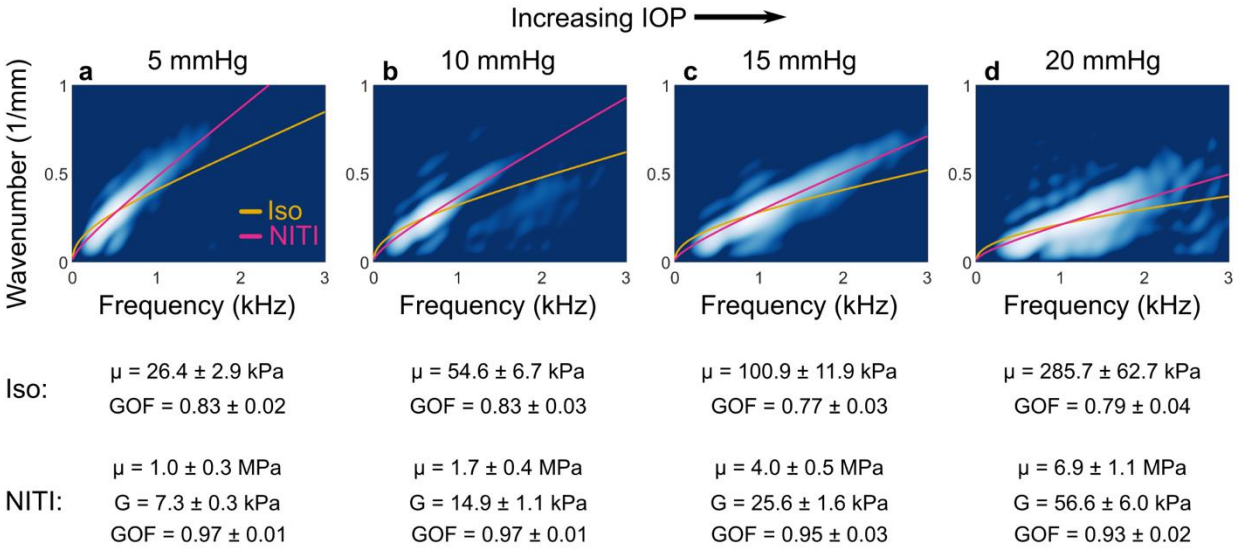

Figure 5-17. **2D Fourier spectra of wave fields generated and tracked with AμT-OCE along the surface of ex vivo porcine cornea at varying intraocular pressure (IOP).** At each IOP, the NITI model (pink line) more closely matched the mode behavior compared to the isotropic model (yellow line). Displayed spectra were on a log scale over a 20-dB dynamic range at 5 mmHg IOP (a), 10 mmHg IOP (b), 15 mmHg IOP (c), and 20 mmHg IOP (d). Parameter estimates and goodness-of-fit (GOF) metrics (mean ± standard deviation, calculated over repeated OCE

measurements for a given cornea/IOP) for each model are shown below their corresponding IOP. This figure was previously published in Ref[27].

Finally, Moduli estimates from the NITI model for all 6 cornea samples inflated between 5mmHg and 20mmHg were summarized in **Figure 5-18**. A multiple order-of-magnitude difference was observed between estimated Young's modulus ($E = 3\mu$) and shear modulus G, consistent with literature values for static tests and OCE measurements. Both moduli increased with IOP over the observed range; however, orders-of-magnitude difference in the moduli remained consistent across all IOP.

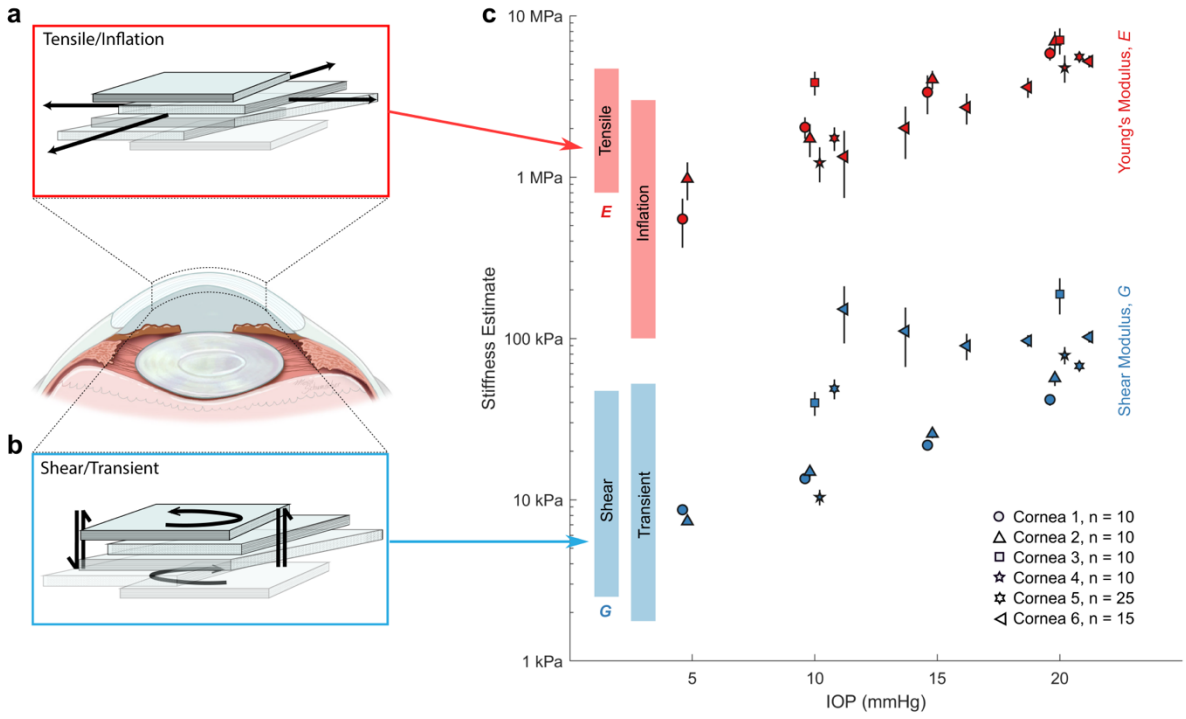

Figure 5-18. NITI elastic moduli estimates (G and μ) obtained from AμT-OCE measurements of porcine cornea. As described in Chapter 3, corneal mechanical response can be divided into (a) tensile/inflation and (b) shear/transient, which can differ by orders of magnitude. (c) Young's modulus (red markers) and shear modulus (blue markers) estimates were obtained from the NITI model for all porcine corneas over a range of IOP. Marker

shape corresponds to six individual porcine corneas. For each cornea sample, 10-25 independent scans were taken at each pressure to minimize system variation. Markers denote the mean modulus estimate from repeated OCE measurements on the same cornea, and error bars denote ± one standard deviation. Modulus estimates corresponded closely to the range of values reported in the literature for static inflation/tensile tests (red bars) and shear/transient measurements (blue bars). This figure was previously published in Ref[27].

In conclusion, corneal microstructure (as well as a number of biomechanical studies) strongly suggest that the cornea is transversely isotropic rather than purely isotropic. In this section, a NITI model was shown to more accurately characterize elastic waves in dynamic OCE studies of the cornea. In particular, elastic waves measured in cornea and isotropic PVA phantoms produced markedly different wave fields and spectra (**Figure 5-16**), demonstrating that an isotropic model was not appropriate for cornea. The NITI model was defined by two shear moduli (G and μ), decoupling tensile/inflation responses from shear responses commonly monitored in torsional tests and dynamic OCE measurements. Results agreed well with literature values, with E > 500 kPa and G in the range of 6 - 200 kPa depending on the IOP (**Figure 5-18**), and generally support the observed orders-of-magnitude difference between the two moduli.

Note that to accurately reconstruct the A0 mode across a wide range of frequencies, the *xt* wave-form was analyzed across all spatial locations. As such, the method provided a single value representative of the mean moduli across the central portion of the cornea. This value was also insensitive to depth-dependent changes in stiffness. Future efforts are required to quantitatively characterize the spatial range over which accurate moduli can be quantified to improve spatial resolution when utilizing the NITI model.

5.4 Direct Comparison of AμT-OCE with destructive mechanical tests

In the previous section, ex vivo porcine cornea was shown to be a highly anisotropic elastic material, with up to three orders of magnitude difference between the in-plane Young's modulus (mainly driving its deformation and shaping) and the out-of-plane shear modulus (mainly responsible for out-of-plane shearing).[27] To directly validate the proposed reconstruction method, a direct comparison between invasive mechanical tests and non-contact AμT-OCE was performed.

In this section, non-contact AμT-OCE measurements of both elastic moduli (*E* and *G*) were taken on inflated porcine corneas of freshly excised whole eye globes (n = 9) at physiologically relevant intraocular pressures and directly compared with mechanical tests performed on the same corneas. Parallel plate rheometry was used to measure the out-of-plane shear modulus; whereas, to quantify the cornea's Young's modulus, tensile measurements were performed with an extensometer.

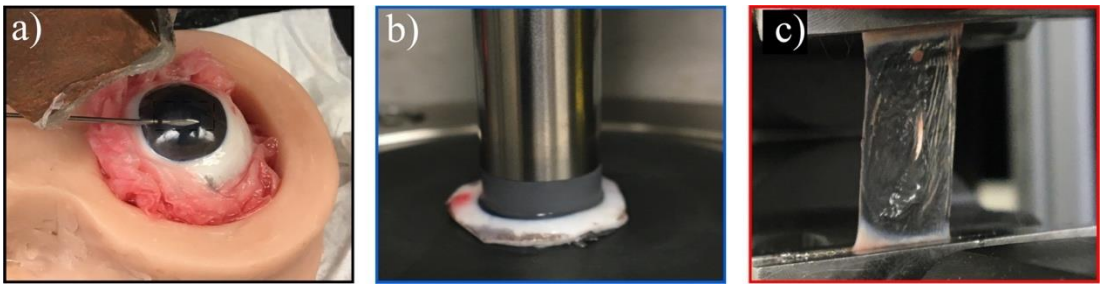

Figure 5-19. Experimental set-up to measure biomechanical properties in the same porcine cornea using a) AμT-OCE, b) parallel-plate Rheometry, and c) strip extensometry.

Corneal moduli measured via AμT-OCE

Porcine eyes were carefully enucleated from healthy adult animals (3-5 months old, 36-75 kg) by a specialist immediately following euthanasia and prepared as described above (**Figure 5-19a**). AμT-OCE measurements were taken at an IOP of 5-20 mmHg. A solution to the dispersion relation

was found by varying the in-plane tensile (μ) and out-of-plane shear (G) moduli as described above.

The resulting moduli (E and G) quantified from the measured wavefields of nine porcine corneas are shown in **Figure 5-20** . On average (statistical mean), in-plane Young's modulus (E) was 12 $\pm$ 5 MPa at 5mmHg and 20 $\pm$ 9 MPa at 20 mmHg. The mean transverse shear modulus (G) was 31 $\pm$ 11 kPa at 5mmHg and 61 $\pm$ 29 kPa at 20 mmHg. The inflation pressure placed the cornea in a state of pre-stress, which varied in magnitude according to the IOP. This result demonstrates that both in-plane tensile and out-of-plane shear moduli increase with increasing IOP, consistent with the non-linear material properties of the cornea. The mean ($\pm$ standard deviation) of corneal thickness (assuming refractive index of 1.389[231]) was 0.76 mm ($\pm$ 0.10 mm) at 5mmHg and thinned on average by 50 µm as the pressure was increased. In all samples the endothelium appeared intact.

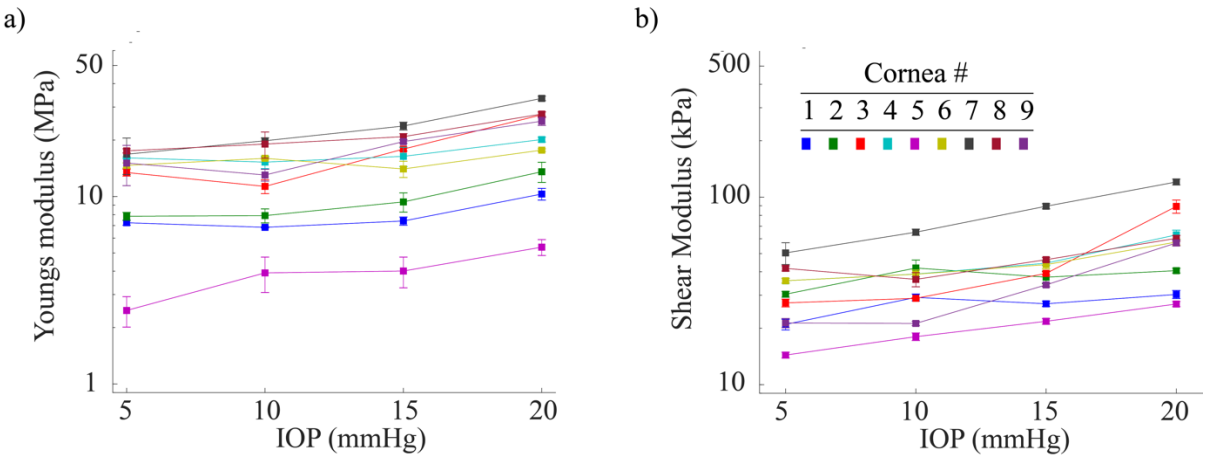

Figure 5-20 Elastic moduli quantified using the NITI model applied to AµT-OCE surface vibrations. (a) Young's modulus ($E = 3\mu$) and (b) transverse shear modulus (G) in porcine whole globe samples quantified using the NITI model applied to AµT-OCE measurements. The line connects moduli of each sample scanned at an IOP of

5, 10, 15, and 20 mmHg to show individual variations in pressure-dependent moduli. Each color corresponds with the respective sample. Error bars correspond with standard error of the mean from each set of repeat scans.

Note that while there was relatively high variability in the absolute values of the moduli at each IOP, each cornea demonstrated a systematic increase with increasing pressure. To visualize this, relative changes in modulus as a function of IOP compared to the baseline value at 5 mmHg are displayed in **Figure 5-21.** As seen, Young's and Shear modulus changed by 98 $\pm$ 29% and 67 $\pm$ 15%, respectively, of the original value as IOP increased from 5 mmHg to 20 mmHg.

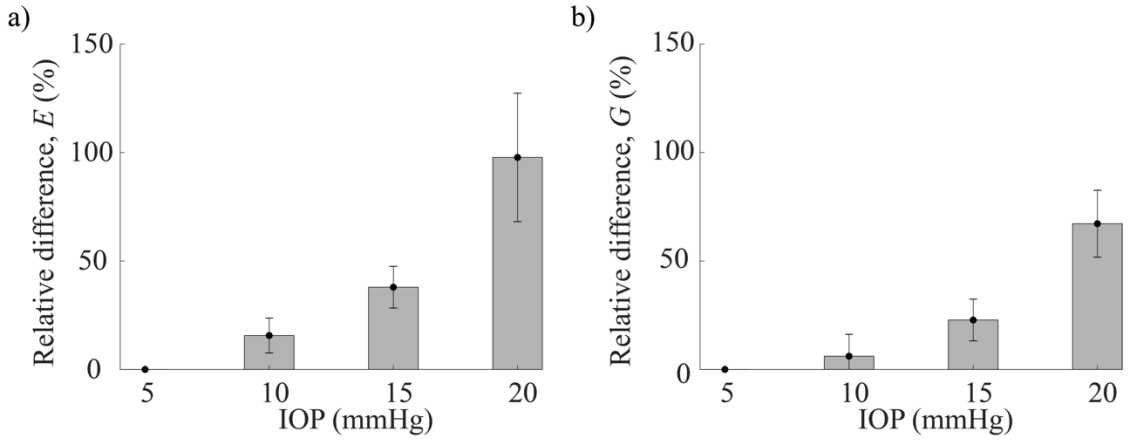

Figure 5-21. Relative change in modulus as a function of IOP compared to the baseline value of a) E and b) G at 5mmHg. Although there were differences in the absolute values of both E and G at different pressure, both moduli appear to increase systematically with increasing IOP.

Corneal moduli measured via Rheometry

Following AμT-OCE, samples were removed from the imaging system and an incision was made approximately 2 mm from the limbus around the sclera to remove the cornea from the globe. The lens, iris, and ciliary body were carefully removed using tweezers. Corneal buttons were rinsed

with BSS and then placed in a damped cloth and immediately transported for rheometry at room temperature.

To measure the out-of-plane shear modulus, a parallel compression plate matching the approximate size of the cornea (12 mm diameter) clamped the anterior and posterior surfaces of the corneal buttons using a pneumatic rheometer (Anton Paar MCR 301 Physica) (**Figure 5-19b**). A relative twisting force (sinusoidal oscillatory shear stress) about an axis perpendicular to the surface was applied under a 5 N compressive pre-load and the resulting shear strain was measured to calculate the out-of-plane shear moduli, G, assuming a homogenous cylindrical material. In general, collagen-rich tissue demonstrate an approximately linear behavior below 1%,[232] thus 0.1% peak strain was applied to the tissue during the frequency sweep (0.1-16 Hz). Rheometry measurements were repeated twice and took approximately 1 hour per sample.

Frequency-dependent storage (G') and loss (G'') moduli, corresponding to the real and imaginary parts of G^*, were determined in the corresponding n = 9 porcine corneas, with statistical mean and standard deviations for each sample plotted in **Figure 5-22.** The shear storage and loss modulus (G'/G'') measured in corresponding porcine corneal-buttons subject to frequency-swept rotational shearing ranged from 82/13 $\pm$ 12/4 kPa to 133/29 $\pm$ 16/3 kPa for 0.16 - 16 Hz at 0.1% peak strain amplitude. Corneal buttons were tested using the smallest compressional pre-load that could be applied without tissue slippage and incorporated a portion of the scleral rim. The unconfined compression caused a portion of the tissue to splay beyond the custom-printed disk during testing. A single frequency sweep took approximately 30 minutes, over which each sample progressively thinned about 27 μm. The mean value of the thickness was 0.80 mm ($\pm$ 0.09 mm), averaged over the duration of each frequency sweep.

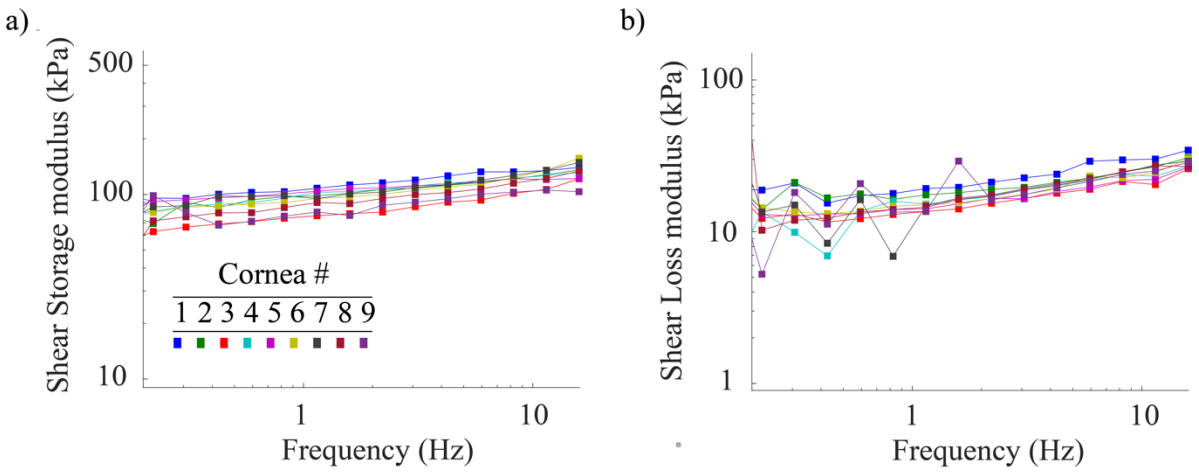

Figure 5-22 Shear modulus under frequency-swept torsional loading at .1% strain. Shear a) Storage (G') and b) Loss (G'') moduli measured during frequency-swept loading at 0.1% strain. The line connects moduli of each independent porcine cornea sample to show biological variations in frequency-dependent moduli.

Because transversely isotropic media require different loading geometries to measure both elastic moduli (E and G), excess sclera was left on the samples during rheometry to ensure sufficient surface area for clamping in tensile testing. Because a portion of the sclera was left on each corneal button during rheometry, the apparent stiffness due to excess tissue was tested in an independent set of three (3) porcine samples. Frequency-swept rheometry was performed on corneal buttons with a 2mm scleral boundary within 1 hour of porcine euthanasia. Immediately following two repeat frequency sweeps, the scleral ring was removed and only the cornea was exposed to a rotating shearing force for an additional two tests. The mean value of the two repeat tests (both with and without sclera) was used for each sample. The results are shown in **Figure 5-23** and suggest that the excess tissue induced a 1.6-2.2-fold (depending on the frequency) increase in the shear modulus compared to rheometry of the cornea alone.

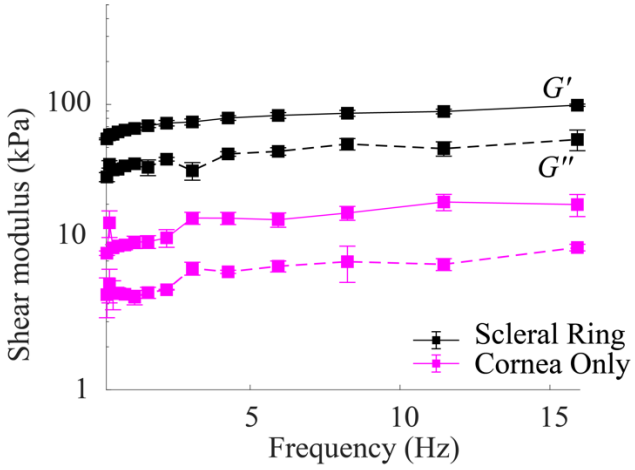

Figure 5-23. Effect of sclera in rheometry of corneal buttons. Mean and standard deviation (n = 3) of the storage (solid line) and loss (dotted line) modulus measured in samples with (black) and without (pink) the scleral ring attached. The excess sclera tissue increased the apparent modulus of the cornea.

Corneal moduli measured via strip extension

Following Rheometry, each cornea button was sectioned into strips approximately 6 mm wide along the nasal-temporal direction, leaving approximately 2 mm of sclera on each end. The strips were transported for tensile testing in the same damp cloth and tested at room temperature within 1 hour of rheometry. Each cornea strip was pneumatically clamped (2752-005 BioPuls submersible pneumatic grips, 250 N max load) at the corneal-scleral boundary (**Figure 5-19c**). A 50 mN axial pre-load was applied and the samples were stretched at 2 mm/min (Instron model 5543) up to 10% strain. For each sample, two load-unload cycles were performed to precondition the tissue, followed by 3 rounds of force-elongation followed by relaxation. The Young's Modulus was determined assuming a beam-like structure and defined by the tangential slope of the stress-strain curve. In this configuration, the tissue was subject to uniaxial tension along the *xx*-direction and the corresponding stress-strain relation in a simplified NITI material where $E = E_T$. All data was acquired within 6 hours of animal euthanasia.

The engineering stress (σ) in the corneal strips was calculated using the cross-sectional area of the central cornea,

$$\sigma = \frac{F}{wh}, \tag{5.9}$$

where w was the width, h the thickness (measured using a digital micrometer), and F the force during elongation. The engineering strain (ε) was defined as

$$\varepsilon = \frac{\Delta l}{l_0} \tag{5.10}$$

where l_0 was the initial length of the clamped cornea under a 50 mN preload and Δl the elongation values recorded by the extensometer. In this configuration, the tissue was subject to uniaxial tension along the nasal-temporal (xx) direction and the corresponding stress-strain relation described by:

$$E = \frac{\sigma_{xx}}{\varepsilon_{xx}}, \tag{5.11}$$

where the strain-dependent Young's modulus was defined as the instantaneous slope of the stress-strain curve.

The stress-strain curve was determined for the corresponding n = 9 porcine cornea (stripped in the temporal-nasal direction) by fitting a second order exponential to each set of raw data. (**Figure 5-24a**). An additional second order exponential was fit to the data which included all (n = 9) stress-strain values and was considered the representative curve for the porcine samples. The strain-

dependent Young's modulus was defined by the instantaneous slope (Tangential Modulus) of the stress-strain curves (**Figure 5-24b**).

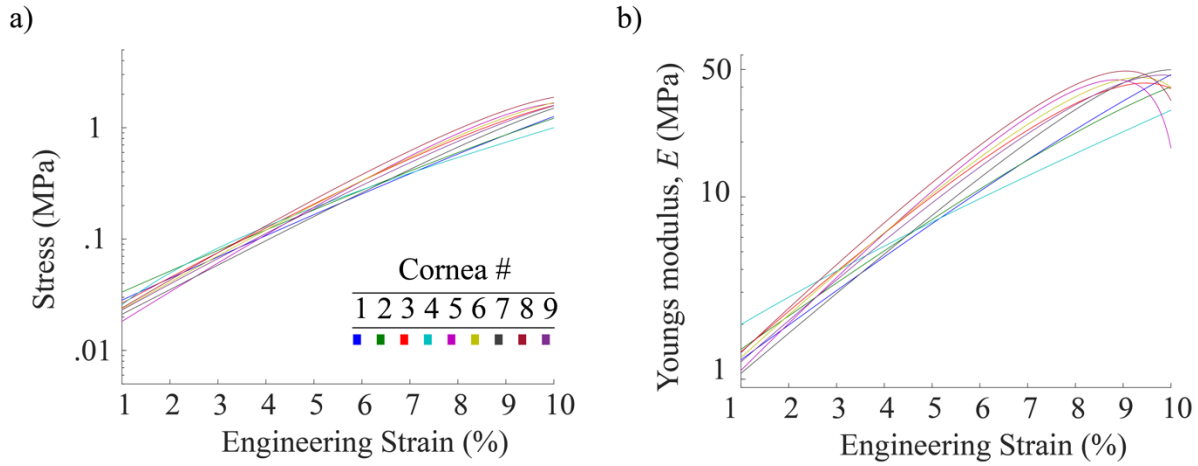

Figure 5-24. Moduli quantified via strip extension testing in porcine cornea. a) Stress, Strain and b) Tangential modulus for 9 independent corneal strips. The displayed curve was the result of a second-degree exponential fit applied to the raw experimental data.

The tangential (Young's) modulus, *E*, measured in tensile testing over a range of engineering strain from 1-10% was 1.39 - 40 MPa. The orientation of the strip lay in the xy-plane and the direction of the loading stress was uniaxial along the nasal-temporal axis. The thickness of each sample was measured prior to extension testing in each sample. Corneal strips were on average 0.77 mm ($\pm$ 0.09 mm) thick and 5.9 mm ($\pm$ 0.4 mm) wide, resulting in a cross-sectional area of 4.6 mm^2.

Compensation for Deformation State in Tension

It is well-documented that the cornea exhibits nonlinear moduli with strain.[10] As the strain was changed in each cornea via IOP or via strip extension, equivalent strain state estimates are required for cross-methodology comparison. In a living organism, the cornea is highly pressurized by IOP, which produces an internal stress and preserves optimal corneal shape. However, when the cornea

was extracted from the whole globe, its shape changed, and internal stress was released. Therefore, it is important to account for the cornea's deformation state and geometry change to compare the modulus estimated by different methodologies.

To compare OCE and tensile testing results, two factors producing different deformation states must be considered: (i) the cornea preserved its curvature in OCE measurements, while the curvature was flattened in tensile testing; (ii) the cornea was under biaxial tension due to the intraocular pressure during whole-globe OCE measurements, while in tensile testing the cornea strip was loaded with a uniaxial stress.

Two models are presented below to address these factors. The first considers the geometry transition (curved to straight) as a reverse beam bending and derives an offset strain required to compensate modulus values estimated in tensile testing. The second uses the internal pressure as a common parameter to bridge uniaxial and biaxial loadings.

Reverse Bending Model

When the cornea strip was excised from the trephinate, one can observe that its curved structure was generally retained. As the tensile force started to stretch the strip, it flattened to a straight piece under 50 mN preload. This geometry transition introduces a complex pre-strain field in the corneal strip as shown in **Figure 5-25a**, yielding part of the strip under compression and the rest under tension. This pre-strain may affect the accuracy of the tensile measurement since the part of the tissue under compression provides limited resistance against the force from the test device, leading to underestimation of the Young's modulus. As stretching continues during the test, we assume that underestimation stops when all compressional pre-strain was compensated. In this condition,

the whole strip was assumed to be under tension. This occurs when the strain applied by the extension device was equal to the maximal compressional pre-strain ε_{max}. Here, we calculate ε_{max} by reversing the beam bending model (as shown in **Figure 5-25b**), similar to the reciprocal to corneal stretching.

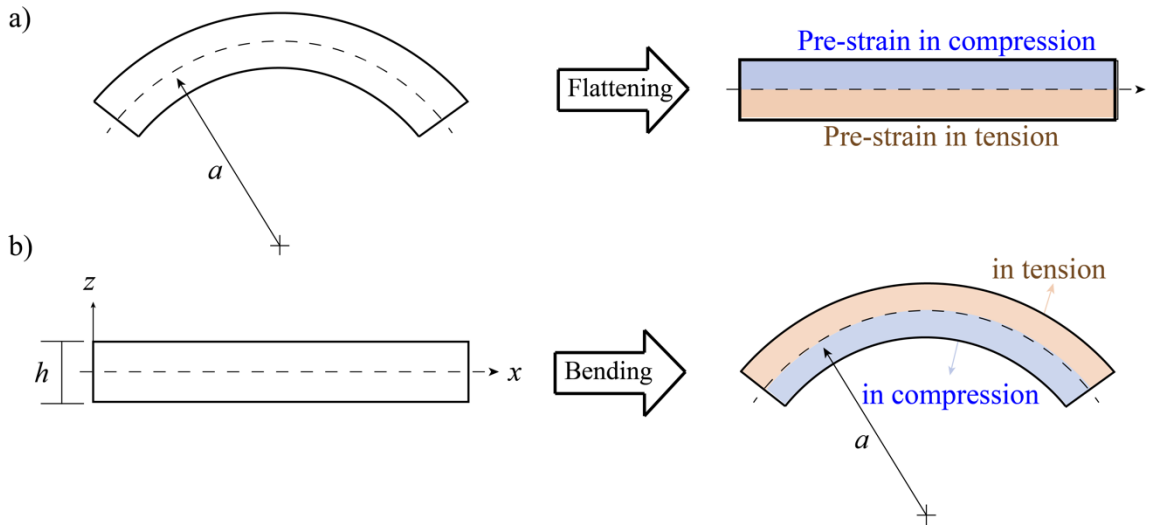

Figure 5-25. Reverse bending model for strain compensation in tensile testing. a) Schematic showing the pre-strain distribution in the cornea strip when flattened at the beginning of tensile testing. b) Beam bending model for calculating the maximal compressional pre-strain in the cornea strip.

In **Figure 5-25b**, the *x*-direction was along the longitudinal axis of the beam and located at the beam center, and the *z*-direction was along the thickness. The axial strain in the beam at different depths $\varepsilon_x(z)$ was defined as

$$\varepsilon_x(z) = \frac{z}{a}, \tag{5.12}$$

where *a* is the radius of curvature. The maximum compressional strain occured at the bottom surface where $z = -\frac{h}{2}$, yielding

$$\varepsilon_{max} = -\frac{h}{2a}, \tag{5.13}$$

where *h* was the thickness of the cornea.

When the corneal strip was stretched by ε_{max} during extension testing, the whole strip was assumed to be under tension. At this point the tensile measurement had passed the underestimation region. Thus, the deformation state at this point is approximately equivalent to the "rest state" in the AμT-OCE measurement, where there was no external pressure loading applied on the cornea (IOP = 0 mmHg). In other words, the rest state was approximated by the point where the geometric transformation from a spherical segment to a flat strip (or vise versa) is complete. Take the first cornea sample as an example, as shown in **Figure 5-26a**, the solid circle at $\varepsilon = \varepsilon_{max} = 3.52\%$ and E_{tensile} = 4.17 MPa marks the modulus estimated by tensile testing at the rest state.

Internal Pressure

AμT-OCE measurements were performed at different IOP (5, 10, 15, and 20 mmHg), which led to different deformation states from the rest condition (0 mmHg); therefore, this state change must be addressed when comparing Young's moduli estimated by both methodologies. Ideally, the comparison between methods should be performed at the same internal pressures; in AμT-OCE it is defined by IOP, and in tensile measurements the pressure is determined by the deformation level.

The internal pressure (p_i) was defined as one-third of the sum of all principal stresses:

$$p_i = \frac{1}{3}(\sigma_{11} + \sigma_{22} + \sigma_{33}). \tag{5.14}$$

For the cornea in the AμT-OCE measurement, Timoshenko's thin shell theory approximation was applied,[164] which yielded the principal stresses

$$\sigma_{11} = \sigma_r = 0$$

$$\sigma_{22} = \sigma_\phi = \frac{P}{2}\frac{a}{h}, \tag{5.15}$$

$$\sigma_{33} = \sigma_\theta = \frac{P}{2}\frac{a}{h}$$

where P was the IOP, a was cornea's radius of curvature, and h its thickness. The first principal stress σ_r was 0 because AμT-OCE was performed on the traction-free boundary condition at the outer surface. Comparing to σ_ϕ and σ_θ, σ_r was much less significant because of the factor a/h in σ_ϕ and σ_θ, as a was generally much larger than h for the cornea. Therefore, we simplify the internal pressure corresponding to different IOP in AμT-OCE measurements as

$$p_{i,OCE} = \frac{1}{3}\left(\frac{P}{2}\frac{a}{h} + \frac{P}{2}\frac{a}{h}\right) = \frac{P}{3}\left(\frac{a}{h}\right). \tag{5.16}$$

Note that $p_{i,OCE}$ is geometry-dependent; that is, each cornea has a different value. For tensile testing, the internal pressure was given by

$$p_{i,tensile} = \frac{1}{3}\sigma_{11} \tag{5.17}$$

where σ_{11} was the uniaxial tensile stress.

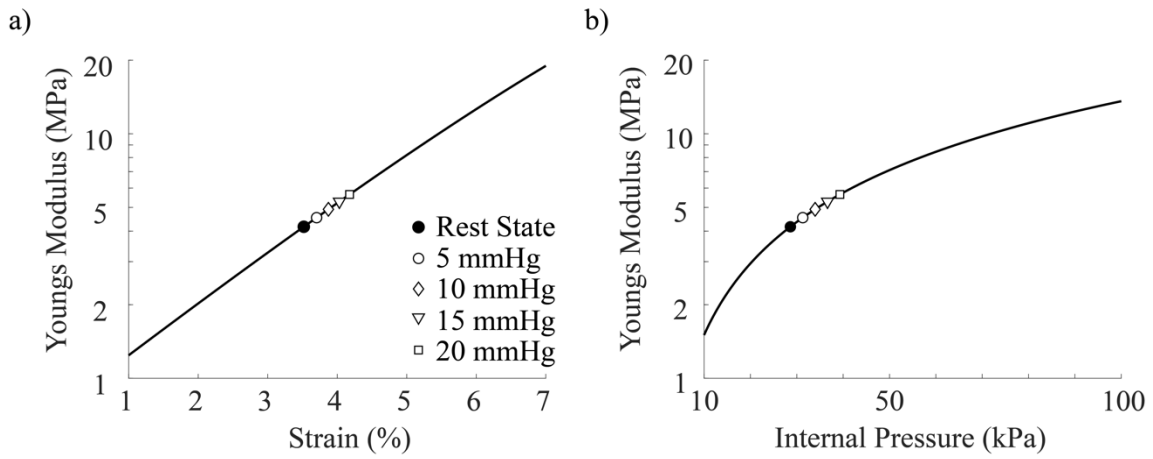

Figure 5-26. **Tensile testing and strain compensation estimates in a single cornea example.** (a) Experimentally measured dependence of Young's modulus on strain in tensile test. The 'rest state' was determined by ε_{max} calculated from the bending model. (b) Tensile modulus versus internal pressure. The internal pressure calculated with Timoshenko's thin shell theory corresponding to different IOP's was added to that of the rest state, yielding the effective IOP values for modulus estimates in tensile measurements.

Figure 5-26b shows the same tensile testing results as that in **Figure 5-26a**, but with estimated internal pressure on the abscissa. The internal pressure was calculated by Equation 5.16. The rest state marked by the solid circle is determined by projecting the same Young's modulus E_{tensile} = 4.2 MPa from **Figure 5-26a**, which has the corresponding internal pressure of 28.6 kPa. From the rest state, internal pressure changes equivalent to those induced by IOP variations (5, 10, 15, and 20 mmHg) are added, leading to the internal pressures 31.9 kPa, 35.3 kPa, 38.4 kPa, and 41.7 kPa, and modulus estimations 4.6 MPa, 5.1 MPa, 5.5 MPa, and 6.0 MPa, respectively. Finally, the hollowed markers are projected back to **Figure 5-26a** by referencing the same moduli from **Figure 5-26b** to determine the uniaxial strains corresponding to the deformation states at the four IOP's. The process was performed for each cornea sample and the mean values reported in **Table 5.1**.

Inflation pressure (OCE)	OCE Young's modulus, E_{OCE} Mean ± SD (MPa)	Measured corresponding strain in tensile test	Calculated corresponding strain in tensile test Mean ± (SD)	Tensile Young's modulus, $E_{tensile}$ Mean ± SD (MPa)	% Error $\frac{\lvert E_{tensile} - E_{OCE} \rvert}{E_{OCE}}$
5 mmHg	12.35 (±5.23)	**5.72%**	**3.95 (±.16)%**	5.76 (±0.88)	53%
10 mmHg	12.57 (±5.53)	**5.78%**	**4.11 (±.14)%**	6.19 (±0.90)	51%
15 mmHg	14.82 (±6.65)	**6.22%**	**4.25 (±.13)%**	6.61 (±0.93)	55%
20 mmHg	20.05 (±9.16)	**7.10%**	**5.76 (±.88)%**	7.03 (±0.96)	65%

Table 5-1. Estimated equivalent strain-dependent moduli

Comparison Between AμT-OCE and destructive mechanical tests

A direct comparison between the mean and standard deviation of the moduli measured via OCE, shear rheometry, and strip extensometry is shown in **Figure 5-27**. Most notably, both the tensile elastic modulus (E) and shear modulus (G) differed by approximately an order of magnitude, consistent with previous results.[27]

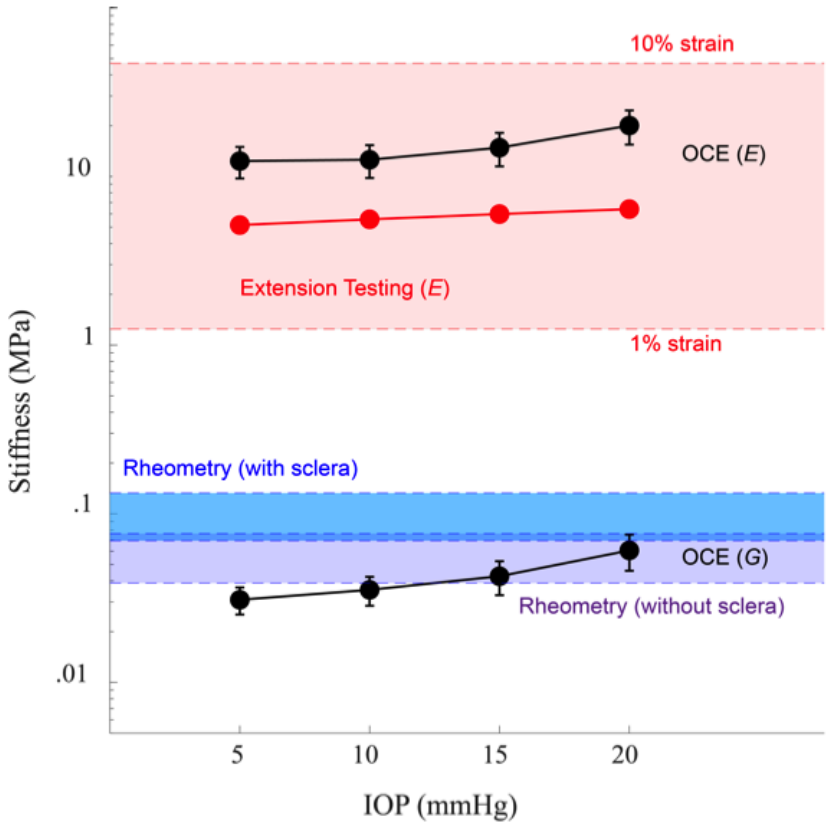

Figure 5-27. Comparison between moduli measured via different loading methods. Moduli (E, assuming tensile isotropy and G) estimates from AμT-OCE (black), parallel-plate rheometry (blue) and strip extension (red). The red box denotes the range of elastic moduli measured at strains of 1%-10% and the red dots denote the equivalent strain estimate at intraocular pressures representative of in vivo conditions. The darker blue box is the storage shear modulus (G') measured via rheometry with the scleral ring attached and the light blue box corresponds to values appropriately scaled to account for the apparent stiffness from inclusion of the scleral ring.

To compare OCE tests of inflated cornea with rheometry and extensometry, boundary conditions and equivalent strain effects were estimated. In rheometry, the scleral rim was retained to provide a surface to grip during tensile loading. To account for the effect of excess sclera, three separate cornea buttons were tested with the scleral ring and then immediately after removing the rim. The results (**Figure 5-23**) indicate that the excess tissue induced an approximately 2-fold increase in the shear modulus compared to rheometry of the cornea alone. Consequently, a scaling factor was applied to rheometry results. Both the apparent (with sclera) and adjusted (without sclera) shear modulus range is displayed for comparison. Of note, the NITI model assumes a negligible viscosity. Thus, we compared the G value from OCE with the storage modulus (G') in rheometry.

As the cornea inflated via IOP was under a state of tension, an estimated strain offset was introduced to account for tensile strain introduced due to IOP as well as compressive forces within the anterior portion of the cornea introduced when flattening a curved structure during elongation. The strain offset first referenced the state where strips were exposed to only tension, then, the internal pressure (within the tissue) was used to predict equivalent strain values within the samples loaded via inflation and strip extension. At an IOP of 5-20 mmHg, the equivalent engineering tensile strain was estimated to be between 3.97% $\pm$ 0.17% and 4.44% $\pm$ 0.14 %. The Young's Modulus estimate from OCE corresponded to an equivalent strain between 5.72% and 7.10% in

strip extensometry. The average Young's modulus measured via strip extension was 1.24-46.8 MPa for 1%-10% strain, respectively. In general, measurements taken via different methods tracked each other but were not highly correlated for the same samples.

Based on this analysis, AμT-OCE provides a functionally equivalent measure of the elastic moduli probed in both shear rheometry (G) and tensile extension (E) but in a single, non-contact acquisition that can be performed non-invasively using intact whole-globe eyes.

5. 5 Conclusions

In this chapter, a method was developed to quantify anisotropic biomechanical properties in the cornea. First, the finite thickness of the cornea was shown to complicate elastic wave propagation, suggesting that mode-tracing across a broadband signal can be used to quantify biomechanical properties using experimental AμT-OCE wave-fields. Next, the finite curvature of the cornea was determined to introduce a negligible effect on wave behavior relative to the flat plate model. Finally, a mode-tracing routine was introduced based on the NITI model that demonstrated accurate reconstruction of anisotropic elastic moduli in porcine cornea inflated at 5-20 mmHg.

One-to-one comparisons were presented between corneal moduli measured with AμT-OCE and with destructive mechanical tests (parallel plate rheometry and tensile extensometry) on the same corneal samples. Nine fresh porcine corneas were measured to limit individual variations in the cornea's mechanical properties.

While the study demonstrated markedly different corneal stiffness under shear versus tensile loading, there were a number of differences between AμT-OCE and destructive mechanical testing methods that made direct comparisons difficult. Indeed, effects such as corneal curvature,

mechanical nonlinearity, boundary conditions in mechanical loading, loading direction, engineering strain, hydration, and pre-conditioning, can influence moduli estimates in mechanical tests. However, estimates provided by AμT-OCE should be more accurate representations of in vivo biomechanics because the non-contact and non-invasive measurement was performed under well-controlled IOP (loading representative of tissue in its normal state).

In extension loading, corneal shape is different from inflation. The cornea preserved its curvature in OCE measurements, while the curvature was flattened in tensile testing. Axial extension, which causes the cornea to flatten, induces compressional forces and produces different strain distributions for cornea under inflation versus extension. Additionally, the cornea was under biaxial tension in OCE and uniaxial tension in extension.

The force was also assumed equally distributed across the cornea considering a true cuboid shape (uniform thickness and cross-section). However, the central cornea thickness is thinner than the periphery and exhibits varied radius along the center line compared to the edge of the strip, complicating interpretation of results.[233] Corneal samples were not uniform thickness, suggesting that the axial strain at the center of the sample may differ from that at the perimeter during loading. This effect that was not adjusted for. Nevertheless, measurements of Young's modulus acquired from both AμT-OCE and extension testing were consistent with those in porcine cornea strips subject to tensile loading (0.3-29 MPa[55,71,72,74,80,234,235]).

The order-of-magnitude difference in the modulus measured under shear loading was higher than previously reported values of G (0.34-9 kPa[77,236,237]). Because corneal-buttons were loaded in unconfined compression, tissue at the corneal-scleral junction splayed outward beyond the probe. Rheometry was performed on an independent set of corneas both with and without the scleral rim

attached. The excess tissue was shown to produce an approximately two-fold increase in the measured modulus (**Figure 5-23**). This suggests that the tissue splayed beyond the probe provides additional resistance to shearing, over estimating the corneal modulus. Additionally, the corneal-scleral boundary may contribute to residual stress within the cornea compared to the corneal button alone.[238] The shear-modulus of the cornea has also been shown to increase with higher compressional pre-load,[77] suggesting that internal forces due to both parallel-plate rheometry and increased residual stress may increase the measured transverse shear modulus. The hypothesis that residual stress within whole-globe samples may contribute to a higher transverse shear modulus likely warrants further study and may describe the discrepancy between the values measured via OCE and those reported in the literature.

Internal pressures estimated in the cornea due to flattening during tonometry do not appear to induce large structural changes within the tissue at low IOP, suggesting that flattening alone had a small effect on the shear modulus.[239] In this case, flattening due to the parallel-plate arrangement was assumed to have a small effect on the measured modulus. It should be noted however that during rheometry, tissue at the center undergoes a smaller shear strain than that at the outer edge. The center of the tissue may also experience different compressive strain due to corneal thinning, an affect that was ignored in this study. Additionally, the frequency range used by OCE differed from that of rheometry. While OCE functionally measures higher frequency vibrations (0.3 kHz – 4 kHz range), the relatively lower frequency (multiple Hz-range) probed in rheometry suggest that frequency-dependent differences likely exist between the moduli measured by the two methods.

Direct mechanical tests performed in this study with different loading methods confirm corneal mechanical anisotropy. At least an order of magnitude difference in elastic moduli determined

from tensile tests compared with rheometry on the same corneas (**Figure 5-27**) cannot be described with the same modulus. The simplest assumption accounting for such difference is corneal transverse isotropy. Indeed, the elastic properties of collagen fibers have been shown to differ from those of corneal connective tissue,[46–48] suggesting that the preferred collagen orientation results in asymmetric elastic properties. The NITI model used to reconstruct mechanical moduli from AμT-OCE produces estimates of both elastic moduli, μ and G, which are in a good agreement with moduli obtained with mechanical tests. However, as noted in Chapter 3, the NITI model is simplified by assuming corneal tensile isotropy, i.e. isotropic Young's modulus (E), though tensile and shear deformations are driven by different moduli.

Young's and shear moduli were assumed non-varying in depth. Quantifying depth-dependent moduli in the cornea will likely require complex models of high frequency content or additional loading techniques. Viscous effects were also not included in this study. Recent models incorporating viscosity suggest a second order effect in the frequency range of mechanical waves considered in this study. To account for viscosity, higher frequency components of propagating elastic waves[240] should be considered. This represents another direction to improve quantitation of corneal visco-elasticity.

Finally, this chapter demonstrates that robust and accurate measurements of corneal elastic moduli can be achieved using non-contact AμT-OCE. While in-plane anisotropy (within the *xy*-plane) has been reported in some studies, the degree of anisotropy remains low at low IOP.[16,74,150,161,162] This suggests that for normal IOPs (below 25 mmHg in porcine cornea), corneal microstructure can be approximated with the NITI model (i.e., symmetric for any direction in the *xy*-plane).

Chapter 6. Future studies and limitations

Significant effort has been directed toward personalized biomechanical models suitable for screening, surgical planning, and treatment monitoring. Because corneal mechanical properties determine its shape, it is important that accurate moduli are input to biomechanical models to predict static deformation and shape.[241] While such static models remain largely in the development stage, advanced models assuming a transverse isotropic tissue structure appear most robust.[242,243] Such personalized models can potentially be used to study disease progression and may play a role in treatment based on simulated interventions.

To-date, reliable measurements of ocular mechanical properties have only been possible on ex vivo samples and have not directly impacted the clinic.[69] While critical to our understanding of corneal mechanics, the destructive nature of most traditional techniques render these approaches impractical for clinical translation.

Anterior segment OCT can map corneal shape, and tonometry can estimate IOP. In this work, a non-contact method has been shown to provide quantitative information on corneal elasticity. This thesis demonstrated that non-contact AμT-OCE can simultaneously assess both corneal moduli, E and G, under physiologic loading conditions.[27] AμT-OCE measured in-plane Young's modulus, E, was shown to be in good correspondence with literature results obtained by destructive ex vivo inflation and tensile tests; whereas the out-of-plane shear modulus G, being a few orders of magnitude smaller than E, reasonably matched literature data on the shear modulus obtained by rheometry. Additionally, one-to-one comparisons of corneal moduli measured with AμT-OCE with two mechanical tests (parallel plate rheometry and tensile extensometry) performed on the same corneal samples was presented to validate corneal shear anisotropy.

Although AμT-OCE measurements appear reliable in ex vivo porcine corneas under well-controlled physiologic conditions and equivalent IOP, we have not yet performed in vivo experiments in human subjects. In this final chapter, preliminary results are included on human corneal buttons treated with a mock CXL procedure to demonstrate that personalized models can potentially be used to study disease progression and may play a role in CXL treatment in progressive keratoconus.

Additionally, as a preliminary test of AμT-OCE monitoring elastic moduli in living subjects, in vivo scans were performed on a group of six (6) anesthetized New Zealand White rabbits. The preliminary results are included to demonstrate the potential for in vivo monitoring of human corneal stiffness.

Finally, although significant effort has been directed toward personalized biomechanical models suitable for screening, surgical planning, and treatment monitoring, there remain a number of unanswered questions regarding the accuracy of the assumed mechanical model. Due to the structural complexity and mechanical nonlinearity (i.e., IOP dependent moduli) of the cornea, a personalized mechanical model to optimize procedure outcomes is not a straightforward task. Additional studies using higher resolution reconstruction methods, and those that include in-plane anisotropy, viscosity, and detailed information on the relationship between stiffness and IOP, are required to fully characterize the biomechanical response of the cornea. As such, a clinically useful model must include in vivo measurements of topography, IOP, and maps of corneal mechanical moduli. Such a model can potentially be used to study disease progression and even play a role in treatment based on simulated intervention.[241]

6.1 Demonstration of AμT-OCE in human cornea during UV cross-linking

In degenerative corneal diseases such as keratoconus, it is well recognized that local changes in mechanical properties result in a bulging conical shape associated with vision loss.[49,51] Keratoconus is commonly treated with a collagen cross-linking (CXL) procedure that has been reported to delay ectasia progression by increasing stiffness with UV light induced crosslinks in stromal collagen of cornea soaked in riboflavin. While cross-linking procedures have shown some success in halting disease progression by greatly reducing the number of required keratoplasties,[244] both long-term and immediate outcomes remain unpredictable for each patient.

In this study, the NITI model was applied to elastic wavefields generated and detected using AμT-OCE to measure the anisotropic biomechanical moduli (E and G) in human donor corneas subject to riboflavin/UVA collagen crosslinking (CXL) at physiologically relevant controlled pressures. Mechanical moduli were measured during a mock CXL procedure to demonstrate the potential for on-line monitoring of corneal stiffness intraoperatively.

Six (6) human corneal-scleral rings stored in Optisol (Chiron Ophthalmics, Irvine, California, USA) were secured through the University of Utah Lion's Eye Bank (Murray, UT). Exclusion parameters included tissue over 2 weeks from enucleation, progressive corneal disease, corneal damage, and over 21 years of age. Such broad exclusion criteria were necessary to obtain research samples and resulted in a wide range of both ages and times between enucleation and analysis.

Each cornea was stored in Optisol, removed from solution upon arrival, and fit to a modified artificial anterior chamber (AAC). The internal pressure (IOP) was controlled using a tube connected to the AAC from a raised bath filled with balanced saline solution (BSS) to apply a controlled internal hydrostatic pressure (IOP).

Each sample was inflated to 15 mmHg and the epithelium was removed using a blunt blade. Each cornea then underwent collagen cross-linking following the Dresden protocol. A 0.146% riboflavin (RF) solution in 20% dextran was prepared using 500,000 weight dextran (Alfa Aesar, Ward Hill, Massachusetts, USA) in isotonic saline. The epithelium was then debrided using a blunt knife and a 50 μL drop of riboflavin solution was placed on the cornea every 2 minutes for 30 minutes. The cornea was exposed to 3 $\frac{\mathrm{mW}}{\mathrm{cm}^2}$ of 370 nm UV light (**Figure 6-1a**) for 30 minutes, and drops were applied every five minutes during this period. Excess solution was removed from the surface of the tissue and the cornea was scanned every 90 seconds during the 30 minute UV exposure.

Elastic moduli of human cornea exposed to CXL were quantified before, during, and after the procedure using wavefields generated and measured with the phase-sensitive OCT system described in Chapter 3. An example of the experimental set-up can be seen in **Figure 6-1a**.

The pulse/M-scan sequence was captured at 256 spatial locations across the imaging plane to create a 3-D cube (*z, x, t*) of corneal structure (**Figure 6-1b,e**) as well as reconstruct propagating guided waves in the cornea at different times. A complete M-B–scan consisted of 1024 depth × 256 lateral locations × 512 temporal frames (captured at 46,000 FPS) with an effective imaging range of 1.5 mm × 6 mm x 3.66 seconds (axial × lateral x temporal).

The surface displacement signal (**Figure 6-1c,f**) was subject to a two-dimensional Fourier transform to the frequency-wavenumber (*fk*) domain (**Figure 6-1d,g**). A solution to the equation for guided wave propagation in a NITI material[27] was found that most closely matched the experimental *fk* spectrum using a minimization routine. The iterative routine converged on a best-fit solution to the dispersion relation by varying both the in-plane (E) and out-of-plane (G) shear

moduli using the corneal thickness (h) as a constraint. In all samples, dispersive energy was contained within the A_0 mode[15,27] and fit to a theoretical solution using the NITI model.[27]

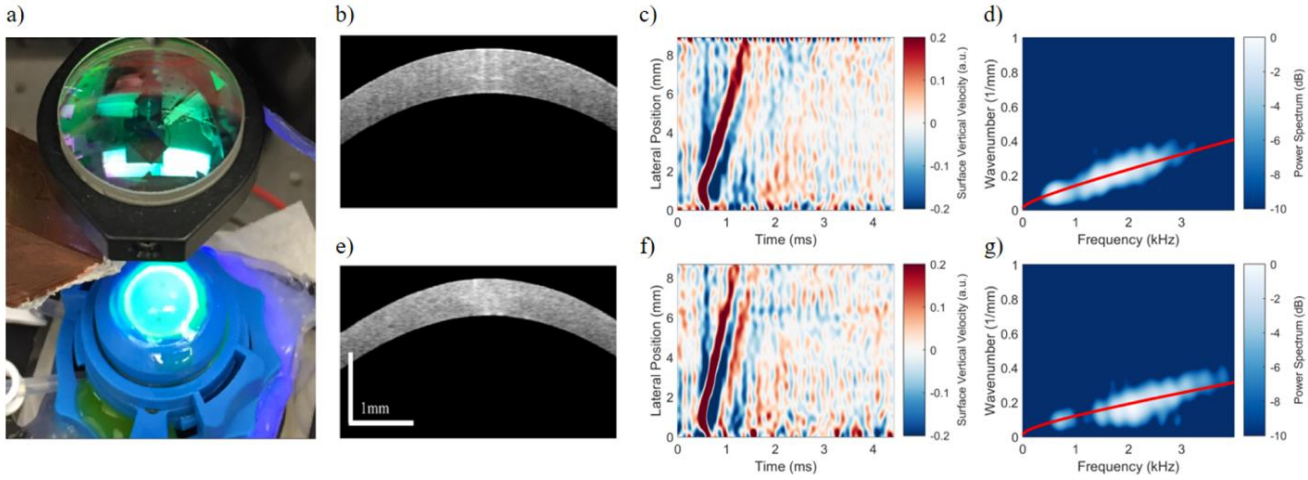

Figure 6-1. AμT-OCE before and after mock CXL procedure. a) Experimental set-up of ex vivo human cornea inflated on an artificial anterior chamber with the UV light on. The (b) central cornea cross-section image used to determine corneal thickness, (c) surface waveform signal, and (d) best-fit A_0 mode overlaid on measured energy before cross-linking. The (b) cross-section image, (c) surface waveform, and (d) best-fit A_0 mode overlaid on measured energy is displayed for the same cornea following the CXL procedure.

To demonstrate the ability of AμT-OCE to directly quantify corneal biomechanics intraoperatively, E, G, and thickness (h) were measured at discrete time points during the procedure (**Figure 6-2a**). The cornea progressively thinned during crosslinking (**Figure 6-2b**).

While both moduli increased with exposure, Young's modulus changed on average by about 2 times (from 14 MPa to 32 MPa) whereas the shear modulus G changed by almost an order of magnitude (from 130 kPa to 1.0 MPa) following CXL (**Figure 6-2c**). The measured thickness before and after cross-linking was 560 μm $\pm$ 70 μm and 340 μm $\pm$ 20μm, respectively.

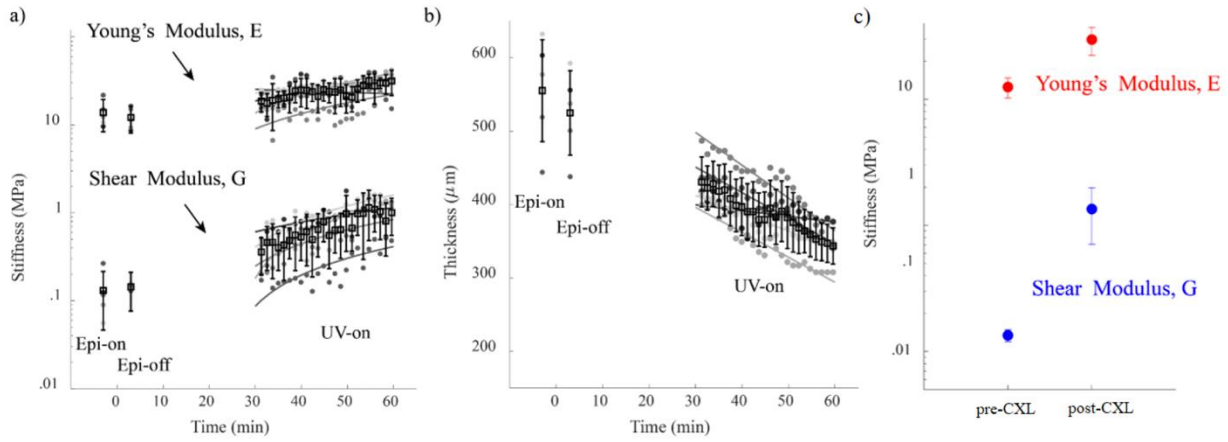

Figure 6-2. **AμT-OCE during mock-CXL procedure.** a) Elastic moduli estimates and b) corneal thickness over time for n = 5 cornea samples. The darkness of each dot and shaded best fit line is matched according to each sample. The squares represent the mean and the lines the standard error of the mean. (d) Average corneal *E* (red) and *G* (blue) before and after crosslinking. The error bars correspond with the standard error of the mean.

One important note is that the mean goodness-of-fit prior to CXL was ~0.9 and following CXL was approximately 0.8. The reduced goodness-of-fit suggests that a non-negligible error existed in the moduli values following CXL. Based on trends in the *fk* -space relative to the best fit results, the absolute values quantified via OCE appear to over-estimate both E and G. A detailed analysis is required to quantify the expected error due to poor fitting quality.

The CXL procedure is intended to better crosslink corneal lamellae, which it appears to do based on the elastic moduli measured in **Figure 6-2**. However, deformational properties under inflation are defined mostly by the Young's modulus, which does not appear to change as much as the shear modulus (largely responsible for inter-lamellar slippage). Evaluating both moduli is very important for quantification of CXL efficiency since E mainly defines the corneal deformation whereas preliminary results suggest that its degree of cross-linkage appears to be mainly defined

by G. Further study of biomechanical and biochemical stability of the cornea following CXL is required to understand both short- and long-term effects on potential refractive changes.

While the moduli quantified with AμT-OCE are generally consistent with both literature and mechanical testing, there remain a number of limitations in using this technique to understand how CXL affects the micro-structure responsible for biomechanical stability. One such limitation is that depth-dependent moduli cannot be measured. It has been shown that CXL is most dramatic in the anterior portion of the cornea,[245] which contains a complex fiber arrangement that likely determines most of its flexural (tensile) strength. It has also been shown that the relative increase in G is much greater in the anterior portion of the cornea.[83] Thus, if there was a significant increase in anterior cross-linking, much of the stroma may still be susceptible to inter-lamellar slippage. Exploring the importance of depth-resolved changes, as well as the interplay between moduli and intraocular pressure, remain directions of future interest.

While additional work is required to understand model-dependent errors following CXL so that AμT-OCE may be generalized for use by different systems, the preliminary results suggest that AμT-OCE may be very useful for future clinical trials. Combined elasticity and thickness changes during CXL will have significant impact on both the overall corneal stiffness and potential refractive changes. Although this experiment required a slight modification of the FDA-approved Dresden protocol (i.e. removal of RF/dextran from the surface of the tissue prior to each scan), the results indicate that AμT-OCE may be useful to monitor treatment progression. Additionally, future studies to assess anisotropy in diseased cornea may further improve our understanding of pathologies and potentially inform treatment. Hopefully, the preliminary results presented here will trigger extended work on developing personalized treatment plans with the potential to use

corneal topography and quantitative maps of elastic moduli prior to and during treatment to determine if predicted moduli changes have occurred.

6.2 In vivo AμT-OCE in a rabbit animal model

Although AμT-OCE measurements were performed in ex vivo human corneas under well-controlled physiological conditions and equivalent IOP, in vivo experiments have not been performed in human subjects. Indeed, non-contact clinical assessment of corneal biomechanics may enable in vivo clinical trials that can provide further insight into the role of biomechanics in cornea function.

As a preliminary test of AμT-OCE to measure elastic moduli in vivo, an in vivo study was performed on a group of six (6) healthy, anesthetized New Zealand White rabbits. All measurements followed the UW IACUC protocol (PROTO202000139). The goal of this study was to test AμT-OCE quantification of elastic moduli in a living rabbit cornea to compare in vivo AμT-OCE (**Figure 6-3b),** ex vivo AμT-OCE (**Figure 6-3e**), and ex vivo mechanical tests (**Figure 6-3f,g**). Corneal topography (**Figure 6-3c**) was also recorded, and IOP (**Figure 6-3d**) tracked with a Tonopen (Reichert, Inc., Buffalo, NY).

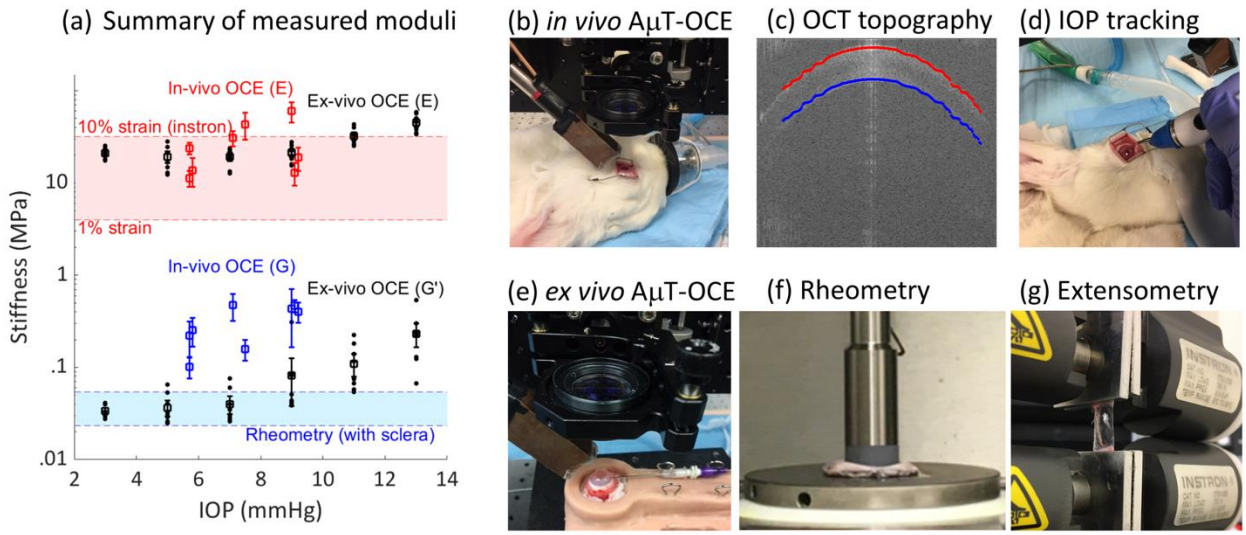

Figure 6-3 Experimental design and summary of corneal stiffness measured on in vivo and ex vivo rabbit tissue. a) Summary of elasticity measurements (both moduli E and G) in 6 animals (both eyes) with in vivo b) AμT-OCE, e) ex-vivo AμT-OCE, f) ex vivo parallel plate rheometry, and g) ex vivo extensometry. c) Corneal shape and thickness were also recorded and d) IOP was tracked with a Tonopen (Reichert, Inc., Buffalo, NY).

The summary presented in **Figure 6-3a** demonstrates that AμT-OCE appears capable of measuring the elastic moduli in vivo using a Rabbit animal model. The in vivo results are slightly higher than the ex vivo values plotted for the corresponding IOP measured with the hand-held Tonopen (Reichert, Inc., Buffalo, NY). Although the Tonopen is the gold standard method to measure IOP, simple tonometry methods are often error prone and can produce estimates of IOP with huge ranges of uncertainty.[246] Once such approach to improve in vivo estimates of IOP would be to physically measure the pressure in the anesthetized rabbit eye using a needle insertion. Future work is needed to directly compare in vivo measurements of elastic modulus with ex vivo values where the IOP is directly controlled.

Of note, in vivo and ex vivo measurements both correlated with the mechanical test results. Thus, the AμT-OCE approach appears capable of clinical studies following additional in vivo validation.

6.3 NITI model error

For practical biomechanical models, it is important that accurate moduli are used to predict static deformation and shape. To date, experiments have demonstrated that corneal deformation can be estimated using at least two shear moduli, contrary to current single-modulus models. Both elastic moduli, E and G have been shown to fluctuate as a function of IOP in ex vivo porcine cornea, ex vivo human cornea, and in vivo rabbit cornea. Quantitative values obtained in porcine corneas were consistent with both tensile and shear tests. However, there are a number of limitations and potential sources of error within the NITI model that must be addressed to fully characterize corneal deformation.

To account for tensile anisotropy, an additional parameter δ is required. **Figure 3- 8** shows the level of the Young's modulus anisotropy allowed by corneal symmetry, with the in-plane Young's modulus possibly varying between 2μ (for the strongest tensile anisotropy) and 3μ (for tensile isotropy). Determining the parameter δ is not easy and is the subject of future studies. Note that the relationship between the tangential and longitudinal Young's Moduli (E_T, and E_L, respectively), as well as the three Poisson's ratios ($\nu_{TT}, \nu_{LT}, \nu_{TL}$) presented in Eq. 3.55 suggest that measurements of local deformations under compression or tension (in addition to elastic wave imaging) may provide an avenue to accurately quantify δ in any sample.

In much of this work, $\delta = 0$ was used, and therefore Young's modulus $E = 3\mu$. The comparison between tensile and AμT-OCE measurements (Section 5.4) for E suggests that its OCE-based value may be overestimated. If the relationship $E = 2\mu$ (corresponding to $\delta = -2\mu$) had been used, both methods would have demonstrated very close agreement. Thus, the in-plane Young's modulus of cornea is likely closer to its lower limit rather than to its highest possible value as

presented here. However, additional studies should be performed to confirm this observation. Nevertheless, it is emphasized that using a simplified NITI material model rather than a simple isotropic model is an important step in quantifying anisotropic properties in the cornea because it separates the effects of μ from G, which are much greater than any possible variations of E introduced by $\delta \neq 0$.

Additionally, OCE-determined E has greater variance relative to that for G. Upon analysis of the dispersion relationship for the A_0 mode of a guided wave in a NITI material with high anisotropy ($\mu \gg G$), the A_0 mode is increasingly insensitive to μ Thus, measurement noise inside the elastic wave bandwidth will have a greater effect on quantitative estimates of μ, with uncertainty increasing with greater degrees of anisotropy. While the measured multiple order-of-magnitude difference between G and μ appears accurate, determining the true value of μ requires increasingly higher signal-to-noise ratio as anisotropy increases. Increasing the OCE measurement SNR should produce more precise estimates of μ. Ideally, new methods designed to excite and accurately measure the A_0 and S_0 modes together could provide more accurate and sensitive estimates of μ.

Note that while in-plane anisotropy (within the *xy*-plane) has been reported in some studies, the degree of anisotropy remains low at low IOP.[16,74,150,161,162] This suggests that for normal IOPs (below 25 mmHg in porcine cornea), corneal microstructure can be approximated with the NITI model (i.e., symmetric for any direction in the *xy*-plane). This effect was experimentally visualized as the IOP was increased in a porcine whole-globe sample. **Figure 6-4** shows two-dimensional spectra and best-fit dispersion curves for a porcine eye measured over a larger IOP range (5, 15, 25, and 35 mmHg). For lower IOP (5 and 15 mmHg), Fourier spectral peaks followed the general A_0 mode shape, and the NITI model closely fit the data (**Figure 6-4a,b**). However, at higher IOP

(25 and 35 mmHg), mode shape changed dramatically and the NITI fit no longer described it well (**Figure 6-4c,d**). As demonstrated in **Figure 6-4,** the model appears to fail at pressures above 30 mmHg.

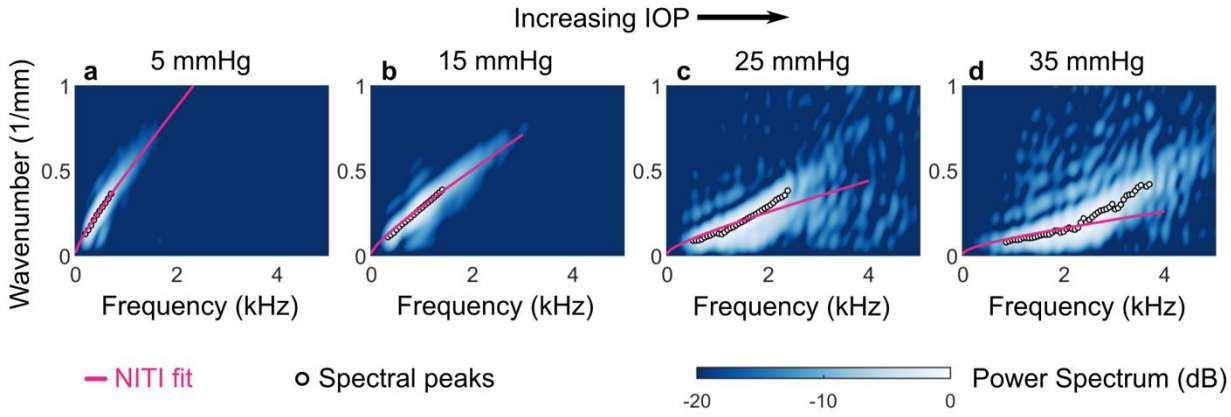

Figure 6-4. **Nonlinear and anisotropic behavior becomes increasingly complex at high intraocular pressure (IOP).** 2D Fourier spectra of wave fields generated and tracked with AμT-OCE along the surface of porcine cornea at varying intraocular pressure (IOP) show increasingly complex behavior as IOP increases. Spectra are displayed on a log scale over a 20 dB display dynamic range with spectral peaks (circles) and best-fit dispersion curves for NITI model (pink) at 5 mmHg IOP (a), 15 mmHg IOP (b), 25 mmHg IOP (c), and 35 mmHg IOP (d). This figure was previously published in Ref[27].

While the NITI model appears to describe wavefields in the cornea well at low IOP, at higher IOP the model clearly needs some modifications. Notably, multiple modes can exist as the structure of the cornea changes at elevated IOP. While mode-separating techniques may improve quantification, there are multiple factors that remain unexplored in the NITI model. For example, nonlinearity, complex anisotropy, and pre-stress can affect elastic wave propagation in the cornea and appear to be IOP dependent.

As pressure (and corresponding strain) increases, the in-plane collagen structure undergoes a two-stage deformation process that contributes to a non-linear response to load.[27] Stress-strain testing

and polarization-sensitive imaging of collagen alignment suggest that the cornea exhibits a relatively symmetric tensile response at low strain.[27] As strain increases, fiber orientation changes in response to the applied load, aligning in the temporal-nasal inferior-superior meridians. Transient elastography studies have also observed in-plane anisotropy in the cornea starting at 15-20 mmHg and increasing with IOP.[16,136,150–152] Together, these studies suggest that corneal biomechanics become more anisotropic at high IOP, and the NITI model may no longer adequately describe it. Such changes in load-bearing characteristics at high IOP may dramatically change wave propagation and/or induce more complex anisotropic behavior. Complex anisotropic models, such as orthotropic or fibril-based models, may be required to describe corneal deformation at high IOP.

While IOP-induced prestress causes some degree of non-linear deformation in the cornea, it is known that prestress alone can strongly affect elastic wave behavior.[247,248] As seen in **Figure 6-5**, as the IOP was increased from 5 mmHg to 20 mmHg in the human cornea, the mode structure not only changes slightly, but also appears to have a low-frequency cut-off which shifts to higher frequencies. Techniques have been suggested based on additional pre-stress terms which may improve the accuracy of the NITI model, particularly over the low-frequency range.[248] Future work is required to quantify both IOP and elastic moduli (as well as their relationship) independently.

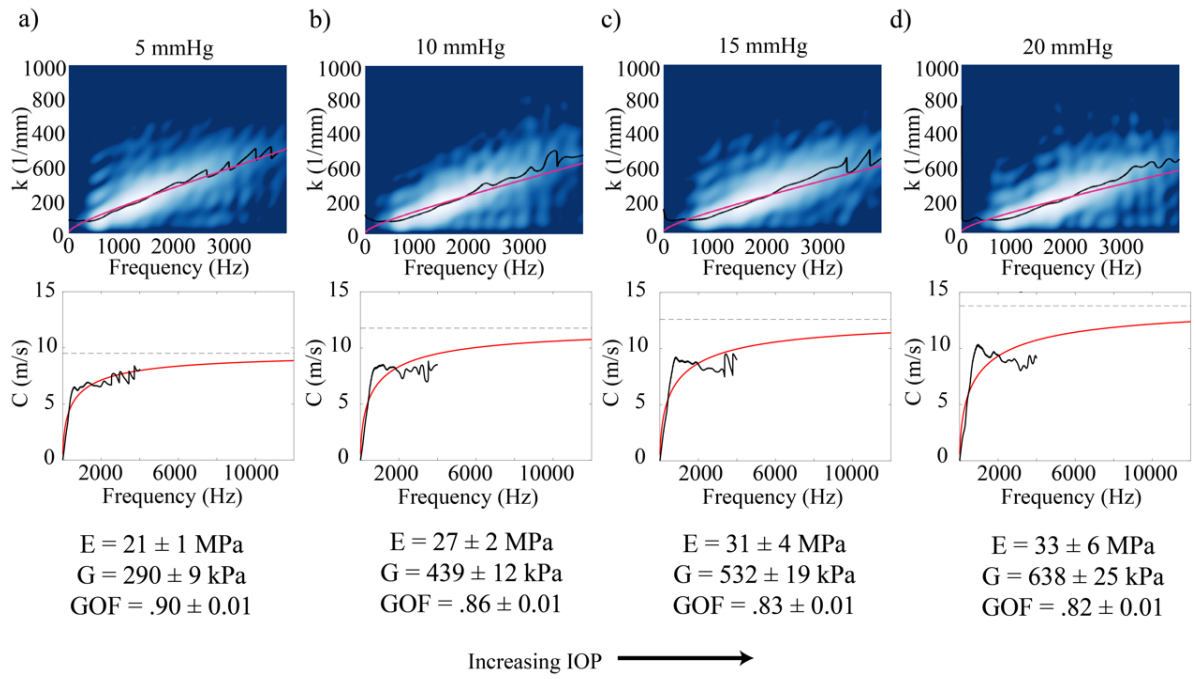

Figure 6-5. Mode structure and NITI fit with increasing IOP in human corneal buttons. Top panel corresponds with *fk*- representations and bottom panel with *cf* - representations of peak tracing (black) and optimal NITI fit (red) in a single cornea example at IOP a) 5 mmHg, b) 10 mmHg, c) 15 mmHg, and d) 20 mmHg. The reported moduli and GOF metrics correspond with the mean and variations in five human corneal samples.

The choice of regularization (used to stabilize the fitting routine) can also affect the exact estimate of μ. Consequently, there is far more uncertainty in estimated μ than G, especially for low SNR measurements, assuming the high-frequency threshold is appropriately fit. In the case where the high-frequency threshold is not appropriately fit (such as in **Figure 6-5d**), additional error in G will likely over-estimate the out-of-plane shear modulus. In this case, estimating the high frequency threshold of measured data may provide improved moduli estimates. Because of this uncertainty and the need to choose a suitable regularization parameter, future work is needed to refine these estimates.

Clearly, higher IOP induces an apparent shift in the A_0 mode structure that results in large confidence intervals for both μ and G in our measurements. However, the goodness of fit (GOF) metric described in Eq. 5.10 does not provide confidence intervals on the parameters derived from the reconstruction method presented in Chapter 5.3. This suggests that while a lower GOF corresponds with increased uncertainty, the confidence intervals remain unknown. While optimization routines posed as least-squares error problems allow for confidence interval estimation, the fitting method presented here seeks to maximize the spectral energy contained in a small weighted window around the A_0 mode which makes traditional confidence interval methods difficult to apply. Complex data fitting algorithms have been proposed to estimate confidence intervals by means such as Jacobian estimation,[249] but have not yet been explored in this work.

6.4 System improvements for real-time clinical imaging

Swept-source OCT for near-real time imaging

The system described in Chapter 4 utilizes M-B scanning, where multiple excitation events are required to reconstruct elastic wave propagation within a 2-D cross section. While M-B scanning provides exquisite phase sensitivity to small tissue motion, the total time required to acquire volumetric information of the sample is relatively long (> minutes). Long scan times are not optimal for clinical translation where imaging time is important to minimize factors such as bulk motion and improve patient comfort.

Recent advances in MHz-rate swept-laser sources can be leveraged to produce OCT B-frame rates (> kHz) fast enough to capture propagating mechanical waves within biological tissue using B-M scanning configurations.[16,220] In B-M scanning, consecutive B-scans are acquired and used to

detect motion within a 2-D cross-section (B-scan) image of wave propagation across an entire region following a single transient excitation. B-M mode provides much faster imaging that can dramatically reduce the total time required for OCE (< 1 second) but requires an ultrafast OCT system of MHz imaging speed. A-scan rates as fast as 1.5 MHz[220] and 1.628 MHz[17] have been reported using an FDML laser source and a single element detection scheme. Increased scan rates make 4-dimensional (3 in space plus time) volumetric data collection feasible for clinical applications.

In 2016, an OCE system capable of launching and tracking mechanical waves in a 6mm x 6mm x 1 mm volume in ex vivo porcine cornea in less than a second was demonstrated.[16,17] 4-dimensional tracking of waves in porcine cornea at different IOP was accomplished with total data collection in under 100 ms.[16] The phase stability was previously reported as low 39 mrad (~3 nm), with large vibration noise at frequencies above 5 kHz.

While advances in SS-OCT systems suggest that multi-megahertz A-line rate systems can provide high-quality, and even phase-stable, OCT scans,[250] technical problems due to FDML jitter, resonant scanner instabilities, single-mode fiber cables, and environmental noise, decrease system stability. An improved SS-OCT design is required for both corneal topography and elasticity to be mapped and then interleaved at speeds necessary for clinical translation of AμT-OCE. Compared to slower SD-OCT systems, the phase noise in SS-OCT systems remain a major limitation in the future development of clinically translatable systems.

Automated focusing via AμT-array

The current system design requires that the AμT-OCE transducer be manually aligned with the corneal surface. This is not a problem for pre-clinical studies, but can be an issue for clinical use, especially for mapping keratoconus patients with highly abnormal shaped cornea. Auto alignment of the imaging head with the sample surface is necessary to facilitate future clinical studies.

To address this issue, an air-coupled CMUT array transducer has been constructed[251] to electronically steer the ultrasound beam without mechanical motion. While a single element piezoelectric array has been demonstrated to efficiently generate a line-source excitation, acoustic radiation force is very flexible in terms of the excitation beam pattern and can be adopted to a specific problem geometry. Thus, phased-array transducers may be used for auto alignment and can expand the imaging range through electronically scanning the pump field across the interface.

There is a working AμT capacitive micromachined ultrasonic transducer (CMUT) array prototype, but it has not yet been tested within the current AμT-OCE system. The current prototype includes a dual-paddle 32-element CMUT phased-array capable of dynamic beam steering for automated focusing and flexible excitation. The final design (**Figure 6-6**) was determined through collaborative efforts with Dr. Omer Oralkin's group at North Carolina State University.

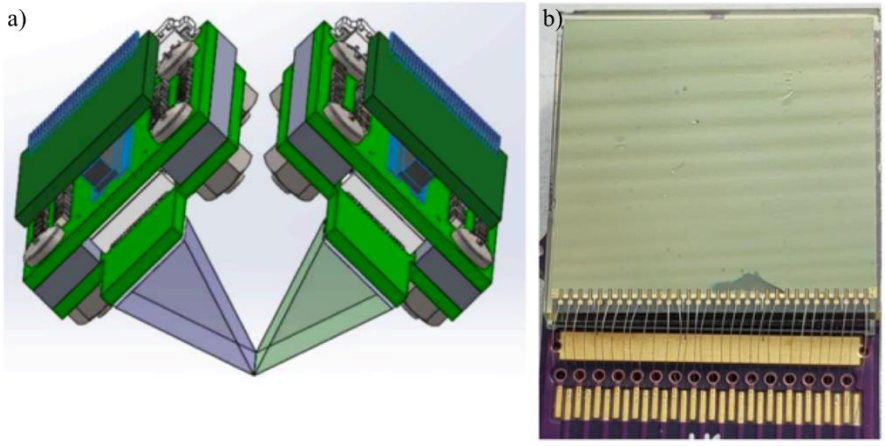

Figure 6-6. AμT CMUT array prototype. a) 3-D rendering of final design including CMUT array, electronic connections, and mounted circuit boards. b) Prototype example of 1D wire-bonded CMUT array.

An alternative design would be to apply spherically symmetric, single element confocal AμT-OCE.[252] The disadvantage of this approach is faster signal attenuation with distance due to diffraction. Clearly, there remains work to be done to optimize alignment with OCT and acoustic excitation for flexible clinical application.

Resolution

Even with typical limitations imposed by a practical measurement system, it was demonstrated in this work that the spatial resolution in dynamic OCE, when tracking mechanical wave propagation near an interface, is ultimately limited by the characteristic wavelength of the mechanical wave. The ability to accurately reconstruct an inclusion with contrast nearing that of the physical modulus breaks down when the mean pulse width is greater than the size of the physical inclusion. However, as demonstrated in Chapter 5, the full-bandwidth of the elastic pulse was required to accurately fit the measured dispersion to the A_0 mode of a NITI material model. The broadband approach suggests long wavelength components are necessary. Some preliminary work has suggested that a kernel-based approach may be used in guided materials to generate maps of spatial variation on the order of 1 to 2 mm. As such, there remains work to be done to quantify spatial resolution using dispersion in the NITI model.

While the ultimate resolution in dynamic OCE struggles to match that of its parent imaging modality, OCT, an advantage that cannot be understated is that high-resolution structural information can be acquired simultaneously with elasticity measurements. Thus, OCE can provide unique information on both mechanical modulus and tissue light scattering at a scale and speed

difficult to achieve with other imaging modalities. It follows that OCE and OCT may be combined with optical microangiography[126] and polarization-sensitive OCT to potentially provide quantitative image contrast based on tissue elasticity, optical properties, and microvasculature in a single acquisition that can be done within seconds. The combination of relatively coarse quantitative elastic modulus mapping with the high-resolution capabilities of OCT, angiography, and birefringence information may provide valuable clinical information that will likely continue to drive the future development of this technique.

Clinical package

Although the AμT-OCE system and reconstruction methods were demonstrated using ex vivo porcine and human corneas, as well as in vivo rabbit cornea, and validated with mechanical tests, significant work remains to optimize a device for clinical measurements.

In most clinical applications of ophthalmic microscopy, a slit lamp biomicroscope[253] with slit beam illumination and an optical microscope is used to enable stereoscopic, magnified, cross-sectional views of the eye. Like slit lamp biomicroscopy, OCT does not penetrate opaque tissues well but enables detailed, cross-sectional views of transparent tissues, with greater detail than with a slit lamp alone.[254] One such system that may enable future cross-validation studies of AμT-OCE will include an ultra-fast, swept-source OCT system incorporated into the slit-lamp machine for accurate alignment of the cornea relative to the OCT focal plane. The OCT optics may be integrated into a slit lamp system with robot-controlled focusing. Test measurements will be required in ex vivo porcine eyes and in healthy human volunteers to optimize all measurement and reconstruction procedures to make the system convenient and robust for ophthalmic applications. Such a design remains a focus of future efforts.

6.5 Conclusions

Because AμT-OCE appears to accurately quantify mechanical properties in the cornea, while OCT simultaneously can image its structure and shape, an OCT-based technique is a very promising direction to develop personalized biomechanical models. Assuming in vivo OCE methods can robustly and reliably measure moduli, it is likely that truly non-contact methods will pave the way for clinical translation.

A major contribution of this work is the introduction of a nearly-incompressible transverse isotropic model to describe corneal biomechanics. The model's relative simplicity should facilitate future clinical trials, as it requires a single non-contact measurement, obtained within seconds, to estimate G and E. Future studies to assess anisotropy in diseased cornea may further improve our understanding of pathologies and potentially inform treatment. The non-contact nature and consistency of AμT-driven OCE strongly support its potential as a practical clinical tool to evaluate corneal elasticity, build personalized biomechanical models, and ultimately study corneal disease as well as its response to ophthalmic interventions.

While there remain a number of limitations standing between technical development and widespread clinical use, the goal of this work is to provide a roadmap for generalization and clinical translation of OCE in the cornea.

References

1. Keeler, C. R. The ophthalmoscope in the lifetime of Hermann von Helmholtz. *Arch*. *Ophthalmol*. **120**, 194–201 (2002).

2. Barraquer, J. I. The history of the microscope in ocular surgery. *Microsurgery* **1.4**, 288–299 (1980).

3. Huang, D. *et al*. Optical Coherence Tomography. *Science (80-.)*. **254**, 1178–1181 (1991).

4. Podoleanu, A. G. *Optical coherence tomography*. *Journal of Microscopy* **247**, (2012).

5. Kashani, A. H. *et al*. Optical coherence tomography angiography: A comprehensive review of current methods and clinical applications. *Prog*. *Retin*. *Eye Res*. (2017). doi:10.1016/j.preteyeres.2017.07.002

6. Fujimoto, J. & Swanson, E. The development, commercialization, and impact of optical coherence tomography. *Investig*. *Ophthalmol*. *Vis*. *Sci*. **57**, OCT1–OCT13 (2016).

7. De Moraes, C. Risk factors for visual field progression in treated glaucoma. *Arch*. *Ophthalmol*. **129**, 878 (2011).

8. Roberts, C. Concepts and misconceptions in corneal biomechanics. *J*. *Cataract Refract*. *Surg*. **40**, 862–869 (2014).

9. Eliasy, A. *et al*. Determination of Corneal Biomechanical Behavior in-vivo for Healthy Eyes Using CorVis ST Tonometry: Stress-Strain Index. *Front*. *Bioeng*. *Biotechnol*. **7**, 1–10 (2019).

10. Chong, J. & Dupps, W. J. Corneal biomechanics: Measurement and structural correlations. *Exp*. *Eye Res*. **205**, (2021).

11. Joda, A., Shervin, M. M. S., Kook, D. & Elshiekh, A. Development and Validation of a Correction Equation for Corvis Tonometry Akram. *Comput Methods Biomech Biomed Engin*. **19**, 943–953 (2016).

12. Hashemi, H. *et al*. Long-term Results of an Accelerated Corneal Cross-linking Protocol (18 mW/cm2) for the Treatment of Progressive Keratoconus. *Am*. *J*. *Ophthalmol*. **160**, 1164-1170.e1 (2015).

13. Roberts, Cynthia J., et al. Introduction of two novel stiffness parameters and interpretation of air Puff–Induced biomechanical deformation parameters with a dynamic scheimpflug analyzer. *J*. *Refract*. *Surg*. **33**, 266–273 (2017).

14. Elsheikh, A. *et al*. Stress free configuration of the human eye. *Med*. *Eng*. *Phys*. **35**, 211–216 (2013).

15. Kirby, M. A. *et al*. Optical coherence elastography in ophthalmology. *J*. *Biomed*. *Opt*. **22**, 1 (2017).

16. Ambroziński, Ł. *et al*. Acoustic micro-tapping for non-contact 4D imaging of tissue elasticity. *Sci*. *Rep*. **6**, 38967 (2016).

17. Song, S. *et al*. Strategies to improve phase-stability of ultrafast swept source optical coherence tomography for single shot imaging of transient mechanical waves at 16 kHz frame rate. *Appl*. *Phys*. *Lett*. **108**, 1–5 (2016).

18. Kirby, M. A. *et al*. Spatial resolution in dynamic optical coherence elastography. *J*. *Biomed*. *Opt*. **24**, 1 (2019).

19. Han, Z. *et al*. Analysis of the effect of the fluid-structure interface on elastic wave velocity in cornea-like structures by OCE and FEM. *Laser Phys*. *Lett*. **13**, 035602 (2016).

20. Song, S. *et al*. Shear modulus imaging by direct visualization of propagating shear waves with phase-sensitive optical coherence tomography. *J*. *Biomed*. *Opt*. **18**, 121509 (2013).

21. Han, Z. *et al*. Quantitative assessment of corneal viscoelasticity using optical coherence elastography and a modified Rayleigh – Lamb equation of corneal viscoelasticity equation. *J*. *Biomed*. *Opt*. **20**, 2–5 (2015).

22. Larin, K. V. & Sampson, D. D. Optical coherence elastography – OCT at work in tissue biomechanics [Invited]. *Biomed*. *Opt*. *Express* **8**, 1172 (2017).

23. Wang, S. & Larin, K. V. Optical coherence elastography for tissue characterization: A review. *J*. *Biophotonics* **8**, 279–302 (2015).

24. Li, C., Guan, G., Cheng, X., Huang, Z. & Wang, R. K. Quantitative elastography provided by surface acoustic waves measured by phase-sensitive optical coherence tomography. *Opt*. *Lett*. **37**, 722 (2012).

25. Zhu, J. *et al*. 3D mapping of elastic modulus using shear wave optical micro-elastography. *Sci*. *Rep*. **6**, 35499 (2016).

26. Zhu, J. *et al*. Longitudinal shear wave imaging for elasticity mapping using optical coherence elastography. *Appl*. *Phys*. *Lett*. **110**, 201101 (2017).

27. Pitre, J. J. *et al*. Nearly-incompressible transverse isotropy (NITI) of cornea elasticity: model and experiments with acoustic micro-tapping OCE. *Sci*. *Rep*. **10**, 1–14 (2020).

28. Gandhi, S. & Jain, S. The anatomy and physiology of cornea. *Keratoprostheses Artif*. *Corneas Fundam*. *Surg*. *Appl*. **37**, 19–25 (2015).

29. Meek, K. M. & Knupp, C. Corneal structure and transparency. *Prog*. *Retin*. *Eye Res*. **49**, 1–16 (2015).

30. Meek, K. M. & Boote, C. The organization of collagen in the corneal stroma. *Exp*. *Eye Res*. **78**, 503–512 (2004).

31. Fratzl, P. & Daxer, A. Structural transformation of collagen fibrils in corneal stroma during drying. An x-ray scattering study. *Biophys*. *J*. **64**, 1210–1214 (1993).

32. Komai, Y. & Ushiki, T. The three-dimensional organization of collagen fibrils in the human cornea and sclera. *Investig*. *Ophthalmol*. *Vis*. *Sci*. **32**, 2244–2258 (1991).

33. Ottani, V., Martini, D., Franchi, M., Ruggeri, A. & Raspanti, M. Hierarchical structures in fibrillar collagens. *Micron* **33**, 587–596 (2002).

34. Koudouna, E. *et al*. Evolution of the vertebrate corneal stroma. *Prog*. *Retin*. *Eye Res*. **64**, 65–76 (2018).

35. Meek, K. M., Blamires, T., Elliott, G. F., Gyi, T. J. & Nave, C. The organisation of collagen fibrils in the human corneal stroma: A synchrotron x-ray diffraction study. *Curr*. *Eye Res*. **6**, 841–846 (1987).

36. Boote, C., Dennis, S. & Meek, K. Spatial mapping of collagen fibril organisation in primate cornea - An X-ray diffraction investigation. *J*. *Struct*. *Biol*. **146**, 359–367 (2004).

37. Borcherding, M. S. *et al*. Proteoglycans and collagen fibre organization in human corneoscleral tissue. *Exp*. *Eye Res*. **21**, 59–70 (1975).

38. Scott, J. E. & Thomlinson, A. M. The structure of interfibrillar proteoglycan bridges ('shape modules') in extracellular matrix of fibrous connective tissues and their stability in various chemical environments. *J*. *Anat*. **192**, 391–405 (1998).

39. Maurice, B. Y. D. M. The Structure and Transparency of the Cornea. *J*. *Physiol*. 263–286 (1956).

40. Winkler, M. *et al*. A comparative study of vertebrate corneal structure: The evolution of a refractive lens. *Investig*. *Ophthalmol*. *Vis*. *Sci*. **56**, 2764–2772 (2015).

41. Quantock, A. J. *et al*. From nano to macro: Studying the hierarchical structure of the corneal extracellular matrix. *Exp*. *Eye Res*. **133**, 81–99 (2015).

42. Winkler, M. *et al*. High resolution macroscopy (HRMac) of the eye using nonlinear optical imaging. *Front*. *Ultrafast Opt*. *Biomed*. *Sci*. *Ind*. *Appl*. *X* **7589**, 758906 (2010).

43. Winkler, M. *et al*. Nonlinear optical macroscopic assessment of 3-D corneal collagen organization and axial biomechanics. *Investig*. *Ophthalmol*. *Vis*. *Sci*. **52**, 8818–8827 (2011).

44. Jester, J. V. *et al*. Evaluating Corneal Collagen Organization Using High Resolution Non Linear Optical (NLO) Macroscopy*. **36**, 260–264 (2011).

45. Fan, R., Chan, T. C. Y., Prakash, G. & Jhanji, V. Applications of corneal topography and tomography: a review. *Clin*. *Exp*. *Ophthalmol*. **46**, 133–146 (2018).

46. Boote, C., Dennis, S., Huang, Y., Quantock, A. J. & Meek, K. M. Lamellar orientation in human cornea in relation to mechanical properties. *J*. *Struct*. *Biol*. **149**, 1–6 (2005).

47. Anderson, K., El-Sheikh, A. & Newson, T. Application of structural analysis to the mechanical behaviour of the cornea. *J*. *R*. *Soc*. *Interface* **1**, 3–15 (2004).

48. Thomasy, S. M. *et al*. Elastic modulus and collagen organization of the rabbit cornea: Epithelium to endothelium. *Acta Biomater*. **10**, 785–791 (2014).

49. Kotecha, A. What Biomechanical Properties of the Cornea Are Relevant for the Clinician ? *Surv*. *Ophthalmol*. **52**, 109–114 (2007).

50. Dupps, W. J. & Wilson, S. E. Biomechanics and wound healing in the cornea. *Exp*. *Eye*

Res. **83**, 709–720 (2006).

51. Andreassen, T. T., Hjorth Simonsen, A. & Oxlund, H. Biomechanical Properties of Keratoconus and Normal Corneas. *Exp*. *Eye Res* **31**, 435–441 (1980).

52. Smolek, M. K. & Klyce, S. D. Is Keratoconus a True Ectasia? **118**, (2000).

53. Hayes, S., Boote, C., Tuft, S. J., Quantock, A. J. & Meek, K. M. A study of corneal thickness, shape and collagen organisation in keratoconus using videokeratography and X-ray scattering techniques. *Exp*. *Eye Res*. **84**, 423–434 (2007).

54. Sorkin, N. & Varssano, D. Corneal collagen crosslinking: A systematic review. *Ophthalmologica* **232**, 10–27 (2014).

55. Wollensak, G., Spoerl, E. & Seiler, T. Stress-strain measurements of human and porcine corneas after riboflavin-ultraviolet-A-induced cross-linking. *J*. *Cataract Refract*. *Surg*. **29**, 1780–1785 (2003).

56. Hamilton, K. E. & Pye, D. C. Young's modulus in normal corneas and the effect on applanation tonometry. *Optom*. *Vis*. *Sci*. **85**, 445–450 (2008).

57. Elsheikh, A., Wang, D. & Pye, D. Determination of the modulus of elasticity of the human cornea. *J*. *Refract*. *Surg*. **23**, 808–818 (2007).

58. Han, Z. *et al*. Optical coherence elastography assessment of corneal viscoelasticity with a modified Rayleigh-Lamb wave model. *J*. *Mech*. *Behav*. *Biomed*. *Mater*. **66**, 87–94 (2017).

59. Singh, M. *et al*. Noncontact Elastic Wave Imaging Optical Coherence Elastography for Evaluating Changes in Corneal Elasticity Due to Crosslinking. *IEEE J*. *Sel*. *Top*. *Quantum Electron*. **22**, 1–32 (2017).

60. Tsaousis, K. T. *et al*. Measurements of elastic modulus for human anterior lens capsule

with atomic force microscopy: The effect of loading force. *Int*. *Ophthalmol*. **34**, 519–523 (2014).

61. Krag, S. & Andreassen, T. T. Mechanical properties of the human lens capsule. *Prog*. *Retin*. *Eye Res*. **22**, 749–767 (2003).

62. Hollman, K. W., O'Donnell, M. & Erpelding, T. N. Mapping elasticity in human lenses using bubble-based acoustic radiation force. *Exp*. *Eye Res*. **85**, 890–893 (2007).

63. Fisher, R. F. the Elastic Constants of the Human Lens. *J*. *Physiol* **212**, 147–180 (1971).

64. Wilde, G. S., Burd, H. J. & Judge, S. J. Shear modulus data for the human lens determined from a spinning lens test. *Exp*. *Eye Res*. **97**, 36–48 (2012).

65. Jones, I. L., Warner, M. & Stevens, J. D. Mathematical modelling of the elastic properties of retina: a determination of Young's modulus. *Eye (Lond)*. **6 (Pt 6)**, 556–559 (1992).

66. Song, S., Le, N. M., Wang, R. K. & Huang, Z. Quantitative shear wave Optical Coherence Elastography (SW-OCE) with acoustic radiation force impulses (ARFI) induced by phase array transducer. *Prog*. *Biomed*. *Opt*. *Imaging - Proc*. *SPIE* **9327**, (2015).

67. Friberg, T. R. & Lace, J. W. A comparison of the elastic properties of human choroid and sclera. *Exp*. *Eye Res*. **47**, 429–436 (1988).

68. Veldhuis, J. H., Flanagan, J. G. & Ethier, C. R. Measuring the biaxial stress-strain characteristics of human sclera. 4–5 (2007).

69. Girard, M. J. A. *et al*. Translating Ocular Biomechanics into Clinical Practice: Current State and Future Prospects. *Curr Eye Res* **40**, 1–18 (2015).

70. Bekesi, N., De La Hoz, A., Kling, S. & Marcos, S. The Effects of Cross-linking on the Static and Dynamic Corneal Viscoelastic Properties. *Assoc*. *Res*. *Vis*. *Ophthalmol*. 520461

(2014).

71. Bekesi, N., Dorronsoro, C., De La Hoz, A. & Marcos, S. Material properties from air puff corneal deformation by numerical simulations on model corneas. *PLoS One* **11**, (2016).

72. Boschetti, F., Triacca, V., Spinelli, L. & Pandolfi, A. Mechanical characterization of porcine corneas. *J*. *Biomech*. *Eng*. **134**, (2012).

73. Elsheikh, A., Alhasso, D. & Rama, P. Biomechanical properties of human and porcine corneas. *Exp*. *Eye Res*. **86**, 783–790 (2008).

74. Elsheikh, A. & Alhasso, D. Mechanical anisotropy of porcine cornea and correlation with stromal microstructure. *Exp*. *Eye Res*. **88**, 1084–1091 (2009).

75. Hatami-Marbini, H. & Etebu, E. An experimental and theoretical analysis of unconfined compression of corneal stroma. *J*. *Biomech*. **46**, 1752–1758 (2013).

76. Hatami-Marbini, H. & Etebu, E. Hydration dependent biomechanical properties of the corneal stroma. *Exp*. *Eye Res*. **116**, 47–54 (2013).

77. Hatami-Marbini, H. Viscoelastic shear properties of the corneal stroma. *J*. *Biomech*. **47**, 723–728 (2014).

78. Kling, S., Ginis, H. & Marcos, S. Corneal biomechanical properties from two-dimensional corneal flap extensiometry: Application to UV-Riboflavin cross-linking. *Investig*. *Ophthalmol*. *Vis*. *Sci*. **53**, 5010–5015 (2012).

79. Kling, S., Bekesi, N., Dorronsoro, C., Pascual, D. & Marcos, S. Corneal viscoelastic properties from finite-element analysis of in vivo air-puff deformation. *PLoS One* **9**, (2014).

80. Zeng, Y., Yang, J., Huang, K., Lee, Z. & Lee, X. A comparison of biomechanical

properties between human and porcine cornea. *J*. *Biomech*. **34**, 533–537 (2001).

81. Hoeltzel, D., Altman, P., Buzard, K. & Choe, K. Strip extensiometry for comparison of the mechanical response of bovine, rabbit, and human corneas. *J*. *Biomech*. *Eng*. **114**, 202-215. (1992).

82. Kling, S. *et al*. Numerical model of optical coherence tomographic vibrography imaging to estimate corneal biomechanical properties. *J*. *R*. *Soc*. *Interface* **11**, 20140920–20140920 (2014).

83. Petsche, S. J., Chernyak, D., Martiz, J., Levenston, M. E. & Pinsky, P. M. Depth-dependent transverse shear properties of the human corneal stroma. *Investig*. *Ophthalmol*. *Vis*. *Sci*. **53**, 873–880 (2012).

84. Sloan, S. R., Khalifa, Y. M. & Buckley, M. R. The location- and depth-dependent mechanical response of the human cornea under shear loading. *Investig*. *Ophthalmol*. *Vis*. *Sci*. **55**, 7919–7924 (2014).

85. Bryant, M., Szerenyi, K., Schmotzer, H. & McFonnell, P. Corneal tensile strength in fully healed radial keratotomy wounds. in *Invest Ophthalmol Vis Sc* 35(7):3022–31 (1994).

86. Litwiller, D. V. *et al*. MR elastography of the ex vivo bovine globe. *J*. *Magn*. *Reson*. *Imaging* **32**, 44–51 (2010).

87. Bekesi, N., Kochevar, I. E. & Marcos, S. Corneal biomechanical response following collagen cross-linking with Rose Bengal-green light and riboflavin-UVA. *Investig*. *Ophthalmol*. *Vis*. *Sci*. **57**, 992–1001 (2016).

88. Singh, M. *et al*. Quantifying the effects of hydration on corneal stiffness with noncontact optical coherence elastography. *J*. *Cataract Refract*. *Surg*. **44**, 1023–1031 (2018).

89. Elsheikh, A. *et al*. Assessment of corneal biomechanical properties and their variation with age. *Curr*. *Eye Res*. **32**, 11–19 (2007).

90. Kennedy, B. F. *et al*. Optical coherence micro-elastography: mechanical-contrast imaging of tissue microstructure. *Biomed*. *Opt*. *Express* **5**, 2113 (2014).

91. Kennedy, K. M. *et al*. Optical palpation: optical coherence tomography-based tactile imaging using a compliant sensor. *Opt*. *Lett*. **39**, 3014–7 (2014).

92. Wang, R. K., Ma, Z. & Kirkpatrick, S. J. Tissue Doppler optical coherence elastography for real time strain rate and strain mapping of soft tissue. *Appl*. *Phys*. *Lett*. **89**, 1–4 (2006).

93. Wang, R. K., Kirkpatrick, S. & Hinds, M. Phase-sensitive optical coherence elastography for mapping tissue microstrains in real time. *Appl*. *Phys*. *Lett*. **90**, (2007).

94. Schmitt, J. OCT elastography: imaging microscopic deformation and strain of tissue. *Opt*. *Express* **3**, 199–211 (1998).

95. Liang, X., Adie, S. G., John, R. & Boppart, S. a. Dynamic spectral-domain optical coherence elastography for tissue characterization. *Opt*. *Express* **18**, 14183–14190 (2010).

96. Qi, W. *et al*. Resonant acoustic radiation force optical coherence elastography. *Appl*. *Phys*. *Lett*. **103**, 1–5 (2013).

97. Adie, S. G. *et al*. Spectroscopic optical coherence elastography. *Opt*. *Express* **18**, 25519–34 (2010).

98. Mulligan, J. A., Untracht, G. R., Chandrasekaran, S. N., Brown, C. N. & Adie, S. G. Emerging Approaches for High-Resolution Imaging of Tissue Biomechanics With Optical Coherence Elastography. *IEEE J*. *Sel*. *Top*. *Quantum Electron*. **22**, (2016).

99. Song, S., Huang, Z. & Wang, R. K. Tracking mechanical wave propagation within tissue

using phase-sensitive optical coherence tomography: motion artifact and its compensation. *J*. *Biomed*. *Opt*. **18**, 121505 (2013).

100. Wang, S. & Larin, K. V. Shear wave imaging optical coherence tomography (SWI-OCT) for ocular tissue biomechanics. *Opt*. *Lett*. **39**, 41 (2014).

101. Zvietcovich, F., Rolland, J. P., Yao, J., Meemon, P. & Parker, K. J. Comparative study of shear wave-based elastography techniques in optical coherence tomography. *J*. *Biomed*. *Opt*. **22**, 035010 (2017).

102. Ford, M. R., Dupps, W. J., Rollins, A. M., Roy, A. S. & Hu, Z. Method for optical coherence elastography of the cornea. *J*. *Biomed*. *Opt*. **16**, 016005 (2011).

103. Manapuram, R. K. *et al*. In vivo estimation of elastic wave parameters using phase-stabilized swept source optical coherence elastography. *JBO Lett*. **17**, 15–18 (2012).

104. Wang, S. *et al*. A focused air-pulse system for optical-coherence-tomography-based measurements of tissue elasticity. *Laser Phys*. *Lett*. **10**, 075605 (2013).

105. Wang, S. *et al*. Noncontact measurement of elasticity for the detection of soft-tissue tumors using phase-sensitive optical coherence tomography combined with a focused air-puff system. *Opt*. *Lett*. **37**, 5184 (2012).

106. Alonso-Caneiro, D., Karnowski, K., Kaluzny, B. J., Kowalczyk, A. & Wojtkowski, M. Assessment of corneal dynamics with high-speed swept source Optical Coherence Tomography combined with an air puff system. *Opt*. *Express* **19**, 14188 (2011).

107. Li, J. *et al*. Air-pulse OCE for assessment of age-related changes in mouse cornea *in vivo*. *Laser Phys*. *Lett*. **11**, 065601 (2014).

108. Li, C., Guan, G., Huang, Z., Johnstone, M. & Wang, R. K. Noncontact all-optical

measurement of corneal elasticity. *Opt*. *Lett*. **37**, 1625 (2012).

109. Qu, Y. *et al*. Acoustic Radiation Force Optical Coherence Elastography of Corneal Tissue. *IEEE J*. *Sel*. *Top*. *Quantum Electron*. **22**, (2016).

110. Song, S., Le, N. M., Wang, R. K. & Huang, Z. Quantitative shear wave Optical Coherence Elastography (SW-OCE) with acoustic radiation force impulses (ARFI) induced by phase array transducer. *Opt*. *Lett*. **40**, **5007**–**5**, (2015).

111. Nguyen, T.-M. *et al*. Shear wave elastography using amplitude-modulated acoustic radiation force and phase-sensitive optical coherence tomography. *J*. *Biomed*. *Opt*. **20**, 016001 (2015).

112. Ambroziński, Ł. *et al*. Air-coupled acoustic radiation force for non-contact generation of broadband mechanical waves in soft media. *Appl*. *Phys*. *Lett*. **109**, (2016).

113. Jin, Z. *et al*. In-vivo 3D corneal elasticity using air-coupled ultrasound optical coherence elastography. *Biomed*. *Opt*. *Express* **10**, 6272 (2019).

114. CR., H. Physical Principles of Medical Ultrasound. in *Telehistology* (ed. CR, H.) 321–337 (Wiley, 1986).

115. Lerner, R., Parker, K., Holen, J., Gramiak, R. & Waag, R. Sono-elasticity: medical elasticity images derived from ultrasound signals in mechanically vibrated targets. *Acoust*. *imaging* pp 317-327 (1988).

116. Krouskop, T. a, Dougherty, D. R. & Vinson, F. S. A pulsed Doppler ultrasonic system for making noninvasive measurements of the mechanical properties of soft tissue. *J*. *Rehabil*. *Res*. *Dev*. **24**, 1–8 (1987).

117. Sarvazyan, A. *et al*. Biophysical bases of elasticity imaging. in *Acoustical imaging* 223–

240 (Springer US, 1995).

118. Ophir, J. *et al*. Elastography: Imaging the elastic properties of soft tissues with ultrasound. *J*. *Med*. *Ultrason*. **29**, 155–171 (2002).

119. Mariappan, Y. K., Glaser, K. J. & Ehman, R. L. Magnetic resonance elastography: A review. *Clin*. *Anat*. **23**, 497–511 (2010).

120. Muthupillai, R. *et al*. Magnetic resonance elastography by direct visualization of propagating acoustic strain waves. *Science (80-.)*. **269**, 1854–1857 (1995).

121. Nguyen, T. M. *et al*. Monitoring of cornea elastic properties changes during UV-A/riboflavin-induced corneal collagen cross-linking using supersonic shear wave imaging: A pilot study. *Investig*. *Ophthalmol*. *Vis*. *Sci*. **53**, 5948–5954 (2012).

122. Tanter, M., Touboul, D., Gennisson, J. L., Bercoff, J. & Fink, M. High-resolution quantitative imaging of cornea elasticity using supersonic shear imaging. *IEEE Trans*. *Med*. *Imaging* **28**, 1881–1893 (2009).

123. Rouze, N. C., Wang, M. H., Palmeri, M. L. & Nightingale, K. R. Parameters affecting the resolution and accuracy of 2-D quantitative shear wave images. *IEEE Trans*. *Ultrason*. *Ferroelectr*. *Freq*. *Control* **59**, 1729–1740 (2012).

124. Li, Y. *et al*. Keratoconus Diagnosis with Optical Coherence Tomography Pachymetry Mapping. *Ophthalmology* **115**, 2159–2166 (2008).

125. Wang, R. K. & Nuttall, A. L. Phase-sensitive optical coherence tomography imaging of the tissue motion within the organ of Corti at a subnanometer scale: a preliminary study. *J*. *Biomed*. *Opt*. **15**, 056005 (2010).

126. Zhang, A., Zhang, Q., Chen, C.-L. & Wang, R. K. Methods and algorithms for optical

coherence tomography-based angiography: a review and comparison. *J*. *Biomed*. *Opt*. **20**, 100901 (2015).

127. Rogowska, J., Patel, N., Fujimoto, J. & Brezinski, M. Optical coherence tomographic elastography technique for measuring deformation and strain of atherosclerotic tissues. *Heart* **90**, 556–62 (2004).

128. Ko, H., Tan, W., Stack, R. & Boppart, S. Optical coherence elastography of engineered and developing tissue. *Tissue Eng*. **12**, 63–73 (2006).

129. Michael D Twa, Gongpu Lan, Manmohan Singh, K. L. In-vivo human corneal elasticity imaging: a phase sensitive optical coherence elastography method. *Invest*. *Ophthalmol*. *Vis*. *Sci*. **58**, 4324 (2017).

130. Vinicius Silbiger De Stefano, Matthew R Ford, Ibrahim Seven, Brent Hughes, W. J. D. In-vivo Assessment of Corneal Biomechanics using Optical Coherence Elastography. *Invest*. *Ophthalmol*. *Vis*. *Sci*. **58**, 4325 (2017).

131. Pitre, J. *et al*. How University of Washington is Developing a Novel Medical Device with OnScale Simulation. *Case Study* **OnScale Ne**, (2020).

132. Pelivanov, I. *et al*. Does group velocity always reflect elastic modulus in shear wave elastography? *J*. *Biomed*. *Opt*. **24**, 1 (2019).

133. Pitre Jr., J. J. *et al*. Super-shear evanescent waves for non-contact elastography of soft tissues. *Appl*. *Phys*. *Lett*. **submitted**, unpublished (2019).

134. Viktorov, Igor, A. *Rayleigh and Lamb waves Physical Theory and Applications*. (Springer, 1967).

135. Rose, J. L. *Ultrasonic Waves in Solid Media*. (Cambridge University Press, 1999).

136. Singh, M. *et al*. Assessing the effects of riboflavin/UV-A crosslinking on porcine corneal mechanical anisotropy with optical coherence elastography. *Biomed*. *Opt*. *Express* **8**, 349–366 (2017).

137. O'Donnell, M. & Skovoroda, A. R. Prospects for Elasticity Reconstruction in the Heart. *IEEE Trans*. *Ultrason*. *Ferroelectr*. *Freq*. *Control* **51**, 322–328 (2004).

138. Landau, L. D. & Lifshitz, E. M. *Theory of Elasticity*. *Butterworth-Heinemann* **3rd ed.**, (Ox, 1986).

139. Viktorov, Igor, A. *Rayleigh and Lamb waves Physical Theory and Applications*. (Springer Science+Business Media, 1967).

140. Nenadic, I. Z., Urban, M. W., Mitchell, S. A. & Greenleaf, J. F. Lamb wave dispersion ultrasound vibrometry (LDUV) method for quantifying mechanical properties of viscoelastic solids. *Phys*. *Med*. *Biol*. **56**, 2245–64 (2011).

141. Mei, C. C. TWO DIMENSIONAL WAVES. *Massachusetts Institute of Technology; 1.138J/2.026J Wave Propagation* Chapter 3 (2004).

142. Slawinski, M. A. *Waves and Rays in Elastic Continua*. *John Wiley & Sons, Inc*. (2007). doi:10.1037/023990

143. Mclaughlin, J. & Renzi, D. Shear wave speed recovery in transient elastography and supersonic imaging using propagating fronts. **22**, 681–706 (2006).

144. Nguyen, T. *et al*. Diffuse shear wave imaging : toward passive elastography using low-frame rate spectral-domain optical coherence tomography. **21**, (2017).

145. Rolland, J. P., Zvietcovich, F., Ge, G. & Parker, K. J. Perspectives and advances in optical elastography. 15 (2019). doi:10.1117/12.2515946

146. Kruse, S. A. *et al*. Magnetic resonance elastography of the brain. **39**, 231–237 (2008).

147. Momoi, T. Scattering of Rayleigh Wave at a Vertical Boundary. *J*. *Phys*. *Earth* **20**, 435–485 (1981).

148. Fujuii, K. The scattering of Rayleigh waves at a variously inclined discontinuity. *J*. *Phys*. *Earth* **34**, 487–515 (1986).

149. Pitre, J. J. *et al*. Super-shear evanescent waves for non-contact elastography of soft tissues. *Appl*. *Phys*. *Lett*. **115**, (2019).

150. Li, J. *et al*. Revealing anisotropic properties of cornea at different intraocular pressures using optical coherence elastography. *Opt*. *Elastography Tissue Biomech*. *III* **9710**, 97100T (2016).

151. Singh, M. *et al*. Investigating Elastic Anisotropy of the Porcine Cornea as a Function of Intraocular Pressure With Optical Coherence Elastography. *J*. *Refract*. *Surg*. **32**, 562–567 (2016).

152. Nguyen, T. M., Aubry, J. F., Fink, M., Bercoff, J. & Tanter, M. In vivo evidence of porcine cornea anisotropy using supersonic shear wave imaging. *Investig*. *Ophthalmol*. *Vis*. *Sci*. **55**, 7545–7552 (2014).

153. Winkler, M. *et al*. Three-dimensional distribution of transverse collagen fibers in the anterior human corneal stroma. *Investig*. *Ophthalmol*. *Vis*. *Sci*. **54**, 7293–7301 (2013).

154. Li, L. Y. & Tighe, B. The anisotropic material constitutive models for the human cornea. *J*. *Struct*. *Biol*. **153**, 223–230 (2006).

155. Auld, B. *Acoustic fields and waves in solids*. (R.E. Krieger., 1990).

156. Barnett, D. M. Synthesis of the sextic and the integral formalism for dislocations, Green's

function and surface waves in anisotropic elastic solids." Ph. *Phys*. *Norv* **13**, (1973).

157. Chadwick, P. & Smith, G. *Foundations of the Theory of Surface Waves in Anisotropic Elastic Materials*. *In Advances in Applied Mechanics*. (Elsevier Science & Technology., 1977).

158. Ting, T. C. T. The Stroh Formalism. *Anisotropic Elast*. *Theory Appl*. 155–184 (1996).

159. Tanuma, K. *Stroh Formalism and Rayleigh Waves*. (Journal of Elasticity, 2007).

160. Eltony, A. M., Shao, P. & Yun, S.-H. Measuring mechanical anisotropy of the cornea with Brillouin microscopy. 1–19 (2020).

161. Nguyen, T. D. & Boyce, B. L. An inverse finite element method for determining the anisotropic properties of the cornea. *Biomech*. *Model*. *Mechanobiol*. **10**, 323–337 (2011).

162. Singh, M. *et al*. Investigating Elastic Anisotropy of the Porcine Cornea as a Function of Intraocular Pressure With Optical Coherence Elastography. *J*. *Refract*. *Surg*. **32**, 562–567 (2016).

163. Elsheikh, A. & Anderson, K. Comparative study of corneal strip extensometry and inflation tests. *J*. *R*. *Soc*. *Interface* **2**, 177–85 (2005).

164. Timoshenko, S. & Woinowsky-Krieger, S. *Theory of plates and shells*. (1987).

165. Yust, B. G., Mimun, L. C. & Sardar, D. K. Optical absorption and scattering of bovine cornea, lens, and retina in the near-infrared region. *Lasers Med*. *Sci*. **27**, 413–422 (2012).

166. Berg, J. T. P. Van Den & Spekreijse, H. Near Infrared Light Absorption in the Human Eye Media. *Vision Res*. **37**, 249–253 (1997).

167. Asam, J. S., Polzer, M., Tafreshi, A., Hirnschall, N. & Findl, O. Anterior Segment OCT.

in *High Resolution Imaging in Microscopy and Ophthalmology* 285–299 (2019). doi:10.1007/978-3-030-16638-0

168. Schulmeister, K. The upcoming new editions of IEC 60825–1 and ANSI Z136.1—Examples on impact for classification and exposure limits. in *Proceeding of the International Laser Safety Conference* 330–337. (2013).

169. Elsner, A. E. & Muller, M. S. Laser applications and system considerations in ocular imaging. *Laser Photonics Rev*. **2**, 350–376 (2008).

170. Hu, Z. & Rollins, A. M. optical design for OCT. *Opt*. *Coherence Tomogr*. *Technol*. *Appl*. *Second Ed*. 357–384 (2015). doi:10.1007/978-3-319-06419-2_11

171. Wojtkowski, M. *et al*. Ultrahigh-resolution, high-speed, Fourier domain optical coherence tomography and methods for dispersion compensation. *Opt*. *Express* **12**, 707–709 (2004).

172. Nassif, N. A. *et al*. In vivo high-resolution video-rate spectral-domain optical coherence tomography of the human retina and optic nerve. *Opt*. *Express* **12**, 367 (2004).

173. Hosseiny, H. & Carmelo Rosa, C. Design and optimization of a spectrometer for spectral domain optical coherence tomography. *Second Int*. *Conf*. *Appl*. *Opt*. *Photonics* **9286**, 92864Z (2014).

174. Song, S. Shear Wave Elastography Based on Optical Coherence Tomography. *University of Dundee* (2014).

175. Gelikonov, V. M., Gelikonov, G. V. & Shilyagin, P. A. Linear-wavenumber spectrometer for high-speed spectral-domain optical coherence tomography. *Opt*. *Spectrosc*. **106**, 459–465 (2009).

176. Rollins, A. M., Hu, Z. & Rollins, A. M. Fourier domain optical coherence tomography

with a linear-in-wavenumber spectrometer Fourier domain optical coherence tomography with a linear-in-wavenumber spectrometer. *Opt*. *Lett*. **32**, 3525–3527 (2007).

177. Dorrer, C. *et al*. Spectral resolution and sampling issues in Fourier-transform spectral interferometry Spectral resolution and sampling issues in Fourier-transform spectral interferometry. (2000). doi:10.1364/JOSAB.17.001795

178. Lan, G. & Li, G. Design of a k -space spectrometer for ultra-broad waveband spectral domain optical coherence tomography. *Nat*. *Publ*. *Gr*. 1–8 (2017). doi:10.1038/srep42353

179. Wang, R. K., Kirkpatrick, S. & Hinds, M. Phase-sensitive optical coherence elastography for mapping tissue microstrains in real time. *Appl*. *Phys*. *Lett*. **90**, (2007).

180. Park, B. H. *et al*. Real-time fiber-based multi-functional spectral- domain domain optical coherence tomography at 1 . 3 μ m. *Opt*. *Express* **13**, 3931–3944 (2005).

181. Xu, J., Song, S., Li, Y. & Wang, R. K. Complex-based OCT angiography algorithm recovers microvascular information better than amplitude-or phase-based algorithms in phase-stable systems. *Phys*. *Med*. *Biol*. **63.1**, (2017).

182. Zhang SX, Chan LS, X. . *J*. *Pure Appl Geophys* **161**, 185–201 (2004).

183. American Society for Metals. & ASM International. Handbook Committee. *Nondestructive evaluation and quality control*. (ASM International, 1989).

184. Gómez Alvarez-Arenas, T. E. Acoustic impedance matching of piezoelectric transducers to the air. *IEEE Trans*. *Ultrason*. *Ferroelectr*. *Freq*. *Control* **51**, 624–33 (2004).

185. Sharma, A. & Soo, M. Acoustic radiation force impulse imaging of in vivo breast masses. *Ultrason. ...* **00**, 728–731 (2004).

186. Song, S., Le, N. M., Huang, Z. & Wang, R. K. High speed imaging of remotely induced

shear waves using phasesensitive optical coherence tomography. *Prog*. *Biomed*. *Opt*. *Imaging - Proc*. *SPIE* **9312**, (2015).

187. Rouze, N. C., Wang, M. H., Palmeri, M. L. & Nightingale, K. R. Robust estimation of time-of-flight shear wave speed using a Radon sum transformation. *Proc*. - *IEEE Ultrason*. *Symp*. **57**, 21–24 (2010).

188. Minton, J. A., Iravani, A. & Yousefi, A. M. Improving the homogeneity of tissue-mimicking cryogel phantoms for medical imaging. *Med*. *Phys*. **39**, 6796–6807 (2012).

189. Yengul, S. S., Barbone, P. E. & Madore, B. Dispersion in Tissue-Mimicking Gels Measured with Shear Wave Elastography and Torsional Vibration Rheometry. *Ultrasound Med*. *Biol*. **45**, 586–604 (2019).

190. Houston, W. V. *Principles of mathematical physics*. (McGraw-Hill Book Company, 1948).

191. Rayleigh, L. Acoustical observations. *London, Edinburgh, Dublin Philos*. *Mag*. *J*. *Sci*. **7.42**, 261–274 (1879).

192. Righetti, R., Srinivasan, S. & Ophir, J. Lateral resolution in elastography. *Ultrasound Med*. *Biol*. **29**, 695–704 (2003).

193. Righetti, R., Ophir, J. & Ktonas, P. Axial resolution in elastography. *Ultrasound Med*. *Biol*. **28**, 101–113 (2002).

194. Dekker, A. J. Den & Bos, A. Van Den. Resolution : a survey. **14**, 547–557 (1997).

195. Hepburn, M. S., Wijesinghe, P., Chin, L. & Kennedy, B. F. Analysis of spatial resolution in phase-sensitive compression optical coherence elastography. *Biomed*. *Opt*. *Express* **10**, 1496 (2019).

196. Deffieux, T., Gennisson, J. L., Bercoff, J. & Tanter, M. On the effects of reflected waves in transient shear wave elastography. *IEEE Trans. Ultrason. Ferroelectr. Freq. Control* **58**, 2032–2035 (2011).

197. Belytschko, T. & Bindeman, L. P. Assumed strain stabilization of the 4-node quadrilateral with 1-point quadrature for nonlinear problems. *Comput. Methods Appl. Mech. Eng.* **88**, 311–340 (1991).

198. Kausel, E. Fundamental solutions in elastodynamics, a compendium. *New York, NY Cambridge Univ. Press.* (2006).

199. De Hoop, A. T. The surface line source problem in elastodynamics. *Ingenieur, Electron. en Telecommunicatie* pp ET19-ET21. (1970).

200. Schroder, C. T. & Scott, W. R. On the complex conjugate roots of the Rayleigh equation : The leaky surface wave. **110**, 2867–2877 (2001).

201. Phinney, R. A. Propagation of leaking interface waves. *Bull. Seismol. Soc. Am.* **51**, 527–555 (1961).

202. Benech, N., Brum, J., Grinspan, G., Aguiar, S. & Negreira, C. A. Analysis of the transient surface wave propagation in soft-solid elastic plates. *J. Acoust. Soc. Am.* **142**, 2919–2932 (2017).

203. Goff, A. Le, Cobelli, P. & Lagubeau, G. Supershear Rayleigh Waves at a Soft Interface. **236101**, 1–5 (2013).

204. Roth, M. & Klaus, H. The non-geometric PS wave in high-resolution seismic data: observations and modelling. *Geophys. J. Int.* **140**, F5–F11 (2000).

205. Scruby, C. B. Some applications of laser ultrasound. *Ultrasonics* **27**, 195–209 (1989).

206. Lipman, S. L., Rouze, N. C., Palmeri, M. L. & Nightingale, K. R. Evaluating the improvement in shear wave speed image quality using multidimensional directional filters in the presence of reflection artifacts. *IEEE Trans. Ultrason. Ferroelectr. Freq. Control* **63**, 1049–1063 (2016).

207. Vogel, F., Holm, S. & Lingaerde, O. C. Spectral Moments and the Time Domain representation of photoacoustic signals used for detection of crude oil in produced water. *Proc. Nord. Symp. Phys. Acoust. Ustaoset, Norway*. (2001).

208. Deffieux, T., Gennisson, J. L., Larrat, B., Fink, M. & Tanter, M. The variance of quantitative estimates in shear wave imaging: Theory and experiments. *IEEE Trans. Ultrason. Ferroelectr. Freq. Control* **59**, 2390–2410 (2012).

209. Oliphant, T. E., Manduca, A., Ehman, R. L. & Greenleaf, J. F. Complex-Valued Stiffness Reconstruction for Magnetic Resonance Elastography by Algebraic Inversion of the Differential Equation. **310**, 299–310 (2001).

210. Palmeri, M. L., Rouze, N. C., Wang, M. H., Ding, X. & Nightingale, K. R. Quantifying the impact of shear wavelength and kernel size on shear wave speed estimation. *Proc. - IEEE Ultrason. Symp.* 13–16 (2010). doi:10.1109/ULTSYM.2010.5935798

211. Venkatesh, S. K., Yin, M. & Ehman, R. L. Magnetic Resonance Elastography of Liver: Technique, Analysis and Clinical Applications. *J Magn Reson Imaging* **37**, 544–555 (2014).

212. Hollender, P., Bottenus, N. & Trahey, G. A multiresolution approach to shear wave image reconstruction. *IEEE Trans. Ultrason. Ferroelectr. Freq. Control* **62**, 1429–1439 (2015).

213. Kennedy, B. F. *et al*. Strain estimation in phase-sensitive optical coherence elastography.

Biomed. *Opt*. *Express* **3**, 1865–79 (2012).

214. Chin, L. *et al*. Analysis of image formation in optical coherence elastography using a multiphysics approach. *Biomed*. *Opt*. *Express* **5**, 2913 (2014).

215. Miller, D. T., Kocaoglu, O. P., Wang, Q. & Lee, S. Adaptive optics and the eye (super resolution OCT). *Eye* **25**, 321–330 (2011).

216. Schmidl, D. *et al*. Ultrahigh-resolution OCT imaging of the human cornea. *Biomed*. *Opt*. *Express* **8**, 1221 (2017).

217. Nahas, A. *et al*. From supersonic shear wave imaging to full-field optical coherence shear wave elastography. *J*. *Biomed*. *Opt*. **18**, 121514 (2013).

218. Nightingale, K. Acoustic Radiation Force Impulse (ARFI) Imaging: a Review. *Curr Med Imaging Rev* **7**, 328–339 (2012).

219. McCracken, P. J., Manduca, A., Felmlee, J. & Ehman, R. L. Mechanical transient-based magnetic resonance elastography. *Magn*. *Reson*. *Med*. **53**, 628–639 (2005).

220. Singh, M. *et al*. Phase-sensitive optical coherence elastography at 1.5 million A-Lines per second. *Opt*. *Lett*. **40**, 2588 (2015).

221. Kennedy, B. F., Wijesinghe, P. & Sampson, D. D. The emergence of optical elastography in biomedicine. *Nat*. *Publ*. *Gr*. **11**, 215–221 (2017).

222. Kennedy, B. F., Kennedy, K. M. & Sampson, D. D. A review of optical coherence elastography: Fundamentals, techniques and prospects. *IEEE J*. *Sel*. *Top*. *Quantum Electron*. **20**, (2014).

223. Papazoglou, S. Physics in Medicine & Biology Algebraic Helmholtz inversion in planar magnetic resonance elastography Algebraic Helmholtz inversion in planar magnetic

resonance elastography. (2008). doi:10.1088/0031-9155/53/12/005

224. Litwiller, D. V., Mariappan, Y. K. & Richard L., E. Magnetic Resonance Elastography. *Curr Med Imaging Rev*. **8**, 46–55 (2015).

225. Boulet, T., Kelso, M. L. & Othman, S. F. Microscopic magnetic resonance elastography of traumatic brain injury model. *J*. *Neurosci*. *Methods* **201**, 296–306 (2011).

226. Othman, S. F., Xu, H., Royston, T. J. & Magin, R. L. Microscopic Magnetic Resonance Elastography (□ MRE). **615**, 605–615 (2005).

227. Berthelot, D. R. & H., C. Y. Dispersion curve analysis of laser- generated Lamb waves. *Ultrasonics* **32**, 249–253 (1994).

228. Alleyne, D. N. & P. Cawley. A two-dimensional Fourier transform for the measurement of propagating multimode signals. *J*. *Acoust*. *Soc*. *Am*. **89**, 1159–1168 (1991).

229. Krauklis, P. V. & Molotkov, L. A. Low-frequency Lamb waves in cylindrical and spherical layers in an elastic medium. *J*. *Math*. *Sci*. **3**, 82–90 (1975).

230. Brekhovskikh, L. M. *Waves in Layered Media*. (Academic Press, 1976).

231. Lin, R. C., Shure, M. A., Rollins, A. M., Izatt, J. A. & Huang, D. Group index of the human cornea at 13-μm wavelength obtained in vitro by optical coherence domain reflectometry. *Opt*. *Lett*. **29**, 83 (2004).

232. Hatami-Marbini, H. Viscoelastic shear properties of the corneal stroma. *J*. *Biomech*. **47**, 723–728 (2014).

233. Khan, M. A., Elsheikh, A., Rizvi, Z. H. & Ahmad Khan, I. Influence of analytical methods versus clamping procedure on biomechanical response of cornea through experimental strip tests. *Mater*. *Today Proc*. (2020). doi:10.1016/j.matpr.2020.10.566

234. Hatami-Marbini, H. & Jayaram, S. M. Effect of UVA/riboflavin collagen crosslinking on biomechanics of artificially swollen corneas. *Investig*. *Ophthalmol*. *Vis*. *Sci*. **59**, 764–770 (2017).

235. Lanchares, E., Del Buey, M. A., Cristóbal, J. A., Lavilla, L. & Calvo, B. Biomechanical property analysis after corneal collagen cross-linking in relation to ultraviolet A irradiation time. *Graefe's Arch. Clin. Exp. Ophthalmol.* **249**, 1223–1227 (2011).

236. Aslanides, I. M. *et al*. Assessment of UVA-Riboflavin Corneal Cross-Linking Using Small Amplitude Oscillatory Shear Measurements. *Invest*. *Ophthalmol*. *Vis*. *Sci*. **57**, 2240–2245 (2016).

237. Søndergaard, A. P., Ivarsen, A. & Hjortdal, J. Corneal resistance to shear force after UVA-riboflavin cross-linking. *Investig*. *Ophthalmol*. *Vis*. *Sci*. **54**, 5059–5069 (2013).

238. Lanir, Y. Mechanisms of residual stress in soft tissues. *J*. *Biomech*. *Eng*. **131**, 1–5 (2009).

239. Racia, A. R., Urita, J. Z. & In, D. P. P. Automatized Patient-Specific Methodology for Numerical Determination of Biomechanical Corneal Response. **44**, 1753–1772 (2016).

240. Ramier, A., Tavakol, B. & Yun, S.-H. Measuring mechanical wave speed, dispersion, and viscoelastic modulus of the cornea using optical coherence elastography. *Opt*. *Express* **27**, 16635 (2019).

241. Schachar, R. A. & Abolmaali, A. Proper Material Properties Are Required for the Finite Element Method. *October* 160–161 (2007).

242. Wang, S. & Hatami-Marbini, H. Constitutive Modelling of Cornea Tissue; Influence of Three-Dimensional Collagen Fiber Microstructure. *J*. *Biomech*. *Eng*. (2020). doi:10.1115/1.4048401

243. Pandolfi, A. Cornea modelling. *Eye Vis*. **7**, 1–15 (2020).

244. Chan, E. & Snibson, G. R. Current status of corneal collagen cross-linking for keratoconus: A review. *Clin*. *Exp*. *Optom*. **96**, 155–164 (2013).

245. Kohlhaas, M. *et al*. Biomechanical evidence of the distribution of cross-links in corneastreated with riboflavin and ultraviolet a light. *J*. *Cataract Refract*. *Surg*. **32**, 279–283 (2006).

246. Liu, J. & Roberts, C. J. Influence of corneal biomechanical properties on intraocular pressure measurement: Quantitative analysis. *J*. *Cataract Refract*. *Surg*. **31**, 146–155 (2005).

247. Pau, A. & Lanza di Scalea, F. Nonlinear guided wave propagation in prestressed plates. *J*. *Acoust*. *Soc*. *Am*. **137**, 1529–1540 (2015).

248. Peddeti, K. & Santhanam, S. Dispersion curves for Lamb wave propagation in prestressed plates using a semi-analytical finite element analysis. *J*. *Acoust*. *Soc*. *Am*. **143**, 829–840 (2018).

249. Donaldson, J. R. & Schnabel, R. B. Computational experience with confidence regions and confidence intervals for nonlinear least squares. *Technometrics* **29**, 67–82 (1987).

250. Wieser, W., Biedermann, B. R., Klein, T., Eigenwillig, C. M. & Huber, R. Multi-megahertz OCT: High quality 3D imaging at 20 million A-scans and 4.5 GVoxels per second. *Opt*. *Express* **18**, 14685–14704 (2010).

251. Coutant, Zachary A., et al. Wideband Air-Coupled CMUT Arrays for Acoustic Micro-Tapping. *2020 IEEE Int*. *Ultrason*. *Symp*. **IEEE**, (2020).

252. Zvietcovich, F. *et al*. Confocal air-coupled ultrasonic optical coherence elastography

probe for quantitative biomechanics. *Opt*. *Lett*. **45**, 6567 (2020).

253. Martin, R. Cornea and anterior eye assessment with slit lamp biomicroscopy, specular microscopy, confocal microscopy, and ultrasound biomicroscopy. *Indian J*. *Ophthalmol*. **66**, 195 (2018).

254. Wong, H. T. *et al*. Comparison of slitlamp optical coherence tomography and scanning peripheral anterior chamber depth analyzer to evaluate angle closure in asian eyes. *Arch*. *Ophthalmol*. **127**, 599–603 (2009).